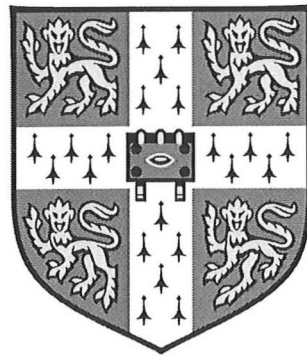


PhD. 32232

UNIVERSITY OF CAMBRIDGE

Department of Engineering



Multistable and morphing
corrugated shell structures

by

Alexander David Norman

Christ's College



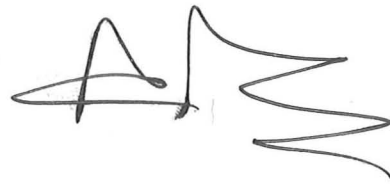
This dissertation is submitted for the degree of

Doctor of Philosophy

Supervisor: Dr K. A. Seffen

March 11, 2009

This dissertation is the result of my own work and includes nothing which is the outcome of work done in collaboration except where specifically indicated in the text. It contains, inclusive of everything, 60,000 words and 105 figures.

A handwritten signature in black ink, appearing to read 'Alex Norman'. The signature is stylized, with a large, looped 'A' and a 'N' that has a long, sweeping tail extending to the right.

Alex Norman
March 11, 2009

Summary

'Compliant' structures, *i.e.*, structures that undergo large deformations as part of their normal behaviour, can perform the function of a complex mechanism with just a single, or very few, components. When multistability is introduced into compliant structures, an even greater simplification can be made, with actuators and/or locking mechanisms becoming redundant. Corrugated shells are commonly encountered at all scales of engineering, providing shell structures of a dramatically increased stiffness at little extra cost or weight. What is historically less understood is the *compliant* behaviour of corrugated shells. The topic of this thesis, therefore, is the development and analysis of new categories of structure incorporating corrugations, utilising their compliancy to achieve morphing behaviours that are not otherwise possible. Three distinct categories of shell are studied:

- (i) 'flat' corrugated sheets, which are multistable under the action of internal stresses, 'snapping' between their flat state and a cylindrically coiled state: these shells are also capable of developing 'twisted' stable states. An algebraic model based on internal strain energy determines the conditions for the various modes of multistability for uniform changes in curvature throughout the shell, and a plastic flow model describes the formation of the internal stresses;
- (ii) 'curved' corrugated sheets, which can morph between shapes of differing Gaussian curvature without plastic deformation. Again, a simplified algebraic model describes their behaviour, as does a numerical model. These models consider the strong coupling that occurs between bending and stretching in corrugated shells; and
- (iii) 'doubly-corrugated' sheets, similar to an eggbox in concept, which, again, can morph between shapes of different Gaussian curvature, and also exhibit synclastic bending behaviour. Some of the analyses performed on the curved corrugated sheets are also applied to these shells.

The qualitative behaviour of the analytical models matches, in every detail considered, the behaviour observed in prototypes. Natural-mode analyses on the category (ii) and (iii) shells demonstrate that the interesting behaviour occurs at relatively low stiffnesses, implying that this behaviour is potentially useful.

Quantitatively, however, the analyses for categories (i) and (iii) above do not prove simple to verify. Physical tests compare the internal stresses of the category (i) shells to those predicted by the plastic flow analysis: the predicted stresses exceed those measured by, typically, 50 %, but it is not established whether the discrepancy is due to the simplifications in the model, inaccuracies in the crude test method or a flaw in our understanding. On its prediction of the curvatures created, the model is more successful.

A test is more easily devised for the category (ii) shells, and measurements of the shape-change are within 4 % of both the finite-element simulations and the simplified algebraic models over 90 % of the test range. In measuring forces, to test the constitutive relations produced; the accuracy is lower, largely due to the difference between our material model and the real properties of the polymer used: there is strong agreement between the finite-element model and the algebraic model.

In conclusion, this thesis is successful in generating new varieties of structure, which have a wide potential for application. A broad range of designs and analyses are presented, describing the behaviour of these structures well enough that our understanding of them seems justified. Nonetheless, this work merely scratches the surface of what may be achieved in this field, demonstrating some of the potential of such shells and leaving much to be done in their further evaluation and development.

Acknowledgements

I would like to acknowledge the abundant effort, time and advice given by my supervisors, both Drs Keith Seffen and Simon Guest. I am also grateful for the practical assistance from Roger Denston, Alistair Ross and Peter Knott; to William Mulholland, my predecessor in multistable corrugated sheets; and to my family, friends and colleagues for their ever-dependable support and encouragement.

Contents

Nomenclature	5
Glossary	8
1 Introduction	10
1.1 The shells studied	15
1.1.1 Multistable corrugated shells	15
1.1.2 Curved corrugated shells	17
1.1.3 Doubly-corrugated shells	18
1.2 Overview of this thesis	20
2 Literature review	21
2.1 Corrugated shells	22
2.1.1 Stiffness and strength	22
2.1.2 Manufacturing	27
2.1.3 Eggboxes	28
2.2 Compliant structures	31
2.2.1 Compliant trusses	31
2.2.2 Compliant shells	33
2.3 Multistable structures	37
2.3.1 Popular applications	37
2.3.2 Academic research	38
2.4 Summary	41
3 Concepts and methods	42
3.1 Lines and surfaces	43
3.1.1 Intrinsic line properties	43
3.1.2 Intrinsic surface properties	43
3.1.3 Corrugation terminology	46
3.2 Elasticity	47
3.2.1 Constitutive relations	47

3.2.2	Energy and stability	48
3.2.3	Modal analysis	50
3.3	Plasticity	56
3.3.1	Ideal plastic material	56
3.3.2	Yield criteria	57
3.3.3	Plastic flow	58
3.4	Equipment	60
4	Flat corrugated (i)	61
4.1	Analysis approach	63
4.2	Analytical model	64
4.2.1	Stiffness and energy	64
4.2.2	Combining the local and global scales	66
4.2.3	Corrugation profile	67
4.2.4	Limitations	69
4.3	Model behaviour	70
4.3.1	Mode I: Coiling bistability	70
4.3.2	Mode II: Twisting bistability	77
4.3.3	Mode III: Tristability	81
4.4	Conclusions	84
5	Flat corrugated (ii)	85
5.1	Manufacturing	86
5.1.1	Manufacturing methods	86
5.1.2	Observations	88
5.2	Plastic flow analysis	95
5.2.1	Analysis of first yield	95
5.2.2	Plastic analysis of forming	96
5.3	Physical testing	109
5.3.1	Plastic testing	109
5.3.2	Internal stresses	111
5.4	Conclusions	115
6	Curved corrugated (i)	116
6.1	Definitions	119
6.2	Unidirectional bending	121
6.2.1	Unidirectional model	121
6.2.2	Unidirectional validation	126
6.3	Bidirectional bending	132
6.3.1	Bidirectional model	132

6.3.2	Bidirectional validation	133
6.3.3	Gaussian curvature	135
6.4	Conclusions	139
7	Curved corrugated (ii)	140
7.1	Modal analysis	141
7.1.1	Finite element model	141
7.1.2	Natural-mode results	142
7.2	Constitutive relations	146
7.2.1	Curvatures and strains	146
7.2.2	Stiffness	148
7.2.3	Testing	151
7.3	Conclusions	154
8	Doubly-corrugated	155
8.1	Physical models	156
8.1.1	Paper models	156
8.1.2	Vacuum-formed models	160
8.1.3	Chocolate trays and eggboxes	161
8.1.4	Summary of behaviour	161
8.2	Modal analyses	165
8.2.1	Folded-plate modal analysis	165
8.2.2	Finite-element modal analysis	170
8.2.3	Discussion of the modal results	171
8.3	Conclusions	176
9	In summary	177
9.1	Further work	178
9.1.1	Quantitative verification	178
9.1.2	More complex forms	178
9.2	Final conclusions	180
	Bibliography	181
A	Bistable sandwich structures	186
B	Elastic properties	188
C	Locking of sinusoidal corrugations	193
D	Differential geometry applied to shape change	197

Nomenclature

Variables

ε	Strain
θ	Angle [degrees °]
κ	Curvature [m^{-1}]
λ	Corrugation wavelength [m]
ν	Poisson's ratio
σ	Stress
τ	Twist
ω	Frequency [rad s^{-1}]
K	Gaussian, or double, curvature [m^{-2}]
Λ	Corrugation wavelength, mapped onto the shell's mid-surface [m]
a	Height of the corrugation above the mid-plane of the sheet at a point
b	Unit normal vector to a line, perpendicular to the plane of its curvature
c	Corrugation curvature [m^{-1}]
d	Vector of cartesian nodal displacements
k	Average curvature over a shell [m^{-1}]
n	Unit normal vector to a line, in the plane of its curvature
p	Vector of cartesian nodal forces
r	Radial axis of a circle or ellipse [m]
s	Intrinsic coordinate along a path [m]
t	Local shell thickness [m]
t	Unit tangent vector to a line
w	Absolute local out-of-plane distortion of the shell [m]
x, y, z	Local coordinates in the shell, with z normal to the plane of the shell
x	Three-dimensional vector describing the position of a point
A	Peak-to-trough amplitude of corrugations [m]
D	Bending stiffness [N m]
E	Young's Modulus [N m^{-2}]
I	Identity matrix

K	Stiffness matrix
M	Bending moment per unit length [N]
M	Mass matrix
N	Force per unit length [N m ⁻¹]
T	Total kinetic energy
U	Energy per unit area relative to an initial state [N m ⁻¹]
V	Total potential energy
X, Y, Z	Coordinates in the equivalent mid-surface of the shell, with Z normal to the plane of the mid-surface and X aligned along a corrugation

Subscripts, superscripts and operators

bold	Vector or matrix quantity, <i>i.e.</i> a first- or second-order tensor
$\bar{()}$	Mean average over the material area/length, generally interpreted as mean average over one corrugation
$\dot{()}, \ddot{()}...$	First, second <i>ℰc.</i> derivative with respect to time
$()', ()''...$	Value at first, second <i>ℰc.</i> iterations of an algorithm
$()_0$	Initial state
$()_g$	(of curvature) Geodesic value
$()_{ij}$	Second-order tensor in local coordinates
$()_y$	Value at yield
$()_E$	Value at an equilibrium point
$()_{IJ}$	Second-order tensor in global coordinates
$()_M$	Value at a local energy minimum, <i>i.e.</i> a stable point
$()^P$	Value at full plasticity
δ	A small incremental change
Δ	Change relative to a predefined initial state

Dimensionless groups

Dimensionless groups for Sections 4.3.1 and 4.3.3

α	Increase in the X -direction stiffness of the shell due to corrugations
β	c/c_0
\hat{c}_0	$c_0 t$
\hat{k}	k/c_0
\hat{M}	$-M/Dc_0$
\hat{U}	$\bar{U}/\frac{1}{2}Dc_0^2$

Dimensionless groups for Section 4.3.2

α	Increase in the X -direction stiffness of the shell due to corrugations
\tilde{k}	k/k_0
\tilde{M}	$-M/Dk_0$
\tilde{U}	$\bar{U}/\frac{1}{2}Dk_0^2$

Dimensionless groups for Chapters 6 and 7

ϵ_{YY}	Λ/λ , interpreted as Y - Y strain relative to the state at which the corrugations are completely flattened out
-----------------	--

Acronyms

CuBe	Copper-Beryllium alloy
CUED	Cambridge University Engineering Department
<i>e.g.</i>	<i>exempli gratia</i> , literally, 'for the sake of example'
<i>& al.</i>	<i>et alii</i> , literally, 'and others'
<i>&c.</i>	<i>et cetera</i> , literally, 'and the rest'
EPP	Elastic-Perfectly-Plastic
FIA	<i>Fédération Internationale de l'Automobile</i> , literally, the 'International Automobile Federation'
HIPS	High-Impact Polystyrene
<i>i.a.</i>	<i>inter alios</i> , literally, 'among others'
<i>i.e.</i>	<i>id est</i> , literally, 'that is (to say)'
RMS	'Root Mean Square' value of a property, <i>i.e.</i> , the square root of the time- or space-average of the property's square
UAV	Unmanned Aerial Vehicle
UTS	Ultimate Tensile Stress

Glossary

Anticlastic	Of a shell: curvature in one principle direction produces a bending stress in the other principle direction of the <i>opposite</i> sense, as seen in an isotropic shell, tending to create a saddle shape; opposite of <i>synclastic</i>
Aeroelasticity	The elastic response of a structure to the aerodynamic loads imposed upon it: this response will, in turn, affect the fluid flows and hence affect the aerodynamic loadings, <i>i.e.</i> aeroelasticity will inevitably involve feedback effects
Angular Defect	Of a vertex made of plates: 360° less the sum of the internal angles of the corners of the individual plates
Anisotropic	Of a material: its stiffness properties vary with the direction of loading
Bistable	Of a structure: see <i>multistable</i> , but with exactly two stable shapes
Compliant	Of a structure: designed to undergo significant elastic deformations within its normal operation
Developable	Of a shell: can be flattened out completely without any stretching of the shell's mid-surface
Double curvature	The product of the shell's principle curvatures, <i>i.e.</i> its curvatures in a coordinate system chosen such that it has no twist. Also called Gaussian curvature
Gaussian curvature	See Double curvature
Geodesic curvature	Of a line on a shell: the curvature of the line if that shell were flattened, <i>i.e.</i> the in-plane curvature
Geodesic line	On a shell: a line which follows the shortest distance between two points, <i>i.e.</i> a line which would lie straight if the shell were flattened
Isotropic	Of a material: its stiffness properties are independent of the direction of loading

Metastable	Of a structure: in at least some modes of deformation, the internal energy of the structure has zero gradient, and therefore the structure has zero stiffness in those modes
Multistable	Of a structure: can be deformed between several different shapes, all of which are in stable equilibrium when unloaded
Natural frequency	Of a structure: a frequency at which the entire structure will vibrate in phase without any externally-applied forcing
Natural mode	Of a structure: a specific deformation in which the entire structure is vibrating at the same frequency (a <i>natural</i> frequency), without externally-applied forcing
Neutral axis	The axis about which the first moment of area is zero; pure bending about the neutral axis produces no average stretching of the material
Orthotropic	Of a material: its stiffness properties vary with the direction of loading, but have orthogonal axes of symmetry
Principal curvatures	Of a shell: the curvatures in a coordinate system in which the shell has no twist
Principal strains	Of a solid: the tensile strains in a coordinate system in which there are no shear strains
Principal stresses	Of a solid: the tensile stresses in a coordinate system in which there are no shear stresses. For an isotropic material, these take the same directions as the <i>principal strains</i> .
Semi-inextensional	Of a shell: it is assumed that the shell only deforms in bending, <i>i.e.</i> the mid-surface does not undergo any strains
Sense	Of the curvature of a shell: defines whether the shell is curving up or down, <i>i.e.</i> whether the centre of curvature is above or below the shell
Stable	Of a structure: a local energy minimum; any changes of shape or position would result in an increase in stored energy and therefore require work to be performed on the structure
Synclastic	Of a shell: curvature in one principle direction produces a bending moment in the other principle direction <i>in the same sense</i> , tending to create a bowl shape; opposite of <i>anticlastic</i>
Tristable	Of a structure: see <i>multistable</i> , but with exactly three stable shapes

Chapter 1

Introduction

The purpose of this work is the discovery, analysis and prediction of large-scale shape change and multistability in corrugated shell structures.

Conventional structures are designed to maintain a single shape throughout their design life, across the full range of loading patterns that the designer expects. The design of such structures is generally governed first by performance, and then by material cost, fabrication cost and/or weight depending on the application. Most structures can be categorised either as truss/lattice type structures or as continuous shells: it is with shells that we are concerned in this thesis. Shells can confer significant weight advantages, in that they combine the function of providing a surface with that of carrying loads: *e.g.*, see their use in most modern cars, replacing the separation of load-bearing chassis frame and non-load-bearing body, as used by most manufacturers prior to the 1960s. In addition, a shell structure typically produces more useable internal space than a lattice.

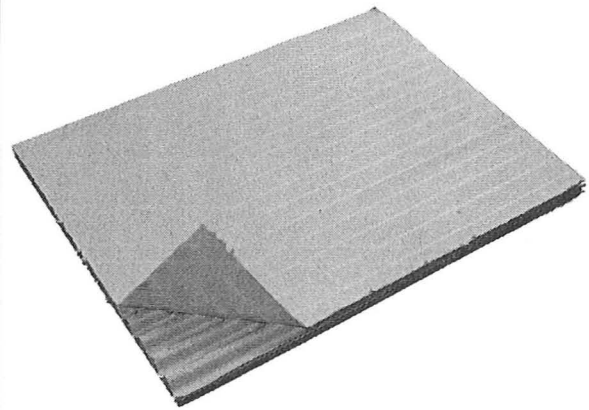
The first specific benefit of *corrugated* shells is that they provide a high bending stiffnesses with much less material than a flat sheet of similar performance, leading to large savings in cost and weight: this has led to their popularity for, *i.a.*, cheap roofing, or their use as a layer in sandwich structures, *e.g.*, cardboard packaging, as shown in Fig. 1.1.

Moving upwards in complexity from simple structures, *machinery* consists of a series of such structures connected by hinges, rods, sliders &c. to provide the relevant degrees of freedom, and driven by actuators such as motors, pneumatic or hydraulic pistons. The result is a complex system of many components, each of which is critical to the performance of the whole and each of which provides vulnerabilities and requires lubrication and maintenance.

An alternative approach is being increasingly considered for some fields (for a literature review, see Section 2.2), including, particularly, unmanned aircraft: 'compliant structures'. They are *compliant* in that, under the influence of actuators, they can elastically deform through the required range of shapes and positions. Thus, a single continuous



(a) Corrugated roof: very cheap and very light, but capable of withstanding high loads



(b) Corrugated cardboard: light and cheap enough for use as packaging, but strong enough to protect contents during transport

Figure 1.1: Two typical examples of corrugated shells, demonstrating their high strength to weight and strength to cost ratio.

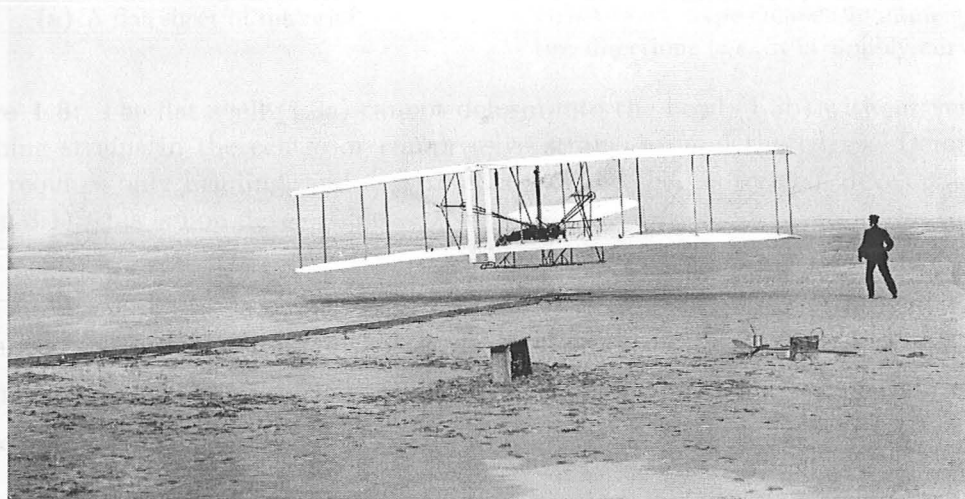
compliant structure has replaced a series of rigid structures connected by mechanical devices. Fig. 1.2 shows a classic and a modern example of this. The Wright Flyer, arguably the first controllable manned heavier-than-air aircraft, is controlled by warping of the wings rather than the ailerons that soon became the norm. The compliant leading edge in Fig. 1.2b is the result of recent research in the Cambridge University Engineering Department by Santer and Pellegrino (2007), being designed with the aid of sophisticated genetic algorithms and intended for application by Alenia-Aeronautica of Italy on unmanned aerial vehicles (UAVs). Various other such concepts have been generated over the last century, and some are documented in Section 2.2.

Compliant structures have the advantages that:

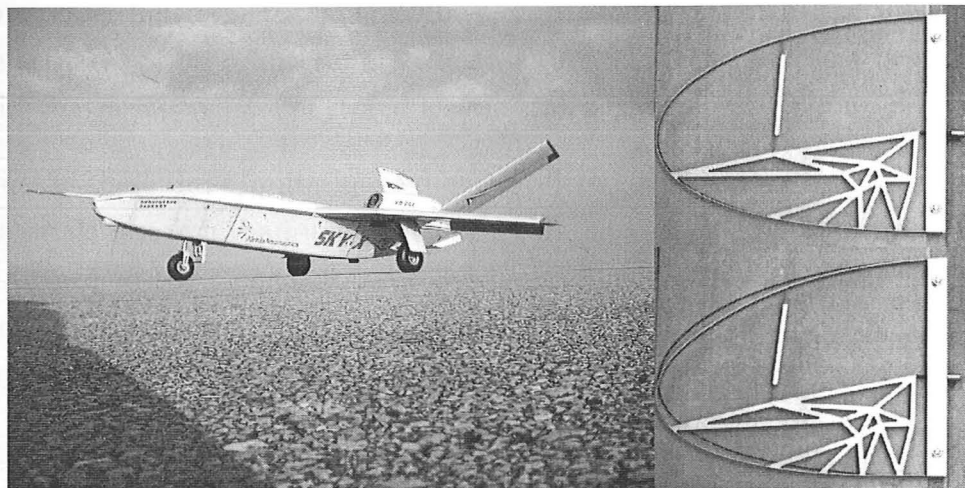
- (i) there are no bearings, sliders &c. to fail, or to require lubrication or maintenance; and
- (ii) since the deformation is distributed over the structure rather than being confined to hinge points, the structure can operate despite damage to or failure of parts of itself: *i.e.*, it has some redundancy or increased robustness.

However, there are attendant problems that must be overcome in design:

- (i) many materials suffer fatigue when undergoing repeated elastic deformation, leading to early failure;
- (ii) avoiding plastic deformation can impose strict limits on the scale of deformation possible. For example, a flat sheet of material, Fig. 1.3a, cannot deform into a bowl



(a) The 'Wright Flyer', arguably the first manned aeroplane, was controlled by warping the wings (photo in the public domain)



(b) A compliant leading edge (right) has recently developed at CUED by Matthew Santer for testing on prototype UAVs from Alenia-Aeronautica of Italy (left, photo © Alenia-Aeronautica S.p.A).

Figure 1.2: Two applications of compliant shells to aircraft wings, ranging from the dawn of aviation to the near future.

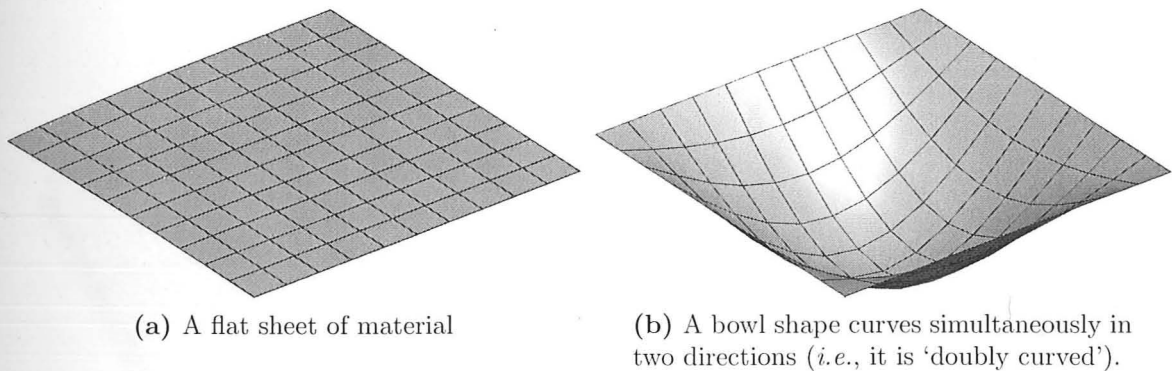


Figure 1.3: The flat shell (1.3a) cannot deform into the bowl (1.3b) without very large stretching strains in the centre or compressive strains around the edges. Deformation which requires only bending, and no stretching, of the shell is termed 'developable' (see Section 3.1): this is non-developable.

shape, Fig. 1.3b, without either large stretching of the centre or an equally large compression of the material in the edges: regular structural materials will, under most circumstances, undergo total failure at much lower strains; and

- (iii) since the deformation is elastic, large internal stresses build up that are not observed in conventional rigid-structure mechanisms. Therefore, larger, heavier or more power-hungry actuators may be required to operate the structures, and should the actuator or its connection to the structure fail, there will be a large and potentially dangerous release of stored elastic strain energy.

The first of these three limitations is not considered in this thesis, falling more properly under materials research than under the structural mechanics approach used here.

With regard to the second of the three limitations listed above, this thesis presents corrugated shells as a novel solution: as Chapters 6–8 demonstrate, corrugated shells can elastically undergo much larger changes of shape than are possible for uncorrugated shells. The key contributors to this behaviour, as explored in Chapter 6, are that:

- (i) as the corrugations bunch up or flatten out, the equivalent mid-surface of the corrugations undergoes very large strains; and
- (ii) there is coupling between these strains across the corrugations and curvature along the corrugations, enabling simultaneous changes in both stretching and bending, which in turn allows changes in the double curvature of the shell.

The third limitation can be alleviated through multistability. This implies that the structure's stiffness in deformation is sufficiently nonlinear that, when deformed far enough from its initial stable equilibrium state, the stiffness in one mode of deformation becomes negative, and the structure 'snaps' to a new stable equilibrium shape. If there are two

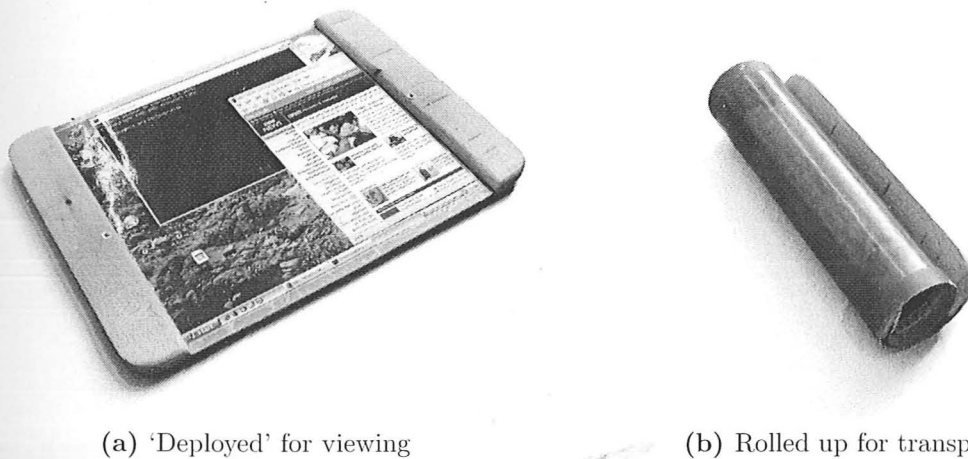
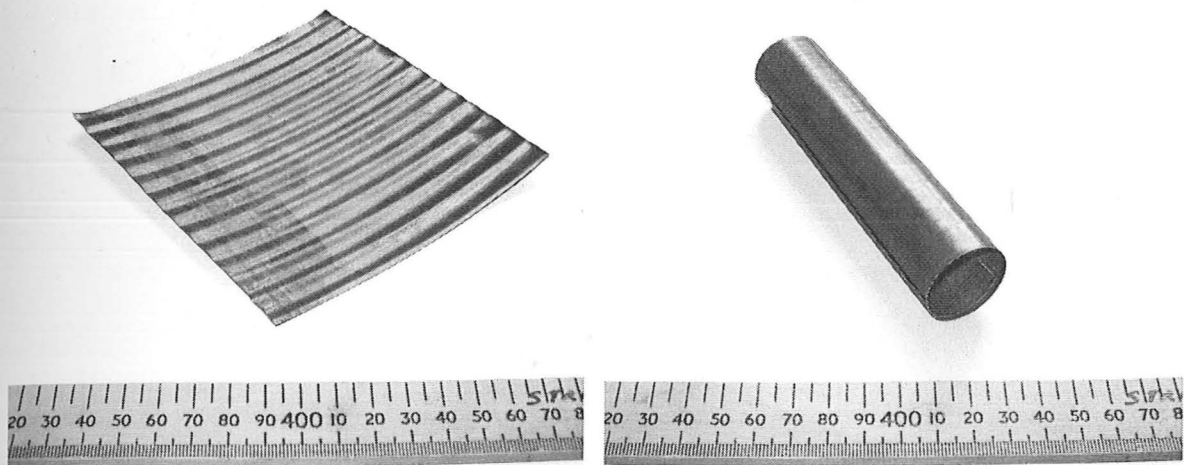


Figure 1.4: A flexible electronic screen can be mounted to a multistable corrugated shell (1.4a) such that it is a rigid and usable, and yet can be ‘snapped’ and rolled up into a second stable configuration (1.4b). This technology has been patented, and is currently the subject of industrial negotiations.

such shapes possible, the structure is ‘bistable’; if three, ‘tristable’; and so on: all such structures can be referred to as being ‘multistable’, having multiple stable states. Actuators are then required *only* to propel the structure between states: when the structure is stationary in one configuration, the actuator is unstressed. Depending on the actuator design, this can produce large savings in power consumption. Similar principles are recognised in display technologies, where it is desirable for a portable display device to require power only when the image changes. In other words, multistable structures allow a greater freedom of actuator selection without a constant consumption of power, while also improving the mechanism’s lifespan, reliability and safety in event of failure.

Chapter 4 demonstrates the usefulness of corrugated shells in multistability, which, again, has yet to be done elsewhere. Multistability in shells generally requires either initial stresses in the shell which are initially ‘trapped’ but are released as the structure deforms, as demonstrated by Kebabze *et al.* (2004), or strong anisotropy in the material properties, as demonstrated by Guest and Pellegrino (2006). Both of these are possible in corrugated shells in ways that are not seen in uncorrugated shells, as Chapter 4 demonstrates. As a result, a patent has been taken on this work by Seffen *et al.* (2006), and it is being specifically pursued as a backing for flexible displays: a screen is mounted to a multistable corrugated shell, which can then be ‘snapped’ and rolled up for transport or storage. Fig. 1.4 shows a mock-up of this technology, which is genuinely multistable but which has a ‘dummy’ screen.



(a) The corrugated flat sheet

(b) The 'coiled' mode

Figure 1.5: A typical bistable shell, constructed, in this case, from CuBe alloy. The initial corrugated state (Fig. 1.5a) is stable, but stressed: when the corrugations are elastically flattened, these stresses are released and the sheet coils up (Fig. 1.5b). This is reversible.

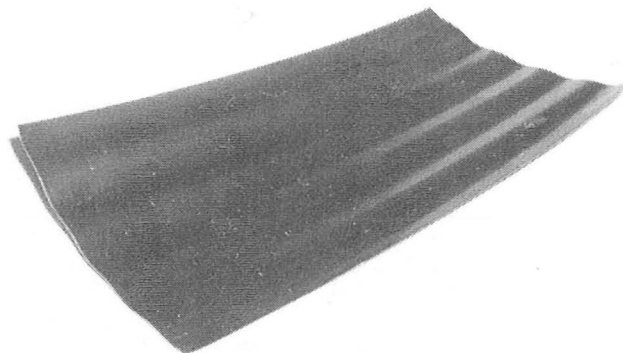
1.1 The shells studied

This section provides a brief introduction to the three main corrugated shell structures that this thesis studies: each of these is introduced more thoroughly in the relevant chapter.

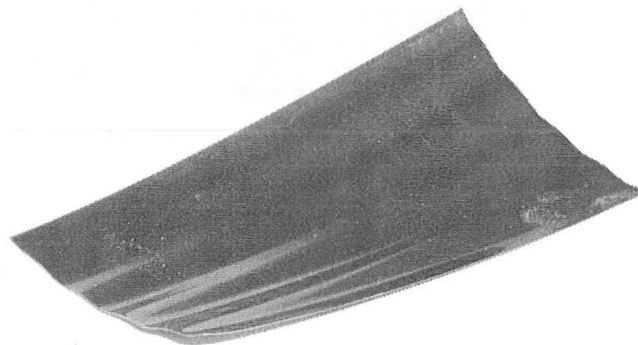
1.1.1 Multistable corrugated shells

Figure 1.5 shows a simple bistable corrugated shell made of an isotropic Copper-Beryllium (CuBe) alloy: this shell is studied in Chapters 4–5. One stable state, Fig. 1.5a, is a globally flat corrugated sheet which is *not* unstressed, for residual bending stresses attempt to coil the sheet. If part of the shell is manually flattened across the corrugations, the effect of these stresses is 'released', and the sheet coils up rapidly into the state in Fig. 1.5b. The shell can be repeatedly and reversibly 'snapped' between the two states, and at no point is the deformation plastic.

During the making of these shells, most prototypes exhibited an unexpected 'twisting' bistability in their corrugated form, making the sheets tristable, with no completely flat mode, as shown in Fig. 1.6. The original single, flat corrugated mode has now split into two corrugated modes of equal global curvature, which are symmetrically arranged about the axis of the corrugations.

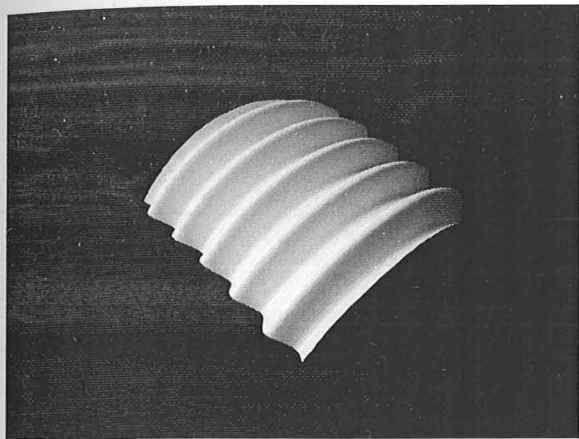


(a) One of the stable 'twisted' corrugated forms

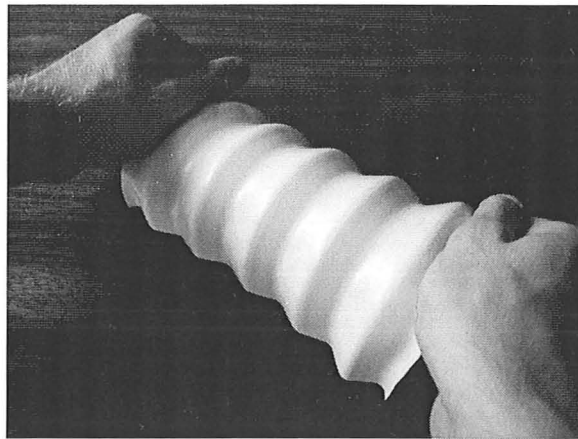


(b) The second 'twisted' position, symmetric with the first about the corrugation axis

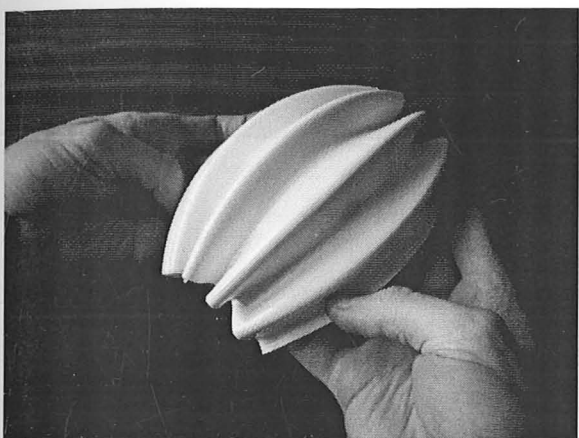
Figure 1.6: The two 'twisted' corrugated stable states. When this behaviour is combined with the bistability of Fig. 1.5, the shell is 'tristable', *i.e.*, it has three stable states: two twisted, one coiled.



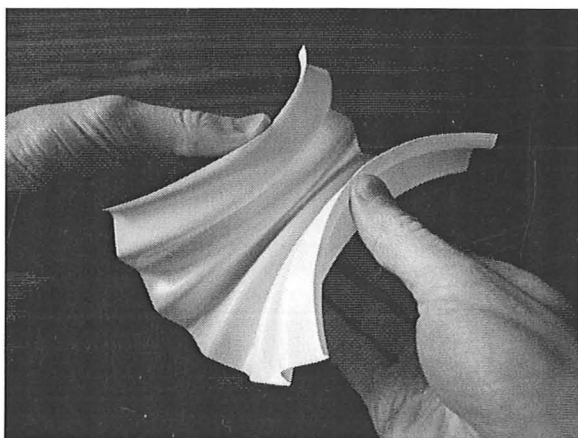
(a) The initial shape, unidirectionally curved along the corrugations



(b) As the curvature increases, so the material expands along the corrugations.



(c) The shell can be inextensionally deformed to a positive Gaussian curvature (*i.e.*, bowl-shaped), or



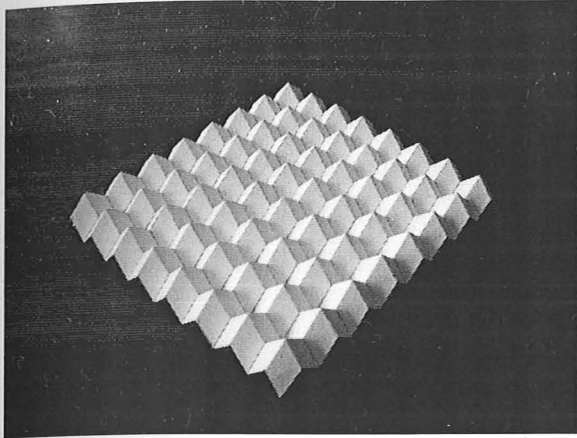
(d) to a negative Gaussian curvature (*i.e.*, saddle shaped).

Figure 1.7: Introducing the curved corrugated forms: these images are all of the same shell, vacuum-formed from 0.5 mm thick HIPS.

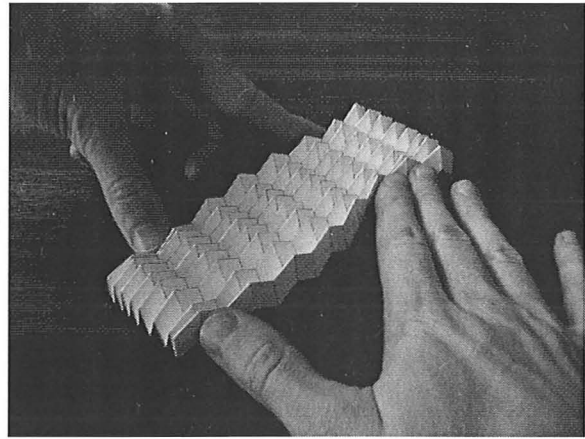
1.1.2 Curved corrugated shells

Figure 1.7a shows a corrugated sheet which is now initially curved along the corrugations: this shell could not be completely flattened out elastically. In this particular case, it is vacuum-formed from a sheet of 0.5 mm-thick 'High-Impact Polystyrene' (HIPS).

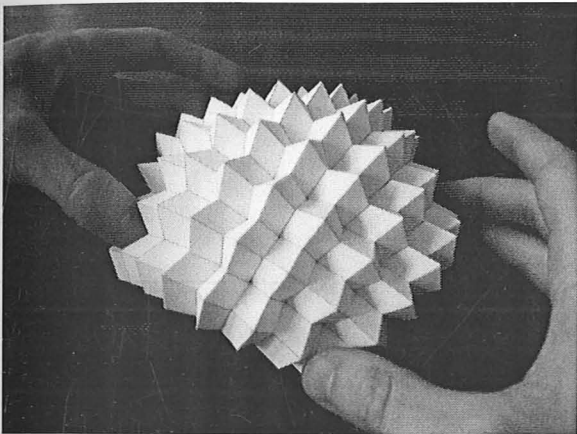
What is significant is the shape change that it can undergo *without* any local stretching in the material. Conventional shell structures, if they are intended to deform at all (*e.g.*, leaf springs), deform in a purely 'developable' fashion, which involves bending but no stretching. This is because a thin sheet can elastically undergo large changes in curvature, but only small stretching strains before the deformation becomes plastic. Some membrane structures, such as cloth, can undergo large shear strains without material failure, and therefore can undergo non-developable shape changes. However, they have very little stiffness unless they are maintained in tension.



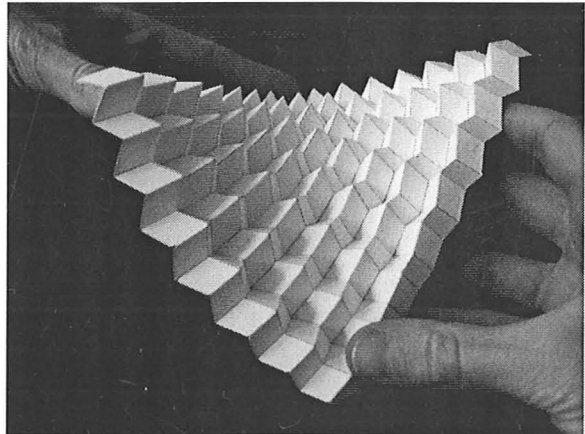
(a) The initial shape, unstressed



(b) Large compressive and tensile strains are possible (the two are coupled together).



(c) A positive curvature in one direction induces a similar curvature in the other direction, and the shell becomes bowl-shaped.



(d) The shell is also flexible in twist, allowing this saddle shape.

Figure 1.8: Introducing the doubly-corrugated forms: these images are all of the same shell, made from light cardboard.

The shell in Fig. 1.7 is, on a local scale, a typical structural shell which has membrane stiffness and is unwilling to stretch. However, looking at the shell as a whole, considering not the local behaviour but the equivalent mid-surface of the corrugations, dramatic shape changes are possible, as dramatic as those in cloth but with a sheet which still exhibits significant stiffness: deforming to a tube, a bowl-shape or a saddle-shape in Figs 1.7b, 1.7c and 1.7d respectively. Chapter 6 demonstrates how this behaviour arises from the coupling between stretching across the corrugations and the curving along them, and Chapter 7 develops a full set of constitutive relations for these shells.

1.1.3 Doubly-corrugated shells

Figure 1.8 shows a doubly-corrugated shell. This shell can, like that in Section 1.1.2, undergo large changes in double curvature, but it is also capable of laying flat. Whereas

the shell in Section 1.1.2 has coupling between one stretch direction and one curvature direction, this shell has a strong coupling between both principle curvature directions which is itself dependent on the stretching strains, as demonstrated in Chapter 8.

The shell in Fig. 1.8 is paper: plastic models are presented in Chapter 8, but the large deformations are easier to observe in a paper shell, involving much lower forces to effect the deformation.

1.2 Overview of this thesis

Chapter 2 reviews the literature relating to corrugated shells, compliant structures and multistable structures, describing the historical development and ongoing research of these topics. Chapter 3 is also heavily literature-based, as it lays out the principles and analytical and experimental methods employed in the research following in Chapters 4–8. In the process, a system of defining and discussing corrugations in general is produced, along with the coordinate systems and other conventions that are used throughout this thesis.

Chapters 4 and 5 are concerned with multistability in flat corrugated shells. Chapter 4 makes assumptions about the principles underlying the behaviour that is observed, and builds an analytical model which qualitatively describes the observed behaviour based on these assumptions. This is sufficient to understand how and why they work, but does not provide any means of qualitatively testing the results. Chapter 5, therefore, explores the forming of these shells, and is the only chapter in this thesis to move away from elastic analyses to study plastic flow effects. These produce results which are compared with experimental data.

Chapters 6 and 7 move away from multistability, and look at shape change in corrugated shells that are initially curved along their corrugations. Chapter 6 analytically models the geometry of their deformation, and is therefore governed by principles of compatibility. Having established the geometric behaviour of these ‘morphing’ shells, Chapter 7 then reintroduces elastic behaviour and strain energy to generate a full set of constitutive relations for the shells. Both chapters make use of experiments and of finite element simulation to test the results of analytical models, which in turn validates the physical understanding underpinning them.

Chapter 8 presents a natural extension to this work, in the form of doubly-corrugated structures. These are introduced, and their behaviour is compared qualitatively to that of the curved corrugated shells of Chapters 6 and 7. Specifically, the natural modes of deformation are found, and the lowest-stiffness modes are matched to the interesting modes of behaviour observed in the physical models. This area is being explored further by other students in the same department.

Finally, Chapter 9 summarises the findings of this dissertation, draws conclusions and outlines unanswered questions and potential directions for further work opened up by this thesis.

Chapter 2

Historical and current literature

This literature review explores both the history and the state of the art regarding corrugated, compliant and multistable shells, which includes not only papers but also patents, since much of the work so far has been in the industrial rather than academic sector. Textbooks and other works on the general engineering principles and methods used are not covered here, being integral to the exposition on methodology in Chapter 3.

Literature relating to corrugated shells is covered in Section 2.1, including, on the one hand, their history, manufacture and current use, and, on the other, the historic development of algebraic models of their elastic properties. Section 2.2 reviews past work on *compliant* structures, giving various examples of concepts and applications thus far. Section 2.3 reviews the field of *multistable* structures, which is a subset of compliant structures, again combining an overview of applications with a summary of relevant academic work.

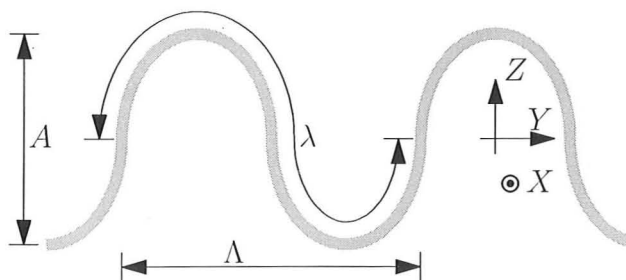


Figure 2.1: Definition of terms defining corrugation geometry. The shell, of thickness t , has a material corrugation wavelength λ , but a shorter corrugation wavelength Λ in the average mid-surface of the corrugations (*i.e.*, the X - Y plane).

2.1 Corrugated shells

The following applications, involving numerous patents and studies of corrugated shells, all focus on their stiffness, strength, weight and other static properties: or, if they consider dynamic behaviour, do so only in terms of buckling or of the forming process. Outside this research project, no work has been found on corrugated structures that incorporates either compliancy or multistability.

2.1.1 Stiffness and strength

Liew *et al.* (2007) is a recent paper on a finite element method of analysing corrugated sheets. In its introduction, there appears a review of past work on the stiffness of corrugated sheets. The earliest work is by Seydel (1931), who produces a set of constitutive relations describing the small-deflection stiffness of a corrugated shell. These results are quoted in numerous textbooks, including Szilard (1974) and Timoshenko and Woinowsky-Krieger (1959). However, Lau (1981) demonstrates that Seydel's equation for the increase in stiffness along the corrugations is highly inaccurate, and produces a much more useful expression with little change in complexity. Briassoulis (1986) tests these results against finite element models, confirming Lau's corrections to Seydel's work, and correcting both with regard to the twisting rigidity of the shell.

Table 2.1 contrasts the principle bending and stretching stiffnesses of Seydel with those of Briassoulis, and includes also those of the uncorrugated sheet for comparison. The terminology is lifted directly from Briassoulis, with the names of the variables changed for consistency with this thesis. This terminology is described in detail in Fig. 2.1 and Eqn 3.6, except for the term $\bar{a}^2 t$, defined as follows.

Referring to Fig. 2.1, the X - Y plane defines the average mid-surface of the corrugations. The bending stiffness in the X - X direction, *i.e.* along the corrugations, is related to the second moment of area of the section about the Y axis, commonly termed I_{YY} . I_{YY} is the integral of Z^2 over the area of the section: if a small increment of the section

Rigidity	Flat plate	Seydel's expressions	Briassoulis' expressions
A_{11}	$Et \frac{1}{1-\nu^2}$	$Et \frac{\lambda}{\Lambda}$	$Et \frac{\lambda}{\Lambda}$
A_{12}	$\nu Et \frac{1}{1-\nu^2}$	νA_{22}	νA_{22}
A_{22}	$Et \frac{1}{1-\nu^2}$	$\frac{2}{3} Et \frac{1}{1-\nu^2} \left(\frac{t}{A}\right)^2$	$Et \frac{1}{1 + \left(\frac{A}{t}\right)^2 \frac{3}{2} (1-\nu^2) \left(\frac{\lambda^2}{\Lambda^2} - \frac{\lambda}{2\pi\Lambda} \sin \frac{2\pi\Lambda}{\lambda}\right)}$
A_{33}	$\frac{1}{2} Et \frac{1}{1+\nu}$	$\frac{1}{2} \nu Et \frac{1}{1+\nu} \frac{\Lambda}{\lambda}$	$\frac{1}{2} Et \frac{1}{1+\nu}$
D_{11}	$\frac{1}{12} Et^3 \frac{1}{1-\nu^2}$	$E \bar{a}^2 t$	$\frac{1}{12} Et^3 \frac{1}{1-\nu^2} + E \bar{a}^2 t$
D_{12}	$\frac{1}{12} \nu Et^3 \frac{1}{1-\nu^2}$	0	νD_{22}
D_{22}	$\frac{1}{12} Et^3 \frac{1}{1-\nu^2}$	$\frac{1}{12} Et^3 \frac{1}{1-\nu^2} \frac{\Lambda}{\lambda}$	$\frac{1}{12} Et^3 \frac{1}{1-\nu^2} \frac{\Lambda}{\lambda}$
D_{33}	$\frac{1}{24} Et^3 \frac{1}{1+\nu}$	$\frac{1}{24} Et^3 \frac{1}{1+\nu} \frac{\lambda}{\Lambda}$	$\frac{1}{24} Et^3 \frac{1}{1+\nu}$

Table 2.1: A comparison between the stretching and bending stiffnesses in global X - Y - Z coordinates of a flat plate, a corrugated shell according to (Seydel, 1931, regularly quoted but inaccurate), and a corrugated shell according to Briassoulis (1986). The terms λ , Λ and A relate to corrugation geometry, and are explained in Fig. 2.1, as is the coordinate system, which has the '1' direction aligned with the corrugations. E and ν are the Young's modulus and Poisson ratio of the shell, and the stiffness terms A_{ij} and D_{ij} are as in Eqn 3.6. t is the local shell thickness, and \bar{a}^2 is defined in the text, as the average of the square of the distance of the local material's midsurface above the X - Y plane: it was calculated incorrectly by Seydel, but corrected by Lau (1981).

has an area $dZdY$, then

$$I_{YY} = \int Z^2 dZdY \quad (2.1)$$

If we say that, at any point, the midsurface of the local material is a distance a above the average mid-surface of the corrugations, and the local material has a thickness t in the Z direction, then a thin Z -wise strip of width δY contributes an increment δI_{YY} of

$$\delta I_{YY} = \delta Y \int_{a-\frac{t}{2}}^{a+\frac{t}{2}} Z^2 dZ = \delta Y \left(\frac{1}{12} t^3 + a^2 t \right) \quad (2.2)$$

We want I_{YY} per unit length, which can be found by integrating over a wavelength and then dividing by the Λ :

$$\begin{aligned} I_{YY} &= \frac{1}{\Lambda} \int_0^\Lambda \left(\frac{1}{12} t^3 + a^2 t \right) dY \\ &= \frac{1}{12} t^3 + t \frac{1}{\Lambda} \int_0^\Lambda a^2 dY \\ &= \frac{1}{12} t^3 + \overline{a^2} t \end{aligned} \quad (2.3)$$

where $\overline{a^2}$ is the average value of a^2 over a corrugation. We now have two terms: the first, $t^3/12$, is the bending of the local shell about its midsurface. The second, $\overline{a^2}t$, gives us the increase over the stiffness of a plate due to the corrugations, and is the effect of the *stretching* of the local material's midsurface. Relating I_{YY} to the bending stiffness D_{11} of Table 2.1 requires consideration of the Poisson's ratio interaction between these terms and κ_{YY} : the component of I_{YY} due to shell bending is multiplied by $E/(1 - \nu^2)$ to give the bending stiffness, while the $\overline{a^2}t$ component is multiplied by E , as it does not interact with κ_{YY} . A calculation of $\overline{a^2}t$ for a specific corrugation profile is given in Section 4.2.3.

Of specific interest in Table 2.1 is that the twisting stiffness, D_{33} , of a corrugated shell is unchanged from the twisting stiffness of the uncorrugated shell. The stiffness along the corrugations rises significantly, as is expected since material has been moved significantly above or below the average surface of the material and hence the shell has a greatly increased second moment of area. The stiffness across the corrugations, however, is reduced, since the shell is longer than the average surface. Briassoulis, unlike the previous authors, realises that the shear stiffness of the mid-surface is identical to the shear stiffness of the uncorrugated shell, since only shear strains parallel to the effective mid-surface of the shell are significant.

With Briassoulis' model, all aspects of the constitutive relations can be logically derived and argued, and all of the stiffness terms agree to a high level of accuracy with the finite element models: it therefore seems that his equations represent the final word on

the subject.

Lau produces the following simplified equations for the ratio of material corrugation wavelength to absolute corrugation wavelength, λ/Λ , and the increase in the second moment of area due to corrugating, $\overline{a^2t}$:

$$\frac{\lambda}{\Lambda} \approx 1 + \frac{\pi^2 A^2}{4\Lambda^2} \quad (2.4)$$

$$\overline{a^2t} \approx \frac{A^2 t}{8} \left(1 + \frac{\pi^2 A^2}{8\Lambda^2} \right) \quad (2.5)$$

These terms assume a corrugation profile made of elliptical arcs, as shown in Fig. 2.1. As Lau demonstrates graphically in his paper, these approximations are excellent for a ratio of corrugation amplitude A to wavelength Λ of up to 0.31, but rapidly become far less suitable above that. This research routinely considers corrugations that are more pronounced than that, and therefore these approximations are not used.

Shimansky and Lele (1995) study the transverse stiffness: *i.e.*, the stretching stiffness across corrugations, of corrugated shells as the thickness of the shell and the amplitude of the corrugations are varied. The stiffness is inevitably reduced from that of a flat plate, as deformation now comes from bending as well as from stretching of the material. For a 'thick' shell ($t/\Lambda = 0.20$), they find that 90 % of the shell deformation is due to bending when the amplitude-to-wavelength ratio, A/Λ , exceeds 1.0. For a 'thin' shell ($t/\Lambda = 0.02$), this occurs at just $A/\Lambda = 0.15$. So, for thin shells of relatively large corrugation amplitudes, which are exclusively studied in this thesis, the deformation involved when stretching the shell across the corrugations comes almost entirely from local bending in the corrugations, with the effect of local stretching becoming negligible.

Shimansky and Lele also study the effect on stiffness of variations in thickness ratio and corrugation amplitude. Again, a thick plate produces a smaller, but still noticeable, effect: for the shell above, of $t/\Lambda = 0.20$ and $A/\Lambda = 1.0$, stiffness is reduced to just 1.5 % of the flat plate value. For a thin, $t/\Lambda = 0.02$, plate of the same corrugation amplitude, the stiffness is reduced by nearly four orders of magnitude. Even with an amplitude ratio of just 0.10, the thin shell has its stiffness reduced to 2.5 % of the flat-plate value. These results use a sinusoidal corrugation rather than the half-ellipses used by Briassoulis.

Most corrugated sheets used in buildings are, in fact, trapezoidal in section, or have some such shape which is formed not from curves but from a series of flat sections, as in Fig. 2.2. Accordingly, a large amount of literature focusses on the stiffness and strength properties of such trapezoidal sheets, often referred to as 'folded plates', since they can be formed by a series of folding processes. Liew *et al.* (2007) mention some of these papers: the most recent of these, and most notable, is that by Samanta and Mukhopadhyay (1999), who, again, present both an analytical model and a finite element simulation.

A third category of corrugated-shell studies concerns corrugated board panels: *i.e.*,

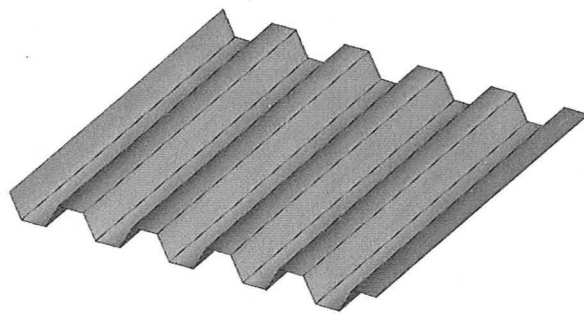


Figure 2.2: A ‘folded plate’ (*i.e.*, a corrugated shell of trapezoidal section), as studied by, *i.a.*, Samanta and Mukhopadhyay (1999).

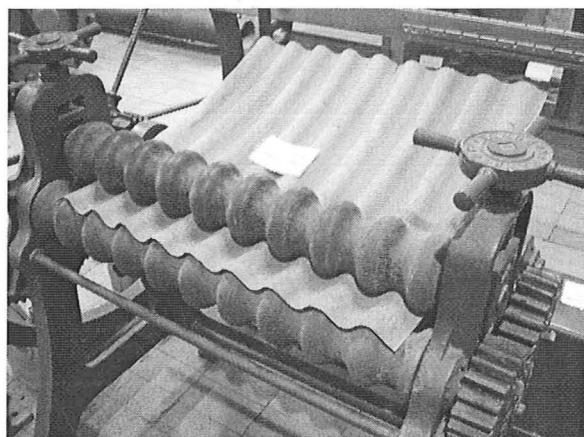


Figure 2.3: An early iron corrugator, on display at Kapunda museum, South Australia. Picture taken in 2007 by Peripitus, and distributed under the GNU public license.

sandwich structures consisting of two flat face sheets and a corrugated shell, as shown in Fig. 1.1b. These are most commonly seen in packaging, when made from cardboard. For a study of them, see Lu and Zhu (2001), where vibration-testing is used to measure the elastic properties and is favourably compared with more traditional experiments and finite element simulations. However, the presence of the face sheets significantly alters the properties and behaviour of the shell: specifically, these sheets are intended to restrict the deformation of the corrugated element, which is contrary to the purpose of this dissertation, and so this dissertation does not at any point consider these phenomena.

Finally, bellows are, in essence, a corrugated shell where each corrugation forms a closed loop about an axis of revolution. However, rather than being of interest just for their static stiffness, bellows are highly compliant, and so the literature is covered below in Section 2.2.2.

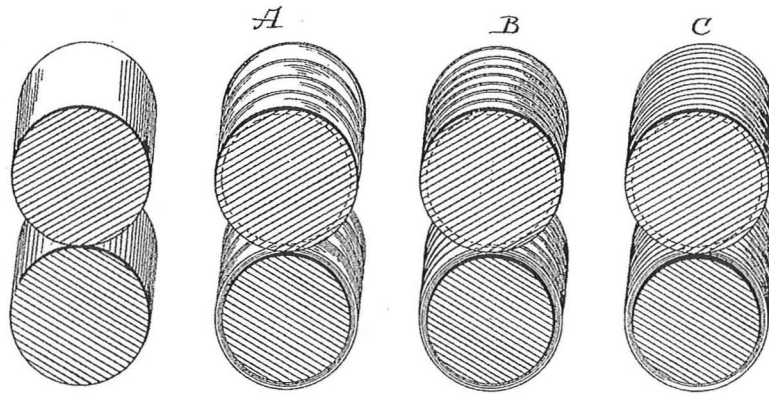


Figure 2.4: A method of corrugating paper invented by Arkell (1899), involving a series of rollers to build up the profile, as the paper passes through the initial rollers and then through rollers *A*, *B* and *C*. A critical element to this process was the hot soaking of the paper to make it ductile.

2.1.2 Manufacturing

Fig. 2.3 shows an early device for manufacturing corrugated iron sheet. This process produces sheets of unlimited length, and does so quickly. Although the complexity and automation of the manufacturing process have since increased dramatically, the basic method of manufacturing iron and aluminium corrugated sheets has not changed. To allow the deep, sharp-edged profiles used today, multiple rollers are used, that gradually build up the corrugation profile: this method is seen as early as a patent by Arkell (1899), which relates specifically to a method for making corrugated paper, an image from which is shown in Fig. 2.4. The method depends upon a ductile material, and Arkell soaked the paper to make it ductile: the use of multiple rollers then limits the deformation, so that the paper is not torn. Polymer corrugated sheet requires a slightly different method, being generally extruded through a forming die before being rolled, as shown by, *i.a.*, Weber (1963).

Work has been done on the manufacture of honeycomb and corrugated-board structures, which must involve the manufacture of corrugated sheets: the methods used for making the individual layers of these structures may be duplicated to make the entirety of our corrugated shells. An example of this is a paper by Wadley (2006), which summarises work done by others in this field. Wadley outlines three methods which are relevant to making corrugated sheets:

- (i) pulling the corrugations out of the plane of a flat sheet, which is especially suited to making expanded honeycombs
- (ii) rolling through a gear press, which is fast and has no limit on the sheet length across the corrugations: note that this gear press has an axis that is 90° to the rollers in Fig. 2.3

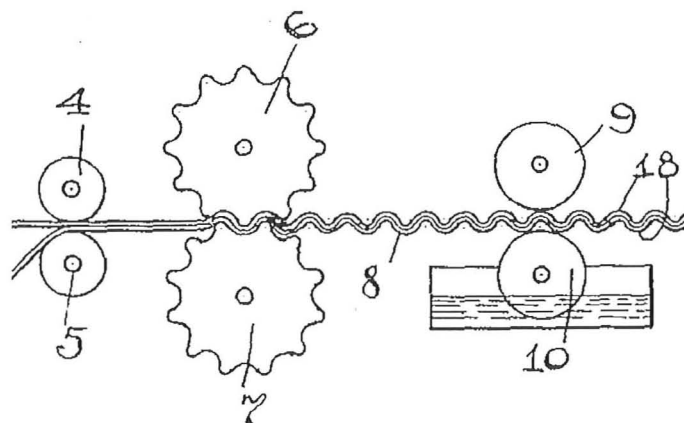


Figure 2.5: A method of corrugating paper invented by Wood (1914), involving a single gear-type roller. This allows a large corrugation profile with just a single set of rollers and no stretching loads on the paper, but it also limits the length of the sheet along the corrugations, which is also the direction in which it is strongest.

- (iii) pressing corrugations individually, which is slower than a gear press but enables the fullest possible array of corrugation profiles.

Item (ii) is the method normally used for corrugated paper/cardboard. Corrugated cardboard was initially patented by Jones (1871), and Fig. 2.5 shows the essence of the typical process, from Wood (1914). While this method is simpler and cheaper than that of Fig. 2.4, the sheet is now limited in length along the corrugations, and unlimited in length along them. While this is perfectly acceptable for corrugated sheet as the filler in a sandwich or as a packaging material, if the corrugated sheet is to be used structurally without facing sheets, it is shortest in the direction in which it has the highest bending stiffness, which limits its usefulness as a structure.

The corrugated shell in Fig. 2.4 is curved along the corrugations: this is a commonly known type of shell. Another similar shell, from a patent by Schluter (2003), is shown in Fig. 2.6, bearing a strong resemblance to the shells studied in Chapters 6–7. However, those chapters consider mainly the non-linear and shape-changing behaviour of these shells: the patent by Schluter is, as with all similar patents, concerned purely with manufacturing methods and methods of joining these shells into structures, and the work in Chapters 6–7 is without precedent.

2.1.3 Eggboxes and other doubly-corrugated shells

Doubly-corrugated shells are studied in the context of compliancy and shape-change in Chapter 8. They are commonly found in food packaging, since they feature regular troughs that can contain eggs, chocolates and so on, in addition to equally regular peaks that can support a similar tray above: see Fig. 2.7 for the example of eggboxes. Other qualities

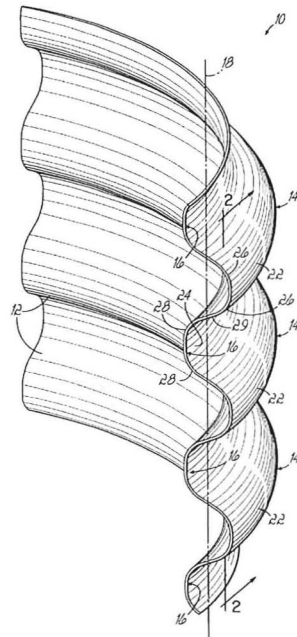
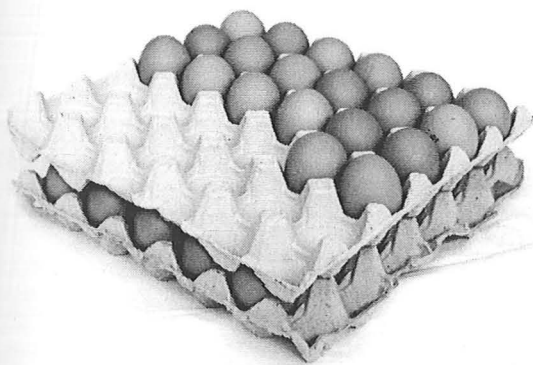
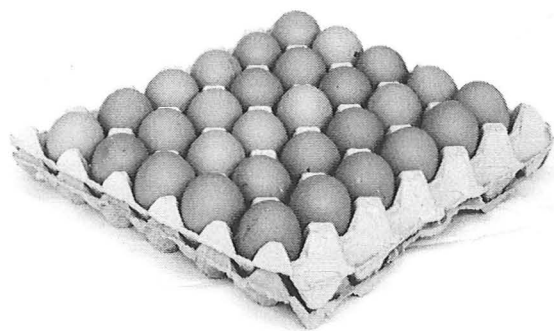


Figure 2.6: A curved corrugated shell from a patent by Schluter (2003). This shell bears a strong resemblance to those of Chapters 6–7, and yet the ‘morphing’ behaviour of such shells, which is the topic of those chapters, is not considered in any of the similar patents on curved, corrugated shells.



(a) The trays stack neatly, with each tray supported by lower trays and no load going through the produce.



(b) When empty, the trays stack to have no wasted space.

Figure 2.7: Egg trays demonstrate a practical application of doubly-corrugated shells.

that commend them to this function include their light weight and ease of manufacture, being usually pressed from a flat sheet, making them very cheap to produce and transport. When not carrying produce, they can also be stacked away very compactly, as in Fig. 2.7b.

Mang *et al.* (1976) present a finite-element simulation of doubly-corrugated shells. However, in contrast to the shells considered here, the corrugations in the two orthogonal directions differ in both wavelength and amplitude by an order of magnitude: in other words, in comparison between the two, the corrugations in one direction appear to be a 'local' phenomenon while those in the other direction are 'global'.

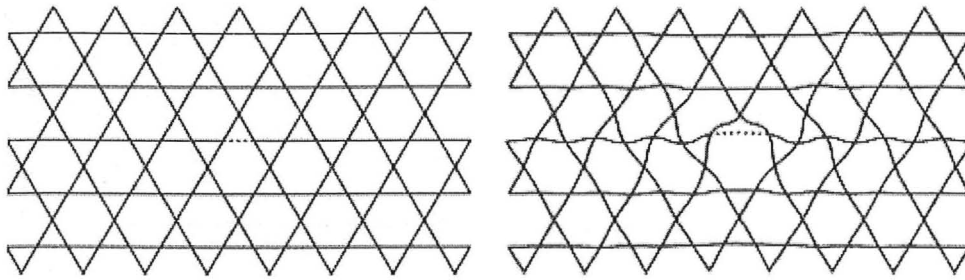


Figure 2.8: A compliant kagome lattice and, right, the same lattice after deformation by stretching a single element (shown as a dotted line): this is from work by Wicks and Guest (2004). Note that a single element has an influence on a large area of the lattice.

2.2 Compliant structures

This section considers firstly truss/lattice-type compliant structures, specifically in aircraft, where much attention is currently being given: it is a field in which a direct application is driving research towards a well-defined goal. Section 2.2.2 then moves closer to the subject of this thesis by looking at applications of continuous compliant shells: these, again, are mostly aeroelastic applications, but focussed more on high-end motorsport technology.

2.2.1 Compliant trusses and aeroelastic wings

Much work has been done on lattices and trusses that exhibit compliant behaviour. A common example is the *kagome* lattice, shown in Fig. 2.8 (the term ‘kagome’ originates with a Japanese basket weave).

Guest and Hutchinson (2003) show that a very large, repetitive truss structure cannot be both statically and kinematically *determinate*. They define a kinematically determinate structure to be one where the only solutions to the compatibility equations for zero bar extensions are rigid-body motions: *i.e.*, it contains no free mechanisms. A statically determinate structure is defined as a structure where the only solution to the equilibrium equations for zero external load is one of zero load in each member. The significance of their findings is that, while actuating just one small member in a large and repetitive truss can induce large deformations in the truss, it must also cause other members to stretch or buckle. This behaviour is indeed observed in the deformation of the kagome lattice in Fig. 2.8.

Hutchinson *et al.* (2003) present the first study of a kagome lattice that is specifically concerned with compliancy. The kagome lattice had been studied in various contexts for its stiffness properties, and earlier still for its magnetic properties in various crystals. Hutchinson *et al.* conclude that the lattice can undergo arbitrary in-plane strains through the minimal bending stiffness of its joints, and yet retain substantial in-plane stiffness,

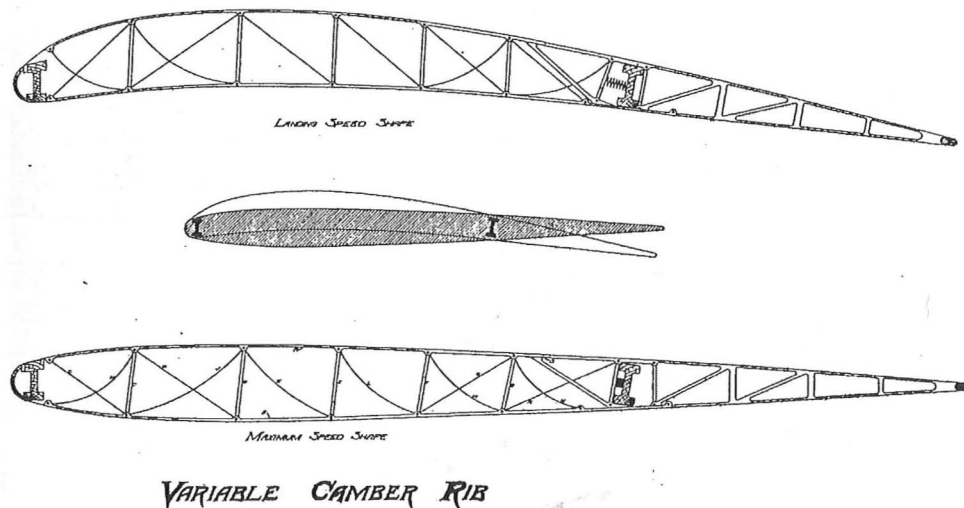


Figure 2.9: An early compliant wing design by Parker (1920), capable of deforming between a high-lift profile for take-off, landing and low-speed manoeuvring (top) and a low-drag profile for high speeds (bottom). This wing is intended to deform solely under the aerodynamic loads on the plane, without any external actuators or control system.

yield and local buckling strengths. These strains can then lead to significant out-of-plane deformation of such a shell, into curved shapes.

Turning to specific applications of compliant trusses, Parker (1920) identifies formally the problem that a rigid wing has a limited speed range. Specifically, if a wing is designed to produce sufficient lift to take off and land at reasonable speeds, it will generate large amounts of drag when flying at much higher speeds and altitudes: conversely, if the wing is optimised for performance at very high speeds, its low-speed and stall characteristics will suffer, creating difficulties when taking off and landing. His own solution is a compliant structure, shown in Fig. 2.9. Its unstressed shape is a high-lift configuration. However, as the aircraft's speed increases, so this configuration will lead to increased lift forces, which in turn deform the wing into a lower-lift, lower-drag form. If the stiffness properties of the wing are just right, the plane will maintain a nearly-optimum wing profile over its entire performance envelope. However, the idea was not put into practice at the time: various possible reasons can be envisaged. For example, without careful damping, the wings could oscillate dangerously. Possibly the most serious issue is that of fatigue, particularly given the limited materials selection in the 1920s: even in relatively modern fixed-wing fighters such as the F-15, fatigue stresses are causing aircraft to fail unexpectedly and within their design life, as highlighted in Aerospace America by Aboulafia (2008).

More recently, the idea has been resurrected. Whilst the concept of a compliant structure is a simple one, Lu and Kota (2003) identify a gap in their understanding: it is difficult to design a structure of complex shape such that it has just one 'soft' degree of freedom, if at the same time the shapes through which that degree of freedom pass

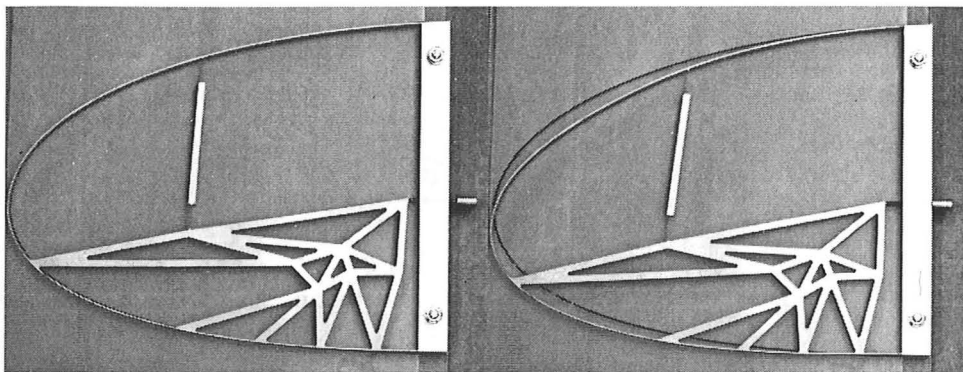


Figure 2.10: A compliant leading edge for an aircraft wing, generated by Santer and Pellegrino (2007) using a load-path-based topology optimisation scheme, building on compliant-structure work by Lu and Kota (2003). It is actuated by the screw thread visible beyond the right-hand edge of the device: on the left, the device is unstressed, and on the right, it is stressed, causing a visible downward deformation.

are tightly constrained (*e.g.*, by aerodynamic considerations). Lu and Kota present the basic elements of a computational method, involving genetic algorithms, to generate the optimum compliant mechanism for a desired morphing structure. In another paper, Kota *et al.* (2003) discuss how this can specifically apply to aircraft wings. Santer and Pellegrino (2007) implement these genetic algorithms, producing a load-path-based topology optimisation system, and their result for a specific problem of a compliant leading edge is shown in Fig. 2.10.

2.2.2 Compliant shells and aeroelastic undertrays

Compliance, in shells, generally involves deformations that are mostly due to the bending of a thin shell, with no stretching effects. This is taken to the limit by what Vlasov (1964, Part I) refers to as *momentless* shells: these are shells in which out-of-plane in-shell forces and bending moments are negligible, and so the only loads within the shell are local in-plane tension and shear. By further defining his momentless shells as inextensional, a shell is defined that is completely free to bend but cannot stretch: in a flat plate, this would, as Vlasov comments, produce infinitesimal modes of instability, but for more complex shapes such as the shells of revolution that Vlasov considers, that is not the case. This momentless, inextensional shell is exactly the assumption on which Chapter 6 is based: however, Vlasov focusses his work on shells of revolution, which the shells of Chapter 6 are not. Shortly after Vlasov, much more work has been done regarding axisymmetric shells by Reissner, Meissner and Reissner: see, for example, the collection of their work, edited by Edwards (1949).

Axelrad (2000) neatly summarises the main approaches that are taken in shell theory under three headings. He describes Vlasov's 'momentless' shells as *membrane theory*, in

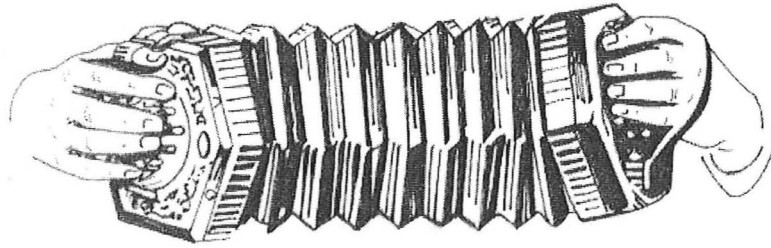


Figure 2.11: Bellows, or a flexible corrugated cylinder. In this case, the bellows provides a variable volume of air, and its operation drives air past the reeds of a Wheatstone concertina, making sound.

which bending stresses are negligible: this is valid for shells whose radii of curvature are tight with respect to the size of their surface features. Shells that are otherwise are *shallow* shells, and membrane theory is not then appropriate: however, other approximations can be used for shallow shells, and Axelrad refers to these approximations as *DMVK-theory*, after the final initials of its founders. In between the two lies what he terms *flexible-shell theory*: this applies to shells with a cartesian local coordinate system in which the curvatures in one direction are far tighter than those in the other. In these cases, Axelrad shows that large deformations involving large rotations but small in-plane strains can be described simply: following Vlasov, Axelrad (1992) describes this as *semi-membrane* deformation.

An example of a structure to which this ‘flexible-shell theory’ applies is a bellows, as shown in Fig. 2.11. A bellows is a commonly-encountered shell that is corrugated, axisymmetric and highly compliant, and the curvature *along* the axis of bellows (*i.e.*, *across* corrugations) is much tighter than that around the bellows (which tracks *along* a single corrugation). Their deformation is *mostly* due to bending, but there is some stretching: note that otherwise, the bellows would be a counterexample to Euler’s conjecture that all simply-connected closed surfaces are rigid, as explored by Gluck (1975).

Moving from academic research to patents, Hale (1970) patented a doubly-corrugated shell as an ‘anticlastic cellular core material’, shown in Fig. 2.12. He points out the many benefits of his shell as a core in a sandwich material, providing a thick (and therefore rigid) sandwich with very low weight and which also provides good support to both the upper and lower surfaces. What is particularly interesting to this thesis is the attention he gives to its compliancy: he states that the core is ‘anticlastic’, *i.e.*, that bending it in one principle direction will cause stresses in the other which cause it to take on a saddle shape. Research and experimentation in Chapter 8 contradicts this, showing such shells to be synclastic, tending towards a bowl shape in their behaviour.

Another doubly-corrugated shell that incorporates compliancy is that patented by Arne (1966), as seen in Fig. 2.13. Curvature of the board is not considered, but Arne claims as a principle feature of his board that it can undergo large stretching in any in-

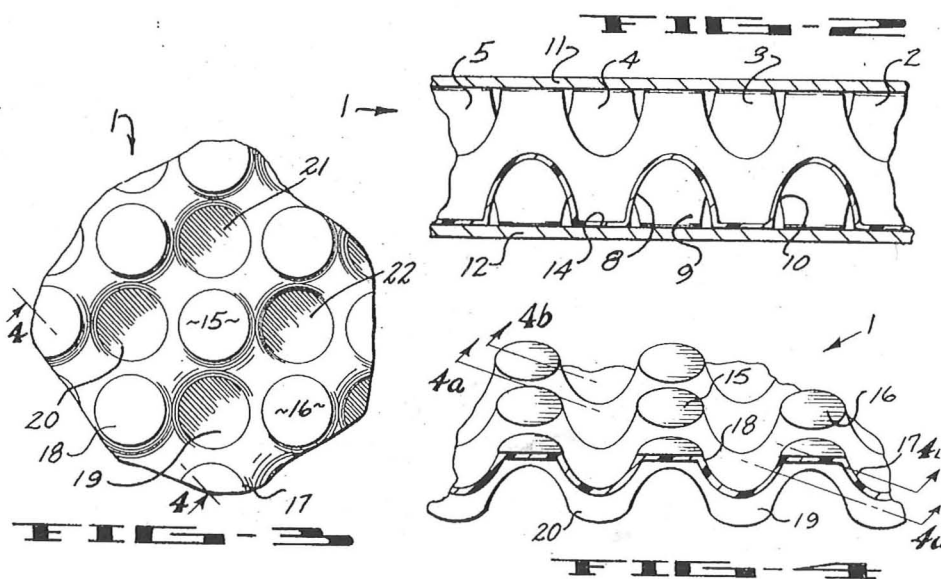


Figure 2.12: Hale (1970) presents this patent for a doubly-corrugated shell as the core for a sandwich matrix, since it provides a good support to both surfaces. Hale claims that this shell is anticlastic: *i.e.*, that bending in one principle direction induces stresses in the opposite sense in the other direction, causing it to take on a saddle shape. However, research in Chapter 8 contradicts this.

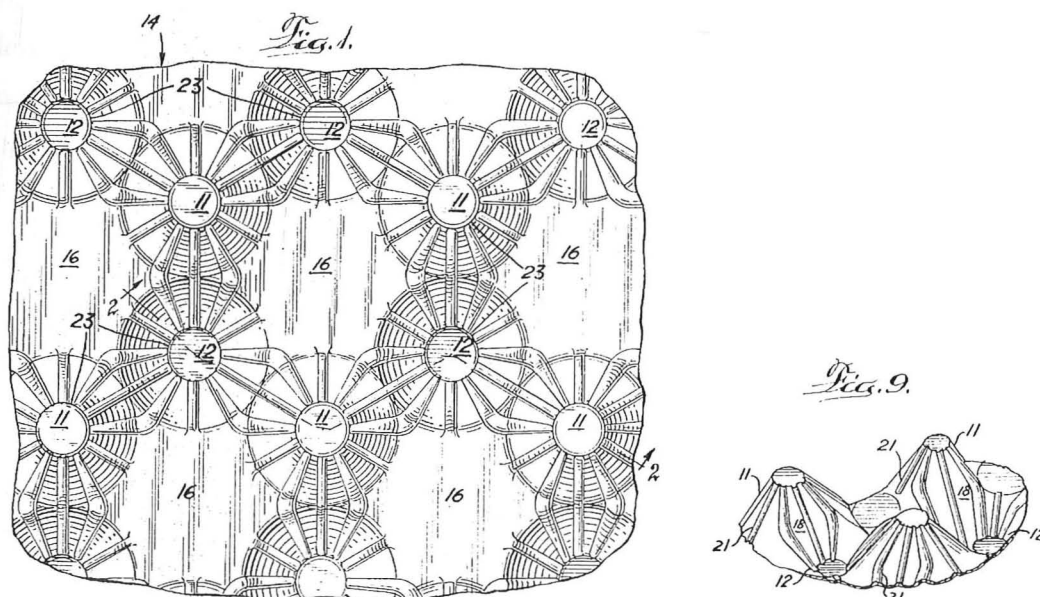


Figure 2.13: A 'plane-expansible corrugated panel' patented by Arne (1966): using an intricate pattern of corrugations, this panel is purported to expand in both in-plane directions.

plane direction. Arne suggests possible applications in packaging, as the sheet can stretch to cover large objects, although it is unclear how effective the sheet would prove.

Moving away from doubly-corrugated shells and to a technology that has already been applied, the relevance of compliant shells and aeroelasticity to motorsport is well known, specifically with regard to Formula 1, where cars tend to be mostly constructed from lightweight carbon-fibre shells, which have the potential to be highly flexible. A 'Fédération Internationale de l'Automobile' (FIA) briefing report by Purnell and Wright (2007) outlines the benefit of what it terms 'aero-elastic tailoring of composite body and wing surfaces', which, as it says, could be employed to vary the shape and downforce and drag characteristics with speed. FIA regulations in Formula 1 have explicitly banned all such devices, but since all structures deflect at least marginally under load, the document acknowledges that this is difficult to police: *e.g.*, see the controversy in mid-2007 when attention was drawn to Ferrari's undertray, which appeared to deflect significantly at speed in a fashion that might have beneficially affected the downforce, as reported by Scarborough and Goren (2007).

The FIA's regulations are concerned with ensuring that the sport remains competitive and exciting to watch. Road cars have no such constraint, and so are free to implement such new ideas, but unlike racing teams, a manufacturer will not put large amounts of money and effort into a new technology that improves performance unless it is also commercially justifiable. Nonetheless, given the increasing costs of fuel and interest of governments in regulating against inefficient cars, many manufacturers are now looking into 'smart' aerodynamic devices that adapt with the car's speed: some concepts, rather than depending upon aeroelasticity, employ actuators. Johnson (2008) explains some of the concepts that General Motors are exploring, including air dams that are deformed by shape memory alloys.

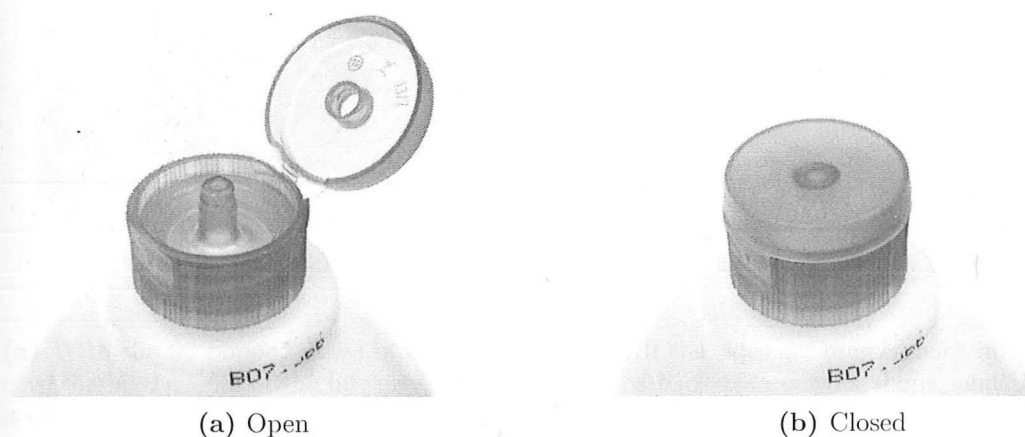


Figure 2.14: A typical plastic bottle-top. It is a single continuous structure, but is compliant and snaps between closed and open positions. In other words, a single structure performs the functions of neck, lid, hinge and catch.

2.3 Multistable structures

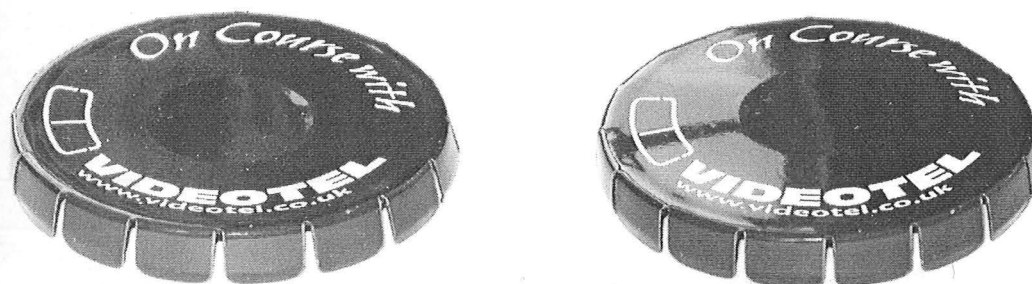
Multistable structures are a subset of compliant structures, since, in order to have multiple stable states, they must be capable of significant deformation in operation. These are very common, being found in a wide array of cheap products, as briefly summarised below in Section 2.3.1. In all of these products, a multistable structure is performing a purpose much more cheaply and reliably than an equivalent mechanism, and in some cases, there is no mechanism that could do the job adequately.

Section 2.3.2 returns to academic studies regarding multistable shells, outlining the main recent fields of research.

2.3.1 Popular applications: bottle-tops to trouser clips

Compliant structures with multiple stable states are already popular in low-cost plastic goods. One of the most commonly used is the bottle-top shown in Fig. 2.14. It is a single continuous structure, but is compliant and snaps between closed and open positions. In other words, a single structure performs the functions of neck, lid, hinge and catch. Unlike the multistable shells considered in this thesis, however, one position (open) is unstressed: the closed position is only stable because of the shape of the shell, in that strong deformation is needed to get it past the catch.

Figure 2.15 shows a jar lid that makes use of multistability. The lid is a single, pressed shell of a thin, hard stainless steel. It makes use of buckling, normally considered a ‘failure’ of a shell, as a routine design feature: as the centre of the lid is popped in or out, so the sides either grip or release the jar. Seffen (2006) explores this idea further, creating a large sheet with several ‘dimples’ that pop through in this fashion, with a significant



(a) With the lid popped down into a concave shape, the sides of the lid spread, and it can be lifted off a jar.

(b) If the sides are pressed back in, the lid pops back to a convex shape, and the lid grips the jar tightly.

Figure 2.15: This jar top is slightly dished, and the sides, as can be seen, are slitted. The lid is bistable, since the bulge in the top can be ‘popped’ through to face either down or up, to unlock or lock the lid.

effect on the overall shape of the shell.

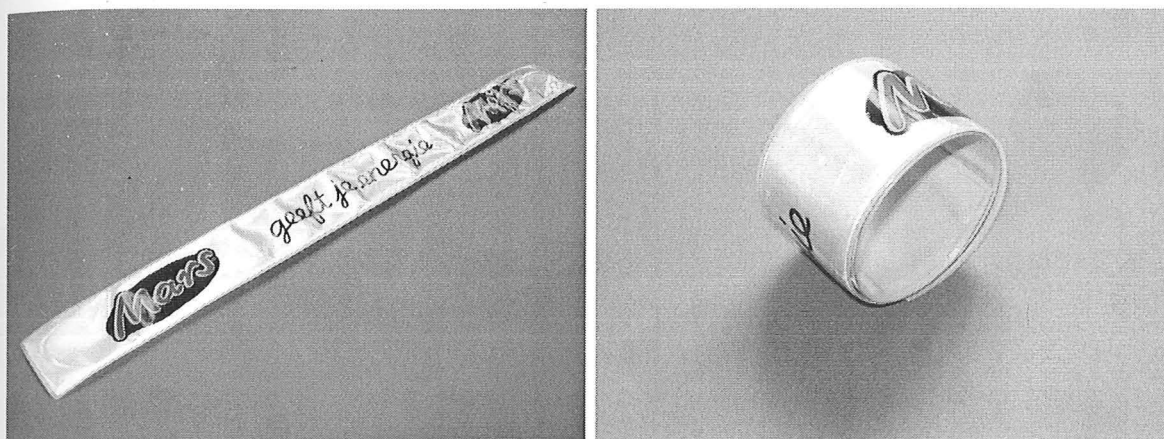
Fig. 2.16 comes closest to the subject of this thesis, as it includes a shell structure which is bistable through the action of internal stresses. Research relating to this type of shell has been done at CUED by Galletly, Guest, Kebabze, Pellegrino and Seffen, and this is reviewed in the next section.

2.3.2 Academic research and high-performance applications

Academic research on multistable compliant shells originates with Hyer (1981). He observes the shapes assumed by asymmetric composite laminates when cured at elevated temperature and then cooled to room temperature. Rather than producing the saddle shape predicted by small-deflection linear theory, they assume one of two approximately cylindrical curvatures of opposite sense. By evaluating the internal strain energy, considering polynomial deformation shapes for the shell and including the thermal stresses, he demonstrates that while, for small laminates, the saddle shape is indeed stable, for larger shells, this becomes unstable and the two cylindrical shapes become the stable solutions. This multistability is due to internal stresses in the laminate.

A natural extension to this is to consider shells that have an initial cylindrical deformation, but are *not* initially stressed. Guest and Pellegrino (2006) study cylindrical shells without thermal stresses, composed of both symmetric and antisymmetric laminates. In this case, when the cylindrical shell is an antisymmetric laminate, there is a second stable shape, which is tightly coiled: if the laminate is symmetric, then the second stable shape is helical.

In the same paper, Guest and Pellegrino make the point that, for many shells, it can be assumed that all interesting behaviour is inextensional, since the bending of a thin



(a) Laid flat

(b) Coiled

Figure 2.16: A slap-on bracelet. Under the soft plastic/cloth cover lies a prestressed tape-spring. Although it is stable when laid flat (left), when it is ‘slapped’ onto a curved surface, the stresses inside propel it to a bracelet shape. They are popular as bracelets, but are more practically used as trouser clips when cycling.

shell involves significantly less energy than the stretching required for double curvature of similar magnitude. What is more important is that twisting curvatures are considered: Galletly and Guest (2004) demonstrate shells that display equilibrium states that are only shown to be unstable when twist is considered.

In all the cases mentioned above that are studied by Guest *et al.*, the two stable curvatures are in the same sense. This technology has been commercialised by ‘Rolatube’ as a ‘Bistable Reeled Composite’. They are formed as long glass-fibre-reinforced-polymer slit cylinders, which can be opened up along the slit and then rolled up along the length of the tube, so that a long and relatively rigid pole can be rolled up into a very compact space, as evident in Fig. 2.17.

All of the above work involves composites, which have anisotropic stiffness properties. Metal shells, which are isotropic, are studied by Kebabze *et al.* (2004), expanding on the work on bistable composite shells performed by the same group. Again, simple cylindrical curvatures are considered. However, it is found that unlike anisotropic composite shells, cylindrically-curved isotropic shells cannot display multistability without some prestress. In addition, except for one special case, the two stable states must have opposite-sense curvatures: the special case is neutrally stable, where the shell’s curvature can take any direction (at the original sense) without an energy penalty. The work by Kebabze *et al.* matches the behaviour observed in the slap-on bracelets of Fig. 2.16, where the ‘straight’ state is actually a tape spring which has a curvature of the opposite sense to the ‘coiled’ state.

These results break down when more complex shells are considered, such as those in which edge effects become significant. As an example, see the multistable shell from

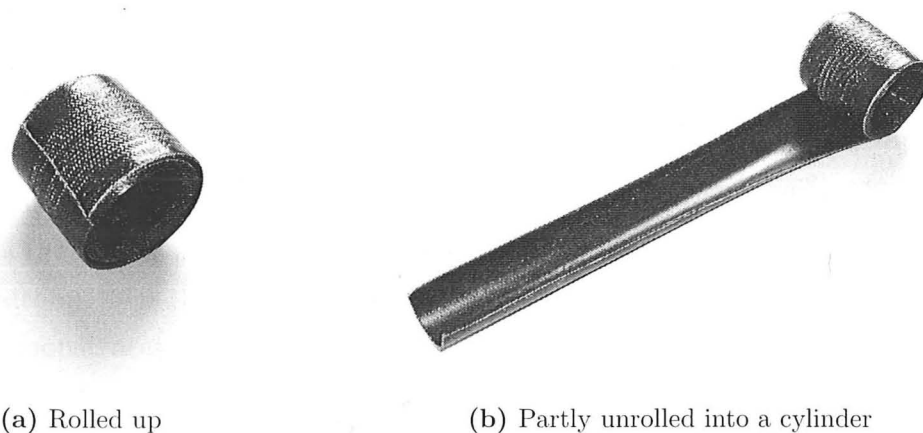


Figure 2.17: The bistable shell produced by ‘Rolatube’. This is a composite shell, which is stable either rolled up or opened out into a slit cylinder.

isotropic materials being studied by Seffen (2006) that employs local ‘dimples’: *i.e.*, approximately spherical indentations which can be ‘popped through’. These dimples have a significant effect on the stresses in the surrounding material, and the popping-through of individual dimples can effect significant global changes of shape, as mentioned above in Section 2.3.1.

A further mode of multistability is described by Schultz (2005). These consist of two layers of material, either anisotropic or isotropic, of different curvatures. They are flattened and joined (typically by gluing), such that their rest curvatures are incompatible, and bistability is produced. This is, in effect, just an alternative means of creating a prestressed shell, after the fashion of Kebabze *& al.* (2004). Since each layer, individually, need not meet the material requirements for multistability, the range of materials and processes is expanded. However, the curvatures of such a shell are only $1/8$ of the rest curvatures of the individual layers, as shown in Appendix A. Since, in this thesis, materials are used which *are* capable of multistability, Schultz’s method is not employed.

2.4 Summary

Section 2.1.1 presents the state-of-the-art regarding analytical expressions governing the stretching and flexural stiffnesses of corrugated sheets. Specifically, the results produced by Briassoulis (1986) are tabulated in Fig. 2.1. However, no useful results have been found to describe in similar terms the behaviour of doubly-curved corrugated sheets, *i.e.*, corrugated sheets that curve along their corrugations or are corrugated in both directions simultaneously, although the latter are frequently encountered in everyday use.

Section 2.2 demonstrates that compliant structures are not a novel idea, having been the focus of research for more than 80 years, but are still at the forefront of high-tech engineering disciplines, including aerospace and motorsport. In Section 2.3 are seen various ‘everyday’ examples of compliant structures, in which this compliancy is coupled with multistability to produce a structure that can ‘snap’ repeatedly between various forms as part of its intended function. Many of these examples have proven cheap and simple to produce in large quantities, especially when compared with equivalent devices that involve only rigid structures, where such an equivalent device is even possible.

In conclusion, we now see that compliant and multistable structures can find, and have found, practical and economical use in a wide range of fields, and that research is continuing to find more such. Despite this, in exploring *corrugated* compliant and multistable structures, it appears that something new is being done in this dissertation.

Chapter 3

Analytical and experimental concepts and methods

This chapter lays out the principles and analytical and experimental methods employed in Chapters 4–8, along with the coordinate systems and other conventions that are used throughout this thesis.

Section 3.1 outlines the geometric principles and terms relating to shells, and the curvatures thereof. In the process, it defines the terms used in this thesis to describe corrugation profiles. Section 3.2 then covers full constitutive relations: *i.e.*, relationships between deformation and stress. Section 3.3 introduces the relevant principles of plastic deformation for Chapter 5. Section 3.4 introduces the basic components of the finite-element simulations used, as well as the experimental equipment and methodologies.

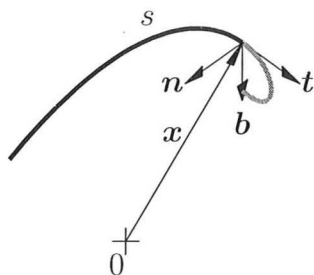


Figure 3.1: A curve in 3D space, defined by a vector \mathbf{x} , which is a function of distance s along the line. At any point, there is a tangent vector $\mathbf{t} = d\mathbf{x}/ds$, a curvature vector $\kappa\mathbf{n} = d\mathbf{t}/ds$ and a twist $\tau = (d\mathbf{n}/ds) \cdot \mathbf{b}$, where the unit vector \mathbf{b} is derived from the unit vectors \mathbf{n} and \mathbf{t} such that $\mathbf{b} = \mathbf{t} \times \mathbf{n}$. In this case, τ will be negative.

3.1 Curvature of lines and surfaces

The concepts of curvature and twist differ for lines and surfaces, and the following sections outline conventional terminology and definitions for each, which will be used throughout this thesis.

3.1.1 Curvature and twist: intrinsic properties of a line

The properties of a curve in three-dimensional space form part of the field of differential geometry, and are derived in greater detail in, *e.g.*, Riley & al. (2002, pp. 346–349).

We begin with a line in 3D space, shown in Fig. 3.1, which can be described by its position \mathbf{x} as a function of distance along the line s : *i.e.*, $\mathbf{x} = \mathbf{x}(s)$. This line has, at any point, a tangent unit vector $\mathbf{t}(s) = d\mathbf{x}/ds$, a curvature magnitude $\kappa(s)$, a normal unit vector $\mathbf{n}(s)$ in the plane of the curvature such that $\kappa\mathbf{n} = d\mathbf{t}/ds$ and a twist $\tau(s) = (d\mathbf{n}/ds) \cdot \mathbf{b}$, where the unit vector $\mathbf{b}(s)$ is defined by $\mathbf{b} = \mathbf{t} \times \mathbf{n}$. All of this is formalised by the *Frenet-Serret* formulae:

$$\frac{d\mathbf{t}}{ds} = \kappa\mathbf{n} \qquad \frac{d\mathbf{n}}{ds} = \tau\mathbf{b} - \kappa\mathbf{t} \qquad \frac{d\mathbf{b}}{ds} = -\tau\mathbf{n} \qquad (3.1)$$

Thus, as we move along the line, the curvature vector $\kappa\mathbf{n}$ is the direction in which the line is curving: this is the definition used for curvature of a *line* throughout this paper.

3.1.2 Curvature and twist: intrinsic properties of a surface

The curvature of the shell is defined as follows:

$$\kappa_{xx} = -\frac{\partial^2 w}{\partial x^2} \qquad \kappa_{yy} = -\frac{\partial^2 w}{\partial y^2} \qquad \kappa_{xy} = -\frac{\partial^2 w}{\partial x \partial y} \qquad (3.2)$$

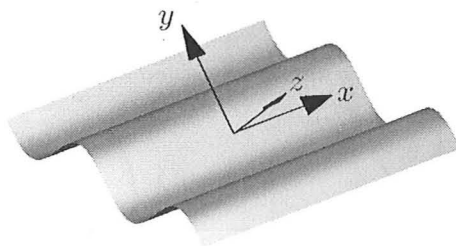


Figure 3.2: An intrinsic coordinate system is used, whereby z is always normal to the shell surface and x and y lie in the centreplane of the shell, and therefore vary in space such that local z -direction displacement w and its first-order spatial derivatives must be zero, as outlined in Calladine (1983, chap. 2). The second-order spatial derivatives of w with respect to x and y give the shell curvature.

where x , y and z are a right-handed *intrinsic* coordinate system. Being intrinsic, this coordinate system varies over the shell such that x and y lie in the plane of the shell at any point, as in Calladine (1983, chap. 2), see Fig. 3.2. w denotes the displacement of the shell from the local x - y plane in the z direction, and the basis vectors vary over the shell such that only second- and higher-order spatial derivatives of w with respect to x and y are non-zero. These equations are derived with the assumption that the material is thin relative to the radii of these curvatures and, given that this is true, this definition is valid for large deflections.

The shell curvature and shell bending moment *vectors* are defined as

$$\boldsymbol{\kappa} = \begin{bmatrix} \kappa_{xx} \\ \kappa_{yy} \\ 2\kappa_{xy} \end{bmatrix} \quad \mathbf{M} = \begin{bmatrix} M_{xx} \\ M_{yy} \\ M_{xy} \end{bmatrix} \quad (3.3)$$

where the x direction is aligned to the corrugations throughout.

A positive shell bending moment is defined such that the incremental increase, δU , in the stored strain energy due to the work done by moment, \mathbf{M} , over an incremental change in curvature, $\delta\boldsymbol{\kappa}$, is given by

$$\delta U = \mathbf{M}^T \delta\boldsymbol{\kappa} \quad (3.4)$$

The *sense* of a curvature refers to its sign; when two curvatures are in the *same* sense, they are both positive or both negative in the z plane, and when they are in the *opposite* sense, one is positive and the other negative. Note that this says nothing about their relative directions in the x - y plane. One physical interpretation is that the centres of their curvature lie above or below the shell.

The choice of directions x and y within a shell can be arbitrary. Fig. 3.3 shows a set of axes x and y within which a shell has some curvatures κ_{xx} , κ_{yy} and κ_{xy} . These can

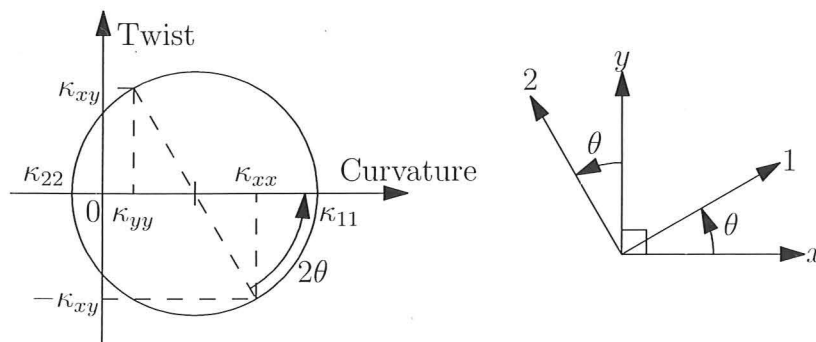


Figure 3.3: Mohr's circle of curvature (left), relating the curvatures κ_{xx} and κ_{yy} and the twist κ_{xy} to the *principal curvatures*, κ_{11} and κ_{22} , at angle θ to the x and y axes respectively. The significance of the 1 and 2 vectors is that, in their coordinate system, there is no twist, *i.e.*, $\kappa_{12} = 0$, and κ_{11} and κ_{22} are, respectively, the maximum and minimum curvatures. These axes, and the relative directions of the principal curvatures, are shown on the right.

be plotted as shown on the left of Fig. 3.3 as a *Mohr's Circle*, as described in Calladine (1983). On this plot, curvatures are plotted on the horizontal axis and twist on the vertical, giving us two points $(\kappa_{xx}, -\kappa_{xy})$ and $(\kappa_{yy}, \kappa_{xy})$. From these two points, a circle can be formed with its centre on the horizontal axis. Then, as derived by Calladine, as our coordinate system is rotated an arbitrary angle θ , so we move an angle 2θ round the Mohr's Circle to find the κ_{xx} , κ_{yy} and κ_{xy} in our new coordinate system. If, specifically, θ is such that the twist in the new coordinate system is zero, as in Fig. 3.3, we have found the *principal curvatures* of the shell, *i.e.*, the curvatures in a coordinate system in which there is no twist, defined as κ_{11} and κ_{22} . There are then two further things to note:

- (i) rotating the coordinate system by 180° moves us 360° round the Mohr's circle: in other words, the curvatures are unchanged if the coordinate system is rotated by 180° about the z axis; and
- (ii) the two principal curvatures tell us a lot about the shell. Specifically, by multiplying the two together, we have the *Gaussian curvature*, also called 'double curvature', $K = \kappa_{11}\kappa_{22}$, which is interpreted thus:
 - (a) if $K = 0$, one of the principal curvatures must be zero, the shell is curved cylindrically at that point, and it can be flattened out completely without any stretching;
 - (b) if $K > 0$, both principal curvatures are in the same sense, and the shell is bowl-shaped, or *elliptically* curved; and
 - (c) if $K < 0$, one principal curvature is positive and the other negative, and the shell is saddle-shaped, or *hyperbolically* curved.

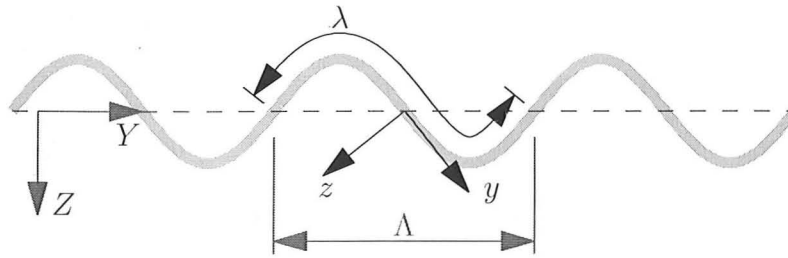


Figure 3.4: Definition of the terms describing corrugation geometry. x , y and z are a right-handed coordinate system in the local plane of the shell: X , Y and Z describe the mid-surface of the shell, with the corrugations ‘smoothed out’. λ denotes the local corrugation wavelength, and Λ the wavelength as projected onto the mid-surface, as in Fig. 2.1.

3.1.3 Corrugation-specific terminology

Throughout this dissertation, the local right-handed shell coordinate system x , y and z is always oriented such that x and y are in the plane of the shell, with x aligned along the corrugations, as in Fig. 3.4. In Chapters 6–8, a second coordinate system is introduced: the system X , Y and Z , which lie not on the local shell surface but in the *mid-surface* of the shell. This is the surface that appears if the shell is averaged over a corrugation, and the properties of the corrugated sheet can be translated to equivalent properties in the mid-surface coordinate system. Again, X is chosen to lay along the corrugations. Then, a complete corrugation wavelength is referred to as λ in the local shell and Λ in the mid-surface, again as shown in Fig. 3.4.

3.2 Elasticity

Section 3.2.1 presents constitutive relations for a general shell structure: from this, Section 3.2.2 produces expressions for the internal strain energy density, and goes on to connect energy analyses with the importance of inextensionality and developability in shells. Section 3.2.3 shows how the elastic properties of a shell are used to calculate its *natural modes* of vibration, and discuss what we can learn from them.

3.2.1 General and shell constitutive relations

Calladine (1983) is a seminal introduction to the elastic analysis of shell structures, deriving, from first principles, the basic equations that cover shell behaviour. This analysis assumes that all materials are linearly elastic, obeying Hooke's law with a Young's modulus E . Further, it is assumed that the shell can be modelled as being thin, leading to assumptions that, in bending, plane sections remain plane (*i.e.*, shear stresses in the z -direction are negligible), and that through-thickness stresses are zero.

For a general, three-dimensional isotropic body, stresses at a point are related to strains by

$$\begin{bmatrix} \sigma_{xx} \\ \sigma_{yy} \\ \sigma_{zz} \\ \sigma_{xy} \\ \sigma_{yz} \\ \sigma_{zx} \end{bmatrix} = \frac{E}{(1+\nu)(1-2\nu)} \begin{bmatrix} 1-\nu & \nu & \nu & 0 & 0 & 0 \\ \nu & 1-\nu & \nu & 0 & 0 & 0 \\ \nu & \nu & 1-\nu & 0 & 0 & 0 \\ \hline 0 & 0 & 0 & 1-2\nu & 0 & 0 \\ 0 & 0 & 0 & 0 & 1-2\nu & 0 \\ 0 & 0 & 0 & 0 & 0 & 1-2\nu \end{bmatrix} \begin{bmatrix} \varepsilon_{xx} \\ \varepsilon_{yy} \\ \varepsilon_{zz} \\ \varepsilon_{xy} \\ \varepsilon_{yz} \\ \varepsilon_{zx} \end{bmatrix} \quad (3.5)$$

The horizontal and vertical lines separate stretching terms from shear terms, for clarity: looking at the top-right and bottom-left 'boxes' of the stiffness matrix, note that there is no coupling between the two.

For a given stress state, the stress components σ_{ij} will change as the basis vectors x , y and z , *i.e.*, the coordinate system, are rotated. Significantly, there will always be a specific coordinate system in which the shear stresses σ_{xy} , σ_{yz} and σ_{zx} are all zero. σ_{xx} , σ_{yy} and σ_{zz} in this coordinate system are termed the *principal stresses*, and are referred to as σ_1 , σ_2 and σ_3 .

Returning to shells, this thesis shall make extensive use of the standard plate equations relating the in-plane forces N_{ij} and bending moments M_{ij} to the strains ε_{ij} and curvatures

κ_{ij} for a linear material, which apply to the local shell:

$$\begin{bmatrix} N_{xx} \\ N_{yy} \\ N_{xy} \\ M_{xx} \\ M_{xy} \\ M_{xy} \end{bmatrix} - \begin{bmatrix} N_{xx_0} \\ N_{yy_0} \\ N_{xy_0} \\ M_{xx_0} \\ M_{xy_0} \\ M_{xy_0} \end{bmatrix} = \begin{bmatrix} A_{11} & A_{12} & A_{13} & B_{11} & B_{12} & B_{13} \\ A_{12} & A_{22} & A_{23} & B_{12} & B_{22} & B_{23} \\ A_{13} & A_{23} & A_{33} & B_{13} & B_{23} & B_{33} \\ B_{11} & B_{12} & B_{13} & D_{11} & D_{12} & D_{13} \\ B_{12} & B_{22} & B_{23} & D_{12} & D_{22} & D_{23} \\ B_{13} & B_{23} & B_{33} & D_{13} & D_{23} & D_{33} \end{bmatrix} \begin{pmatrix} \begin{bmatrix} \varepsilon_{xx} \\ \varepsilon_{yy} \\ 2\varepsilon_{xy} \end{bmatrix} - \begin{bmatrix} \varepsilon_{xx_0} \\ \varepsilon_{yy_0} \\ 2\varepsilon_{xy_0} \end{bmatrix} \\ \begin{bmatrix} \kappa_{xx} \\ \kappa_{yy} \\ 2\kappa_{xy} \end{bmatrix} - \begin{bmatrix} \kappa_{xx_0} \\ \kappa_{yy_0} \\ 2\kappa_{xy_0} \end{bmatrix} \end{pmatrix} \quad (3.6)$$

The initial shape here is ε_{ij_0} , κ_{ij_0} , at which there are initial forces, or *prestress* forces, N_{ij_0} and prestress moments M_{ij_0} .

For a thin shell, it is also assumed that through-thickness stresses σ_{zz} , σ_{xz} and σ_{yz} are zero (*i.e.*, plane-stress conditions). Thus, from Eqn 3.5, $\varepsilon_{zz} = -\frac{\nu}{1-\nu}(\varepsilon_{xx} + \varepsilon_{yy})$. For isotropic materials, $B_{ij} = 0$: *i.e.*, stretching and bending are mutually independent. In addition, shear and normal strains are decoupled, as are twist and uniaxial curvature, such that $A_{13} = A_{23} = D_{13} = D_{23} = 0$. From Eqn 3.5, the generalised Hooke's laws can be modified for stretching and bending as performed by Calladine (1983):

$$\begin{bmatrix} M_{xx} - M_{xx_0} \\ M_{yy} - M_{yy_0} \\ M_{xy} - M_{xy_0} \end{bmatrix} = \mathbf{M} - \mathbf{M}_0 = \mathbf{D}(\boldsymbol{\kappa} - \boldsymbol{\kappa}_0) = \mathbf{D} \begin{bmatrix} 1 & \nu & 0 \\ \nu & 1 & 0 \\ 0 & 0 & \frac{1-\nu}{2} \end{bmatrix} \begin{bmatrix} \kappa_{xx} - \kappa_{xx_0} \\ \kappa_{yy} - \kappa_{yy_0} \\ 2(\kappa_{xy} - \kappa_{xy_0}) \end{bmatrix} \quad (3.7)$$

$$\begin{bmatrix} N_{xx} - N_{xx_0} \\ N_{yy} - N_{yy_0} \\ N_{xy} - N_{xy_0} \end{bmatrix} = \mathbf{N} - \mathbf{N}_0 = \mathbf{A}(\boldsymbol{\varepsilon} - \boldsymbol{\varepsilon}_0) = \frac{Et}{1-\nu^2} \begin{bmatrix} 1 & \nu & 0 \\ \nu & 1 & 0 \\ 0 & 0 & \frac{1-\nu}{2} \end{bmatrix} \begin{bmatrix} \varepsilon_{xx} - \varepsilon_{xx_0} \\ \varepsilon_{yy} - \varepsilon_{yy_0} \\ 2(\varepsilon_{xy} - \varepsilon_{xy_0}) \end{bmatrix} \quad (3.8)$$

where D is the shell bending stiffness, defined by

$$D = \frac{Et^3}{12(1-\nu^2)} \quad (3.9)$$

3.2.2 Energy and stability

The study of the behaviour of multistable structures involves finding multiple states in which they are in *stable equilibrium*. One interpretation of a stable state is that all modes of deformation have *positive stiffness*. A second useful definition of stable states is that they are local *energy minima*: *i.e.*, energy must be put into the system in order to deform it in any fashion. These can be combined into two criteria:

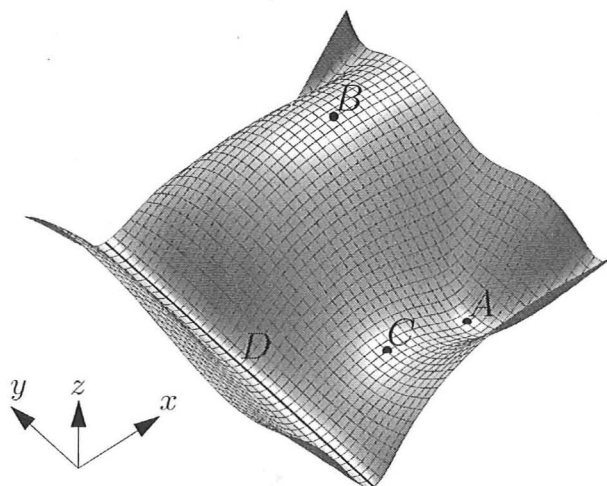


Figure 3.5: A graphical demonstration of a stability landscape, plotting a hypothetical function of energy with two variables, represented here by x and y , with the height z of the surface representing energy. A is a minima, *i.e.*, a *stable* point at which the structure can rest: B is a maximum, and is a point of *unstable* equilibrium. C is a *saddle* point, being stable in y but unstable in x . Finally, the line D is stable in x , but is flat in y , corresponding to a zero-stiffness *metastable* state.

- (i) for equilibrium, there must be no mechanism driving the system in any direction; therefore, the local energy gradient (partial derivatives with respect to any shape factors) must be zero; and
- (ii) for stability, the stiffness matrix must be *positive* definite at that point, so that any small deformation will place the structure in a state from which it has a direct mechanism back to the previous form. It is simpler and clearer, and generally done here, to check that the second-order partial derivatives of energy with respect to the shape factors are positive.

Equilibrium points which do not fulfil the second criteria come in three forms:

- (i) maxima, with all second-order derivatives zero or negative: *i.e.*, they are unstable, and the structure may deform in any direction;
- (ii) saddle points with some negative second-order derivatives and some positive, which are unstable only in one direction, and stable in orthogonal directions;
- (iii) metastable points: the second derivatives are zero in some or all directions, and positive in any remaining directions, and the structure is stable but has zero stiffness in some modes of deformation.

This can all be determined analytically. However, once the equilibrium points are found, it can be quicker to examine a contour plot of energy (or equivalent, depending on how many independent variables govern deformation) to determine whether they are minima,

maxima or metastable. These are demonstrated by Fig. 3.5, which plots a hypothetical function of energy with two variables, x and y .

The only energy term considered here is that stored as elastic strain energy. Gravitational and other potential fields are not considered, and nor are thermal expansion effects. If we define change in curvature $\Delta\boldsymbol{\kappa} = \boldsymbol{\kappa} - \boldsymbol{\kappa}_0$ and change in linear strain $\Delta\boldsymbol{\varepsilon} = \boldsymbol{\varepsilon} - \boldsymbol{\varepsilon}_0$, the elastic strain energy density at a given point for a given state is the integral of the work done ($\mathbf{M}^T \Delta\boldsymbol{\kappa} + \mathbf{N}^T \Delta\boldsymbol{\varepsilon}$) over deformation from the initial state to that state. This is a conservative system, and therefore history-independent, so that only the initial state and the end-state matter. Therefore, energy density U relative to the initial state $\boldsymbol{\kappa}_0, \mathbf{M}_0$ is:

$$\begin{aligned} U &= \int_{\boldsymbol{\kappa}_0}^{\boldsymbol{\kappa}} \mathbf{M}^T d\boldsymbol{\kappa} + \int_{\boldsymbol{\varepsilon}_0}^{\boldsymbol{\varepsilon}} \mathbf{N}^T d\boldsymbol{\varepsilon} \\ &= \int_{\boldsymbol{\kappa}_0}^{\boldsymbol{\kappa}_0 + \Delta\boldsymbol{\kappa}} \left((\boldsymbol{\kappa} - \boldsymbol{\kappa}_0)^T \mathbf{D}^T + \mathbf{M}_0^T \right) d\boldsymbol{\kappa} + \int_{\boldsymbol{\varepsilon}_0}^{\boldsymbol{\varepsilon}_0 + \Delta\boldsymbol{\varepsilon}} \left((\boldsymbol{\varepsilon} - \boldsymbol{\varepsilon}_0)^T \mathbf{A}^T + \mathbf{N}_0^T \right) d\boldsymbol{\varepsilon} \quad (3.10) \end{aligned}$$

Noting that $\mathbf{D}^T = \mathbf{D}$ and $\mathbf{A}^T = \mathbf{A}$ and integrating,

$$U = \frac{1}{2} (\Delta\boldsymbol{\kappa}^T \mathbf{D} \Delta\boldsymbol{\kappa} + \Delta\boldsymbol{\varepsilon}^T \mathbf{A} \Delta\boldsymbol{\varepsilon}) + \mathbf{M}_0^T \Delta\boldsymbol{\kappa} + \mathbf{N}_0^T \Delta\boldsymbol{\varepsilon} \quad (3.11)$$

Comparing Eqns 3.7, 3.8 and 3.11, it can be seen that while the strain energy due to stretching of the shell varies with t , the energy due to bending varies with t^3 . Therefore, as a shell becomes very thin, so stretching causes a much greater increase in internal strain energy than bending. Rayleigh (1877, p. 396) demonstrates how we can infer from this that a shell will ‘prefer’ to bend rather than stretch: since only a slight stretching of a shell will induce a very large strain energy, a shell will not stretch at all if it can meet the imposed loads or boundary conditions by bending instead.

The significance of developable shells, discussed above in Section 3.1.2, now becomes clear: any developable shells can deform inextensionally to a large array of other developable shapes with only bending, and therefore only small energy inputs. A non-developable shell has, in general, much less freedom, and in many cases the only modes of inextensional deformation are infinitesimal modes: a spherical shell does not even have these. Therefore, non-developable shells tend to be much stiffer than developable shells. Chapters 6–8 explore some unexpected exceptions to this rule.

3.2.3 Modal analysis

A modal analysis is a simple method to explore the stiffness of a structure in response to shape changes. The method described below is taught in more detail by Coates *et al.* (1988), and is also taught by Riley *et al.* (2002, pp. 232–240). The modal analysis in

this thesis will involve finding the natural modes of vibration of the structure. Natural modes of vibration are modes of vibration whereby all points of the shell vibrate at the same frequency and in phase. The frequency of these modes relates to the stiffness of the structure. Thus, the lowest-frequency modes describe the least-stiff modes of global deformation of the structure, which potentially tells us something about its preferred shape-change behaviour.

Equations of natural modes

The modal analysis begins by dividing a structure into a finite number of simple elements. In other words, the shell is divided up into a grid, which is defined by a two-dimensional array of nodes. If there are a total of n nodes, the x -, y - and z -direction displacements of a node i are termed d_{xi} , d_{yi} and d_{zi} . Then, a single vector \mathbf{d} of size $3n \times 1$ can be used to define the displacement of all n nodes:

$$\mathbf{d} = [d_{x1} \ d_{x2} \ \dots \ d_{x(n-1)} \ d_{xn} \ d_{y1} \ d_{y2} \ \dots \ d_{y(n-1)} \ d_{yn} \ d_{z1} \ d_{z2} \ \dots \ d_{z(n-1)} \ d_{zn}]^T \quad (3.12)$$

Similarly, the cartesian components of the force on each node are represented by a vector \mathbf{p} :

$$\mathbf{p} = [p_{x1} \ p_{x2} \ \dots \ p_{x(n-1)} \ p_{xn} \ p_{y1} \ p_{y2} \ \dots \ p_{y(n-1)} \ p_{yn} \ p_{z1} \ p_{z2} \ \dots \ p_{z(n-1)} \ p_{zn}]^T \quad (3.13)$$

For small values of \mathbf{d} , the relationship between forces and displacements can be linearised, producing a stiffness matrix \mathbf{K} of size $3n \times 3n$ such that

$$\mathbf{p} = \mathbf{K} \mathbf{d} \quad (3.14)$$

where, by Maxwell's theorem of reciprocity, \mathbf{K} must be symmetric, such that $\mathbf{K} = \mathbf{K}^T$. This matrix can also be defined in terms of energy: the potential energy, V , of a system is given as

$$V = -\frac{1}{2} \mathbf{d}^T \mathbf{K} \mathbf{d} \quad (3.15)$$

Having found the stiffness matrix, \mathbf{K} , a second matrix is needed: the *inertia matrix*, \mathbf{M} . This is most simply defined in terms of energy: the *kinetic* energy, T , of the system for small displacements is given by

$$T = \frac{1}{2} \dot{\mathbf{d}}^T \mathbf{M} \dot{\mathbf{d}} \quad (3.16)$$

We assume that the system is *conservative* (i.e., that energy is not 'lost' to friction &c.).

Riley & al. (2002) then derive the equation of motion for the system:

$$\mathbf{p} = \mathbf{K}\mathbf{d} = \mathbf{M}\frac{d^2\mathbf{d}}{dt^2} \quad (3.17)$$

In the simplest case, the mass is concentrated purely on the nodes of the system, producing an inertia matrix \mathbf{M} that is purely diagonal, *i.e.*, all terms off the main diagonal are zero, and, moreover, all non-zero terms must be positive: \mathbf{M} is therefore not singular, and has a non-zero determinant.

We are looking for modes of vibration; specifically, since we have made this a linear stiffness problem, the vibration of the structure will be a simple harmonic motion of frequency ω radians per unit of time, following the equation

$$\frac{d^2\mathbf{d}}{dt^2} = -\omega^2\mathbf{d} \quad (3.18)$$

so that

$$-\omega^2\mathbf{M}\mathbf{d} + \mathbf{K}\mathbf{d} = 0 \quad (3.19)$$

$$\therefore (\mathbf{K} - \omega^2\mathbf{M})\mathbf{d} = 0 \quad (3.20)$$

For a non-trivial mode-shape \mathbf{d} , this requires that

$$|\mathbf{K} - \omega^2\mathbf{M}| = 0 \quad (3.21)$$

$$\therefore |\mathbf{M}(\mathbf{M}^{-1}\mathbf{K} - \omega^2\mathbf{I})| = 0 \quad (3.22)$$

Recalling that \mathbf{M} is non-singular and of non-zero determinant,

$$|\mathbf{M}^{-1}\mathbf{K} - \omega^2\mathbf{I}| = 0 \quad (3.23)$$

This has become an eigenvalue problem. The natural modes of vibration are the eigenvectors of the matrix $\mathbf{M}^{-1}\mathbf{K}$, and the squares of the corresponding natural frequencies, ω^2 , are its eigenvalues. Many commercial computational mathematics packages can solve eigenvector problems, such as the Mathworks' *MATLAB*; SIMULIA's *ABAQUS* finite element software contains commands to produce the desired natural modes and frequencies by the same method.

Limitations and problems with modal analyses

Firstly, care has to be taken when converting a continuous shell into discrete elements. Chapter 7 contains a modal analysis using *ABAQUS*, which considers the shell to be

divided into shell elements: as long as the elements are small enough to capture the detail of the model, this does not constrain the model in any fundamentally unjustifiable way. However, the modal analysis in Chapter 8 converts the shell into a folded-plate structure, the in-plane stiffness of which is modelled as rigid bars between the nodes, with some small bending stiffness between adjacent facets. In that section, there are two 'obvious' ways to orient the folds between facets, which correspond to the obvious hinge lines in a physical shell. For the curved corrugated shell of Chapter 7, this method would be inappropriate, since the 'hinges' can be anywhere along the shell and can take any direction, and the hinges of a folded-plate model would overly constrain the modes.

A second issue relates to boundary conditions. If the only forces arise from the relative displacements of adjacent nodes, then the shell has zero stiffness in 'rigid-body' modes: *i.e.*, if the shell is being translated or rotated without deformation. Boundary conditions can be applied to prevent these modes: these conditions are created by imposing reaction forces relating to the absolute displacement of the nodes, and if the forces involved are large, they can effectively be used to hold certain nodes still. However, if all translations and rotations are to be constrained, care is needed lest valid non-rigid-body modes are also being suppressed. There is an alternative method: since these modes are of zero stiffness, they are of zero frequency. So, we need only to ignore all zero-frequency modes, as these are irrelevant to our study of the structure.

The final issue relates to the small-deflection approximations inherent in the method. Since the modes are solutions to the linear stiffness matrix at the initial shape, the deformation considered is completely linear, neglecting any effect due to the rotation of elements. Fig. 3.6 demonstrates the problem if this is applied to a flat shell.

In Fig. 3.6a, the initial shell is shown: it is a flat sheet, modelled in this case as a grid of 10×10 thin 4-node shell elements. Figs 3.6b–3.6d then show the first three modes of deformation. These modes all display significant stretching of the shell. In a real shell with finite deformation, these are very high-energy deformations, and the shell will prefer purely developable deformations. In other words, the modal analysis fails to predict the behaviour of a real shell when the deformations are larger than infinitesimal. The problem arises because a linear analysis is applied to a geometrically linear shell, and therefore the model does not pick up stretching of the shell: in Chapters 7–8, the shell is strongly geometrically non-linear, and therefore even a linear analysis must pick up stretching effects. The safest conclusion is that, as ever, common sense is needed when interpreting the results.

To reinforce the claim that the non-physical behaviour in Fig. 3.6 is a 'freak' effect for specific geometries, Fig. 3.7 demonstrates the same analysis for a flat shell with fewer degrees of symmetry: specifically, a rectangle. In this case, the doubly-curved modes are now shifted to much higher stiffness than the developable modes, which dominate.

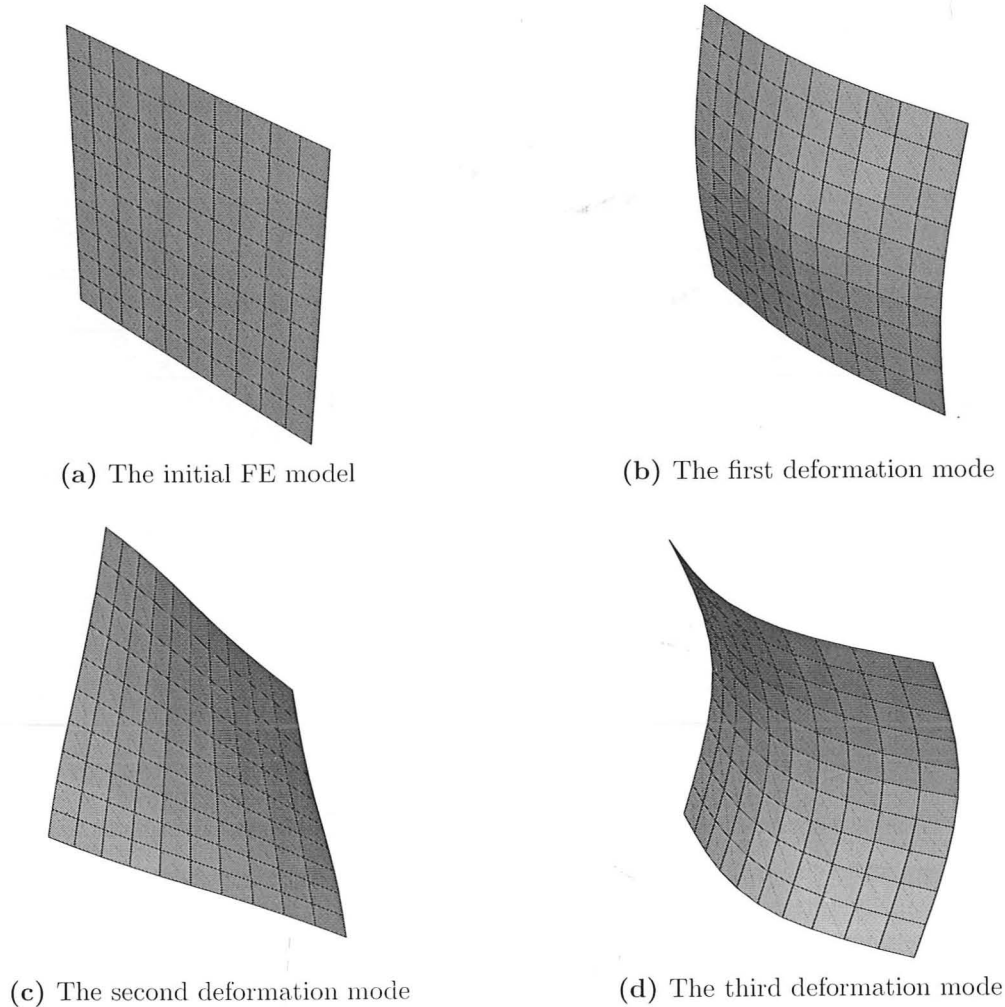


Figure 3.6: A finite-element modal analysis of a flat plate (Fig. 3.6a). Note that the lowest-frequency deformation modes all involve stretching of the shell, and will not be observed in finite deformations of a real shell, which will only deform in a developable fashion. In other words, the lowest-stiffness (*i.e.*, lowest-frequency) modes as found by the analysis are actually relatively high-stiffness modes in reality, when large deflections are involved, as these modes violate inextensibility in a fashion that is not apparent in a linear analysis.

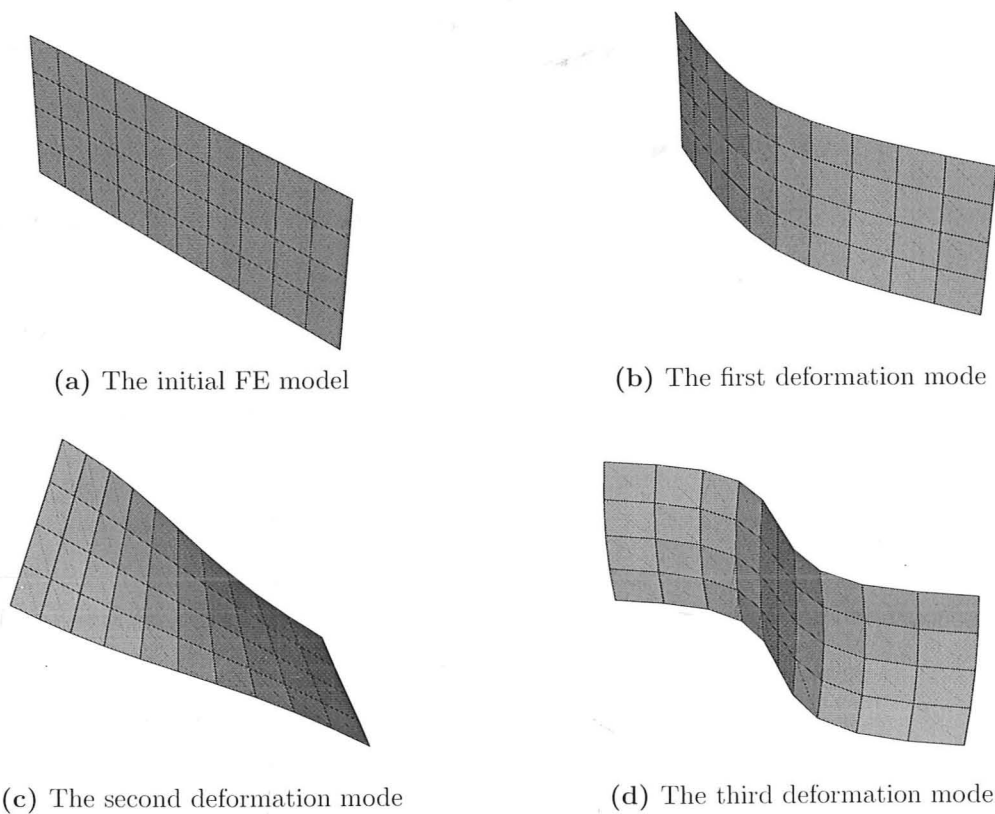
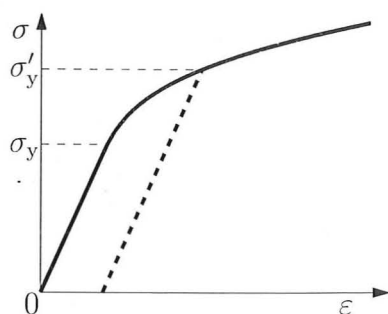
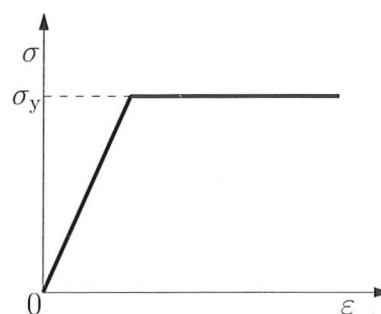


Figure 3.7: A finite-element modal analysis of an oblong flat plate (Fig. 3.7a). Compared to Fig. 3.6, the non-physical modes have moved away from being the lowest-stiffness modes, and the behaviour now matches what we would expect for a real shell.



(a) An example of the elastic-plastic behaviour of a real material. Initial yield is at σ_y : after loading to σ'_y , note the new 'elastic' regime, denoted by a heavy dashed line, with a higher yield stress. This is work-hardening.



(b) The EPP model of material behaviour, with distinct linear-elastic and linear-plastic regimes of behaviour.

Figure 3.8: Elastic-plastic material properties. All plastic analyses assume that the material is *elastic-perfectly-plastic* (EPP), as the material on the right. σ_y denotes the yield stress, at which the material changes from linear Hookian elastic behaviour (with elastic modulus E) to plastic strain at a constant stress σ_y .

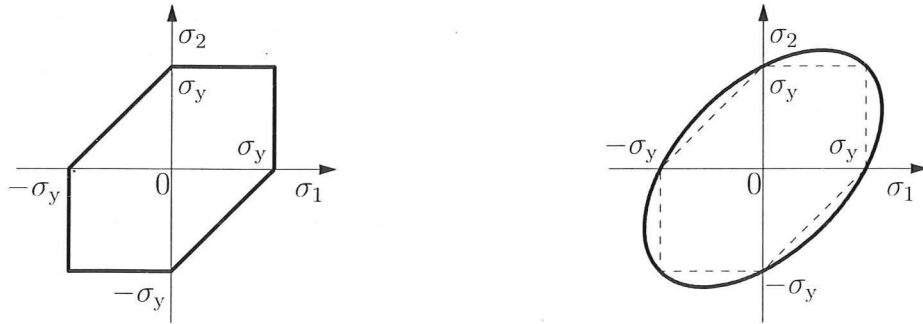
3.3 Plasticity

Chapter 5 considers not only elastic but also plastic behaviour: *i.e.*, the ductile 'failure' of the material such that work has been done upon it, and it will not return to its original shape when unloaded. A second textbook by Calladine (2000) covers, in one volume, all of the principles of plastic analysis that are used in Chapter 5. It does not cover deformation that is time-dependant (*i.e.*, *creep*) or temperature-dependant, but nor does this thesis. In addition, Calladine does not provide detailed references, preferring to produce an easy-to-read textbook and leaving the reader to either trust "that most of the facts and ideas are attributable to others, (or) to consult any of the works cited in the Bibliography to trace the work back to its sources" (Calladine, 2000, p. xiii). These sources, respectively, are Lee and Symonds (1960), which is singled out as an excellent review of a wide range of literature up to that date, Hill (1950), Nadai (1950), Prager and Hodge (1951), Hodge (1959), Heyman and Leckie (1968), Martin (1975) and Johnson and Mellor (1983).

This section begins with a definition of a plastic material, including the simplifications made in this thesis, and goes on to consider yield in Section 3.3.2 and then, in Section 3.3.3, the plastic flow that follows yield.

3.3.1 An ideal plastic material

Figure 3.8a shows an example of a generic one-dimensional stress-strain curve for a material. It behaves in a linear-elastic fashion up to the yield stress, σ_y , whereafter there is some plastic deformation which is *not* recovered during unloading, and therefore work



(a) Graphical representation of the Tresca yield criterion

(b) Graphical representation of the Mises yield criterion, with the Tresca as a dashed line

Figure 3.9: The von Mises and Tresca yield criteria, for *plane stress* (*i.e.*, all out-of-plane stresses are zero).

has been done on the material. Typically, a material will work-harden, *i.e.*, the stress will rise as plastic deformation occurs, as shown in Fig. 3.8a. If the material is unloaded and reloaded after some plastic deformation, the material will still be capable of elastic deformation, denoted by a heavy dashed line, but yield is now at σ'_y .

There are various ways to simplify this behaviour, many of which are detailed in Calladine (2000): one of the simplest is presented in Fig. 3.8b, and is referred to as an *elastic-perfectly-plastic* (EPP) model. The one-dimensional stress-strain curve now contains two distinct linear regions: a linear-elastic region of stiffness E up to a stress of σ_y , and then a flat region as the stress remains constant at σ_y throughout all plastic deformation. This is particularly useful since at no point is the material undergoing changes in both plastic and elastic strain, and hence this is the material model used in Chapter 5. It requires two material properties to be defined: a Young's Modulus, E , and a plastic deformation stress, σ_y . These can be found by experiment.

3.3.2 Yield criteria

There are two common yield criteria used for plastic analyses: the Tresca and von Mises criteria, both explained in detail in Calladine (2000). Each relates the principal stresses to the material's one-dimensional tensile yield stress σ_y , described above in Section 3.3.1. The Tresca criterion is as follows: at yield,

$$\max(|\sigma_1 - \sigma_2|, |\sigma_2 - \sigma_3|, |\sigma_3 - \sigma_1|) = \sigma_y \quad (3.24)$$

while the von Mises criterion is that

$$(\sigma_1 - \sigma_2)^2 + (\sigma_2 - \sigma_3)^2 + (\sigma_3 - \sigma_1)^2 = 2\sigma_y^2 \quad (3.25)$$

In both yield surfaces, it can be seen that what is significant is not the scale of the stresses themselves, but rather the greatest *difference* between two principal stresses.

On the upper and lower faces of a shell structure, the through-thickness tensile and shear stresses σ_{zz} , σ_{yz} and σ_{zx} are zero. For a thin shell, we therefore assume that these stresses are zero throughout the shell: this is a case of *plane stress*, *i.e.*, the only non-zero stresses are σ_{xx} , σ_{yy} and σ_{xy} . Then, the principal stresses σ_1 and σ_2 lie in the x - y plane, and the third principal stress $\sigma_3 = 0$. Therefore, Fig. 3.9 shows the Tresca and von Mises yield surfaces for the case of plane stress, and the criteria become, respectively:

$$\max(|\sigma_1|, |\sigma_2|, |\sigma_1 - \sigma_2|) = \sigma_y \quad (3.26)$$

$$\sigma_1^2 + \sigma_2^2 + \sigma_1\sigma_2 = \sigma_y^2 \quad (3.27)$$

For analytical solutions, the von Mises yield surface has the obvious advantage that it is a continuous function, which can be algebraically differentiated and integrated in a way that equations involving Tresca cannot. However, if a computational approach is used, numerical methods will involve dividing the loading into a series of discrete steps. In this case, the Tresca yield surface is preferable, since it consists of just six linear regions (an upper and lower bound on each of the three terms in Eqn 3.24), each of which can be calculated exactly. A von Mises surface, solved numerically, will have to be artificially divided into a large number of discrete steps, reducing the accuracy while increasing computation time, equation complexity and the risk of numerical instability. Simple computational algorithms can easily work with the discontinuities in the Tresca function, while the simple nature of the six linear facets greatly reduces the number of computational steps needed to process the strains and loadings. For this reason, the Tresca yield surface is used in Chapter 5, where the plastic flow is solved numerically.

3.3.3 Post-yield: plastic flow

The following discussion of plastic flow involves not only the principal stresses, but also principal strains. For strains, as for stresses, there is a coordinate system in which there is zero shear, producing the three principal strains, ε_1 , ε_2 and ε_3 . For an isotropic material, Calladine (2000) demonstrates that the directions of principal stresses and principal strains must coincide. There are two principles upon which the flow model is built, namely, *constant volume* and *normality*, which are outlined below. Note that the principal strains are, in a small increment of time, subject to incremental changes $\delta\varepsilon_1$, $\delta\varepsilon_2$ and $\delta\varepsilon_3$. A strain ε_i is composed of elastic and plastic components, ε_i^E and ε_i^P , and this plastic flow model is concerned with incremental changes in the plastic strain components, *i.e.*, $\delta\varepsilon_1^P$, $\delta\varepsilon_2^P$ and $\delta\varepsilon_3^P$. These can be assembled into a vector, $\delta\boldsymbol{\varepsilon}^P = (\delta\varepsilon_1^P, \delta\varepsilon_2^P, \delta\varepsilon_3^P)$.

Constant volume

Throughout plastic deformation, it is assumed that the volume of the material does not change. Over our incremental shift in strains, the incremental change in volume of a unit volume of the material is given by

$$\delta\varepsilon_1^P + \delta\varepsilon_2^P + \delta\varepsilon_3^P = 0 \quad (3.28)$$

Normality

This principle arises from the postulate that, during plastic deformation, work must always be put *into* the shell: the plastic work done cannot, for a conventional material, be negative. The principle is that the plastic deformation vector $\delta\varepsilon^P$ must be normal to the yield surface. So, if (on our Tresca yield surface) the greatest principal stress difference is $\sigma_1 - \sigma_2$, the normal to the yield surface is the vector $(1, -1, 0)$, while if the largest difference is $\sigma_3 - \sigma_1$, our normal is $(1, 0, -1)$, and so on. Note that these plastic deformation vectors automatically fulfil the criterion of normality: if the vector $\delta\varepsilon$ is in the direction $(1, -1, 0)$, $(1, 0, -1)$ or $(0, 1, -1)$, which, allowing reversals of sign, are the only options for a Tresca yield surface, the volume change $\delta\varepsilon_1^P + \delta\varepsilon_2^P + \delta\varepsilon_3^P$ will automatically be zero.

If the stress state is at a 'corner' of the yield surface, the incremental plastic strain vector will be indeterminate. However, here it helps to know that the volume change must be zero, and as soon as there is some change to the plastic strain, some stresses will relax, moving the stress state away from the corner.

3.4 Experimental and numerical equipment

Chapters 6, 7 and 8 include finite-element numerical simulations. In all cases, these are performed using ABAQUS finite-element software. Since we are studying shell structures rather than membranes, the interesting behaviour comes from the bending of the shell rather than from stretching. Consequently, the shell elements in the simulation need only deal with thin shells and small strains. A suitable element, and the one used almost throughout, is the element referred to in ABAQUS as *S4R5*, which is a quadrilateral thin-shell element defined by its four corner nodes, designed for small strains only. A detailed description of the element, its governing equations and its usage is given in the ‘Abaqus Version 6.7 Theory Manual’: see Hibbitt *et al.* (2008).

The elastic and plastic analyses all depend upon material models, including material properties which can be found by experiment. The relevant properties are the Young’s modulus of the shell, E , the Poisson’s ratio relating stresses to strains in orthogonal directions, ν , the flexural rigidity, D (related to the E , ν and the shell thickness t), and, for the simple model of plasticity outlined in Section 3.3.1, the yield stress, σ_y . Two materials are used for the experiments in this thesis: Copper-Beryllium (‘CuBe’) alloy and High-Impact Polystyrene (‘HIPS’). Both are isotropic, and are supplied in sheet form.

The CuBe is ‘Alloy 25’ from Brush Wellman, to UNS C17200 specification (UNS is the ‘Unified Numbering System’ for alloys). Detailed descriptions of the forms in which it is available, and its physical, mechanical and other properties, can be found in Brush Wellman, Inc. (2008), or in the relevant SAE UNS standards. The alloy is specified as 1.80–2.00 % beryllium, 0.20 % minimum cobalt-nickel, 0.60 % maximum cobalt-nickel-iron, 0.02 % maximum lead and the balance is copper (all percentages by weight). It is supplied solution-annealed, to UNS temper designation TB00. However, we age-harden it for 3 hours at 315 °C, bringing it to a hard temper, TF00. Typical density is given by Brush Wellman as $8.36 \times 10^3 \text{ kg m}^{-3}$, typical coefficient of thermal expansion $17 \times 10^{-6} \text{ }^\circ\text{C}^{-1}$ and typical melting temperature 870–980 °C. More useful are the mechanical properties: typical elastic modulus $E = 131 \text{ GPa}$, tensile strength 1130–1350 MPa, yield stress $\sigma_y = 960\text{--}1210 \text{ MPa}$, elongation to failure of 3–15 % and a fatigue strength of 280–310 MPa over 10^8 cycles. The elastic modulus is checked by tests in Appendix B, which finds an elastic modulus of 124 GPa to fit the flexural behaviour of the shell better: however, the difference has not been found to have any significant effect on the results of this thesis. The yield behaviour is studied in Section 5.3.1.

The elastic modulus of the HIPS is also tested in Appendix B, and is measured as 131 GPa. The HIPS sheet has a thickness before forming of 0.5 mm.

All force-displacement experiments are carried out on an Instron machine. The machine is displacement-controlled, with a range of load cells. The tests in this thesis use either a 200N load cell or a 2kN load cell, depending on the predicted loadings.

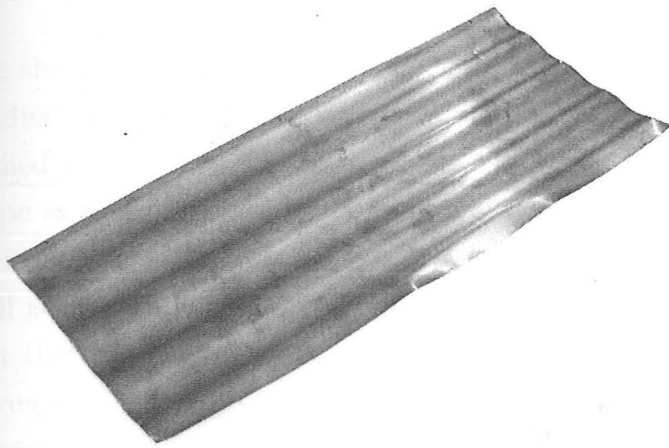
Chapter 4

Flat corrugated shells (i): elastic analysis

Figure 4.1 shows a simple bistable corrugated shell, of CuBe alloy. As described in Section 1.1.1, one stable state, Fig. 4.1a, is a globally flat corrugated sheet which is not unstressed, for residual bending stresses attempt to coil the sheet. If part of the shell is manually flattened across the corrugations, these stresses are released, and the sheet coils up rapidly into the state shown in Fig. 4.1b. The shell can be repeatedly and reversibly ‘snapped’ between the two states, and at no point is the deformation plastic. This coiling/uncoiling will be referred to as the ‘Mode I’ bistability.

During the making of these shells, most prototypes exhibited an unexpected ‘twisting’ bistability in their corrugated form, making some sheets tristable, with no completely flat mode. This is shown in Fig. 4.2. The original single, flat corrugated mode has now split into two corrugated modes of equal global curvature, which are symmetrical about the axis of the corrugations. This twisting mode will be referred to as the ‘Mode II’ bistability. If both modes are present, the shell is tristable with two twisted states and one coiled state: this is referred to as ‘Mode III’ behaviour, also seen in Fig. 4.2. In all of this behaviour, the ‘mid-surface’ of the corrugated shells appears to have a uniform, developable curvature, and this assumption underpins the analysis in this chapter.

This chapter develops a simplified theoretical analysis to explain, from elastic principles, the presence and behaviour of Modes I, II and III, exploring a qualitative explanation of the behaviour of these shells that is related to a simple physical understanding. Unlike the work in the following chapter, Chapter 5, this chapter does *not* produce results that can be conveniently verified numerically through either finite-element modelling or physical test, for reasons explained in Section 4.4. In Chapter 5, a plastic flow model of the forming process attempts to capture the subtle effects that cause Mode II behaviour: this analysis *can* be related to physical tests, as attempted in Section 5.3. The bulk of the work in this chapter has been published as an article by Norman *et al.* (2008b).

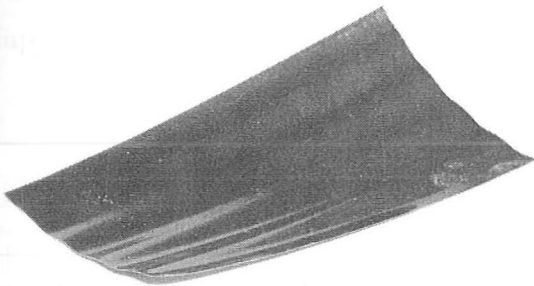


(a) The corrugated flat sheet

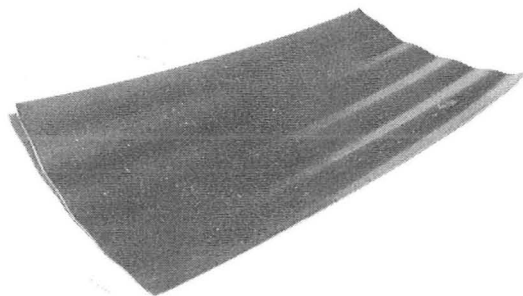


(b) The 'coiled' mode

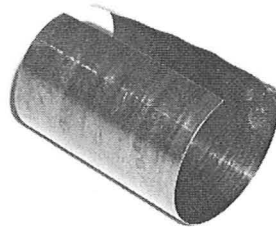
Figure 4.1: A typical shell exhibiting the 'Mode I' bistability, constructed from a conventional isotropic metal alloy (in this case, Copper-Beryllium). A bending prestress is held in equilibrium by the moment arm of the membrane stresses in the corrugated sheet (left): when the corrugations are elastically flattened, the prestresses are released and the sheet coils up.



(a) One of the stable 'twisted' corrugated forms



(b) The second 'twisted' position, symmetric with the first about the corrugation axis



(c) The coiled state, untwisted, with the corrugations flattened out

Figure 4.2: The two 'twisted' corrugated stable states of the 'Mode II' bistability, and the coiled state for Mode III. The Mode II stable states are in fact a cylindrical curvature of the corrugated sheet about an axis not aligned with the corrugations.

4.1 Approach to manufacture and analysis

The shells here are multistable because, in any given configuration, there are significant residual stresses, which are constrained by geometrical effects. When the shells are deformed in certain ways, these prestresses are released, leading to a dramatic change of shape as these stresses drive the rest of the transformation.

In prototypes, these stresses are deliberately caused during manufacture: firstly, the shell is plastically coiled; secondly, the shell is elastically flattened and held that way, so that there are bending stresses throughout the shell; and finally, the shell is plastically corrugated, which prevents the shell from coiling again. The two plastic processes can be reversed in order. A material is required with sufficient hardness and ductility that the second working stage does not eradicate the stresses from the first; steels are suitable, but Copper-Beryllium alloy has been used here, due to the ease with which it can be hardened.

The layout of this chapter is as follows. Section 4.2 develops an analytical model to simulate the general observed behaviour of the prototype shells. Section 4.3 then applies appropriate initial conditions and limits on deformation to predict and explain the three modes of multistability in terms of the principles upon which the analytical model of Section 4.2 is based. Finally, Section 4.4 presents some conclusions, leading into Chapter 5.

4.2 The analytical model

This section sees the development of a simplified model that separates the curvature of the shell into the *global*, or average, curvature of the shell and the *local* curvature of the corrugations themselves, which are assumed to be uniformly curved upwards or downwards.

The interaction of these two curvatures causes the shell to have local double curvature, so that during deformation, in addition to bending strains, there are significant stretching strains. However, a simple trick enables us to expedite simply the consideration of stretching: the stiffness of the shell, in so far as it interacts with the *global* curvature, is modified to the anisotropic stiffness of the *mid-surface* of a corrugated shell. These effective mid-surface properties of a corrugated shell have a greatly increased bending stiffness in the direction of the corrugations relative to the local shell, and this increased stiffness accounts exactly for the stretching stresses. Note that the stiffness is actually orthotropic but the principle holds generally. Analysing corrugated shells through an equivalent orthotropic surface is a commonly used procedure; a recent historical review of this method, and the results produced, has been presented in detail in Section 2.1.1.

Where this analysis differs from those described in Section 2.1.1 is that, as the shell undergoes large changes of shape, some of these global properties will vary as the local corrugations deform, so that although the two scales are modelled independently, they interact. Nonetheless, the separation of these two scales gives the model a marked simplicity and, by attempting to capture the behaviour with a minimum complexity, meaningful insights can be inferred on how they operate, without recourse to expensive computational simulations.

Throughout this chapter, these shells undergo no stresses in their mid-plane, so that $N_{XX} = N_{YY} = N_{XY} = 0$, and the only moment acting on the shell is that due to the prestress, M_{xx} .

4.2.1 Stiffness and energy

The shell material is assumed to be linearly elastic and to obey Hooke's law with a Young's modulus, E , and Poisson's ratio, ν . Furthermore, it is assumed that the shell can be modelled as being thin, leading to assumptions that, in bending, plane sections remain plane, shear stresses in the z -direction are negligible, and through-thickness stresses are zero. From Section 3.2.1, the generalised Hooke's law for the bending of such an *isotropic*

shell is given by:

$$\begin{bmatrix} \Delta M_{xx} \\ \Delta M_{yy} \\ \Delta M_{xy} \end{bmatrix} = \Delta \mathbf{M} = \mathbf{D} \Delta \boldsymbol{\kappa} = D \begin{bmatrix} 1 & \nu & 0 \\ \nu & 1 & 0 \\ 0 & 0 & \frac{1}{2}(1 - \nu) \end{bmatrix} \begin{bmatrix} \Delta \kappa_{xx} \\ \Delta \kappa_{yy} \\ 2\Delta \kappa_{xy} \end{bmatrix} \quad (4.1)$$

where Δ denotes the change from an initial state and D is the flexural rigidity, defined by Eqn 3.9.

Let us now consider the stiffness of the corrugated sheet. Modelling the detail of the shell within the corrugations can be complex, but the goal here is to derive a simplified model involving the properties of the mid-surface of the corrugated shell.

Section 2.1.1 presents the bending stiffness properties of a corrugated sheet in the equivalent mid-surface plane (the X - Y plane of Fig. 3.4). However, in the large deformations explored in this chapter, the corrugation shape changes significantly, and therefore the mid-surface undergoes large strains in the Y direction. A model which considers the mid-surface behaviour would therefore have to:

- (i) produce a coupled relationship between X - X bending and Y - Y stretching; and
- (ii) vary the Y -direction limits over which internal strain energy is integrated when finding its average value.

These are both extremely complex problems to solve. If, instead, we work with the local x - y - z coordinate system of Fig. 3.4, our integration limits do not vary, and we are working with an isotropic material in which bending and stretching are not coupled. However, now, as we vary the curvature κ_{XX} , there is marked stretching in the peaks of the corrugations and compression in the troughs, and this stretching, again, complicates our equations.

A simple solution is to use a *local* coordinate system, but deal with κ_{XX} as if we were in a *global* coordinate system: we assume that $\kappa_{xx} = \kappa_{XX}$ throughout. In the coiled mode of Fig. 4.1b, this is approximately true, and while this is not remotely true in the corrugated mode of Fig. 4.1a, both curvatures are then very small. Now, we can account for all stretching/compression effects by modifying the *local* material stiffness matrix of Eqn 3.7 with the additional *global* stiffness term in the X - X direction added by, *i.a.*, Briassoulis (see Section 2.1.1). This increase was described in Table 2.1 as $\bar{a}^2 t$ per unit length in the global coordinate system: in the local system, this must be multiplied by Λ/λ . If we introduce a new dimensionless variable α , which is a function of the corrugated shape such that $E\bar{a}^2 t \Lambda/\lambda = \alpha D$, then the bending stiffness of our sheet in x - y - z coordinates

becomes

$$\mathbf{D} = \begin{bmatrix} (1 + \alpha)D & \nu D & 0 \\ \nu D & D & 0 \\ 0 & 0 & \frac{1}{2}(1 - \nu)D \end{bmatrix} \quad (4.2)$$

This simple relationship is only valid if the equivalent mid-surface is developable (*i.e.*, singly curved); any double curvature, or non-zero Gaussian curvature, would lead to stretching across the corrugations, which in turn has a significant effect on bending stiffnesses, so that bending moments are coupled with stretching forces in a strongly non-linear fashion. Note that α varies during Mode I deformation as the corrugations flatten. This flattening of corrugations affects energy on a local scale within the corrugations, where the material is isotropic, and described by Eqn 4.1. This is pursued further in the coming section.

From Eqn 3.11, for bending only, the strain energy density is given as

$$U = \frac{1}{2} \Delta \boldsymbol{\kappa}^T \mathbf{D} \Delta \boldsymbol{\kappa} + M_0^T \Delta \boldsymbol{\kappa} \quad (4.3)$$

This equation and its derivation can also be found in Kebabze *et al.* (2004).

4.2.2 Combining the local and global scales

Let us now divide the curvature of the corrugated shell into two components; the ‘global’ curvature vector, denoted by \mathbf{k} , and the corrugation curvature, \mathbf{c} . \mathbf{k} is the average curvature of the shell whilst \mathbf{c} is the local variation away from \mathbf{k} due to the corrugations themselves and so must average to zero over the sheet. The sum of these two curvatures is inserted into the strain energy density equation, Eqn 4.3, as follows.

Following Section 4.2.1, only the global curvature \mathbf{k} is married to the additional stiffness αD . Since αD corresponds to the axis of the corrugations, it is perpendicular to the corrugation curvatures, which do not vary along the corrugations, and thus the only non-zero component of \mathbf{c} is in the y - y direction, with $c_{yy} = c(y)$.

Furthermore, due to the assumption of inextensional behaviour, the global sheet is limited to a developable curvature, which is approximately uniform across the shell from observation. This curvature has some magnitude k in a direction making an angle θ to the x axis, as shown in Fig. 4.3, and k and θ are both assumed to be uniform over the shell. The global shell curvatures are then derived from a Mohr’s circle of curvature, as in Guest and Pellegrino (2006), to be

$$k_{xx} = \frac{1}{2}k(1 + \cos 2\theta) \quad k_{yy} = \frac{1}{2}k(1 - \cos 2\theta) \quad k_{xy} = -\frac{1}{2}k \sin 2\theta \quad (4.4)$$

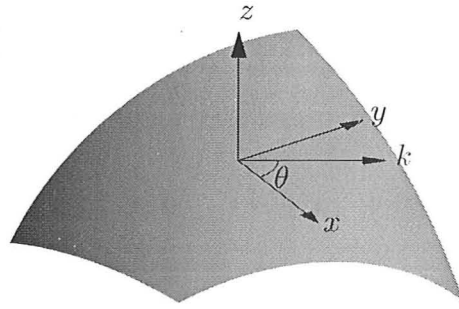


Figure 4.3: Definitions of the global cylindrical curvature k and its angle θ to the x axis.

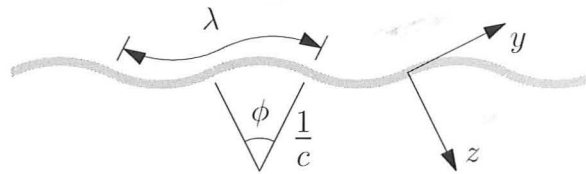


Figure 4.4: The circular-arc corrugation profile. The profile is repeated every wavelength, λ . The curvature has constant magnitude, but changes sign every half-wavelength; each half-corrugation is a circular arc subtending an angle ϕ .

Therefore, the total curvature is given as follows:

$$\Delta\kappa = k - k_0 + c - c_0 \quad k = \frac{1}{2}k \begin{bmatrix} 1 + \cos 2\theta \\ 1 - \cos 2\theta \\ -\sin 2\theta \end{bmatrix} \quad c = \begin{bmatrix} 0 \\ c(y) \\ 0 \end{bmatrix} \quad (4.5)$$

where k_0 and c_0 are initial values. Note, again, that α is a function of the corrugations (*i.e.*, a function of c).

4.2.3 Corrugation profile

Our prototype shells were constructed with circular-arc corrugations that repeat every wavelength λ (see Fig. 4.4). In addition to being simply made, this profile is expeditious in theoretical analysis, since the corrugation curvature c then has constant magnitude across the corrugations, swapping direction every half-wavelength. In other words, the initial corrugation curvature $c_0(y)$ is

$$c_0(y) = \pm c_0 \quad (4.6)$$

where c_0 is a constant.

The deformed local curvature may not be uniform, but we make the simplifying assumption that, while the corrugations may be flattened out, they remain as circular arcs.

Let us assume also that the λ does not change: *i.e.*, the curvature $c(y)$ is always in phase with the initial curvature $c_0(y)$. Thus, the corrugation curvature is always a simple multiple of the initial corrugation curvature, denoted by the coefficient β :

$$c(y) = \beta c_0(y) = \pm \beta c_0 \quad (4.7)$$

and the current angle subtended by each half-corrugation is

$$\phi = \frac{1}{2} \lambda c = \frac{1}{2} \beta \lambda c_0 = \beta \phi_0 \quad (4.8)$$

The initial corrugated shell has $\beta = 1$, and once the corrugations have been flattened and the sheet coils up, $\beta = 0$.

From this function c , we can calculate α as a function of β . Considering each element of length dy and thickness t to be a distance a from the centreplane of the corrugations,

$$\alpha D = \frac{1}{\lambda} \int_0^\lambda E a^2 t dy \quad (4.9)$$

Over a quarter-corrugation, a can be written as

$$a(y) = \frac{1}{c} \left[\cos(cy) - \cos\left(\frac{\phi}{2}\right) \right] = \frac{1}{\beta c_0} \left[\cos(\beta c_0 y) - \cos\left(\frac{\beta \phi_0}{2}\right) \right] \quad (4.10)$$

The integral of Eqn 4.9 then becomes

$$\alpha(\beta) = \frac{E}{D} \frac{4}{\lambda \beta c_0} \int_0^{\frac{\lambda}{4}} \left[\cos(\beta c_0 y) - \cos\left(\frac{\beta \phi_0}{2}\right) \right]^2 dy \quad (4.11)$$

This integral is solvable, giving

$$\alpha(\beta) = \frac{12(1 - \nu^2)}{\hat{c}_0^2} \left[1 + \frac{1}{2} \cos(\beta \phi_0) - \frac{3}{2\beta \phi_0} \sin(\beta \phi_0) \right] \quad (4.12)$$

and, necessary for Section 4.3.1,

$$\frac{d\alpha}{d\beta} = \frac{12(1 - \nu^2)}{\hat{c}_0^2} \left[\frac{3}{2\phi_0 \beta^2} \sin(\beta \phi_0) - \frac{3}{2\beta} \cos(\beta \phi_0) - \frac{\phi_0}{2} \sin(\beta \phi_0) \right] \quad (4.13)$$

In Section 4.3.1, it would be useful, although it is not done there, to invert Eqns 4.12–4.13, giving β in terms of α . However, this is impossible unless the sine and cosine terms in α are broken down into integer series. It is then found that the lowest powers of $\beta \phi_0$ cancel, and the higher-power terms become very small indeed even for ϕ_0 values of up to π . This

creates a polynomial rather than sinusoidal expression for α , which is much simpler to solve explicitly in various directions. In this fashion, α is approximated to within 1 % of its exact value for values of $\beta\phi_0$ of up to $\pi/2$ (the limit before the corrugation curvature becomes re-entrant) by

$$\alpha = \frac{12(1 - \nu^2)}{\hat{c}_0^2} \left[\frac{(\beta\phi_0)^4}{120} - \frac{(\beta\phi_0)^6}{2520} + \frac{(\beta\phi_0)^8}{120960} - \frac{(\beta\phi_0)^{10}}{9979200} + O((\beta\phi_0)^{12}) \right] \quad (4.14)$$

$$\frac{d\alpha}{d\beta} = \frac{12(1 - \nu^2)}{\hat{c}_0^2} \left[\frac{(\beta\phi_0)^3}{30} - \frac{(\beta\phi_0)^5}{420} + \frac{(\beta\phi_0)^7}{15120} - \frac{(\beta\phi_0)^9}{997920} + O((\beta\phi_0)^{11}) \right] \phi_0 \quad (4.15)$$

For $\beta\phi_0 \leq 1$, we can neglect all but the first two terms, and for $\beta\phi_0 \leq \frac{1}{4}$, we can neglect all but the first, making this much simpler than the exact expression.

4.2.4 Limitations of the analysis

The Mode I and Mode III analyses have a prestress moment which is entirely composed of a bending stress in the local sheet. In a corrugated sheet, there can also be a bending stress that is due to strains in the shell, but this, if it is present when the sheet is globally flat, implies that the sheet is not developable, and the corrugations can not therefore be flattened out. This form of bending stress can be present in the Mode II analysis since it does not require the corrugations to flatten out.

The β model of corrugation flattening described in Section 4.2.3 is simplistic: the corrugations are likely to flatten in a more complex fashion. As we are restricting possible modes of deformation, our results will give an upper bound on the moment at which the shell buckles. Also, note that edge effects are neglected throughout, on the assumption that they do not have a significant effect on the bulk behaviour. Finally, this analysis only applies to deformations that are uniform over the entire sheet, and does not tell us anything directly about the behaviour or stability of a shell when local external loadings are applied. However, due to these simplifications, the analysis is extremely compact, and yet, as is seen in Section 4.3 and in Chapter 5, it captures very accurately the essence of the behaviour.

4.3 Analytical model behaviour

The curvature defined in Eqn 4.5 has three terms that may be varied: global curvature magnitude k ; global curvature direction θ ; and the function describing corrugation curvature, $c(y)$. This section considers the variation of:

- (i) k and $c(y)$, with θ held at 0° , to describe the coiling Mode I bistability;
- (ii) k and θ , for the twisting Mode II bistability, where the corrugations do not flatten significantly and so, given that $c(y)$ is fixed, α is constant; and
- (iii) k , θ and $c(y)$, to model the tristable Mode III behaviour and also to determine stability conclusively: *i.e.*, whether or not the stable points found in previous models are still stable when all other modes of deformation are present.

In all cases, there is a prestress moment in the direction of the corrugations: this moment is modelled by a constant externally applied moment, M_{xx_0} . For simplicity, we will refer to it just as M for the rest of this chapter.

4.3.1 Mode I: Coiling bistability

The global curvature of the shell is along the corrugations, in the direction in which stiffness is increased by αD , so $\theta = 0$. The initial state is chosen to be globally flat, *i.e.* $k_0 = 0$, but locally corrugated. We expect to see that such a structure can have two distinct stable states: one which is globally flat and corrugated, and one which is uncorrugated and coiled up along the corrugations. This initial state is undeformed, so there are no internal membrane stresses: it cannot, therefore, be in equilibrium with the imposed bending prestress. However, we might expect equilibrium to be restored by only a small amount of curvature along the corrugations, producing the corrugated stable state observed in physical models.

Substituting the curvatures of Eqn. 4.5 and the prestress moment into Eqn 4.3 gives the strain energy density equation

$$U = Mk + \frac{1}{2}D \left\{ (1 + \alpha)k^2 + 2\nu k(1 - \beta)c_0(y) + [(1 - \beta)c_0(y)]^2 \right\} \quad (4.16)$$

This must be integrated over the entire sheet, but can be simplified. The sheet is assumed to be uniform, and hence to find the average energy density, we integrate Eqn 4.16 over one corrugation wavelength in the y direction and divide by the corrugation wavelength to find the average energy density over the sheet. No integration in the x direction is needed, since the curvatures are uniform along the corrugations. The average curvature of the shell in the y direction is the integral of $c(y)$ over one wavelength λ , divided by λ .

Since, in the initial state, the sheet has no global curvature in the y direction,

$$\frac{1}{\lambda} \int_0^\lambda c(y) dy = 0 \quad (4.17)$$

Both the Mk and $k^2(1 + \alpha)$ terms, in Eqn 4.16, are constant over the shell. Since, according to Eqn 4.17, c averages to zero, where the spatially-constant value $2\nu k$ is multiplied by c , that term also vanishes. As β is assumed not to vary over the sheet, neither does $(1 - \beta)^2$, and thus the average strain energy density, denoted by \bar{U} , is revealed as

$$\bar{U} = Mk + \frac{1}{2}D \left[(1 + \alpha)k^2 + \frac{(1 - \beta)^2}{\lambda} \int_0^\lambda c_0^2(y) dy \right] \quad (4.18)$$

From the corrugation profile described in Section 4.2.3, the integral within Eqn 4.18 equals λc_0^2 . For a more compact description, dimensionless variables are now introduced:

$$\hat{c}_0 = c_0 t \quad \hat{k} = \frac{k}{c_0} \quad \hat{M} = -\frac{M}{Dc_0} \quad \hat{U} = \frac{\bar{U}}{\frac{1}{2}Dc_0^2} \quad (4.19)$$

Note the minus sign in the equation for \hat{M} , which is explained thus: M , that is, M_{xx_0} , is an initial externally applied moment. Since the initial state is globally flat, this moment is an equal and opposite reaction *against* the positive prestress, which is trying to coil the shell up. Thus, by introducing the minus sign, moment-displacement plots such as Fig. 4.5 show positive stiffness when the structure is stable.

The dimensionless energy equation now reduces to

$$\hat{U} = \hat{k}^2(1 + \alpha) + (\beta - 1)^2 - 2\hat{M}\hat{k} \quad (4.20)$$

where α is given as a function of β by Eqn 4.12. Equilibria are formally obtained by setting $d\hat{U}/d\hat{k} = d\hat{U}/d\beta = 0$. Dealing first with equilibrium in \hat{k} :

$$\frac{d\hat{U}}{d\hat{k}} = 2[\hat{k}(1 + \alpha) - \hat{M}] = 0 \quad (4.21)$$

resulting in the expressions

$$\hat{k} = \frac{\hat{M}}{1 + \alpha} \quad (4.22)$$

$$\hat{U} = (\beta - 1)^2 - \frac{\hat{M}^2}{1 + \alpha} \quad (4.23)$$

To find equilibrium in β :

$$\frac{d\hat{U}}{d\hat{\beta}} = \hat{k}^2 \frac{d\alpha}{d\beta} + 2(\beta - 1) = 0 \quad (4.24)$$

We can now substitute our equilibrium value of \hat{k} , from Eqn 4.22, into Eqn 4.24 to produce an equation defining the equilibrium value of β as a function of \hat{M} (recall that α is also a function of β):

$$\hat{M}^2 \frac{d\alpha}{d\beta} = 2(1 - \beta)(1 + \alpha)^2 \quad (4.25)$$

This poses a problem: Eqn 4.25 is not conveniently solvable, after substituting in Eqns 4.12 and 4.13. Instead, for a given value of β , we can plot the equilibrium moment \hat{M} for a given value of β . On the resulting plot, we can then identify the equilibrium value of β for our specific moment \hat{M} by a numerical approach. Using subscript 'E' to denote equilibrium solutions, we find that

$$\hat{k}_E = \frac{\hat{M}}{1 + \alpha_E} \quad (4.26)$$

$$\hat{U}_E = (\beta_E - 1)^2 - \frac{\hat{M}^2}{1 + \alpha_E} \quad (4.27)$$

$$\hat{M} = (1 + \alpha_E) \sqrt{2(1 - \beta_E) \left[\frac{d\beta}{d\alpha} \right]_E} \quad (4.28)$$

The above equations define equilibrium, but we must now check that these equilibrium points are stable. This is done by testing the sign of second-order derivatives, which must be positive. In \hat{k} ,

$$\frac{d^2\hat{U}}{d\hat{k}^2} = 2(1 + \alpha) > 0 \quad (4.29)$$

Since α is always positive, this second derivative is always positive, and so the shell will *always* be stable in \hat{k} . However, determining stability in β involves finding the value of

$$\frac{d^2\hat{U}}{d\beta^2} = \hat{k}^2 \frac{d^2\alpha}{d\beta^2} + 2 \quad (4.30)$$

Again, we encounter the problem that we cannot determine β analytically. Hence, we determine this stability graphically from the generalised load-displacement plots, where a positive gradient equates to positive stiffness and stability but a negative gradient equates to negative stiffness and instability. With Eqns 4.12–4.28, we can now describe

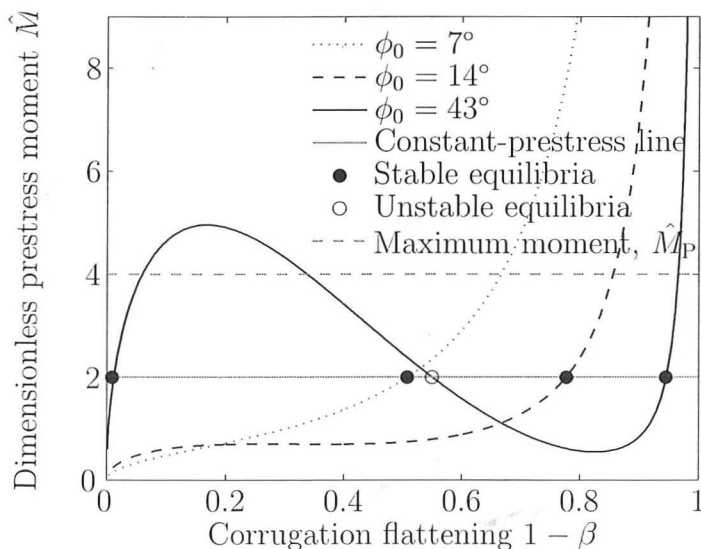


Figure 4.5: Equilibrium plot of moment, \hat{M} , against corrugation flattening, $1 - \beta$, with $\hat{c}_0 = 6.25 \times 10^{-3}$. The gradient of the equilibrium curve is the stiffness of the shell in flattening, so positive gradient = positive stiffness (stable) and negative gradient = unstable. A given prestressed shell has a constant \hat{M} (in this example, 2). Where the line of constant \hat{M} crosses the equilibrium curve, there is an equilibrium point. Below $\phi_0 = 14^\circ$, the unstable region vanishes and the structure becomes monostable. Also labelled is the maximum moment that CuBe alloy can provide, \hat{M}_P ; note that bistability is possible for moments well below it. $\phi_0 = 7^\circ$ corresponds to $\alpha = 0.5$ here: $\phi_0 = 14^\circ$ to $\alpha = 8.3$, and $\phi_0 = 42^\circ$ to $\alpha = 720$, all from Eqn 4.12

the behaviour of the global and local curvature of the sheet under any moment \hat{M} .

Figure 4.5 plots Eqn 4.28, showing the equilibrium prestress moment \hat{M} related to the corrugation curvature β , for $\hat{c}_0 = 6.25 \times 10^{-3}$, which is chosen to match the physical shells where $c_0 = 50 \text{ m}^{-1}$ and $t = 0.125 \text{ mm}$. The gradient is the flattening stiffness of the shell in response to an applied moment: in this case, this moment is applied by the prestress, and is therefore fixed for a given shell. There are two regions of positive stiffness, between which there is one region of negative stiffness.

Given that \hat{M} is fixed for a specific shell, that shell is in equilibrium where the line of constant \hat{M} crosses the equilibrium curve. In Fig. 4.5, as an arbitrary example, the equilibrium points are labelled for $\hat{M} = 2$. In fact, for a range of values of \hat{M} , if $\phi_0 > 0.25$, there are three equilibrium solutions for a given moment. Two of these lie on regions of positive gradient and are therefore stable; the point in between has negative stiffness and is unstable.

If the prestress moment is too low, there is no stable coiled mode, at low β ; if the prestress is too high, there will be no stable corrugated mode, at high β . In addition, as ϕ_0 becomes small, the corrugations tend towards a flat sheet, which is not bistable. From Fig. 4.5, it can be seen that for the specified sheet properties and corrugation

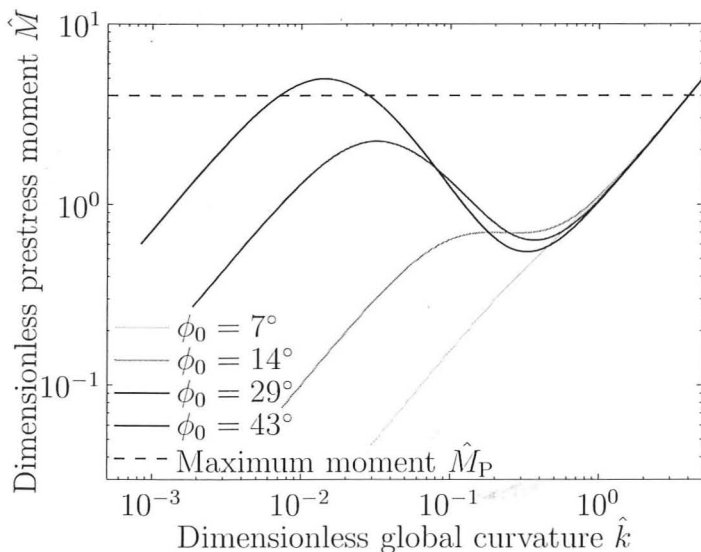


Figure 4.6: Log-log equilibrium plot of moment, \hat{M} , against global curvature, \hat{k} , with $\hat{c}_0 = 6.25 \times 10^{-3}$. Again, a given shell has a constant moment \hat{M} , and the equilibrium points for the shell are where the constant- \hat{M} line crosses the equilibrium curve. This shows clearly the linear-elastic nature of the stable regimes, with the second stable state corresponding to the linear stiffness of an uncorrugated sheet. Also labelled is the maximum moment that CuBe alloy can provide, \hat{M}_P , and bistability can occur at lower moments. $\phi_0 = 29^\circ$ corresponds to $\alpha = 150$.

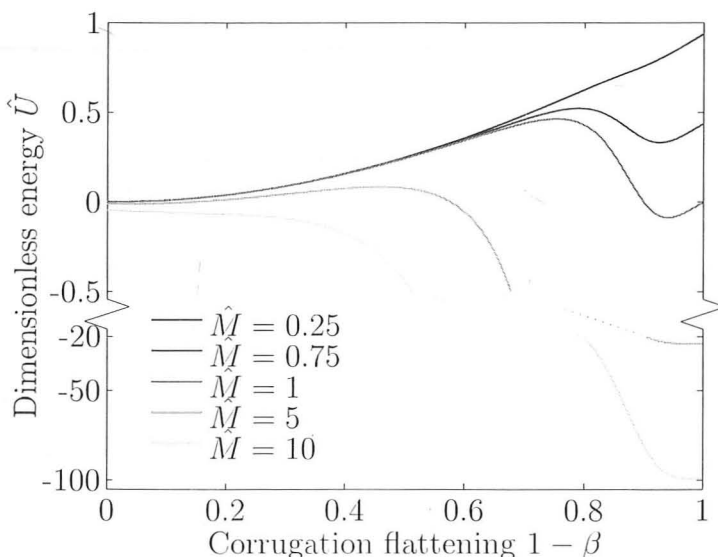


Figure 4.7: Plot of energy density relative to the initial state, \hat{U} , against corrugation flattening, $1 - \beta$, at $\hat{c}_0 = 6.25 \times 10^{-3}$ and $\phi_0 = 57^\circ$ for various moments \hat{M} . A large section of the \hat{U} axis has been cut out so as to give detail around $\hat{U} = 0$ whilst showing features down to $\hat{U} = -100$. At higher \hat{M} , the coiled mode (β small) is lower-energy; at lower \hat{M} , the corrugated mode is lower-energy. For very large or small \hat{M} , the bistability vanishes.

curvature, this occurs when the subtended angle of corrugations falls below 14° , which, in this case, has an initial $\alpha = 8.3$. Note that, as the corrugations become deeper, so α increases dramatically, being the second moment of area of the corrugations about the mid-surface. In other words, the bending stiffness of the shell along the corrugations is very strongly dominated by the effect of the corrugations themselves, the shell bending stiffness becoming negligible by comparison.

For shallow corrugations, Fig. 4.5 shows that the coiled state still has significant corrugations, as β is still rather greater than zero: even at deeper corrugations, the coiled state will never quite reach $\beta = 0$. This occurs because, if the shell is coiled, it cannot be in equilibrium if the corrugations are *completely* flattened. While the shell is coiled, the reappearance of corrugations would compress the 'peaks' and stretch the 'troughs', which is why the corrugations are suppressed in the coiled mode. However, if the corrugations were completely flattened, then this stretching and compressing that prevents the corrugations is not present. A small amount of corrugation must introduce just enough stretching and compressing to prevent any further corrugation reappearing.

Figure 4.6 shows the same data but plots \hat{M} against global curvature \hat{k} . This is the moment-curvature response of the shell, and its gradient is the bending stiffness of the shell. It can be seen that the corrugated stable form has very low global curvature. In the coiled mode, the moment-curvature relationship becomes linear with gradient D , or unity in our dimensionless form.

In relation to a physical shell, it is important to ask whether this behaviour can be achieved within the elastic limits of the material. The precise nature of the internal stresses that produce the moment is determined by the forming process history, but the maximum moment per unit length of shell that the material can sustain is the fully plastic moment, approximated by the beam-section expression approximated by the beam-section expression

$$M_P = \frac{1}{4} \sigma_y t^2 \quad (4.31)$$

given from the assumption that the stress has a magnitude of the yield stress σ_y throughout the depth of the shell. The moment's dimensionless magnitude is then

$$|\hat{M}_P| = \frac{M_P}{Dc_0} = \frac{\sigma_y}{E} \cdot \frac{3(1-\nu^2)}{\hat{c}_0} \quad (4.32)$$

For Copper-Beryllium alloy, the yield stress, $\sigma_y = 1200$ MPa, and Young's modulus, $E = 130$ GPa (see Section 5.1, below), giving a dimensionless plastic moment $\hat{M}_P \simeq 4$. Figs 4.5 and 4.6 show that, for relevant values of ϕ_0 , bistability is possible with moments less than \hat{M}_P . This is implied to be conservative by Section 5.3.1, which fits an elastic-perfectly-plastic ('EPP') material model to physical tests, and finds $\sigma_y = 1500$ MPa to

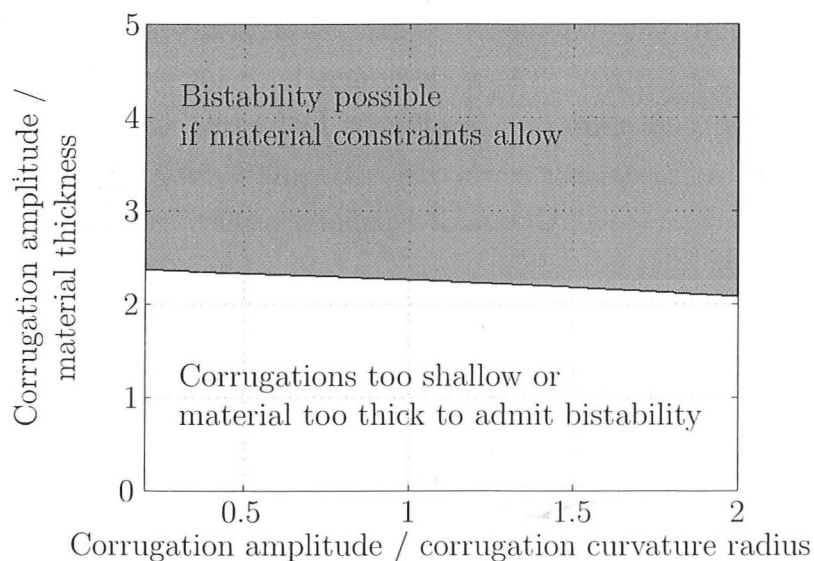


Figure 4.8: A design chart of the corrugation shapes over which coiling bistability is possible. On the x axis is the ratio of corrugation trough-to-peak amplitude to corrugation curvature radius, defined as $2[1 - \cos(\phi_0/2)]$, which is purely a measure of corrugation shape, independent of material. The y axis gives the ratio of corrugation amplitude to material thickness, defined as $2[1 - \cos(\phi_0/2)]/\hat{c}_0$. As can be seen, bistability requires a corrugation amplitude at least 2 or 3 times the material thickness. Smaller corrugation radii, or tighter corrugation curvatures, also help bistability, but only very weakly.

produce a good match.

For bistable shells, if the shell is held such that half is coiled and the other half is corrugated, one of these states may have lower energy, in which case the transition region between them will move to the opposite end and the shell will globally take on the lower energy state. It is intuitively obvious that, if there is a stable-equilibrium corrugation curvature \hat{c}_E and a stable coiled-mode curvature \hat{k}_E , the lower-energy mode will be whichever state has the tighter curvature. In other words, if the corrugated-mode corrugations have a tighter curvature than the coiled-mode coil, the corrugated mode will be lower-energy and the sheet will prefer to snap to the corrugated mode from a half-and-half transition state; if the coiled-mode coil is tighter, it will snap to the coiled state.

Figure 4.7 shows the variation with β of the internal strain energy, relative to the strain energy at the initial state, for a range of moments at $\phi_0 = 29^\circ$; note that the lower energy state is the corrugated state at low moment, but the coiled state at high moment. There is one moment at which both states have approximately the same energy, and any half-transformed shell will rest without becoming fully corrugated or fully coiled: it is effectively 'neutrally stable', with no energy gradient in either direction. This feature occurs in Fig. 4.7 when $\hat{M} = 0.88$. It is reasonable that negative values of \hat{U} appear on Fig. 4.7, since the initial state of the sheet is neither unstressed nor stable.

In summary, Fig. 4.8 shows the conditions required for bistability. A simple algorithm produced the \hat{M} - β curve for each combination of \hat{c}_0 and ϕ_0 , and determined that that state was bistable if this curve had some local maximum and minimum different from $\beta = 0$ and $\beta = 1$ respectively. This \hat{M} - β curve was then transformed into a curve in two dimensionless groups such that the main determining factor for bistability becomes obvious. These groups were found by trial to correspond to the ratio of corrugation amplitude to material thickness, and to the ratio of corrugation amplitude to corrugation curvature radius. This provides a general design guide for the bistable shells. The relevance of this model to physical behaviour is explored further in Section 5.1.2.

4.3.2 Mode II: Twisting bistability

The shell has a prestress moment in the x direction as before. However, the corrugations are not permitted to flatten or buckle (*i.e.*, $\beta = 1$ at all times), but the global curvature is now no longer constrained to be in the x direction, *i.e.*, θ is allowed to vary.

Several specimens intended to display Mode I were also displaying Mode II. Observing this, it became obvious that, once the corrugated shell is given its prestress, a curvature across the corrugations appears, caused by the plastic forming process, described later in Section 5.1.2. This curvature is unstable in θ , snapping to one of the two twisted modes. Therefore, in our attempt to model this bistability, we predicate a prestress moment M_{xx0} , as before, and an initial non-zero curvature k_0 for $\theta_0 = 90^\circ$, *across* the corrugations.

Considerations of plasticity and the maximum moment permitted by the material are not relevant to this model since, first, the profile of the corrugations is irrelevant except in that they increase the stiffness by a factor α and, second, since the corrugations need not be flattened out, the sheet is not constrained to be developable; this means that the prestress moment can consist not only of a shell bending moment but also of shell strains.

Since the exact corrugation profile is no longer significant, it is now convenient to make variables dimensionless against the initial curvature k_0 rather than c_0 . To contrast with Section 4.3.1, these are denoted by ‘ \checkmark ’:

$$\checkmark k = \frac{k}{k_0} \quad \checkmark M = -\frac{M}{Dk_0} \quad \checkmark U = \frac{\bar{U}}{\frac{1}{2}Dk_0^2} \quad (4.33)$$

Equation 4.3 then becomes

$$\checkmark U = \checkmark k^2 \left[1 + \frac{\alpha}{8} (3 + 4 \cos 2\theta + \cos 4\theta) \right] + \checkmark k [(1 - \nu) \cos 2\theta - (1 + \nu)] + 1 - \checkmark M \checkmark k (1 + \cos 2\theta) \quad (4.34)$$

Equilibrium configurations are given by $d\checkmark U/d\theta = 0$ and $d\checkmark U/d\checkmark k = 0$, and solutions are obtained in closed form as follows. Stability is separately assessed and recorded:

- (i) $\check{k}_E = 0$, $\cos 2\theta_E = \frac{1+\nu+\check{M}}{1-\nu-\check{M}}$, if $\check{M} < -\nu$. This is not a stable solution;
- (ii) $\check{k}_E = 1$, $\theta_E = 90^\circ$. This is the initial state, is an equilibrium point for all cases, and is only stable when $\check{M} < 1 - \nu$;
- (iii) $\check{k}_E = 1$, $\cos 2\theta_E = 2\frac{\check{M}-1+\nu}{\alpha-1}$. This solution only exists for $1 - \nu < \check{M} < \alpha + 1 - \nu$, and is always stable. Note that since 'cos 2 θ ' is a symmetric function, there is a symmetric pair of stable solutions;
- (iv) $\check{k}_E = \frac{\check{M}+\nu}{\alpha+1}$, $\theta_E = 0$. This always exists, but is only stable when $\check{M} > \alpha + 1 - \nu$.

Henceforth, the values of \check{k} and θ at stable equilibrium points are referred to as \check{k}_M and θ_M , where the subscript 'M' denotes a value at a local energy minimum.

A contour plot of stored energy yields this information more intuitively. Stable equilibrium points are then evident as minima, and unstable equilibrium points appear as either maxima or saddle points. The two independent variables controlling the shape of the sheet are curvature magnitude and direction, and so a polar plot makes the most sense, as adopted by Kebabze *et al.* (2004). Figure 4.9a shows the plot coordinates: the distance from the origin denotes tightness of curvature \check{k} (so at the origin, the sheet is flat), while the angle on the plot denotes 2θ , rather than θ , since curvature repeats every 180° . Figure 4.9b is an identical plot, but with contours of the cartesian curvature components, κ_{xx} , κ_{yy} and κ_{xy} , calculated from Eqn 4.4.

From the enumerated solutions above, there are three distinct modes of behaviour in which the stable points are located by different expressions. The bistable mode is found as solution (iii), where \check{M} lies in the range

$$1 - \nu < \check{M} < \alpha + 1 - \nu \quad (4.35)$$

and only this range of prestress moments will provide bistability. For smaller or negative prestresses, there is just one stable point, at $\theta = 0$, which is solution (ii), the initial state. For larger prestresses, the sole stable point is at $\theta = 90^\circ$, which is solution (iv). Both of these solutions are present as saddle points on a bistable sheet. Fig. 4.10 shows all of this behaviour, giving contour plots of internal strain energy for a variety of prestress moments. As can be expected, as the corrugations become very strong (as in Fig. 4.10c), the energy penalty associated with any change in κ_{xx} becomes very strong. As an aside, a negative \check{k}_0 produces a bistability described by Kebabze *et al.* (2004), but this is not related to the Mode II twisting. Rather, the effect is that of a shell given two conflicting curvatures of perpendicular orientations of opposite sense, which are the two stable states.

We have shown that the observed twisting behaviour can arise from the interaction between an initial curvature across the corrugations and a prestress moment along them.

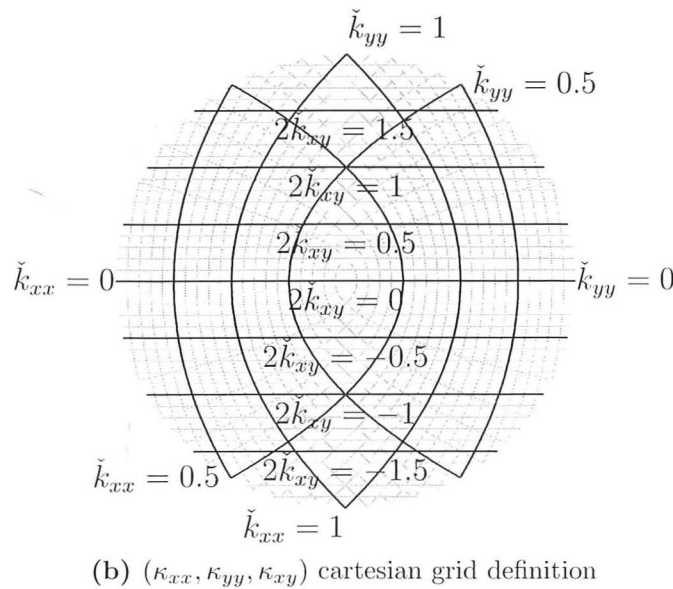
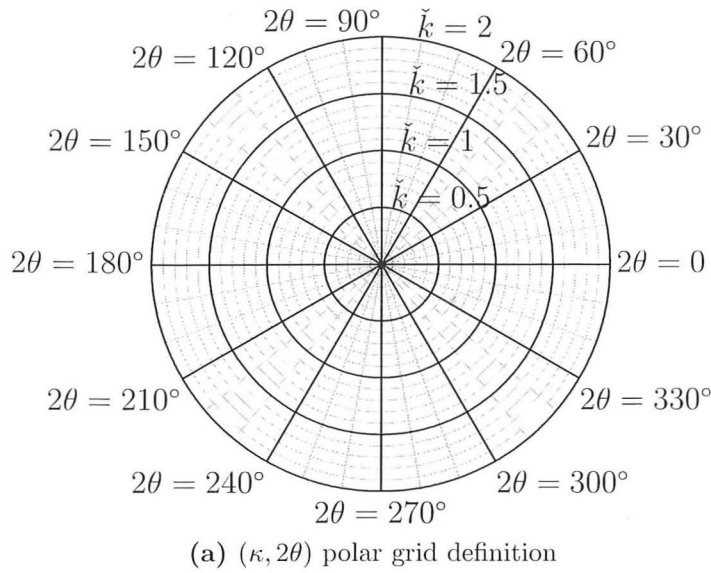
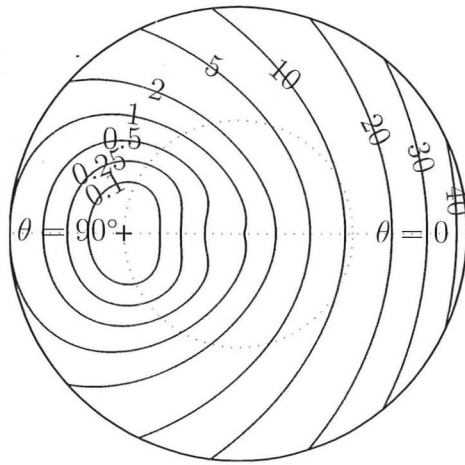
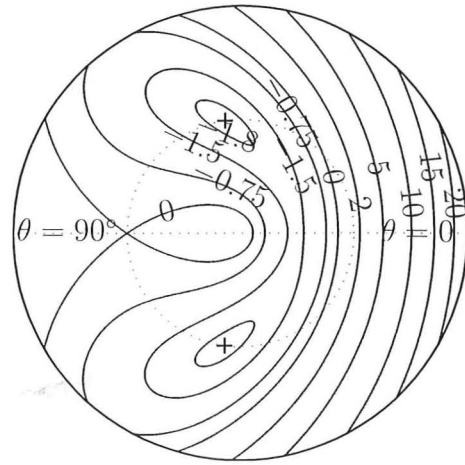


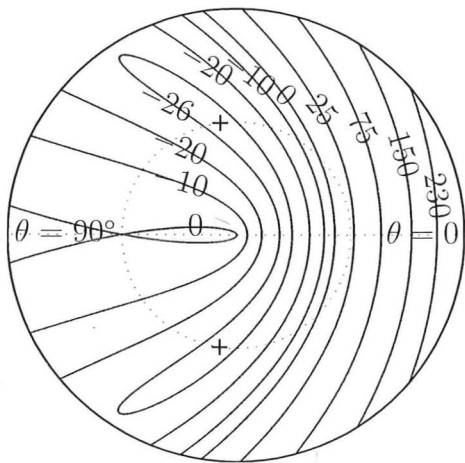
Figure 4.9: The grid definition for the energy-density contour plots in Fig. 4.10. Fig. 4.9a shows how the coordinate system is derived: it is a polar plot with radius representing curvature and angle representing twice the angle of curvature, since curvature repeats every 180° . Fig. 4.9b shows contours of cartesian curvature components κ_{xx} , κ_{yy} and κ_{xy} on the same plot.



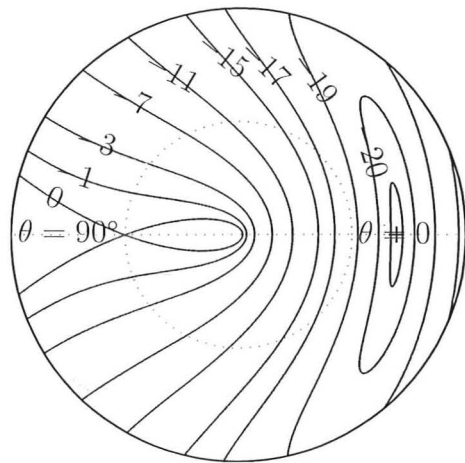
(a) Monostable: $\check{M} = 0$, and so is too small for bistability, and the one stable point is at $\check{k}_M = 1$, $\theta_M = 90^\circ$. There is a small saddle point at $\check{k} = 0$. $\alpha = 10$



(b) Intermediate moments; two stable states at $\check{k}_M = 1$, at angle $\pm\theta_M$ given by $\cos 2\theta_M = 2(\check{M} - 1 + \nu)/\alpha - 1$. There are saddle points on $\theta = 90^\circ$ (at $\check{k} = 1$) and on $\check{k} = 0$. $\check{M} = 5$, $\alpha = 10$.



(c) Deeper corrugations, at $\alpha = 145$, with a higher moment $\check{M} = 63$ to give equilibria at the same points as Fig. 4.10b. The energy wells are deeper, and the energy contours follow almost exactly the \check{k}_{xx} contours of Fig. 4.9b.



Equally, this can be seen as the result of two conflicting, mutually perpendicular, prestresses, and only arises when one prestress is not too much greater than the other; initial conditions consisting of two non-zero components of prestress, M_{xx_0} and M_{yy_0} , with $k_0 = 0$, gives the same behaviour. Without the corrugations (*i.e.*, in isotropic shells, at $\alpha = 0$), the range in Eqn 4.35 vanishes, θ_M becomes indeterminate and the twisting bistability becomes impossible to create. Note also that, once α has been calculated, this behaviour is completely independent of the corrugation profile, and for a constant α , triangular, sinusoidal, circular-arc or any other corrugation shape will behave identically. This is *not* true of the coiling bistability.

The final practical success of this model lies in its confirmation that the twisting bistability occurs when, due to plastic flow effects in manufacture, the shell acquires an unintended curvature across the corrugations. By plastically working this curvature out of the shell, the twisting modes can be eradicated. The relevance of this model to physical behaviour is explored further in Section 5.1.2.

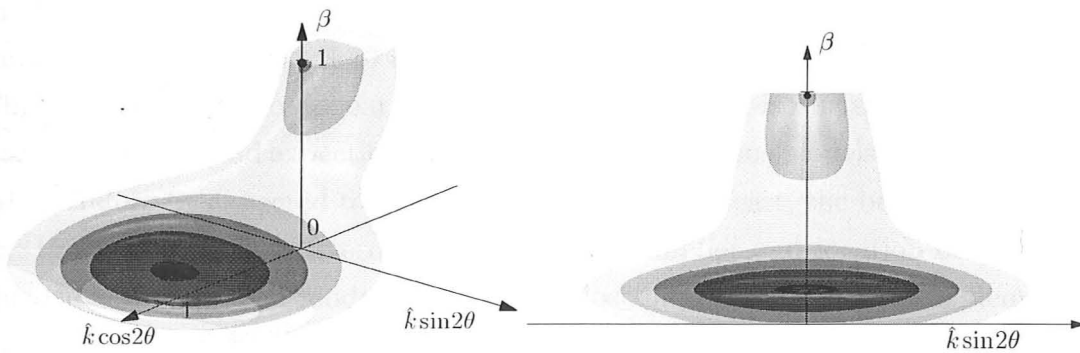
4.3.3 Mode III: Tristability

Allowing κ , θ and β to vary simultaneously provides a full model of the behaviour of the shells. The resulting model is more complex, but it captures the tristable behaviour of the combined Mode I and Mode II bistabilities. Rather than solving the equilibrium equations, we will plot the variation of stored energy with the three independent variables, using the dimensionless groups from Mode I, as in Eqn 4.36;

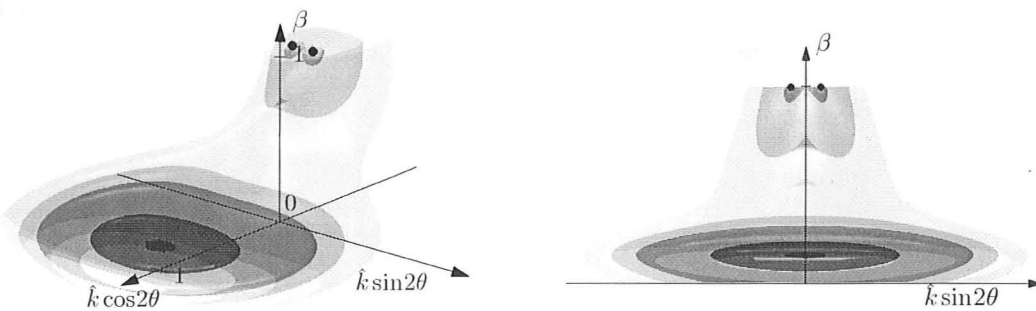
$$\hat{U} = \hat{k}^2 \left[1 + \frac{1}{8} \alpha (3 + 4 \cos 2\theta + \cos 4\theta) \right] + \hat{k} \hat{k}_0 [(1 - \nu) \cos 2\theta - (1 + \nu)] + \hat{k}_0^2 + (\beta - 1)^2 - \hat{M} \hat{k} (1 + \cos 2\theta) \quad (4.36)$$

Graphically representing the variation of energy with three variables requires care. In the contour plots of Section 4.3.2, each point corresponds to a unique shape in two variables (\hat{k} , θ) which has a strain energy density. Adjacent points of identical strain energy density can be joined together to produce a contour line of constant \hat{U} ; each contour line, in Fig. 4.10, encloses a region of higher or lower energy than that contour, and therefore must enclose at least one maximum or minimum.

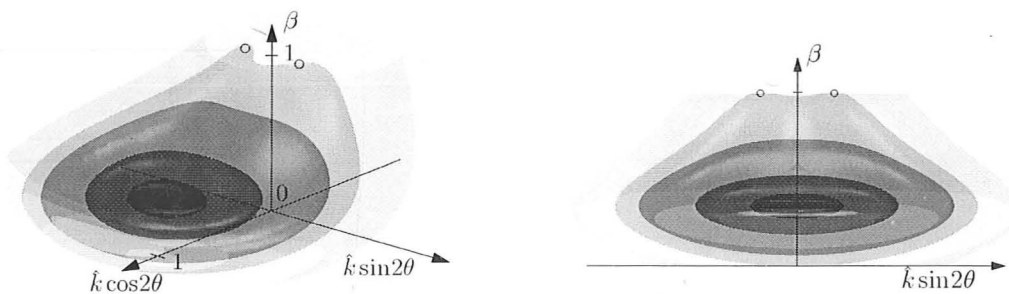
For three independent variables, the strain energy occupies a three-dimensional space, as shown in Fig. 4.11. The horizontal axes are the same as in Fig. 4.10, but there is also a vertical axis, representing corrugation amplitude β relative to the initial corrugation amplitude. Again, each point corresponds to a unique shape and has an associated energy. However, when points of identical \hat{U} are joined up, they now form a surface rather than a line, and that surface, again, encloses at least one maximum or a minimum. These



(a) The bistable Mode I, demonstrating that the stable points are also stable in θ . Both are located in the $\hat{k} \cos 2\theta$ - β plane, as shown by the end-on view (right). $\hat{k}_0 = 0$, $\phi_0 = 29^\circ$



(b) A tristable shell. The coiled shape ($\beta \sim 0$) is lower-energy. $\hat{k}_0 = 0.2$, $\phi_0 = 29^\circ$



(c) This demonstrates the value of the tristable model. The second model predicts this shell to be bistable when corrugation flattening is not allowed: the plane $\beta = 1$ matches Fig. 4.10b, with 'stable' points marked by open circles. This plot shows these points to be not in equilibrium when the corrugations are circular-arc, and flattening (changes in β) is allowed. There is a unique energy minimum, and the shell is monostable. $\hat{k}_0 = 0.2$, $\phi_0 = 14^\circ$, $\hat{M} = 1$

Figure 4.11: 3-D energy isosurfaces for the 'combined' Mode III model. The coordinates are cylindrical polar: radius represents \hat{k} , angle represents 2θ and height β . Any point represents a global shape of the corrugated sheet, with a certain value of internal strain energy density, and the surfaces on these plots are surfaces of constant energy. Filled black circles denote stable points. Darker surfaces are isosurfaces of lower energy. $\hat{c}_0 = 6.25 \times 10^{-3}$ and $\hat{M} = 1$ throughout; the latter should produce Mode I bistability for $\phi_0 = 29^\circ$ but not for $\phi_0 = 14^\circ$, according to Fig. 4.6.

surfaces are *isosurfaces*: *i.e.*, surfaces over which the energy is constant. If a slice is taken through one of these plots, then a conventional contour plot results; if that slice is horizontal, the plots in Fig. 4.10 are produced.

Three stable states do appear, each contained within an isosurface of low energy, and they are where we would expect to find them from the previous models. The previous models can therefore be expected to describe, qualitatively at least, the behaviour of tristable shells. Producing quantitative descriptions of the number and location of stable points for this three-dimensional model is complex. Most importantly, Fig. 4.11c demonstrates that a structure which appears to be bistable following the second elastic model can in fact be monostable when all three degrees of freedom are considered. This is a limitation only of the Mode II model, since the Mode I shell does not have the cross-corrugation curvature necessary for twisting bistability.

4.4 Conclusions

Uniform corrugated shells can be manufactured which are bistable in either or both of two modes: a corrugated sheet which coils up when the corrugations are flattened, and a corrugated sheet which, in addition to curvatures along and perpendicular to the corrugations, has a 'twist' which is stable at both its positive and negative value. When these modes are combined in one shell, that shell is tristable. In both modes, multistability arises due to a *prestress*: *i.e.*, a residual bending moment in the shell in the initial corrugated state which interacts with nonlinear changes in geometry.

We now have an elastic model, which evaluates the strain energy density of the shell as the shape is changed, in order to determine the stable shapes. Despite very simple assumptions of internal stresses, the results are non-trivial and reproduce a number of details of the behaviour of the prototypes. Furthermore, having produced these models, they have been sufficiently useful to guide our construction of prototypes, teaching us how to build in or eradicate specific modes of behaviour, and how to tailor the properties of the shells to suit the situation for which they are intended.

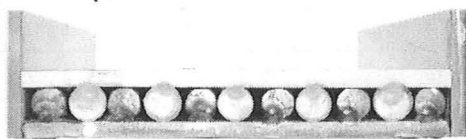
What the results of this chapter do not, unfortunately, comprise is a set of data that can be conveniently and quantitatively verified by physical tests. The bending moments applied in this analysis are uniform throughout the shell, with no other loads being applied. This is not the case in either three-point or four-point bending, both of which involve a decrease in bending moment away from the centre section. Therefore, the transition moment will be reached in the centre *before* it is reached further out: the centre will transform between states before the edges do, creating a 'plop' region between coiled and corrugated regions. Since this 'plop' is not an energy minimum, and has a complex shape that must involve some stretching, it must have a relatively large strain energy density, and so the snap-through moment is, accordingly, larger, to provide this energy input. This is, indeed, found by physical test: in a three-point bending test, with a setup carefully designed to avoid crushing the corrugations, the moment exceeds the predicted value by up to 100 %. Further work demonstrating this has been done using finite-element simulations by Gentilini *et al.* (2008).

The next step, covered in the next chapter, is to look in more detail at how the forming process produces these effects, and to see whether any quantitative support for this model can be gleaned.

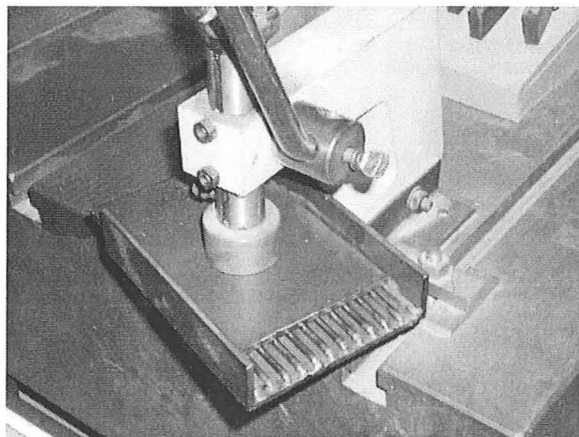
Chapter 5

Flat corrugated shells (ii): forming and experiment

This chapter contains various themes, united by their involvement of physical testing and prototyping, and is divided into three main sections. Firstly, the manufacture of the prototypes is described and the materials used are introduced, and observations are given as to the behaviour of the prototypes, in Section 5.1. Specifically, in Section 5.1.2, the prototypes are compared to the analytical modes of Chapter 4. Secondly, in an attempt to explain some of the effects observed in the prototypes, Section 5.2 presents a plastic flow model, to simulate the forming process. Finally, a series of tests are performed: firstly, to evaluate the material properties to greater accuracy than the manufacturer's data, and secondly, to verify the analytical results produced so far: in Section 5.3.2, an attempt is made to measure the internal stresses of the shell and to compare them with those predicted by Section 5.2.



(a) End-on view of the two 'former' pieces, when assembled



(b) The former pieces, mounted in the press

Figure 5.1: The initial corrugation press, forming all corrugations at once. Note that this will cause material at the sides to be pulled in as the corrugation progresses, creating uneven corrugations.

5.1 Manufacturing methods and observations

The material used for most prototypes and tests is CuBe alloy, as described in Section 3.4. The reason for using CuBe here lies in its combination of hardness and ductility. The latter is important for the cold-working process that imparts prestress to the shells: the former results in a high failure strain, and enables very thin sheets to be used, so that high changes in curvature can occur *within* the elastic regime. Stainless and spring steels exhibit the same properties to a lesser degree, and are used for the slap-on bracelets described earlier in Section 2.3 and shown in Fig. 2.16. A shim-steel corrugated shell has been made, and is discussed in Section 5.1.2.

During age-hardening, the stresses within CuBe are relieved: if it is conformed to a former during age-hardening, it will emerge from the process with that shape. In fact, it will even emerge with slightly tighter curvatures than those to which it has been deformed, because compressive stresses intensify the ageing response while tensile stresses inhibit it. This is covered in more detail in an article by the Technical Service Department, Brush Wellman Inc. (2004).

5.1.1 Manufacturing methods

Initially, corrugations were produced by one of two similar press sets of differing corrugation curvature, one of which sets is shown in each image of Fig. 5.1. This produced various successful samples. However, it placed strict limits on the size of the sample. In addition, as it is pressed down, material is pulled in towards the centre, creating corrugations which are not uniform across the sheet. This is a fundamental problem with any method that

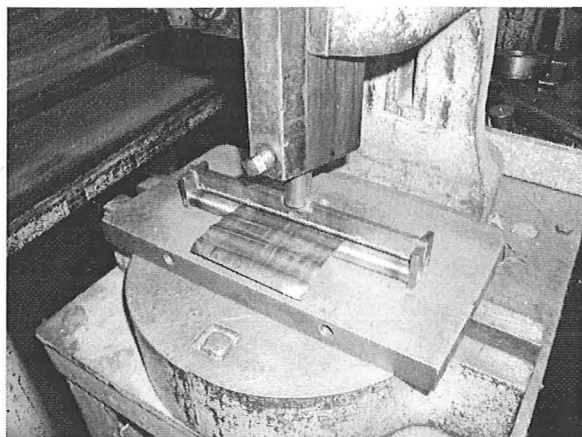


Figure 5.2: This press creates just one region of curvature, 5.7 mm wide and up to 220 mm long, at a time. These regions can, with some patience and care, be built up very accurately into a corrugation profile. The piece of CuBe currently in the press has a corrugation wavelength of 22.7 mm, and so requires 4 pressings per wavelength.

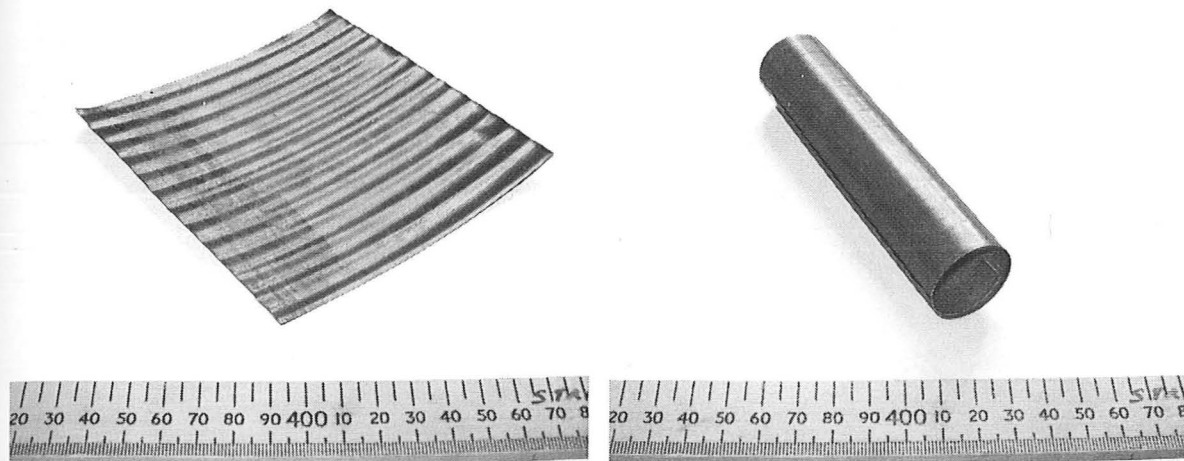
stamps several corrugations at once to their full depth in a single pressing.

The second corrugation device, shown in Fig. 5.2, imparts each corrugation individually. This device can also put in corrugations at any angle, for sheets up to 220 mm long and of unlimited width. The press has a radius of 3.5 mm, forcing a curvature of 286 m^{-1} . While the corrugation curvature is fixed, the wavelength can be continuously varied down to a minimum of 11.4 mm by partially overlapping subsequent pressing actions. This matches the corrugation profile shown in Fig. 4.4, since it produces a constant corrugation radius.

In order to apply the prestress moment, a simple roller is used. This, again, has a radius of 3.5 mm, and a length of 98 mm, which limits the sheet width. Conventionally, when a metal plate is rolled, a series of passes are made in which the curvature is gradually increased, but always remains well below that of the roller. In this case, with a very thin and hard CuBe sheet, plastic deformation is only achieved with the roller tightened to the point where the sheet was being completely conformed to the roller, and so the rolling process only takes a single pass.

A second method for prestressing is to wrap the alloy around a tube before age-hardening, to relax the stresses while the shell is coiled, and corrugating afterwards. This removes the limitation on sheet width, but means that the prestress cannot be adjusted by rolling after corrugation. The same principle of creating a shape before age-hardening can be applied to the corrugations, if the sheet is corrugated in the annealed state. Note that at least one of the two processes, of forming and corrugating, must be carried out after age-hardening, since the sheet cannot maintain significant prestresses in its annealed state, and even these internal stresses disappear during the age-hardening process.

While many samples have been formed with the initial press of Fig. 5.1 during early



(a) The corrugated flat sheet

(b) The 'coiled' mode

Figure 5.3: This sheet achieves very short-wavelength corrugations, through having very tight corrugation curvatures: this enables the corrugated state and a similarly tightly-curved coiled state to have similar energy densities. These were imparted using a folder, rather than a press or a roller.

prototyping and development of the analytical models of Chapter 4, only those formed with the second design, as in Fig. 5.2, will be studied quantitatively, because they conform to the assumptions about corrugation shape made in the analytical model. However, when producing prototypes to demonstrate the potential of this technology to industrial organisations, we want tighter corrugations and a smaller corrugation wavelength. As is noted in Section 4.3.1, the state with the tighter curvatures will be lower-energy and hence preferred. For a 'flexible display' or similar device, the two states should ideally have similar energy so that the transformation is not particularly violent (*i.e.*, releasing much energy) in either direction. Therefore, improving the tightness of the coiled mode should be accompanied by tighter corrugations. Such is the hardness and high yield-strength of CuBe alloy that a sheet-metal-folding machine proved appropriate, with a forming radius of just 1 mm, on CuBe alloy of 0.1 mm thickness. A resulting shell is shown in Fig. 5.3.

5.1.2 Observations from prototyping

The initial aim was to produce the type of behaviour described in Chapter 4 as 'Mode I'. However, most of the initial samples were in fact 'Mode III', combining the coiling bistability with a twisting bistability. Fig. 5.4 shows an example of a strongly tristable shell, along with an identical shell to which the corrugation process had been performed a second time, eradicating the twist. An explanation for this is based on the concept of the *sense* of curvatures, outlined in Section 3.1.2. The corrugation process had been the same

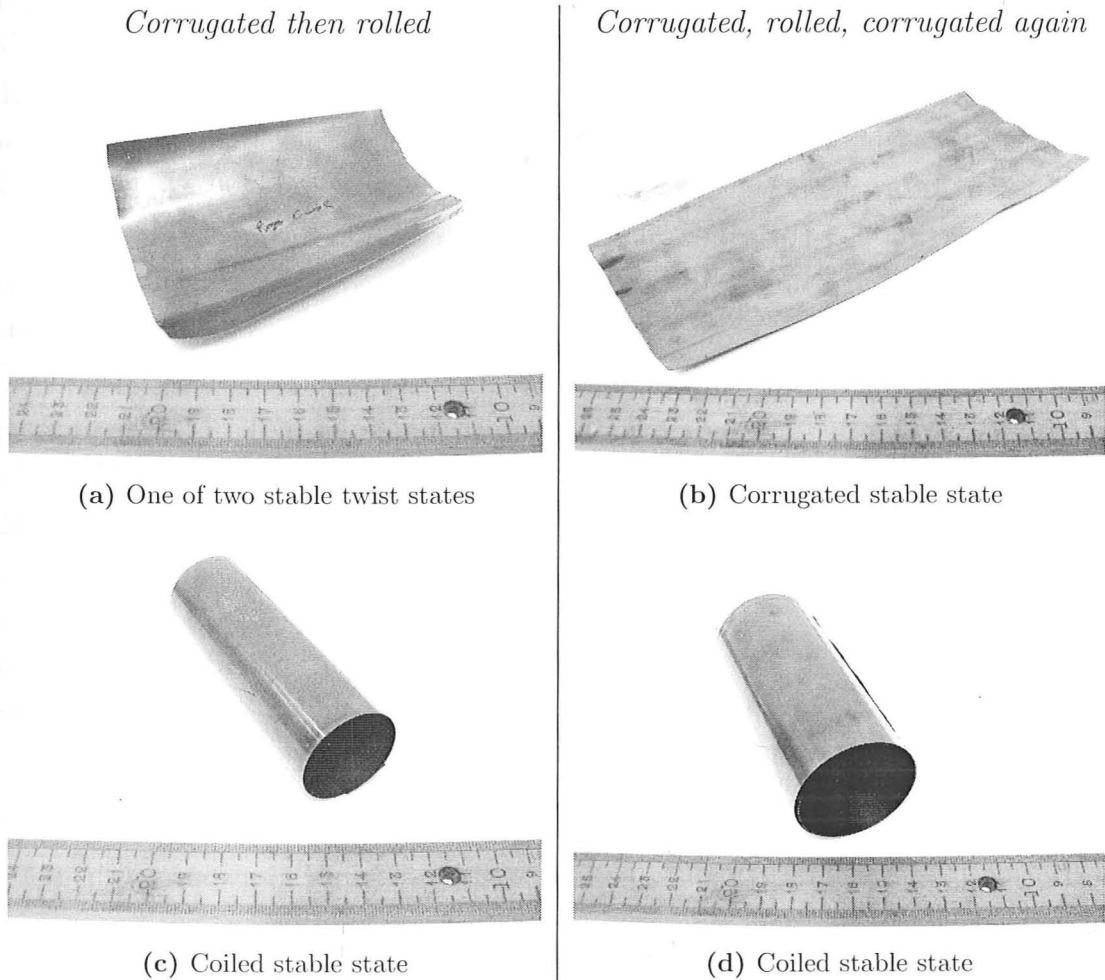


Figure 5.4: An example of how to remove the twisting mode; the initial corrugation & rolling process leaves a large global curvature across the corrugations, producing twist and tristability. Reinforcing the corrugations to remove this curvature removes the twist mode, as on the right, but slightly relaxes the coiled-mode curvature. The left-hand sample is 100 mm \times 130 mm; the right sample is 100 mm \times 230 mm.

for positive- and negative-curvature regions of the shell. However, this implies that in the 'troughs', the corrugation curvature is in the *same* sense as the rolling curvature, and in the 'peaks', they are in *opposite* senses. These two regions respond very differently to the cold working process, leading to two regions of different curvatures. If the troughs and the peaks have different curvature magnitudes, then the shell as a whole has some initial curvature across the corrugations, which interacts with the prestress moment along the corrugations, producing the twisting effect. This is the basis for the model of Section 4.3.2, which supports this theory by replicating the twisting mode.

Repeating the corrugating stage of manufacture is a trial-and-error-found method to remove the twist mode, in some cases: following on from the analysis of Section 4.3.2, which firmly links the Mode II bistability to across-corrugation curvature, it is found that the twisting effect can be imparted or removed by adjusting the curvature across the corrugations. In all prototypes since, it has proved possible to impart or eradicate the twisting mode at will by using cold working to remove, or even just reduce, this curvature: the significant result given in Eqn 4.35 is that there is a specific range of ratios of prestress moment to curvature that allows twisting bistability, and that curvatures too large or too small will not experience it.

Having explored the basic physical points, we will now compare the prototypes to the specific modes analysed in Chapter 4.

Mode I: coiling bistability

According to Section 4.3.1, the Mode I bistability vanishes for $\phi_0 < 14^\circ$ for $\hat{c}_0 = 6.25 \times 10^{-3}$. At low bistable values of ϕ_0 , slightly above 14° , the bistability is weak: the corrugated mode also exhibits noticeable curvature along the corrugations under the action of the moment, as shown in Fig. 4.6, because it is only slightly stiffer than an uncorrugated flat sheet, and the energy barrier between the two stable modes is small. This is exactly what has been found with samples at $\phi_0 = 16^\circ$, as shown in Fig. 5.5.

Of the many samples that have been created, there are samples in which the *corrugated* state is lower-energy and samples in which the *coiled* state is lower-energy. The former are more of a challenge to create, because it is harder to make tight uniform corrugations than it is to make a tight rolling prestress, and it is a tighter average corrugation curvature that causes the corrugated mode to be lower-energy: but we have made them.

Modes II and III: twisting bistability

The analysis of the twisting bistability in Section 4.3.2 predicted two features of interest, beyond what was known before the analysis, both of which have been confirmed in prototyping:

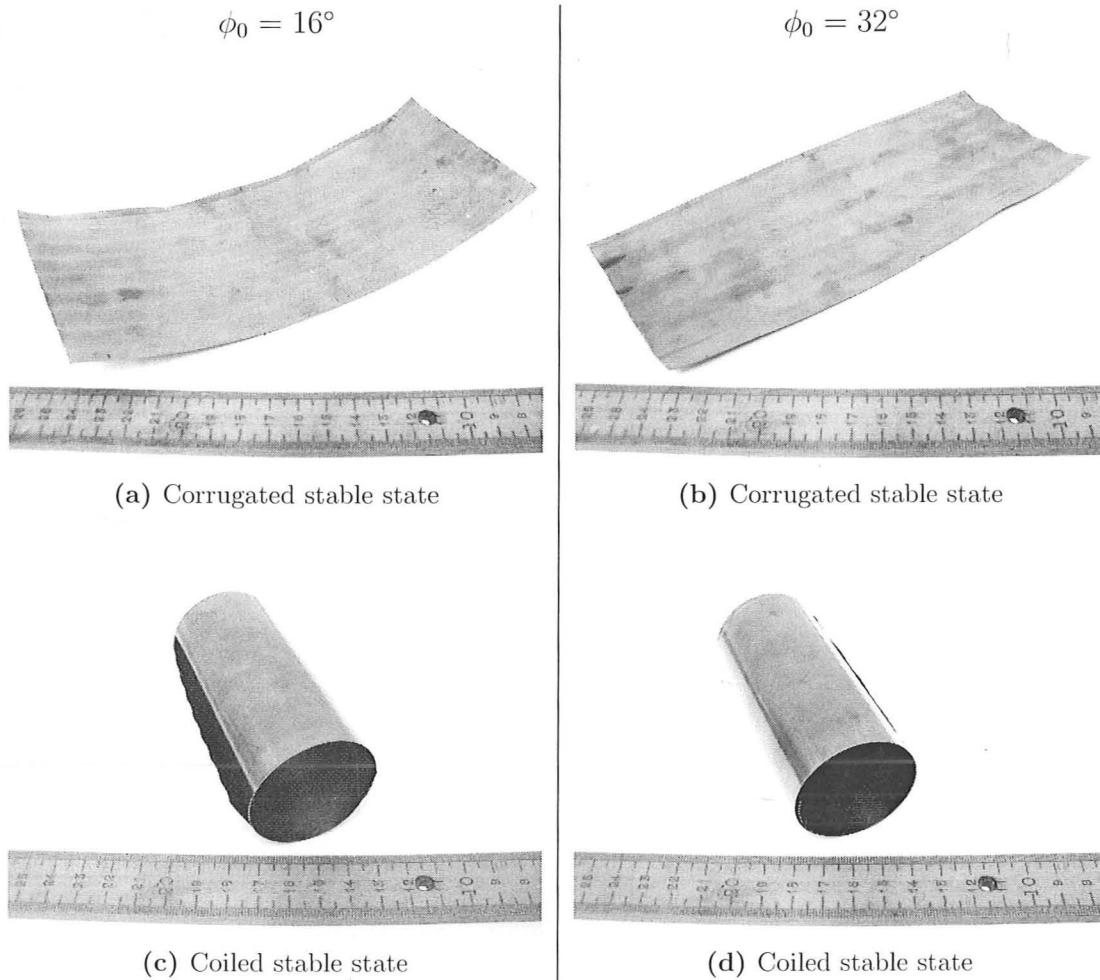
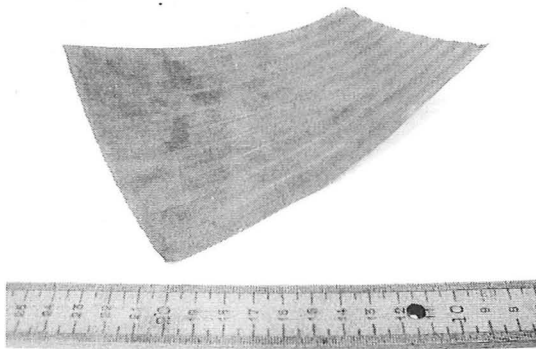


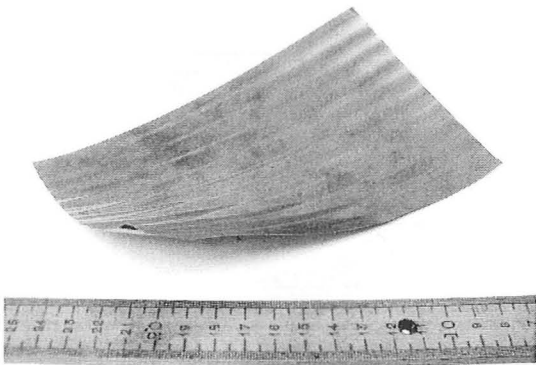
Figure 5.5: These two shells display pure coiling bistability, having been formed by corrugating, then rolling, then corrugating. On the left is a low corrugation amplitude: on the right, high corrugation amplitude. Since they have identical prestress moments, their coiled states are similar. For a low corrugation amplitude, the corrugated shell has a lower stiffness, and accordingly the prestress moment induces a much larger global curvature in the corrugated mode, as predicted by Chapter 4. In addition, the lower-amplitude corrugations lead to a lower energy barrier between the two states, so the transition is easier to implement and ‘softer’ in its action.

- (i) This twisting mode of bistability does not depend on the corrugation profile, nor does it require large elastic deformations of that profile to be permissible: accordingly, it functions equally well with a range of profiles. Fig. 5.6 shows a strong twisting bistability in a shim steel, relatively soft in comparison with CuBe, whose corrugations even exhibit local buckling effects from the manufacture.
- (ii) Given a particular cross-corrugation curvature, a certain range of moments, defined by Eqn 4.35, cause twisting bistability; in other words, for too small or too large a moment, the bistability does not occur. This has been demonstrated in Fig. 5.7.

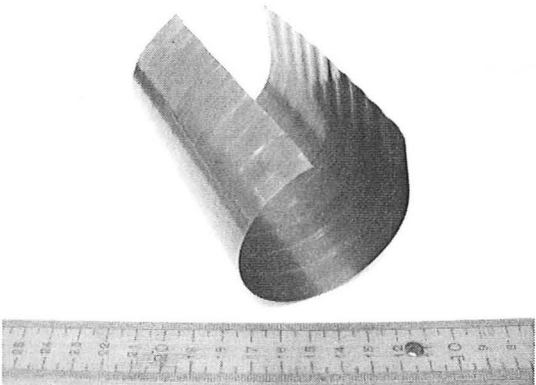
CuBe shell



(a) One stable twist state

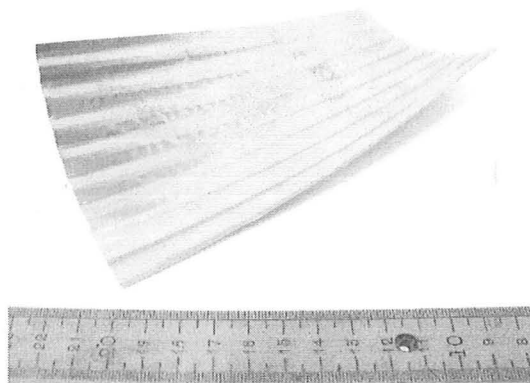


(c) Other stable twist state

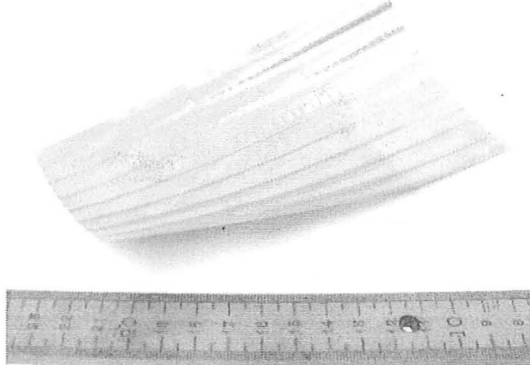


(e) Stable coiled state

Shim steel shell

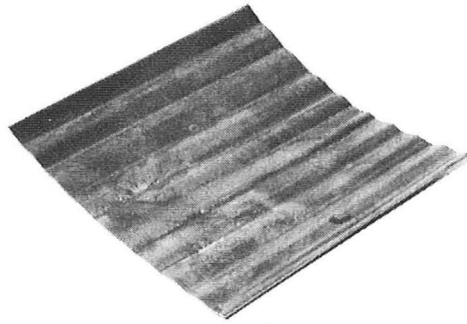


(b) One stable twist state

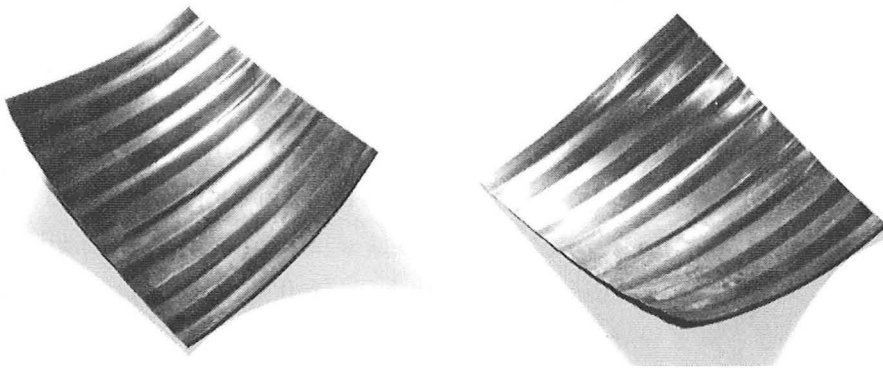


(d) Other stable twist state

Figure 5.6: These shells are both bistable in twist (the CuBe shell is tristable). Both have similar twist behaviour: however, the shell made from shim steel demonstrates a very different corrugation profile to the CuBe shells. It was given a tight corrugation profile that could not be flattened elastically, and was then rolled to impart a moment (the rolling partly and locally crushed the peaks of the corrugations, as can be seen in the photographs).



(a) Low prestress moment: monostable. Note that the along-corrugation prestress has not overcome the across-corrugation curvature.



(b) Medium prestress moment: bistable in twist



(c) High prestress moment: monostable. The along-corrugation prestress has now completely overcome the across-corrugation curvature, although, due to imperfections in the rolling process, its curvature is not quite perfectly aligned with the corrugations.

Figure 5.7: One CuBe shell is given a tight corrugation before being age-hardened: it is too tightly corrugated to allow the coiling bistability. It is then rolled lightly, creating a prestress too small for the twisting bistability, and one third is cut off (a); it is then rolled more heavily, creating twisting bistability, before another third is cut off (b), and the remainder is rolled until bistability vanished (c).

5.2 Plastic flow: analysis of forming

The manufacturing process involves loading into a plastic regime and then unloading multiple times. This produces a number of subtle effects whereby the corrugating and rolling stages of forming interact in a manner that, it is theorised, produces the initial global cross-corrugation curvature κ_0 that initiates twisting bistability, causing tristability when combined with coiling bistability. The plastic analyses below attempt to understand this process through a simplified model. So far, trial and error has found manufacturing methods which can eradicate κ_0 in the final stages of processing, but it is hoped that with the following models, we can predict the outcome of a manufacturing programme in advance, and alter our process to eliminate undesired modes from the outset.

These models will also provide more detail on the internal stresses created, in order to evaluate the previous assumption of a uniform M_{xx0} in Section 4.3.

5.2.1 Analysis of first yield

A simple indicator of how the two processes interact and, critically, how this interaction differs between regions of positive and negative corrugation curvature is to find the point at which yield first occurs. Suppose a sheet has an initial curvature κ_{xx} and no internal stresses. The sheet is elastically flattened and then given a curvature κ_{yy} which increases until yield first occurs on the material surface, at a distance $z = \frac{t}{2}$ from the centreplane. The strains on the top surface are

$$\varepsilon_{xx} = -\frac{t}{2}\kappa_{xx} \quad (5.1)$$

$$\varepsilon_{yy} = \frac{t}{2}\kappa_{yy} \quad (5.2)$$

$$\varepsilon_{xy} = \varepsilon_{yz} = \varepsilon_{zx} = 0 \quad (5.3)$$

Putting these into Eqn 3.5 gives the stresses

$$\sigma_{xx} = \frac{E}{1-\nu^2} (\kappa_{yy} - \nu\kappa_{xx}) \frac{t}{2} \quad (5.4)$$

$$\sigma_{yy} = \frac{E}{1-\nu^2} (\nu\kappa_{yy} - \kappa_{xx}) \frac{t}{2} \quad (5.5)$$

$$\sigma_{zz} = \sigma_{xy} = \sigma_{yz} = \sigma_{zx} = 0 \quad (5.6)$$

where σ_{xx} and σ_{yy} are principal stresses. A yield criterion is required, using either the Mises or Tresca conditions; given plane strain, $\sigma_{zz} = 0$, the Mises condition in terms of

principal stresses, Eqn 5.7, rearranges thus:

$$2\sigma_y^2 = (\sigma_{xx} - \sigma_{yy})^2 + (\sigma_{yy}^2 - \sigma_{zz})^2 + (\sigma_{zz} - \sigma_{xx})^2 \quad (5.7)$$

$$\begin{aligned} \sigma_y^2 &= \sigma_{xx}^2 + \sigma_{yy}^2 - \sigma_{xx}\sigma_{yy} \\ &= \frac{Et}{2(1-\nu^2)} [(\kappa_{yy} - \nu\kappa_{xx})^2 + (\nu\kappa_{yy} - \kappa_{xx})^2 - (\kappa_{yy} - \nu\kappa_{xx})(\nu\kappa_{yy} - \kappa_{xx})] \\ &= \frac{Et}{2(1-\nu^2)} [(\kappa_{xx}^2 + \kappa_{yy}^2)(1 + \nu^2 - \nu) + \kappa_{xx}\kappa_{yy}(1 + \nu^2 - 4\nu)] \end{aligned} \quad (5.8)$$

The only part of Eqn 5.8 which depends on the relative sense of the two curvatures is the final component, $\kappa_{xx}\kappa_{yy}(1 + \nu^2 - 4\nu)$. If $(1 + \nu^2 - 4\nu) > 0$, yield will occur first in regions of corrugation which are in the same sense as the rolled curvature: else, it will occur first in regions of opposite sense. Solving the quadratic for ν gives a critical value of $\nu = 0.268$, at which yield is simultaneous in both regions.

In regions of opposite-sense curvature, the stresses σ_{xx} and σ_{yy} are either both compressive or both tensile, leading to low shear stresses in the $x - y$ plane; hence, yield is in the $x - z$ or $y - z$ planes, *i.e.*, the material thins or thickens. At large ν , these stresses reinforce each other, so first yield occurs in this region if $\nu > 0.268$. Same-sense curvatures, however, produce their largest shear stresses in the $x - y$ plane. For large ν , these stresses partially cancel, so that this region yields first if $\nu < 0.268$. CuBe has a $\nu = 0.3$, so we expect the opposite-sense regions to yield first: certainly, it is observed that these areas undergo larger plastic deformation, which is consistent.

The same analysis for Tresca yield produces a more complex expression whereby the critical Poisson ratio varies with the ratio of the two curvatures, but the general behaviour is the same.

5.2.2 Plastic analysis of forming

In order to predict how the curvatures and stresses created will change through the forming process and differ between regions of same-sense and opposite-sense curvature, upper- or lower-bound models will not suffice; a plastic flow analysis is needed. The method used for this is described in Section 3.3.

The forming process is a strain-controlled process, where the forming dictates the total strains as a function of material depth. These will be composed of elastic and plastic strains, both of which must be captured by the model. The simplest model which does this is an 'Elastic-Perfectly Plastic' model (EPP), again defined in Section 3.3. In Section 5.3.1, tests are performed that suggest that 1500 MPa is a suitable value to use for the yield stress for such a model, after making use of the equations developed below.

Equations and algorithms

This algorithm considers a specific depth in the material, assuming that strains in the z direction are small with respect to the z coordinate so that the system is explicit, since, at a constant shell curvature, the x and z strains are dependant on the distance from the neutral axis, which is affected by z -direction strains. The algorithm considers a single stage of manufacture at a time, moving from one strain state to another.

It is best understood by studying a single strain 'step' considered by the algorithm, *e.g.*, the transition from strain state 'n' to state (n + 1). For the initial state 'n', the vectors for elastic, plastic and total strains are known, and from the elastic strains, the principal stresses can be calculated. There are no shear stresses, because we stipulate that there is no twisting in the forming process: therefore, there are no shear strains. This also means that the principal stresses are σ_{xx} and σ_{yy} , and in this section, we will refer to them simply as σ_x and σ_y , and at a time-step 'n', they are referred to as σ_{nx} and σ_{ny} . We also know the total strains of state (n + 1), since the forming is a strain-controlled process: for uniformity over an infinite sheet, it follows that total strain $\varepsilon_{ij} = z\kappa_{ij}$. Therefore, we have a linear vector for the change in strain.

The six regions of the Tresca yield surface are defined, from Eqn 3.26, by the three pairs of equations

$$\sigma_{nx} = \pm\sigma_y \quad (5.9)$$

$$\sigma_{ny} = \pm\sigma_x \quad (5.10)$$

$$\sigma_{ny} - \sigma_{nx} = \pm\sigma_y \quad (5.11)$$

and are shown on Fig. 5.8, labelled 'A' through 'F'.

Defining the strain vector ε_n as the sum of elastic and plastic strains, and recall that total strains are the product of the curvature κ_n and the distance from the neutral axis z :

$$\varepsilon_n = \varepsilon_n^e + \varepsilon_n^p = z\kappa_n \quad (5.12)$$

From the shell equations in Section 3.2, assuming that through-thickness stresses are zero,

$$\sigma_n = \begin{bmatrix} \sigma_{nx} \\ \sigma_{ny} \end{bmatrix} = \frac{E}{(1-\nu^2)} \begin{bmatrix} 1 & \nu \\ \nu & 1 \end{bmatrix} \begin{bmatrix} \varepsilon_{nx}^e \\ \varepsilon_{ny}^e \end{bmatrix} = \frac{E}{(1-\nu^2)} \begin{bmatrix} 1 & \nu \\ \nu & 1 \end{bmatrix} \varepsilon_n^e \quad (5.13)$$

Thus, given the initial stress state σ_n , Eqn 5.13 enables us to convert the step in strain $\Delta\varepsilon = \varepsilon_{n+1} - \varepsilon_n$ to a stress vector $\Delta\sigma$, of which an example is shown on Fig. 5.8.

Is this in yield? We now, instead of applying $\Delta\varepsilon$, apply a strain vector $\Lambda\Delta\varepsilon$, where Λ is some coefficient. We then solve to find the value of Λ for which the stress vector $\Lambda\Delta\sigma$

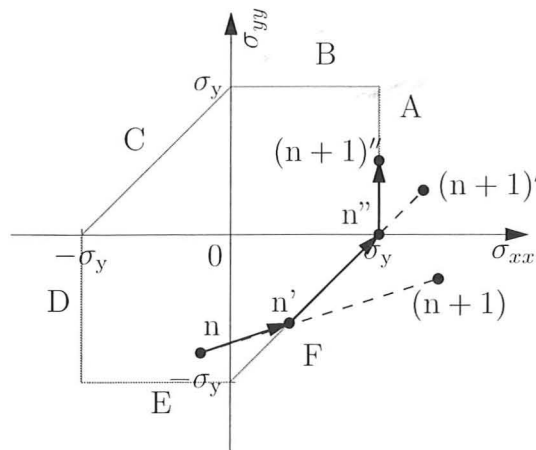


Figure 5.8: The Tresca yield surface in the space of principal stresses, assuming plane stress, with sections labelled 'A'-'F'. An example of plastic flow is shown, from strain state n to $(n+1)$: labelled on the diagram is the stress at which that strain state is achieved if deformation is purely elastic. However, $\sigma_{(n+1)}$ is outside the yield surface: so, we move just to $\sigma_{n'}$ on surface F, and now yield with a plastic strain vector in the (1,-1) direction. For this plastic strain vector, our final strain state is reached at $\sigma_{(n+1)'}$, which, again, is beyond yield, and so we move only to yield surface A at $\sigma_{n''}$. Taking the new plastic vector (1,0), we 'slide' along surface A to $(n+1)''$, at which our final strain state is met. The point vectors are defined in the table below:

$$\begin{aligned} \sigma_{(n+1)} &= \sigma_n + \Delta\sigma \\ \sigma_{n'} &= \sigma_n + \Lambda_F \Delta\sigma \\ \sigma_{(n+1)'} &= \sigma_{n'} + (\Delta\sigma)' \\ \sigma_{n''} &= \sigma_{n'} + \Lambda_A^p (\Delta\sigma)' \\ \sigma_{(n+1)''} &= \sigma_{n''} + (\Delta\sigma)'' \end{aligned}$$

takes us to each of the curves which make up the Tresca yield surface. This produces the following six values of Λ :

$$\Lambda_A = \frac{\frac{\sigma_y}{E}(1 - \nu^2) - (\varepsilon_{nx}^e + \nu\varepsilon_{ny}^e)}{\Delta\varepsilon_x + \nu\Delta\varepsilon_y} \quad (5.14)$$

$$\Lambda_B = \frac{\frac{\sigma_y}{E}(1 - \nu^2) - (\varepsilon_{ny}^e + \nu\varepsilon_{nx}^e)}{\Delta\varepsilon_y + \nu\Delta\varepsilon_x} \quad (5.15)$$

$$\Lambda_C = \frac{-\frac{\sigma_y}{E}(1 + \nu) - (\varepsilon_{nx}^e - \varepsilon_{ny}^e)}{\Delta\varepsilon_x - \Delta\varepsilon_y} \quad (5.16)$$

$$\Lambda_D = \frac{-\frac{\sigma_y}{E}(1 - \nu^2) - (\varepsilon_{nx}^e + \nu\varepsilon_{ny}^e)}{\Delta\varepsilon_x + \nu\Delta\varepsilon_y} \quad (5.17)$$

$$\Lambda_E = \frac{-\frac{\sigma_y}{E}(1 - \nu^2) - (\varepsilon_{ny}^e + \nu\varepsilon_{nx}^e)}{\Delta\varepsilon_y + \nu\Delta\varepsilon_x} \quad (5.18)$$

$$\Lambda_F = \frac{\frac{\sigma_y}{E}(1 + \nu) - (\varepsilon_{nx}^e - \varepsilon_{ny}^e)}{\Delta\varepsilon_x - \Delta\varepsilon_y} \quad (5.19)$$

Since the sections of the Tresca surface are in matching, parallel pairs, and we are always within or on the surface, three of these coefficients must be positive and three negative. If all positive Λ values are more than 1, then the full step $\Delta\sigma$ lies within yield, and we proceed from step 'n' to step 'n + 1' without a change to the plastic strains. If not, then the smallest positive Λ value denotes the point of yield: in the example shown in Fig. 5.8, this is Λ_F .

Now, if the smallest of these is Λ and it is less than 1, we move the distance $\Lambda\Delta\sigma$ to the yield surface, and from this point, we have a non-zero plastic strain vector which is perpendicular to the yield surface. For the example of surface A, this would mean that $\Delta\varepsilon_y^p = 0$, from which we can conclude that $\Delta\varepsilon_y^e = \Delta\varepsilon_y$. For, as an example, surface A, σ_x cannot change. From Eqns 5.12 and 5.13, holding σ_x constant requires that

$$\Delta\varepsilon_x^e + \nu\Delta\varepsilon_y^e = \Delta\varepsilon_x^e + \nu\Delta\varepsilon_y = 0 \quad (5.20)$$

We also know that our x -direction plastic strain component $\Delta\varepsilon_x^p = \Delta\varepsilon_x - \Delta\varepsilon_x^e$, giving our complete plastic strain vector:

$$\begin{bmatrix} \Delta\varepsilon_x^p \\ \Delta\varepsilon_y^p \end{bmatrix} = \begin{bmatrix} \Delta\varepsilon_x + \nu\Delta\varepsilon_y \\ 0 \end{bmatrix} \quad (5.21)$$

However, it is possible that as we deform plastically, we will move along the Tresca surface until we reach a new regime. Let's now define a plastic coefficient Λ^p which is a coefficient of our remaining strain vector that will take us to the next section of the Tresca surface. This occurs, for the example of surface A, at $\sigma_y = \sigma_y$ and $\sigma_y = 0$. Combining these with

Eqns 5.13 and 5.20 enables us to find

$$\Lambda_F^p = \frac{-(\varepsilon_{ny} + \nu\varepsilon_{nx})}{(1 - \nu^2)\Delta\varepsilon_y} \quad (5.22)$$

$$\Lambda_B^p = \frac{\frac{\sigma_y}{E}(1 - \nu^2) - (\varepsilon_{ny} + \nu\varepsilon_{nx})}{(1 - \nu^2)\Delta\varepsilon_y} \quad (5.23)$$

One of these Λ^p values will be positive and one negative. Again, if the positive value is more than 1, then the entire plastic step will occur on section A. If not, the step Λ^p is made, and the process begins again on the new section. (in the example on Fig. 5.8, yield is first on section F, then on section A, where it ends)

A similar set of equations for surface B: σ_{yy} is constant, and plastic deformation is given by

$$\begin{bmatrix} \Delta\varepsilon_x^p \\ \Delta\varepsilon_y^p \end{bmatrix} = \begin{bmatrix} 0 \\ \Delta\varepsilon_y + \nu\Delta\varepsilon_x \end{bmatrix} \quad (5.24)$$

$$\Lambda_A^p = \frac{\frac{\sigma_y}{E}(1 - \nu^2) - (\varepsilon_{nx} + \nu\varepsilon_{ny})}{(1 - \nu^2)\Delta\varepsilon_x} \quad (5.25)$$

$$\Lambda_C^p = \frac{-(\varepsilon_{nx} + \nu\varepsilon_{ny})}{(1 - \nu^2)\Delta\varepsilon_x} \quad (5.26)$$

For surface C: $\sigma_{xx} = \sigma_{yy}$ is constant, which, from Eqn 5.13, implies that $\Delta\varepsilon_x^e = \Delta\varepsilon_y^e$. The plastic strain vector, again, is normal to the yield surface, so that

$$\Delta\varepsilon_x^p = \varepsilon_{nx} - \Delta\varepsilon_x^e = -\Delta\varepsilon_y^p = \varepsilon_{ny} - \Delta\varepsilon_y^e \quad (5.27)$$

giving the plastic deformation vector,

$$\begin{bmatrix} \Delta\varepsilon_x^p \\ \Delta\varepsilon_y^p \end{bmatrix} = \begin{bmatrix} \frac{1}{2}(\Delta\varepsilon_x - \Delta\varepsilon_y) \\ \frac{1}{2}(\Delta\varepsilon_y - \Delta\varepsilon_x) \end{bmatrix} \quad (5.28)$$

and Λ^p values come from knowing that, where surface C intersects surface B, $\sigma_x = 0$, and where C intersects D, $\sigma_y = 0$:

$$\Lambda_B^p = -2 \frac{\varepsilon_{nx} + \nu\varepsilon_{ny}}{(1 + \nu)(\Delta\varepsilon_x + \Delta\varepsilon_y)} \quad (5.29)$$

$$\Lambda_D^p = -2 \frac{\varepsilon_{ny} + \nu\varepsilon_{nx}}{(1 + \nu)(\Delta\varepsilon_x + \Delta\varepsilon_y)} \quad (5.30)$$

For surface D: σ_{xx} is constant, and plastic deformation is given by

$$\begin{bmatrix} \Delta \varepsilon_x^p \\ \Delta \varepsilon_y^p \end{bmatrix} = \begin{bmatrix} \Delta \varepsilon_x + \nu \Delta \varepsilon_y \\ 0 \end{bmatrix} \quad (5.31)$$

$$\Lambda_C^p = \frac{-(\varepsilon_{ny} + \nu \varepsilon_{nx})}{(1 - \nu^2) \Delta \varepsilon_y} \quad (5.32)$$

$$\Lambda_E^p = \frac{-\frac{\sigma_y}{E}(1 - \nu^2) - (\varepsilon_{ny} + \nu \varepsilon_{nx})}{(1 - \nu^2) \Delta \varepsilon_y} \quad (5.33)$$

For surface E: σ_{yy} is constant, and plastic deformation is given by

$$\begin{bmatrix} \Delta \varepsilon_x^p \\ \Delta \varepsilon_y^p \end{bmatrix} = \begin{bmatrix} 0 \\ \Delta \varepsilon_y + \nu \Delta \varepsilon_x \end{bmatrix} \quad (5.34)$$

$$\Lambda_D^p = \frac{-\frac{\sigma_y}{E}(1 - \nu^2) - (\varepsilon_{nx} + \nu \varepsilon_{ny})}{(1 - \nu^2) \Delta \varepsilon_x} \quad (5.35)$$

$$\Lambda_F^p = \frac{-(\varepsilon_{nx} + \nu \varepsilon_{ny})}{(1 - \nu^2) \Delta \varepsilon_x} \quad (5.36)$$

For surface F: $\sigma_{xx} - \sigma_{yy}$ is constant, and plastic deformation is given by

$$\begin{bmatrix} \Delta \varepsilon_x^p \\ \Delta \varepsilon_y^p \end{bmatrix} = \begin{bmatrix} \frac{1}{2} (\Delta \varepsilon_x - \Delta \varepsilon_y) \\ \frac{1}{2} (\Delta \varepsilon_y - \Delta \varepsilon_x) \end{bmatrix} \quad (5.37)$$

$$\Lambda_E^p = -2 \frac{\varepsilon_{nx} + \nu \varepsilon_{ny}}{(1 + \nu)(\Delta \varepsilon_x + \Delta \varepsilon_y)} \quad (5.38)$$

$$\Lambda_A^p = -2 \frac{\varepsilon_{ny} + \nu \varepsilon_{nx}}{(1 + \nu)(\Delta \varepsilon_x + \Delta \varepsilon_y)} \quad (5.39)$$

The variation in strains with z will consist of a series of linear segments through the shell thickness, being discontinuous in gradient when a new section of the Tresca surface is reached, so a further algorithm finds the values of z at which the elastic or plastic strain gradients $d\varepsilon_{xx}^e/dz$ and $d\varepsilon_{yy}^p/dz$ are discontinuous, from which data points the strains in the whole of the material can be calculated. A final algorithm 'releases' the shell to find its rest curvature in either the x or y directions, and then calculates the prestress moment.

Model results

Figures 5.9 to 5.12 show the plastic strains, corrugation curvatures and prestress moments predicted by this model for a variety of forming processes which have been attempted. They will be compared to physical test results in Section 5.3.2. For this reason, all post-age-hardening forming processes apply a curvature of 285 m^{-1} , to match the forming process. This has been found to be sufficiently large that the deformed sheet cannot be elastically flattened: hence, in all these cases, the sheet is then plastically flattened before being released and the plastic strains plotted. Where the samples are worked before age-hardening, they have an initial curvature of 100 m^{-1} .

The figure captions make most of the relevant points: namely, that in most cases, the two regions end up with very different magnitudes of curvature. This would lead to a strong average curvature across the sheet when in the corrugated state.

According to Fig. 5.4, the process in Fig. 5.9 should result in equal curvatures in the two different regions, whereas this plastic flow model finds a difference of 10 %. Possible reasons for this inaccuracy are given below. However, the model has successfully captured the important trend, that the final corrugating stage has reduced this discrepancy (from 21 % after rolling). From the model, the optimum work-flows are (as expected) those that finish with corrugating, especially the work-flows in Fig. 5.10, for identical corrugation curvatures in the two regions, and Fig. 5.12, for slightly worse agreement but much higher prestresses. Only forming *before* age-hardening enables plastic strains to penetrate to the centre of the shell, leading to the higher prestresses achieved in Fig. 5.12 and the higher corrugation curvatures in Fig. 5.11.

If the corrugated shell is required to be globally flat, there is another solution, which accepts that the same- and opposite-sense regions will have different corrugation curvatures: adjusting the relative sizes of the regions, so that each corrugation is not evenly but unevenly divided into same- and opposite-sense regions. For example, if the same-sense region would have double the curvature, make it half as long in the y direction. This will, however, create a different corrugation profile to that of Fig. 4.4, being made of circular arcs of varying angle, length and radius.

Figure 5.13 depicts the plastic strains from Figs 5.9d and 5.11d, comparing them with similar results for the initial yield value, $\sigma_y = 1200 \text{ MPa}$. The reduced yield strain results in a noticeable ‘clipping’ of the yield strains, as significant plastic deformation occurs as the shell is flattened out: this will tend to reduce the curvatures and moments generated. However, the plastic strains also penetrate deeper into the shell thickness, which will tend to *increase* the curvatures and moments. Section 5.3.2 compares the results for both yield strains with measurements of prototype shells.

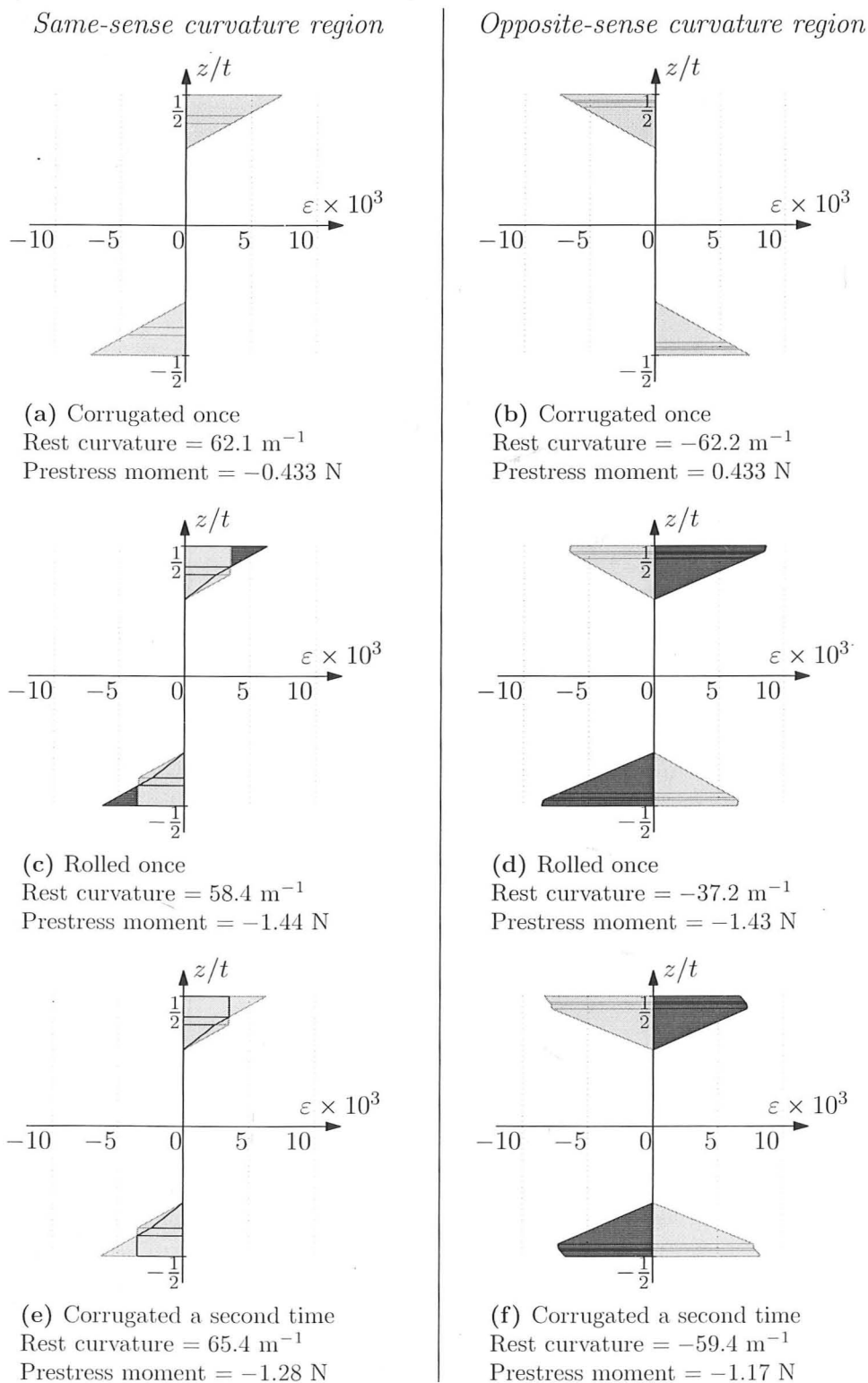


Figure 5.9: Tresca model of the forming process, when the sheet is corrugated first (on the left, regions of same-sense curvature: on the right, opposite-sense). Variations through the shell thickness of plastic strains, ε_{xx}^p (dark grey) and ε_{yy}^p (light grey), are plotted after each forming stage; 'rest curvature' is released in the y - y direction so $\kappa_{yy} = c$, $\kappa_{xx} = M_{yy} = 0$. The prestress moment is M_{xx0} . After rolling, curvatures of the regions are very different: the final corrugation stage partially corrects this at the expense of greater variation in prestress.

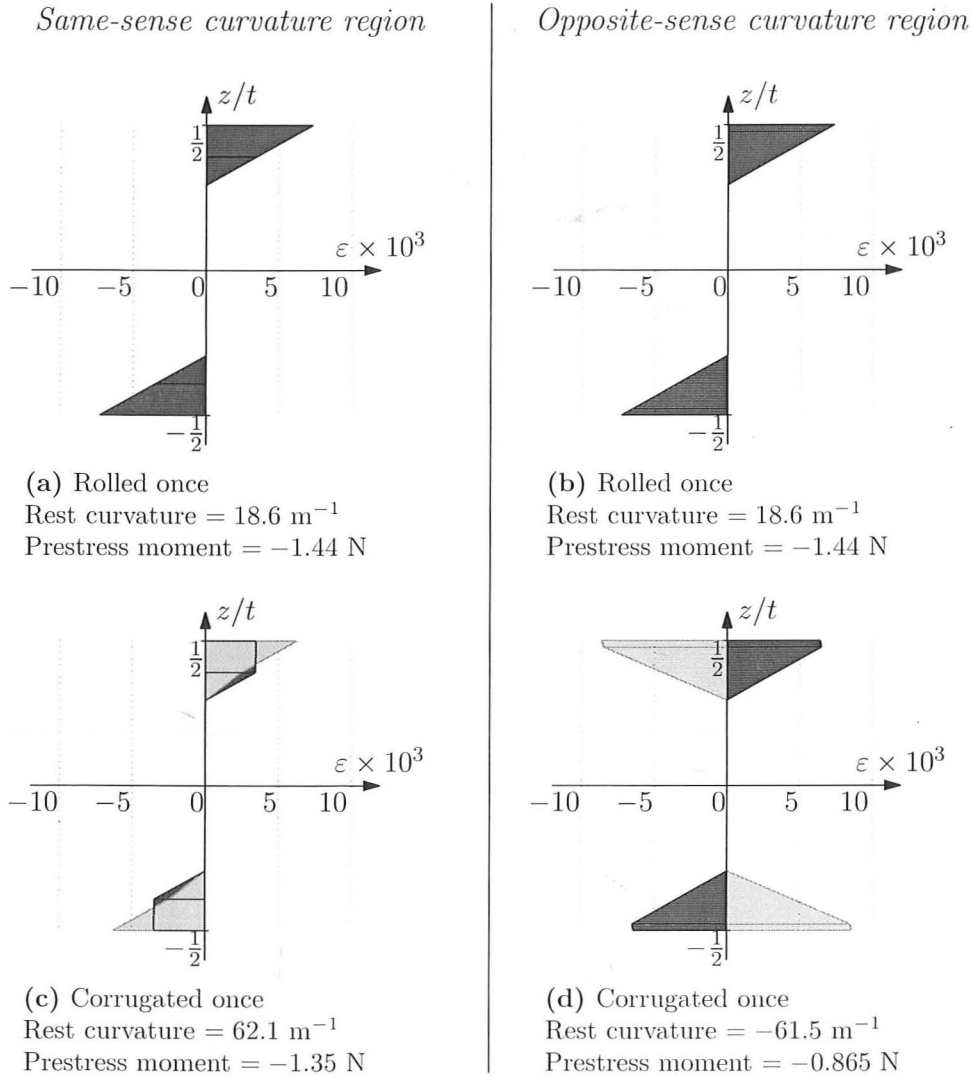
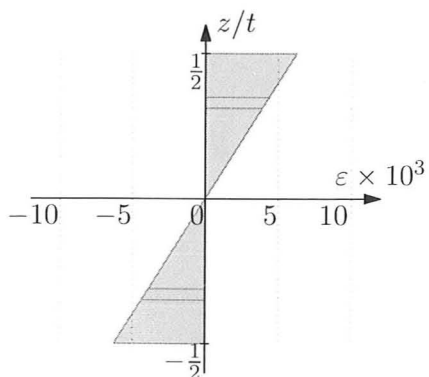
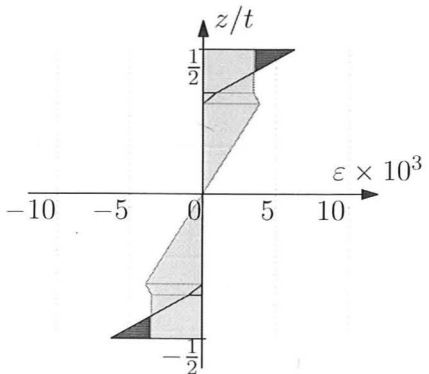


Figure 5.10: The Tresca model of the forming process, when the sheet is rolled first (on the left, regions of same-sense curvature: on the right, opposite-sense). This process produces similar results to those in Fig. 5.9, in which the figure axes and colours are also explained.

Same-sense curvature region

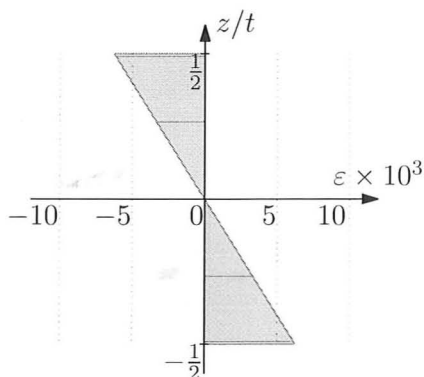


(a) After age-hardening and then being flattened
 Rest curvature = 100 m^{-1}
 Prestress moment = -0.697 N

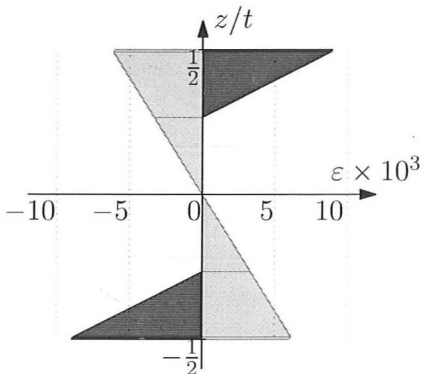


(c) Rolled once
 Rest curvature = 89.7 m^{-1}
 Prestress moment = -1.62 N

Opposite-sense curvature region



(b) After age-hardening and then being flattened
 Rest curvature = -100 m^{-1}
 Prestress moment = 0.697 N



(d) Rolled once
 Rest curvature = -73.9 m^{-1}
 Prestress moment = -1.32 N

Figure 5.11: The Tresca model of the forming process, when the sheet is corrugated before age-hardening, and rolled after (on the left, regions of same-sense curvature: on the right, opposite-sense). Again, the figure axes and colours are explained in Fig. 5.9. Note that the two regions end up with very different curvature magnitudes: *i.e.*, the corrugated sheet will not be globally flat.

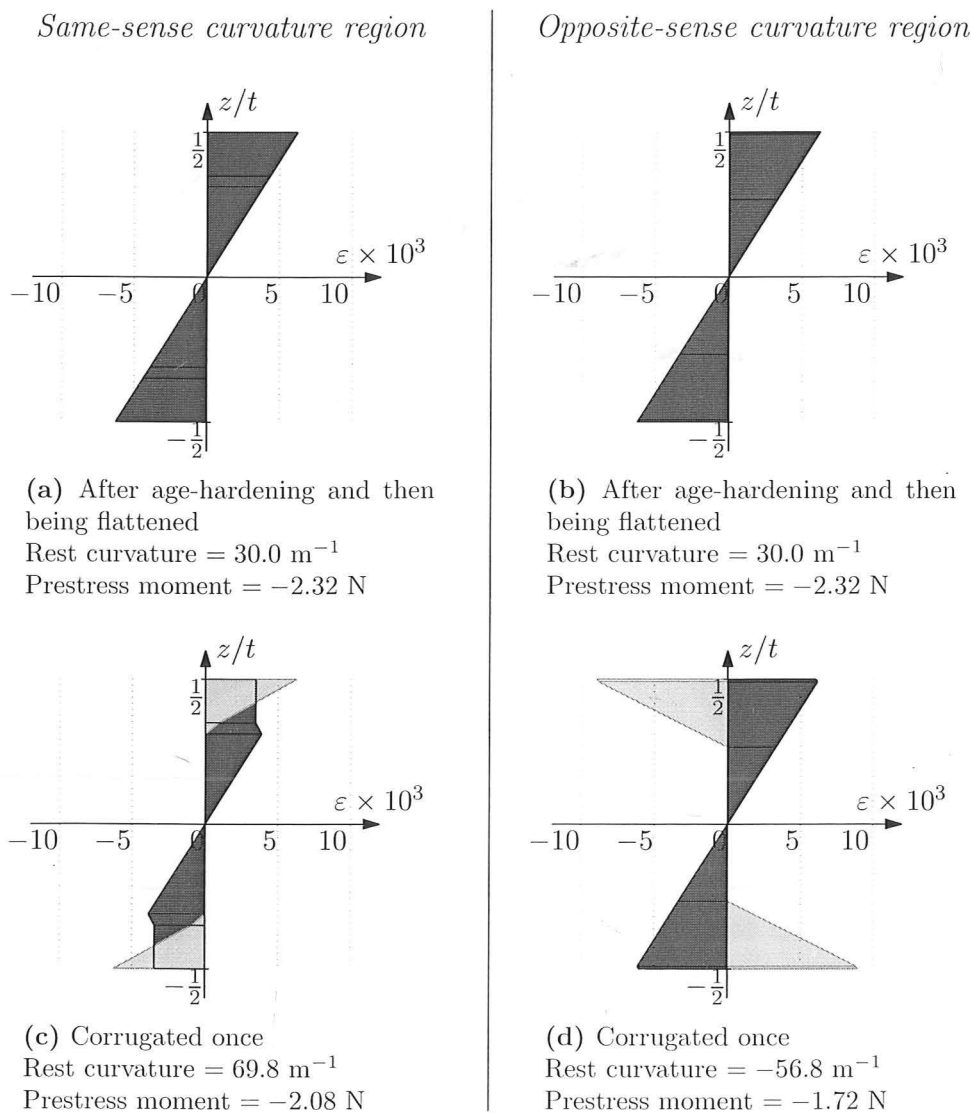
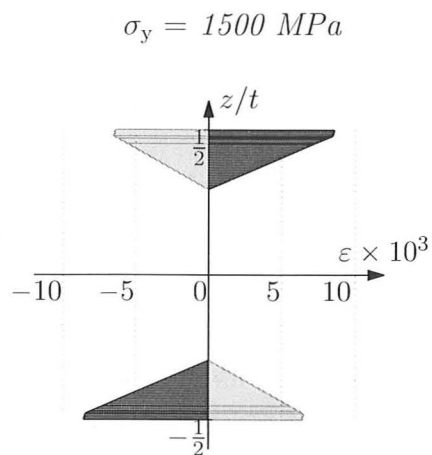
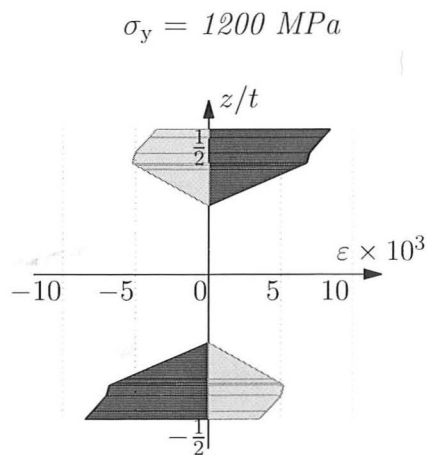


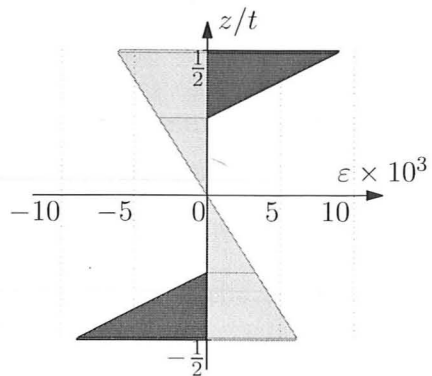
Figure 5.12: The Tresca model of the forming process, when the sheet is wrapped round a cylinder before age-hardening, and corrugated after (on the left, regions of same-sense curvature: on the right, opposite-sense). Again, the figure axes and colours are explained in Fig. 5.9. Unlike Fig. 5.10, to which this process bears strong similarity, this case produces (again) a large difference between the curvatures of the different regions.



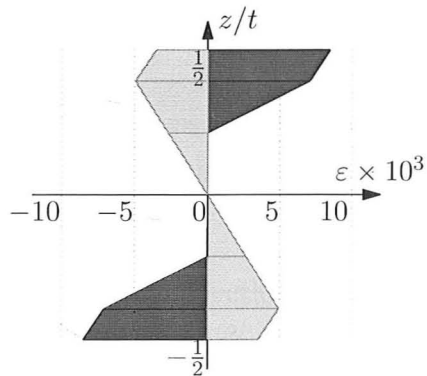
(a) Age-hardened before corrugating
Rest curvature = 37.2 m^{-1}
Prestress moment = -1.43 N



(b) Age-hardened before corrugating
Rest curvature = -37.4 m^{-1}
Prestress moment = -1.99 N



(c) Age-hardened after corrugating
Rest curvature = 73.9 m^{-1}
Prestress moment = -1.32 N



(d) Age-hardened after corrugating
Rest curvature = -53.1 m^{-1}
Prestress moment = -2.00 N

Figure 5.13: The Tresca model of the forming process, comparing different values of the yield stress σ_y . The reduction in yield stress (right) results in ‘clipping’ of the plastic strains, since large plastic strains cannot be elastically recovered. However, in these cases, this clipping is more than balanced by the increased depth of material to which the plastic strains penetrate, so that the prestress created is larger for the lower value of yield strain. Again, the figure colours and axes are explained in Fig. 5.9.

Limitations

There are a number of limitations to this model, which account for the discrepancies between the model and observed behaviour:

- (i) this model captures a number of subtle effects of plastic flow. However, it neglects any work-hardening, which CuBe *does* undergo. This would add significantly to the model's complexity, but would add another order of subtlety to its effects, which we would expect to increase its accuracy;
- (ii) the model neglects boundary conditions at the interface between regions of same-sense and opposite-sense curvature. When the sheet is relaxed in the corrugated direction, there is no moment at the interface, which is fine, but there will be a discontinuity in the through-thickness strains. Other assumptions based on uniform curvatures over an infinite shell also break down, such as the assumption of there being no through-thickness shear stresses;
- (iii) following on from (ii), the forming process involves a press against one surface of the material, so that there are some through-thickness stresses at the inner surface, even though the outer surface is stress-free. Thus, for equilibrium, there are through-thickness shear stresses; and
- (iv) the model assumes pure bending in the forming process: in practice, there must also be tensions induced in the forming process, to balance the pressure of the rollers/press.

In order to evaluate the accuracy of the plastic flow model, Section 5.3.2 attempts to measure the real internal stresses in the shells.

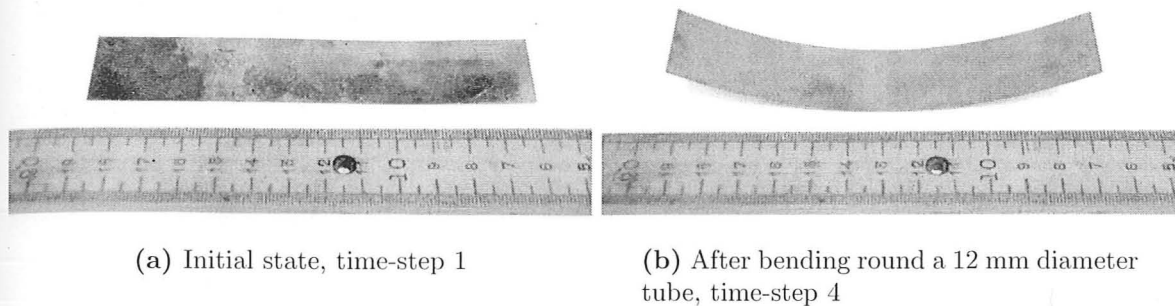


Figure 5.14: A test sample for the plastic model calibration.

5.3 Quantitative physical testing

In this section, we begin by testing CuBe alloy to find an appropriate yield stress for our EPP model, and then, in Section 5.3.2, perform a test to verify the findings of the various analytical models.

5.3.1 Plastic material testing of CuBe alloy

This test method evaluates the yield stress for CuBe in order to establish whether it changes due to work hardening. In the process, we seek to find an appropriate value of σ_y for an elastic-perfectly-plastic model of the material, as described in Section 3.3.1. The test method is based on applying curvatures to a strip of age-hardened CuBe, and measuring the elastic spring-back.

This process is then modelled with the EPP Tresca model of Section 5.2, and the material values in the model are tailored to produce the closest possible match. Section 5.3.1, below, outlines the model and results, to which Section 5.3.1 then fits the EPP model.

Experimental method and results

The CuBe sample is shown in Fig. 5.14. It is 0.125 mm thick, 25 mm wide and 133 mm long. It is wrapped round a series of cylindrical bars of decreasing diameter, from 25 mm down to 8 mm, before then being reversed. The tightest curvature is then applied in opposite directions sequentially until the behaviour settles, when transient effects disappear. The applied curvatures and the resulting curvatures of the sheet after spring-back for two iterations of the test are shown in Fig. 5.15. Each iteration of the test is conducted on a fresh sample, cut from a coil of quarter-hard CuBe alloy and then age-hardened as per the manufacturer's instructions.

To measure the curvature, a series of concentric circles are printed on a sheet of paper. The radius of these circles is known, and the CuBe strip is laid on the paper on its curved edge, to match it to the closest circle: this method is free from any parallax or similar

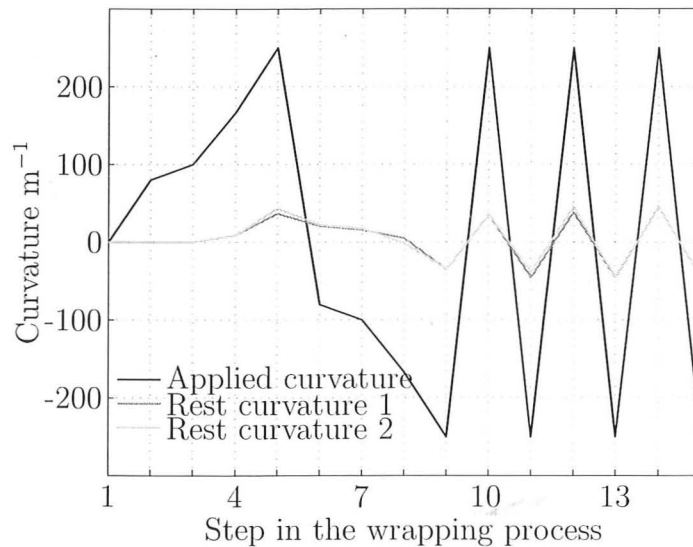


Figure 5.15: Test results, when wrapping a strip of CuBe round cylindrical bars of varying diameter. Shown are the applied curvatures and, for two tests labelled 1 and 2, the rest curvatures after the strip has been deformed to the ‘applied’ value and then allowed to elastically spring back. The rest curvature is measured by laying the shell on its curved edge on a sheet of paper printed with a series of concentric circles, and matching the shell to the closest of these radii.

errors. Finally, tighter and tighter curvatures are applied until the shell snaps, giving the failure strain.

Analysis

Figure 5.16 compares the test results, for two tests, with the predictions for the given applied curvatures from the Tresca model of Section 5.2, for a range of assumed yield stresses. For the first yield stage, a yield of 1200 MPa matches perfectly, which fits the range of initial yield values given by Brush Wellman and discussed in Section 5.1. At the end of the test, stages 13–15, a yield of 1400 MPa fits perfectly. In the middle of the test, 1500 MPa fits best. This is consistent with a material which rapidly work-hardens, in this case to $\sigma_y = 1500$ MPa, before then displaying slight strain softening until failure at the ‘Ultimate Tensile Stress’ (UTS). Therefore, 1500 MPa has been used in Section 5.2.

This analysis must remain a broad approximation: while the Tresca model with $\sigma_y = 1400$ MPa fits the data towards the end of the test, it has assumed $\sigma_y = 1400$ MPa throughout, whereas in practice σ_y has varied. In such a strongly history-dependent system, correlation between the two sets of data does *not* definitively prove that we have the correct yield stress. However, it does suggest that our plastic model has the potential to model the observed behaviour.

One puzzle remains, in steps 6 and 7, where the test results produce a result significantly softer than 1200 MPa. This is consistently found in the process of reversing the

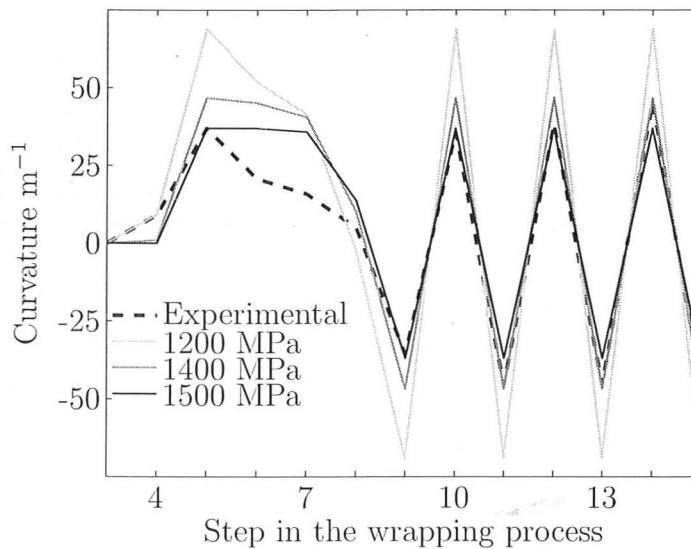


Figure 5.16: The average test data, compared with the predicted rest curvatures from the Elastic-Perfectly Plastic (EPP) Tresca model assuming a range of values for yield stress σ_y . Note that initial yield (step 4) matches a yield stress of 1200 MPa. However, it quickly seems to work-harden, coming closer to 1500 MPa on the Tresca model before then softening slightly to 1400 MPa. That this process is based on a number of greatly simplifying assumptions is emphasised by the large discrepancy in steps 6 and 7, where the curvature is reversed.

curvature. The discrepancy may well be due to the assumption of a Tresca yield surface: if the yield surface is significantly different, then the plastic strain vectors will change.

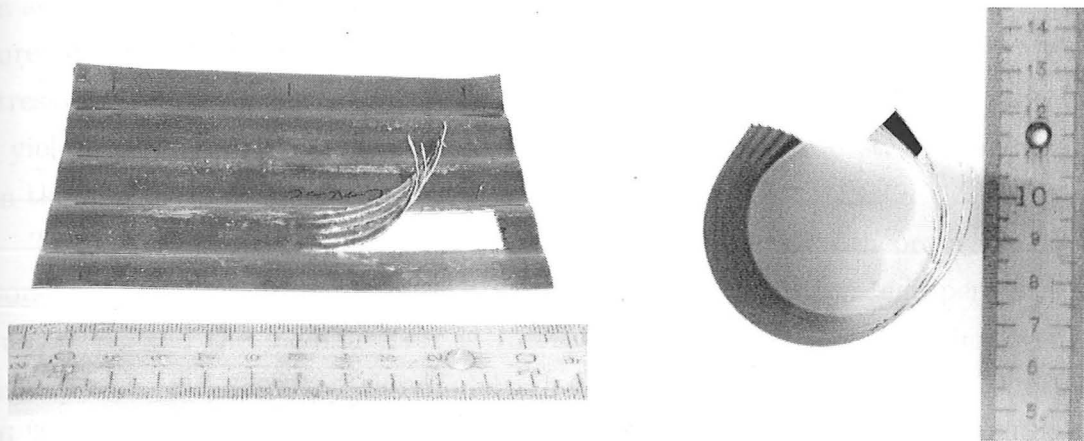
As a final note from this test, the shells snapped on a tube of diameter 3 mm. This gives a failure curvature between 500 m^{-1} and 667 m^{-1} , which correspond to strains at the surface of 3.1–4.2 %.

5.3.2 Internal stress measurements

The elastic model of Chapter 4 assumes a uniform prestress in the shells. The plastic model of Section 5.2 predicts more detailed bending prestresses that vary across the shell, assuming that said prestress is constant only in regions of constant-sense curvature. In this test, slices are taken from prototyped shells, releasing these bending stresses. From the final shape taken by the sliced sections, the original prestresses are inferred, and in the process, the plastic flow model can be tested.

Experimental method

Crucial to this test is the ability to slice apart the CuBe shell without inducing or modifying the internal stresses. This eliminates shearing methods as an option, so a miniature grinding disc is used. This does not put out enough heat to soften the CuBe; due to the



(a) View along the y -axis (with elevation), with the shell in its corrugated state

(b) View along the y -axis, with the shell in its coiled state

Figure 5.17: Example images of a bistable shell after strips have been cut out by grinding, to release the prestress moment, resulting in the visible coiling of the strips.

high thermal conductivity of CuBe, at no point do the ground surfaces get even noticeably hot to the touch.

It has been assumed that within the sheet, away from edge effects, the stresses are uniform along the corrugations but vary across them. Therefore, thin (relative to the corrugation wavelength) slices are cut along the corrugations for about 50 mm, then being cut free of the shell at one end to release their stresses, as demonstrated in Fig. 5.17. The samples have a wavelength of 22.7 mm, and from a single quarter-wavelength, four slices of approximately 3 mm width are cut: one in the ‘trough’, the region where the prestress and corrugations are in the same sense; one in the ‘peak’; and two in between, so that in total, there are two slices of same-sense curvature and two of opposite-sense curvature.

Results and analysis

From the measured curvatures of the released strips, we need to find the moment within prior to their release. We assume that their initial strain state is such that they can be released to equilibrium without any part of the material having to plastically yield. Since the strips are so thin in the y direction, we also assume that $M_{yy} = 0$. Given that $M_{yy0} = \kappa_{xx0} = 0$, and that, once the shell is released, $M_{xx} = M_{yy} = 0$, Eqn 3.7 becomes

$$\begin{bmatrix} -M_{xx0} \\ 0 \end{bmatrix} = D \begin{bmatrix} 1 & \nu \\ \nu & 1 \end{bmatrix} \begin{bmatrix} \kappa_{xx} \\ \kappa_{yy} - \kappa_{yy0} \end{bmatrix} \quad (5.40)$$

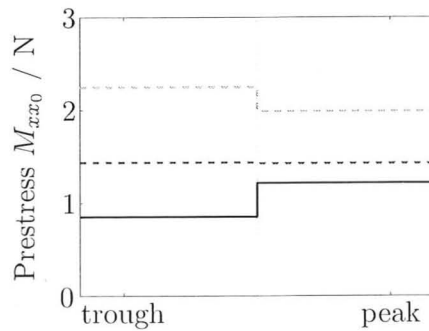
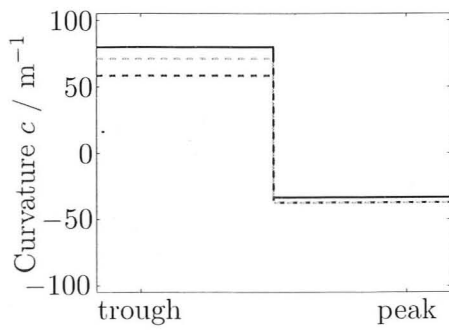
rearranging to

$$M_{xx0} = -D(1 - \nu^2)\kappa_{xx} \quad (5.41)$$

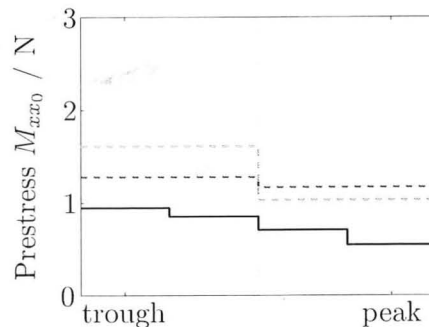
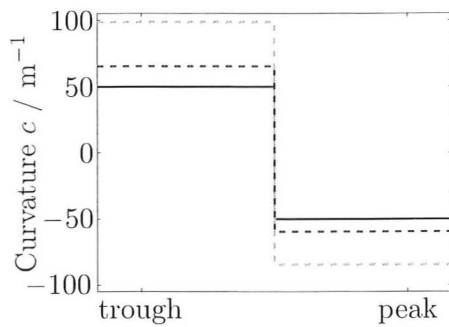
In addition to the prestress moment thus calculated, the results in Fig. 5.18 contain measurements of the corrugation curvatures, c . These are compared with the predicted prestress and predicted curvatures from the plastic model of Section 5.2. From Section 5.3.1, a yield stress of 1500 MPa is assumed to match the material best, but predictions based on the initial yield stress, 1200 MPa, are also shown in Fig. 5.18.

The curvatures show a fair agreement with the 1500 MPa theoretical model: in the worst case, the prediction is out by 54 %, but the mean *magnitude* percentage error is just 21 %, and the median error is 15 %. The measured moments, however, are consistently overestimated by the model: the mean error magnitude is 62 %, the median 56 %, and in the worst case, the prediction exceeds the measurement by 128 %, all for the larger-wavelength corrugations. In addition, for the case in Fig. 5.18a where the pre-hardened shell is corrugated and then rolled, the same-sense-curvature region has the lower prestress, which is counter to all expectations from Section 5.2, with the expected predicted trend re-emerging if the sheet is then corrugated again, as in Fig. 5.18b.

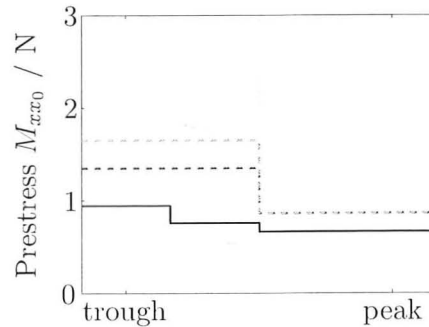
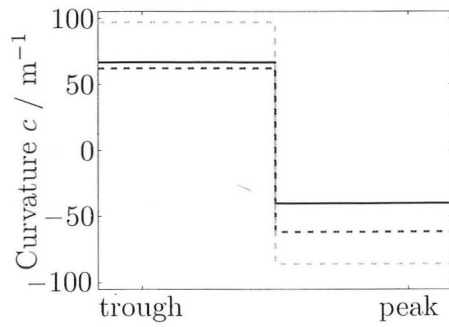
Using the lower initial-yield value of 1200 MPa results in yield occurring over more of the thickness of the material, with the effect that the moments and curvatures are, almost invariably, increased, so that the correlation between prediction and results in Fig. 5.18 becomes almost uniformly worse.



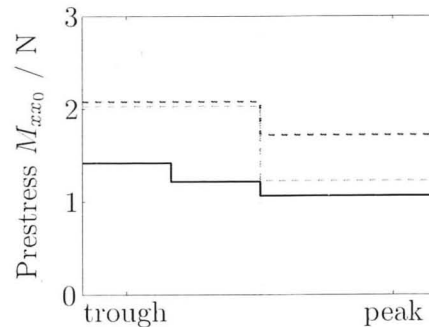
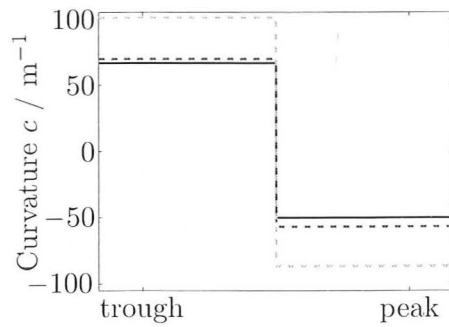
(a) Age-hardened, corrugated, and then rolled, as modelled in Fig. 5.9



(b) Age-hardened, corrugated, rolled, and then corrugated again, as in Fig. 5.9



(c) Age-hardened, rolled, and then corrugated, as modelled in Fig. 5.10



(d) Rolled, age-hardened, and then corrugated, as modelled in Fig. 5.12

Figure 5.18: Results of prestress measurements, compared with the Tresca plastic flow model predictions. Solid lines denote test measurements; dark dashed lines, the Tresca model for $\sigma_y = 1500$ MPa; and light dashed lines, the Tresca model for $\sigma_y = 1200$ MPa. The left-hand graphs plot the corrugation curvature, c , across a corrugation, while right-hand graphs plot the prestress moment M_{xx0} . ‘Trough’ and ‘peak’ regions have, respectively, the same and opposite curvature sense as/to the coiled mode.

5.4 Conclusions

Section 5.2 has produced a plastic flow model to analyse the forming process of the corrugated shells, which has, in turn, been based upon the material tests of Section 5.3.1. Ways have been found to test the quantitative and qualitative predictions of this model against the real shells in Section 5.3.2. These tests found a good agreement in some areas with the model: given the inherent limitations of the model, the agreement is felt to be as good as can be expected without dramatically increasing the plastic flow model's complexity. The most critical simplification of the model, which is most likely to produce discrepancies between the model results and reality, is the assumption of an elastic-perfectly-plastic material, because it neglects work-hardening of the CuBe.

Observations in Section 5.1.2 agree well with the behaviour of the elastic model in Chapter 4: the increased curvature of the corrugated mode as the corrugation amplitude nears its lower limit is observed, as are the upper and lower bounds on initial cross-corrugation curvature for the twisting bistability.

Throughout this and the previous chapter, it has been assumed that all global curvatures of the corrugated sheet are developable, and this, too, has been borne out through observations and experiment. In all of these shells, the initial corrugated form is developable; however, if the initial corrugated shell is *not* developable, but is curved along the corrugations, a whole new set of deformations becomes possible, and that is the subject of the next chapter.

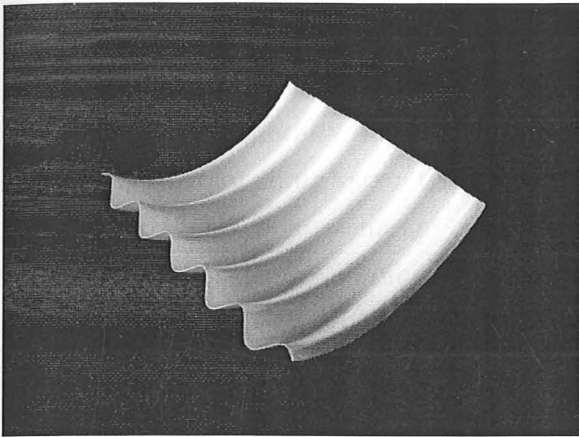
Chapter 6

Curved corrugated shells (i): shape-change and compatibility

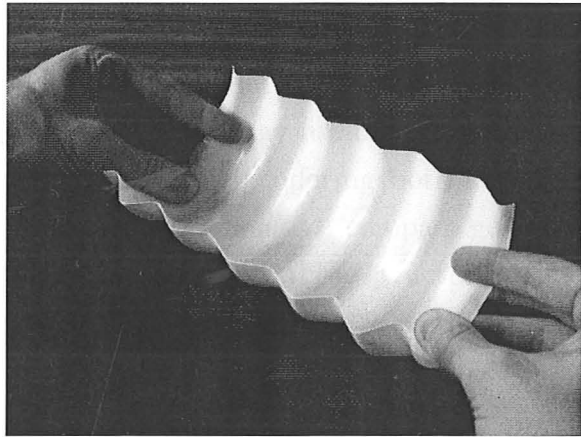
The shells of Chapters 4–5 deform only between shapes of uniform cylindrical curvature. However, a simple modification produces shell capable of a far greater variety of morphing shapes. In this chapter, we study corrugated sheets that are also curved along their corrugations, which can be transformed into a remarkable variety of shapes by purely inextensional bending. To demonstrate, we have prototypes constructed from both paper and HIPS, which materials are much easier to form into the initial, doubly-curved shapes than CuBe alloy.

Figure 6.1 shows an example, made by vacuum-forming a sheet of 0.5 mm-thick HIPS. The initial shape, Fig. 6.1a, has some global curvature along the corrugations, $\kappa_{XX_0} \neq 0$. All other curvatures are zero, and there are no residual stresses, so that $\kappa_{YY_0} = \kappa_{XY_0} = \mathbf{M}_0 = \mathbf{N}_0 = 0$. We assume, in this chapter, that the material is semi-inextensional: *i.e.* the local strains $\varepsilon_{xx} = \varepsilon_{yy} = \varepsilon_{xy} = 0$ throughout.

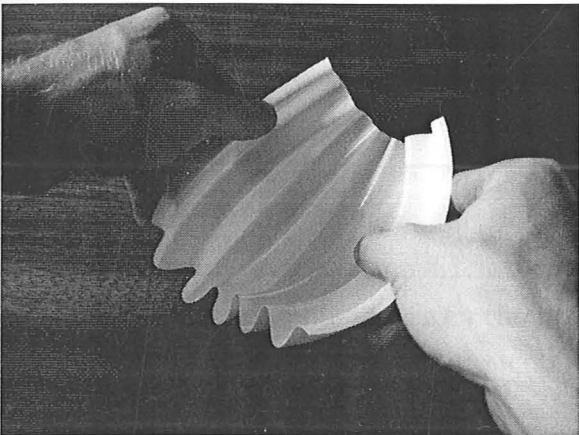
When handled, the shell can deform to, *e.g.*, a tube, a bowl-shape or a saddle-shape in Figs 6.1b, 6.1c and 6.1d respectively. As stated already, the shell accomplishes these significant changes in shape *without* local stretching of the surface: such behaviour is common for shell structures, where it is energetically favourable to deform by bending rather than stretching. However, it is clear that the equivalent mid-surface of the corrugations experiences an overall extension, and that this extension also couples to significant extra curving along the corrugations, as shown in Fig. 6.1b. Ordinary shells do not behave in this manner, nor are they prone to the double curvature indicated in Figs 6.1c and 6.1d. Depending on the direction of bending across the corrugations, the shell deforms either elliptically, so that the mid-surface acquires positive Gaussian curvature, or hyperbolically into a saddle shape with negative Gaussian curvature. Although not shown, it is difficult to bend the shell back on itself in the opposite sense to the curved line of corrugations without damage.



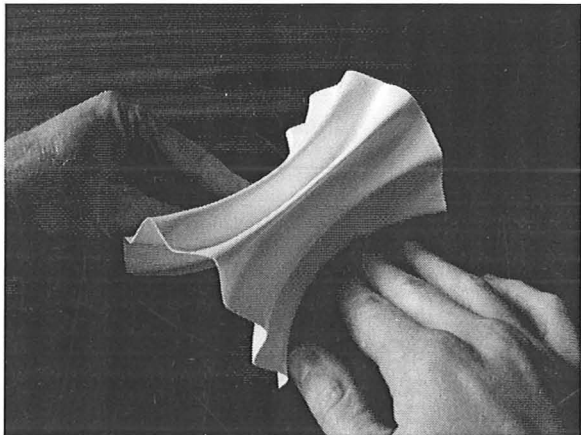
(a) The initial shape, unidirectionally curved along the corrugations



(b) As the curvature increases, so the shell expands across the corrugations.



(c) The shell can be inextensibly deformed to a positive Gaussian curvature, *i.e.*, bowl-shaped, *or*



(d) to a negative Gaussian curvature, *i.e.*, saddle shaped.

Figure 6.1: Introducing the curved corrugated forms: these images are all of the same shell, with no significant stretching of the plastic membrane between shapes.

The shell of Fig. 6.1a bears a strong superficial resemblance to a section from a bellows. However, its analysis is very different. A bellows is a shell of revolution: each 'corrugation' forms a closed loop of fixed length, and therefore has a fixed curvature, until it buckles in some asymmetric form, and its deformations always involve some local stretching, as described in Section 2.2.2. Since the shell of Fig. 6.1a is *not* closed, its curvature about its axis of rotational symmetry is free to change, as in Fig. 6.1b: it is still axisymmetric, but the amount of material in a full revolution has changed. Therefore, the axisymmetric analyses performed by, *i.a.*, Vlasov (1964), do not apply.

This simple structure may not prove attractive for use in traditional engineering structures, which are generally designed to be stiff. However, they may usefully serve the new generation of 'morphing' structures described in Section 2.2.2, offering both structural integrity and large shape-change capabilities. This chapter pursues a compact geometrical model of their shape-changing behaviour. Note that although these structures bear a superficial resemblance to bellows, the inextensional nature of the shells in this chapter makes this analysis fundamentally different. For comparison, see the solution of a bellows problem in (Calladine, 1983, chap. 12).

Section 6.1 defines our initial system, including the vector expressions used to describe curvatures. Section 6.2 explains how a curved corrugated shell can exhibit shape changes not possible from a 'conventional' uncurved corrugated sheet. Section 6.2.1 relates their stretching across the corrugations to their curvature, and Section 6.2.2 tests this coupling relation against measurements of a vacuum-formed plastic shell, and also against a finite-element analysis. This exercise shows an excellent agreement. It validates the assumptions made about the geometric behaviour and paves the way for a full set of compatibility relations in Section 6.3.1, which is then compared to a more general behaviour of prototypes in Section 6.3.2. Even though the shell *appears* to endure very large changes in Gaussian curvature, it is assumed that shells can generally only deform *inextensionally*: Section 6.3.3 resolves this paradox by demonstrating that while the mid-surface of the corrugated sheet does indeed undergo large changes in Gaussian curvature, on a local level the sheet does not. Finally, conclusions are drawn in Section 6.4.

6.1 Definition of coordinate systems and curvatures

The definitions of the coordinate systems in the corrugated sheet are given in Section 3.1.3. Fig. 6.2 repeats this with a section through a typical corrugation, but also shows a three-dimensional view of the corrugated shell. As before, there is a local right-handed coordinate system, x , y and z . Also shown is the equivalent mid-surface of the corrugations, which is defined by the coordinate system of X , Y and Z . However, the shell now has an initial curvature in the X - X direction.

The important feature that is new to this chapter is the decomposition of the vector defining the curvature of the mid-surface in the X direction, κ_{XX} . The corresponding radius of curvature, $1/\kappa_{XX}$, lies in a vertical plane. Now, however, we decompose that curvature into two other curvatures relevant to the curving properties of a thin strip running along the shell in the x direction. The strip is taken to be thin in the y -direction and is inclined to the vertical at an angle θ . The centreline of this strip must, like the mid-surface, have a curvature equal to the shell curvature κ_{XX} . This curvature, expressed as a curvature vector in the $-Z$ direction in Fig. 6.2b, can be decomposed into two perpendicular components: the out-of-plane curvature of the local shell at that point, equal to κ_{xx} , and the *geodesic* curvature of the strip, denoted by κ_g . κ_g is the curvature that the strip centreline would have were the strip removed from the rest of the shell and laid on a flat surface; and this curvature lies in the $x-y$ plane of the shell. These curvatures are all defined as curvatures of a line in 3-D space, as outlined in Section 3.1.1.

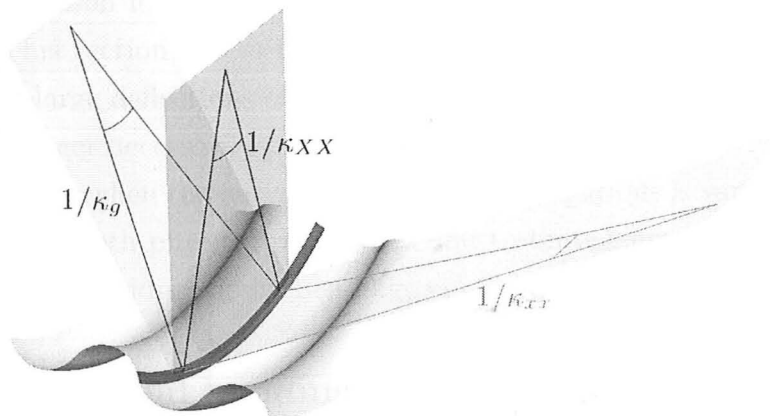
Throughout this, and the following, chapters, it is assumed that the radius of curvature of the shell, $1/\kappa_{XX}$, is much greater than the amplitude of corrugations. Therefore, as the corrugations are considered as a large number of thin strips, each of these strips can be assumed to have exactly the same global curvature κ_{XX} , even though they do not all lie exactly on the mid-surface of the shell.

In addition to the conventional understanding of strain as change in length with regard to the initial length, we consider a property related to strain, but independent of the initial shape of the shell. This property, referred to as ϵ_{YY} , is the strain relative to the Y -direction length of the shell when the corrugations are completely flattened out. In the terms of Fig. 6.2, it can be defined as the average value

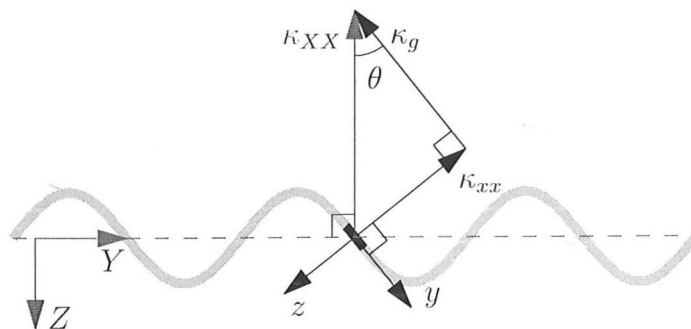
$$\epsilon_{YY} = \overline{\left(\frac{dY}{dy}\right)} - 1 \quad (6.1)$$

where the overbar $\overline{(\)}$ denotes average. From Eqn 6.1, ϵ_{YY} will always be negative. In the terms of Fig. 3.4,

$$\epsilon_{YY} = \frac{\Lambda}{\lambda} - 1 \quad (6.2)$$



(a) A typical corrugated shell. Looking at a specific strip along the corrugation, shaded black, the strip has some curvature of radius $1/\kappa_{XX}$. This curvature can be split into a component of curvature in the plane of the strip, of radius $1/\kappa_g$, and an out-of-plane component, $1/\kappa_{xx}$.



(b) A section through the corrugations, showing the coordinate system used by this chapter. (x, y, z) is a local right-handed coordinate system in the shell; (X, Y, Z) is a coordinate system in the equivalent mid-surface, or average surface, of the sheet, shown as a dashed grey line. Both x and X are aligned along the corrugations. The curvatures shown in Fig. 6.2a are represented by the vectors κ_{XX} , κ_{xx} and κ_g . Each length is the magnitude of the curvature, *i.e.*, the inverse of the radius of curvature, and the curvature direction is normal to the tangent of the line and lies in the plane of the curvature.

Figure 6.2: A typical corrugation, showing the coordinate systems and curvature definitions of this chapter. In the X direction, the sheet has an upwards curvature, κ_{XX} . κ_{xx} is the out-of-plane curvature of the strip (*i.e.*, its shell curvature), while κ_g denotes the *geodesic* curvature of the strip: this is the curvature that the strip's centreline would follow if it were laid on a flat surface. These two curvature vectors are mutually perpendicular, and are the components of the vector κ_{XX} .

6.2 Unidirectional bending

As is found in Section 4.3, the bending stiffness of a shell along its corrugations can be more than two orders of magnitude greater than the local shell bending stiffness: this is a primary reason for their use in conventional structural applications, as covered in Chapter 2. This section shows that when the corrugated sheet is curved along the corrugations, and large deflections of the corrugation profile are considered, that increase in stiffness is no longer necessarily present. An analytical model is derived to explore the behaviour of the shell when the curvature along the corrugations is varied, and this model is then compared to both physical prototypes and to finite-element simulations. As this section considers only unidirectional bending, $\kappa_{YY} = \kappa_{XY} = 0$ throughout.

6.2.1 Unidirectional bending model

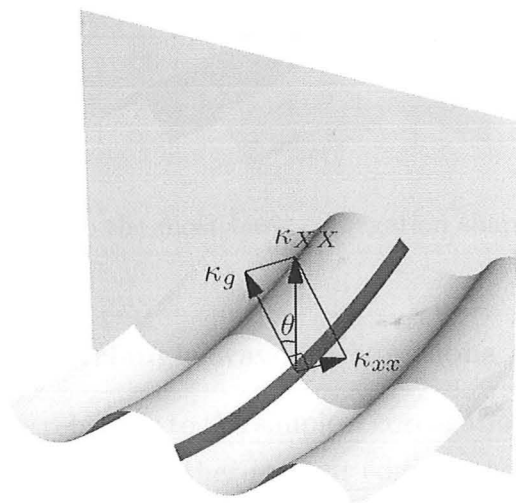
Following the definitions in Section 6.1, we consider a thin x -wise strip of material, at an angle θ to the vertical, with shell curvature, κ_{xx} , and geodesic curvature κ_g . Importantly, only κ_g is fixed by the construction of the shell. The initial shape is shown in perspective view in Fig. 6.3a. The corrugations are then given a tighter curvature along their corrugations, Fig. 6.3b, and the overall curvature of the strip, κ_{XX} , has increased. Since κ_g cannot vary, θ increases: *i.e.*, the strip of material rotates so that κ_{xx} increases, maintaining the direction of κ_{XX} . In other words, when the overall curvature of the corrugated sheet, κ_{XX} , is varied, θ and κ_{xx} also vary at a given point of geodesic curvature κ_g , according to

$$\kappa_g = \kappa_{XX} \cos \theta \qquad \kappa_{xx} = \kappa_{XX} \sin \theta \qquad (6.3)$$

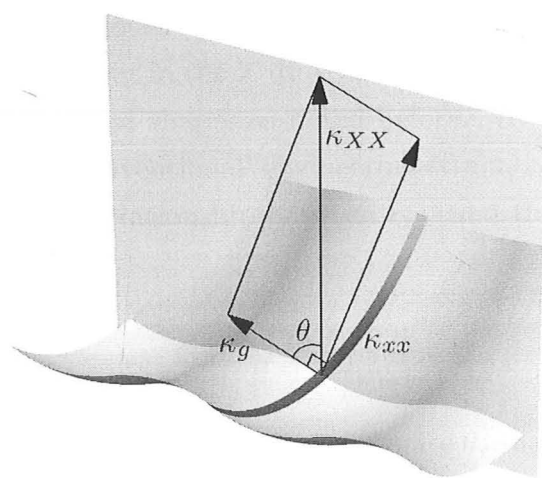
Note that these are *vector* transformations, being applied to *second-order tensors*: this is because the curvature of a shell, which is a second-order tensor, is being converted into the curvature of a line, which is a vector. In the process, it is κ_{yy} that is lost: this is irrelevant as these x -wise strips become infinitesimally wide in the y direction. As they do so, the shell can be considered as being continuously curved in both the x and y directions, so that the y – y curvature can be defined as

$$\kappa_{yy} = \frac{\partial \theta}{\partial y} \qquad (6.4)$$

For a smooth shell, θ and κ_{XX} are initially continuous across the corrugations, and therefore, so is κ_g . If κ_{XX} remains continuous throughout deformation, θ must also remain continuous, and the curvature κ_{yy} always has a finite value. Thus, changes in κ_{XX} are achieved without stretching, but by changes in corrugation curvature, κ_{yy} .



(a) A perspective view of the corrugation profile shown in Fig. 6.2b. Each thin strip has an out-of-plane curvature κ_{xx} and an in-plane, or geodesic, curvature κ_g , which together make the shell curvature, κ_{XX} , of the equivalent mid-surface of corrugation.



(b) As the sheet is rolled more tightly, κ_{XX} is increased, and so θ is increased, since κ_g is fixed by the construction of the shell and the vectors of κ_g and κ_{xx} are mutually perpendicular.

Figure 6.3: Unidirectional bending behaviour.

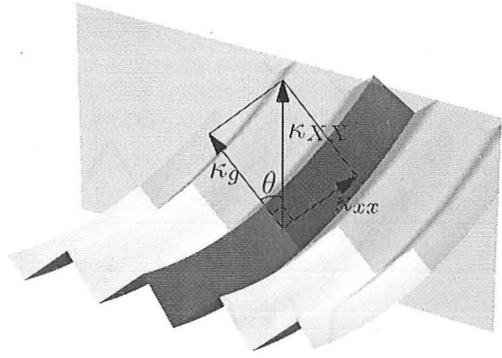


Figure 6.4: Simplified to the most basic corrugation shape, a triangular wave.

Unidirectional bending in triangle-wave corrugations

Figure 6.4 applies the above relations to the simplest corrugation: a triangle wave. A single corrugation is created by hinging together at their edges two, initially curved, membrane strips. The stretching and bending of the entire sheet are then easily calculated from

$$\epsilon_{YY} = \sin \theta - 1 \tag{6.5}$$

$$\kappa_{XX} = \kappa_g \sec \theta \tag{6.6}$$

where ϵ_{YY} refers to the strain relative to the length of the mid-surface when the corrugations are completely flattened out in the Y direction, defined by Eqn 6.1, and *not* to strain relative to some arbitrary initial shape, as noted before. We define the initial shape to have an initial strain ϵ_{YY_0} . ‘Conventional’ engineering strain, ε_{YY} , is the strain relative to this initial shape, and so the relationship between ϵ_{YY} and the conventional engineering strain, ε_{YY} , is thus:

$$\varepsilon_{YY} = \frac{\epsilon_{YY} - \epsilon_{YY_0}}{1 + \epsilon_{YY_0}} \tag{6.7}$$

It is useful to rearrange Eqns 6.5 and 6.6 to eliminate θ , and to give a coupled relationship between the global strain, ϵ_{YY} , and curvature, κ_{XX} in terms of the fixed property, κ_g :

$$\epsilon_{YY} = \sqrt{1 - \left(\frac{\kappa_g}{\kappa_{XX}}\right)^2} - 1 \quad \text{or} \quad \kappa_{XX} = \frac{\kappa_g}{\sqrt{1 - (1 + \epsilon_{YY})^2}} \tag{6.8}$$

The limits of behaviour become evident from these equations: ϵ_{YY} cannot be less than -1 , the point at which the corrugations are completely folded up and κ_{XX} reaches its minimum value of $\kappa_{XX} = \kappa_g$; however, ϵ_{YY} must always be negative, lying in the range from -1 to zero, and as ϵ_{YY} tends towards zero, κ_{XX} goes to infinity.

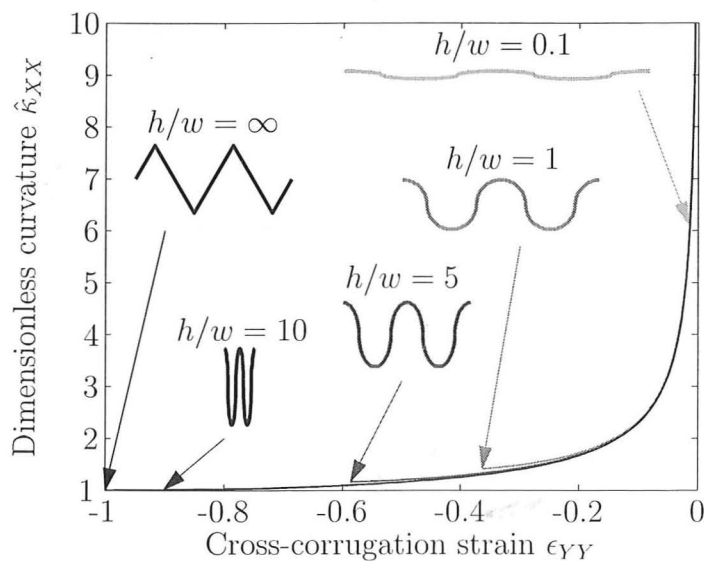


Figure 6.5: Strain–dimensionless curvature plots for various initially semi-elliptical corrugations, calculated numerically, with each corrugation split into 50 segments, and for a triangular-wave corrugation, calculated analytically. h/w is the ratio of height to width for a quarter corrugation in the locked state: all except the triangular wave are shown in this locked state.

Unidirectional bending in smooth corrugations

The coupled relationships between ϵ_{YY} and κ_{XX} in Eqn 6.8 are straightforward for the given simple triangular corrugation. This section compares their performance to the behaviour of those obtained for a smoothly corrugated profile. An equivalent set of closed-form expressions is not possible for a general corrugation profile. Instead, the cross-section must be reduced to a discrete number of curved strips, in order to approximate by numerical solution the resulting change in shape.

For any generic corrugation profile, as κ_{XX} is reduced, a length-wise strip of corrugation may rotate sufficiently so that $\theta = 0$. Although over the rest of the corrugation, θ still has some non-zero value, there can be no further increase in κ_{XX} for a fixed κ_g over the strip for which $\theta = 0$. Such behaviour defines a lower limit for κ_{XX} without the strain reaching $\epsilon = -1$: when one part of the corrugation has become completely ‘vertical’ ($\theta = 0$), the shell has ‘locked’, it cannot flatten any more in the $X - X$ direction, and κ_{XX} has reached a minimum. However, there is no upper limit to κ_{XX} : as the corrugations are completely flattened out, such that θ tends to $\pi/2$, κ_{XX} tends to infinity.

We must now choose some initial corrugation profile to study. Two mathematically convenient forms are a sinusoid and a semi-elliptical profile of alternating half-ellipses. As noted in the last paragraph, a corrugation profile becomes ‘locked’ when it cannot be further compressed in the Y -direction, during which, part of the corrugation profile becomes vertical. A semi-elliptical profile is therefore locked from the outset whereas a

sinusoid is not. But a convenient result presents itself, as proven in Appendix C: the locked shape of an initially sinusoidal corrugation is exactly a semi-elliptical corrugation; conversely, as an initially semi-elliptical corrugation is flattened, it will occupy an exactly sinusoidal profile at some stage in the deformation. In the process, it is found that the relationship between an initial profile and its locked shape is independent of the initial value of κ_{XX} .

The particular variation of ϵ_{YY} with κ_{XX} is found by considering a quarter wavelength of corrugation sub-divided into large number of strips. Each strip has the same κ_{XX} , assuming, as stated in Section 6.1, that the radius of curvature, $1/\kappa_{XX}$, is much greater than the amplitude of the corrugations. A quarter circle is first divided into discrete segments of equal arc-lengths: these are then shortened in the y direction to form an elliptical profile of the desired aspect ratio, before the actual arc-length, δs , and initial angle, θ_0 , of each segment is calculated. From Eqns 6.3, the final angle θ of each segment is related to the initial curvature, κ_{XX_0} , and final curvature, κ_{XX} , by

$$\cos \theta = \frac{\kappa_g}{\kappa_{XX}} = \frac{\kappa_{XX_0} \cos \theta_0}{\kappa_{XX}} \quad (6.9)$$

As the angle, θ , of each segment is known, the strain at a given κ_{XX} can be obtained by summing the contribution from strips of width δs :

$$\epsilon_{YY} = \frac{\sum \sin \theta \delta s}{\sum \delta s} - 1 \quad (6.10)$$

The above can be re-cast as a continuous integral as follows, performed between limits from $s = 0$ to $s = \lambda$, where λ is the material wavelength of each corrugation: *i.e.*, the width of each corrugation when flattened out so that $\epsilon_{YY} = 0$. The geodesic curvature, κ_g , varies in a known manner across the corrugations such that $\kappa_g = \kappa_g(s)$, and

$$\epsilon_{YY} = \frac{1}{\lambda} \int_0^\lambda \sin \theta ds - 1 = \frac{1}{\lambda} \int_0^\lambda \sqrt{1 - \left(\frac{\kappa_g(s)}{\kappa_{XX}} \right)^2} ds - 1 \quad (6.11)$$

While the variation with κ_{XX} of ϵ_{YY} becomes known, the performance between different initial shapes must be compared in a meaningful way. A convenient point is at small ϵ_{YY} , where the results for all shapes are scaled to match the triangular-wave corrugation, and the corresponding results for curvature are then made dimensionless with respect to the 'locked' curvature of the triangular-wave corrugation. This 'locked' curvature is exactly the geodesic curvature for the triangular-wave corrugation, which we refer to as κ_{gT} , so that the dimensionless curvature $\hat{\kappa}_{XX}$ is given by

$$\hat{\kappa}_{XX} = \frac{\kappa_{XX}}{\kappa_{gT}} \quad (6.12)$$

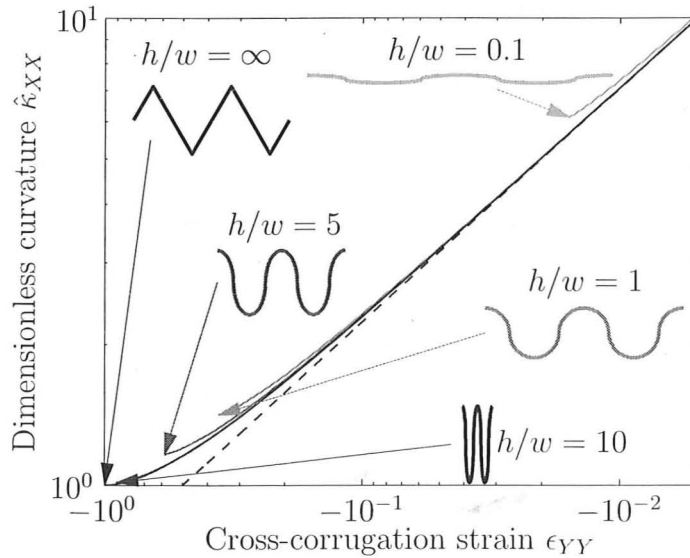


Figure 6.6: Log-log strain-curvature plots for various corrugations, as in Fig. 6.5. All terms are as in Fig. 6.5, but a dashed line has been added representing the equation $2\epsilon_{YY}\hat{\kappa}_{XX}^2 = -1$, to which all lines tend at large $\hat{\kappa}_{XX}$, which is to say, at small negative ϵ_{YY} .

Dimensionless solutions for a range of semi-elliptical corrugations are shown in Fig. 6.5.

Figure 6.5 appears to show a very close correlation between the various shapes, clearly implying that the simple, fully analytical triangular-wave solution remains usefully valid for shapes that are quite different from being a triangular-wave. This is particularly true at high $\hat{\kappa}_{XX}$ and small ϵ_{YY} . At larger, more negative ϵ_{YY} , the shape curves also appear to be close, but their shallow gradients are deceptive in that, for a given value of $\hat{\kappa}_{XX}$, the variation in ϵ_{YY} between curves is of the order of 20 %.

A logarithmic version of this plot is furnished in Fig. 6.6, and demonstrates that at small strains, the relationship tends to

$$2\epsilon_{YY}\hat{\kappa}_{XX}^2 = -1 \tag{6.13}$$

This equation can also be derived from Eqns 6.5 and 6.6 by approximating ϵ_{YY} to be relatively small.

6.2.2 Validation of unidirectional bending models

Equation 6.11 gives a relationship between strain and curvature that depends upon the fixed shape property of the formed shell $\kappa_g(s)$, which is compared in this section against measurements of a physical prototype and a finite-element analysis.

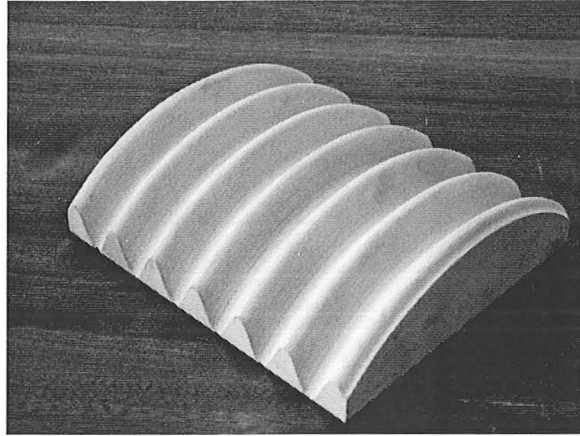


Figure 6.7: The mould used for vacuum-forming the plastic shell. This is produced on a computer-controlled milling machine.

Plastic prototype

A prototype shell in polymer was constructed by vacuum forming: Fig. 6.7 shows the computer-machined mould. The material is High-Impact Polystyrene ('HIPS'), gloss-coated on one side and with an initial nominal thickness of 0.5 mm.

In order to compare its stretching across corrugations, ϵ_{YY} , with along-corrugation curvature, κ_{XX} , the shell must be held such that a force in the Y direction is applied without any significant load in the X or Z directions, *despite* the large deflections which accumulate in both those directions as κ_{XX} changes. To enable this, the shell is mounted in an Instron displacement-controlled load testing rig by long wires, as shown in Fig. 6.8. When in tension, these wires only transmit force along their own axis. They are fashioned to be as long as the rig allows, so that as the shell coils up, the wire rotates imperceptibly, and the axial force is maintained in the Y direction. Fig. 6.9 demonstrates that this holds for most of the deformation, being less valid as the corrugations become almost flat where $\epsilon_{YY} \rightarrow -1$ and κ_{XX} becomes large.

The strain, ϵ_{YY} , is calculated by measuring the length of the mid-surface over six corrugations and dividing this by the material length, the latter being found by measuring the width of a flattened thin strip cut from the shell after testing. The curvature, κ_{XX} , was calculated from the chord subtended by the shell in the X direction and its arc-length in the same direction. Three separate tests are performed on three separate shells, with the following variations in measurement method:

- (i) The Instron's displacement value gives the extension of the shell in the Y direction: a ruler is used to manually measure the chord of the shell in the X direction.
- (ii) A digital camera is directed squarely at the shell and photos taken at 2 mm intervals of stretch. By manually picking out the coordinates on the image of various points

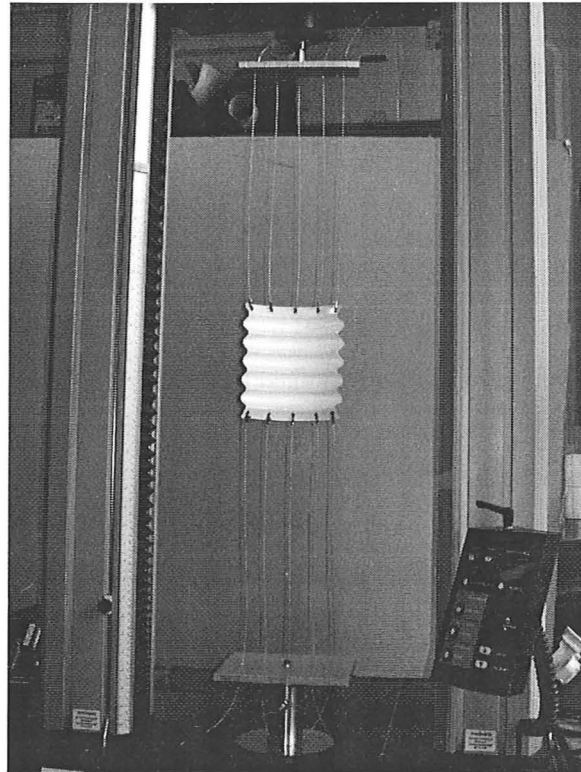


Figure 6.8: The test rig for performing a tensile test in the Y direction. The long cables transmitting the force are intended to ensure that the stretching is uniform over the shell throughout deformation.

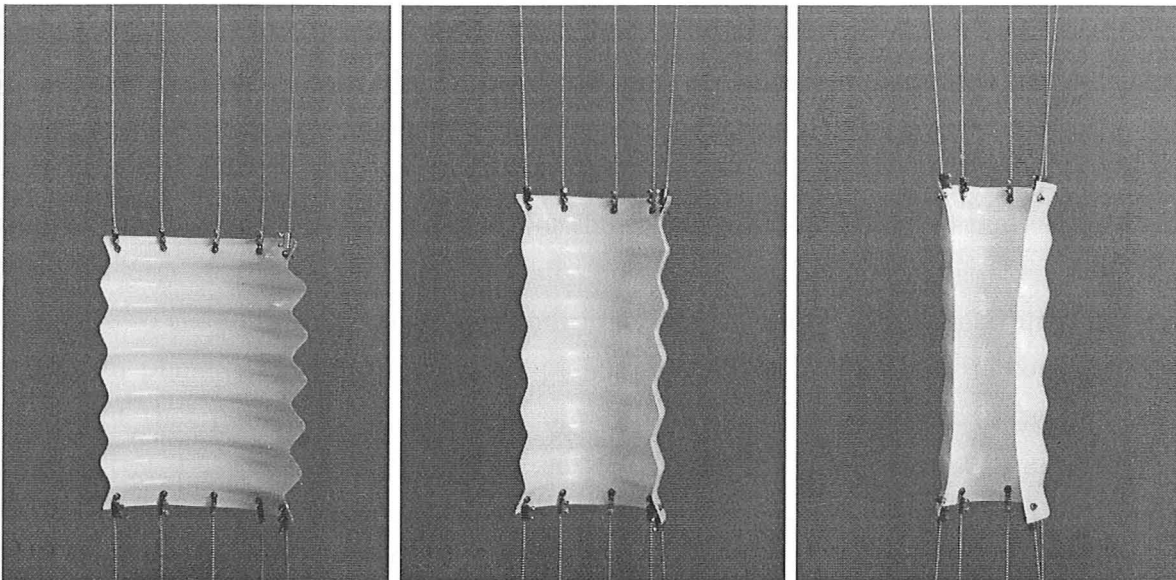


Figure 6.9: These images show the shell under deformation, at ϵ_{YY} values of (left-to-right) -0.25 , -0.12 and -0.01 . In the highly deformed state (right), the wires are no longer transmitting the force perfectly vertically, and κ_{XX} is no longer uniform in the Y -direction of the shell.

on the corrugations, the changes in lengths can be calculated as ratios of the original lengths, which are measured by ruler.

- (iii) As the first test, but a ruler is used to measure the length of the shell in the Y direction, so that there can be no error from the settling of the cables.

Results and discussion are given in Section 6.2.2.

Finite element simulation

This analysis is developed to mirror the plastic prototype in terms of its material properties and initial geometry, and is performed using the commercially available software package, ABAQUS, as outlined in Section 3.4. However, rather than a shell element 'S4R5', element 'S4' is used, which can handle finite strains, proving necessary for convergence as the corrugations began to flatten out. This implies that there is some non-negligible stretching of the shell.

A Young's modulus for the material of 1.61 GPa is given from tests conducted on samples of the material that had been through the vacuum-forming process, described in Appendix B: these are significant when constitutive relations for the shell are being produced in Chapter 7, but do not matter here. From Rinde (1970), the Poisson ratio $\nu = 0.34$. The thickness of the finite element model is taken to be 0.3 mm, while that of the prototype varies from 0.2 mm to 0.4 mm due to the manufacturing process. Again, this variation in thickness affects stiffness relations but not the geometric properties considered here, as long as the assumption that the shell is thin remains valid. A less robust assumption is that of a linearly elastic behaviour. In practice, the elastic modulus softens at high deformations as the HIPS begins to undergo plastic deformation, crazing, and creep, none of which are included in the finite element simulation.

The shell is rendered as a quarter model using the four-node S4 shell elements, which interpolate independently the positions of the corner nodes and the normal vector to the shell. A large-displacement, geometrically non-linear static analysis is then performed according to the following boundary conditions: the bottom edge is constrained to move in its own plane, which is a stationary plane; the top surface is likewise constrained in plane, but that plane is then displaced upwards. The right-hand edge is free, as in the physical test, but the left edge is subjected to a symmetric boundary condition, since the shell in the finite-element simulation is one quarter of the physical shell. There is no need to apply symmetry conditions to the top or bottom edges: they are each constrained to move in their own plane, and the upper plane is then displaced upwards to stretch the shell.

Figure 6.10 shows the initial and deformed shapes. The vertical displacement of the top edge yields ϵ_{YY} , and the absolute position of the right-hand edge gives the chord length used to calculate κ_{XX} .

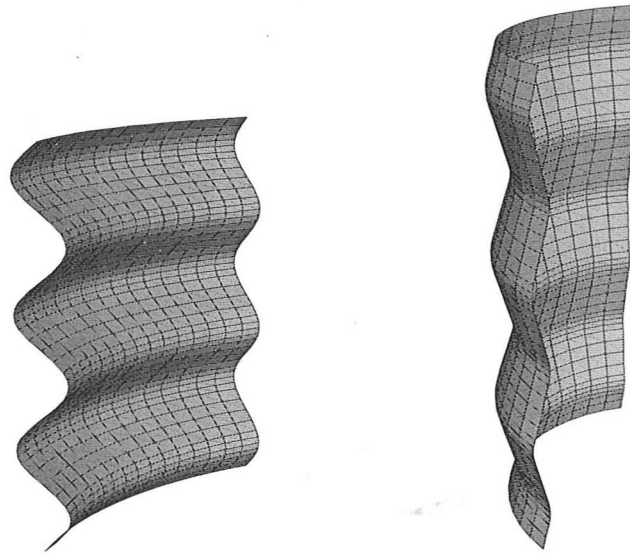


Figure 6.10: Finite element analysis of the shell. On the left is the initial, unstressed form: on the right, the stressed form. The lower edge is constrained not to move out of its plane, but movement within its plane is free. The left-hand edge has a symmetry constraint. The upper edge has an upwards displacement rate applied to it, but is unconstrained in other directions.

Results and discussion

Figure 6.11 presents the analytical results following the numerical integration method described in Section 6.2.1, the finite element analysis output and the measurements from the physical test. In addition, it presents the result for a triangular-wave corrugation, which has the very simple closed-form expression given in Eqn 6.8. This requires the selection of a suitable value of κ_g for the triangular-wave corrugation: the value is chosen so that the curve meets the physical test and FE results at the initial state (*i.e.*, the lowest ϵ_{YY}). Owing to this matching of the initial conditions, it is more sensible to plot the conventional engineering strain of the shell relative to its initial state, rather than the strain, ϵ_{YY} , of mid-surface length to the material length in the corrugations: recall that the relation between ϵ_{YY} and ε_{YY} is given in Eqn 6.7.

The correlation between these results is very good, such that it is hard to distinguish the results, even for the triangular-wave model. Specifically, the finite-element simulation and the unsimplified analytical model agree to within 1 % over most of the range, rising to 2 % error at the highest curvatures: the simplified analytical model is always within 1 % of the finite-element simulation and within 2 % of the unsimplified model. This difference can be accounted for by shell strains: the FE analysis only converges if an element is used that is capable of finite strains, whereas the analytical models assume no shell strains at all.

For 90 % of the test's strain range, all test results are within 4 % of all of the models: at larger deformations, the plastic shells deform a little more than expected due to the

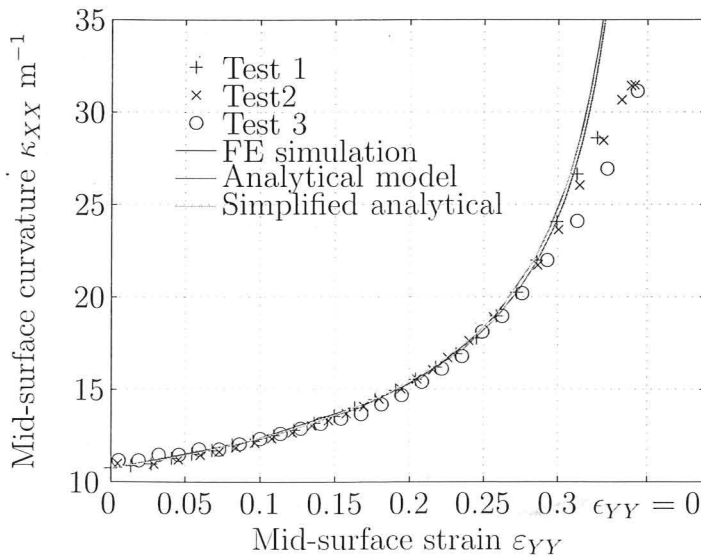


Figure 6.11: Plot of mid-surface curvature κ_{XX} in m^{-1} against mid-surface engineering strain ϵ_{YY} . The test begins at the initial strain and curvature shown at the leftmost edge of the curves, in which state the shell is unstressed. The finite-element simulation and both analytical models take this as their initial point. The FE analysis and the 'exact' analytical expressions begin from a sinusoidal shape at this point, which matches the plastic shell tested: the simplified model assumes a triangular-wave corrugation. The tailing-off of the results at high κ_{XX} corresponds to stretching of the plastic shell.

stretching and possible creeping of the plastic shell. It can be concluded therefore that the assumptions hold well, namely, that:

- (i) the local shell deforms purely in bending: stretching in the material is not significant, as demonstrated by the correlation between the geometric analytical model and the finite element simulation;
- (ii) nonlinearities in the material are not significant, as shown by the correlation between the finite element simulation and physical test;
- (iii) the radius of curvature $1/\kappa_{XX}$ is sufficiently much greater than the amplitude of corrugations; and
- (iv) the relationship between cross-corrugation strain and along-corrugation curvature of an initially triangular-wave corrugation is only negligibly different from that of a sinusoidal corrugation.

In addition, the results validate the methodological assumption, in physical tests, that the long wires do not rotate sufficiently to change the direction of axial force in the wires acting on the sheet, except at very high values of κ_{XX} .

6.3 Bidirectional bending

Section 6.2 has outlined a model of the geometric behaviour of these curved, corrugated shells when they are curved only *along* their corrugations. From that basis, this section develops a model to describe the full morphing behaviour demonstrated in the introduction to this chapter, and compares the resulting model to the behaviour of prototypes. The initial shape, again, has $\kappa_{YY_0} = \kappa_{XY_0} = 0$, but both κ_{YY} and κ_{XY} are now allowed to vary.

6.3.1 Bidirectional bending model

To simplify the analysis, a hypothetical uncorrugated structure is considered whose strains and curvatures match those of the mid-surface of the corrugated shell: in this sense of strain, we initially refer to conventional engineering strain, which is denoted by ε . This section is concerned with physically compatible shape-change rather than with stiffness, and certain stretching/bending strains are defined to be free with effectively zero stiffness and others to be fixed with infinite stiffness.

Since stretching in the X direction or X - Y shear must involve stretching of the membrane, $\varepsilon_{XX} = \varepsilon_{XY} = 0$. In the Y direction, the corrugations can flatten out and cause the homogenised mid-surface to stretch, so ε_{YY} is free. The curvatures, κ_{YY} and κ_{XY} , are also free; κ_{XX} is free but, as noted above in Section 6.2.1, it is coupled to the transverse strain, where both are generally a function of θ and κ_g , as in Eqn 6.11. However, nothing has been said about their relationship to the cross-wise curvature, κ_{YY} , and it is necessary to introduce one simplifying assumption, namely: *the relation between ε_{YY} and κ_{XX} is independent of the variation of κ_{YY}* . This is valid if κ_{YY} has a negligible effect on the corrugation profile, requiring that the radius of curvature $1/\kappa_{YY}$ is significantly greater than the amplitude of the corrugations, as per κ_{XX} .

The Gaussian curvature, K , of a shell is described in Section 3.1.2 as the product of the two principle curvatures κ_1 and κ_2 : as derived by Calladine (1983), it is also equal to the solid angle subtended per unit area of the shell. It can also be defined from the local membrane strains and their spatial rates of change. Calladine (1983, p. 154) derives this relationship for small strains; large strains affect the area over which solid angle is measured, and his equation, when appropriately modified for large strains (as he describes), becomes

$$K = \left[2 \frac{\partial^2 \varepsilon_{XY}}{\partial X \partial Y} - \frac{\partial^2 \varepsilon_{XX}}{\partial Y^2} - \frac{\partial^2 \varepsilon_{YY}}{\partial X^2} \right] (1 + \varepsilon_{XX})^{-1} (1 + \varepsilon_{YY})^{-1} \quad (6.14)$$

Several of these terms have already been defined to be zero. Let's now define our initial configuration, $\epsilon_{YY} = 0$, to have the corrugations completely flattened out, *i.e.*, at $\theta = 0$, $\kappa_{XX} = \text{inf}$. Now, at $\epsilon_{YY} = 0$, $\epsilon_{YY} = 0$: we can then substitute ϵ_{YY} for ϵ_{YY} , and

$$K = -\frac{\partial^2 \epsilon_{YY}}{\partial X^2} (1 + \epsilon_{YY})^{-1} \quad (6.15)$$

From Eqn 6.5, ϵ_{YY} and its derivatives are

$$\epsilon_{YY} = \sin \theta - 1 \quad \frac{\partial \epsilon_{YY}}{\partial X} = \frac{\partial \theta}{\partial X} \cos \theta \quad \frac{\partial^2 \epsilon_{YY}}{\partial X^2} = \frac{\partial^2 \theta}{\partial X^2} \cos \theta - \left(\frac{\partial \theta}{\partial X} \right)^2 \sin \theta \quad (6.16)$$

and substituting these into Eqn 6.15,

$$K = \left(\frac{\partial \theta}{\partial X} \right)^2 - \frac{\partial^2 \theta}{\partial X^2} \cot \theta \quad (6.17)$$

Here, for simplicity, shells with no twist are considered, so that $\kappa_{XY} = 0$; the principal curvatures are κ_{XX} and κ_{YY} , such that

$$K = \kappa_{XX} \kappa_{YY} \quad (6.18)$$

$$\therefore \kappa_{YY} = \kappa_g^{-1} \cot \theta \left[\left(\frac{\partial \theta}{\partial X} \right)^2 - \frac{\partial^2 \theta}{\partial X^2} \cot \theta \right] \quad (6.19)$$

All other bending and stretching strains are zero. Thus, the shape of mid-surface is defined, beginning with $\kappa_g(X, Y)$ and $\theta(X, Y)$. Note that κ_g is a physical property of the model, so that shape change comes through manipulation of θ .

6.3.2 Validation of models of bidirectional bending

This section uses the model of the equivalent mid-surface and compares its results, in a crude fashion, to paper models. These paper models use triangular corrugations, for they are simple to make, and their geodesic curvature is constant over the whole shell, equal, in this case, to 3.5 m^{-1} , or a radius of 28 cm. These paper shells have a square planform of 0.3 m by 0.3 m.

The simplest variation in θ to produce interesting results is a polynomial of order n in the X direction:

$$\theta = \sum_{n=0}^m a_n X^n = a_m X^m + a_{m-1} X^{m-1} + \dots + a_2 X^2 + a_1 X + a_0 \quad (6.20)$$

Figure 6.12 compares the physical models with this mathematical model, using a polynomial for θ of order 2 or less, *i.e.*, $a_n = 0$ for $n > 2$. In other words, this shell has

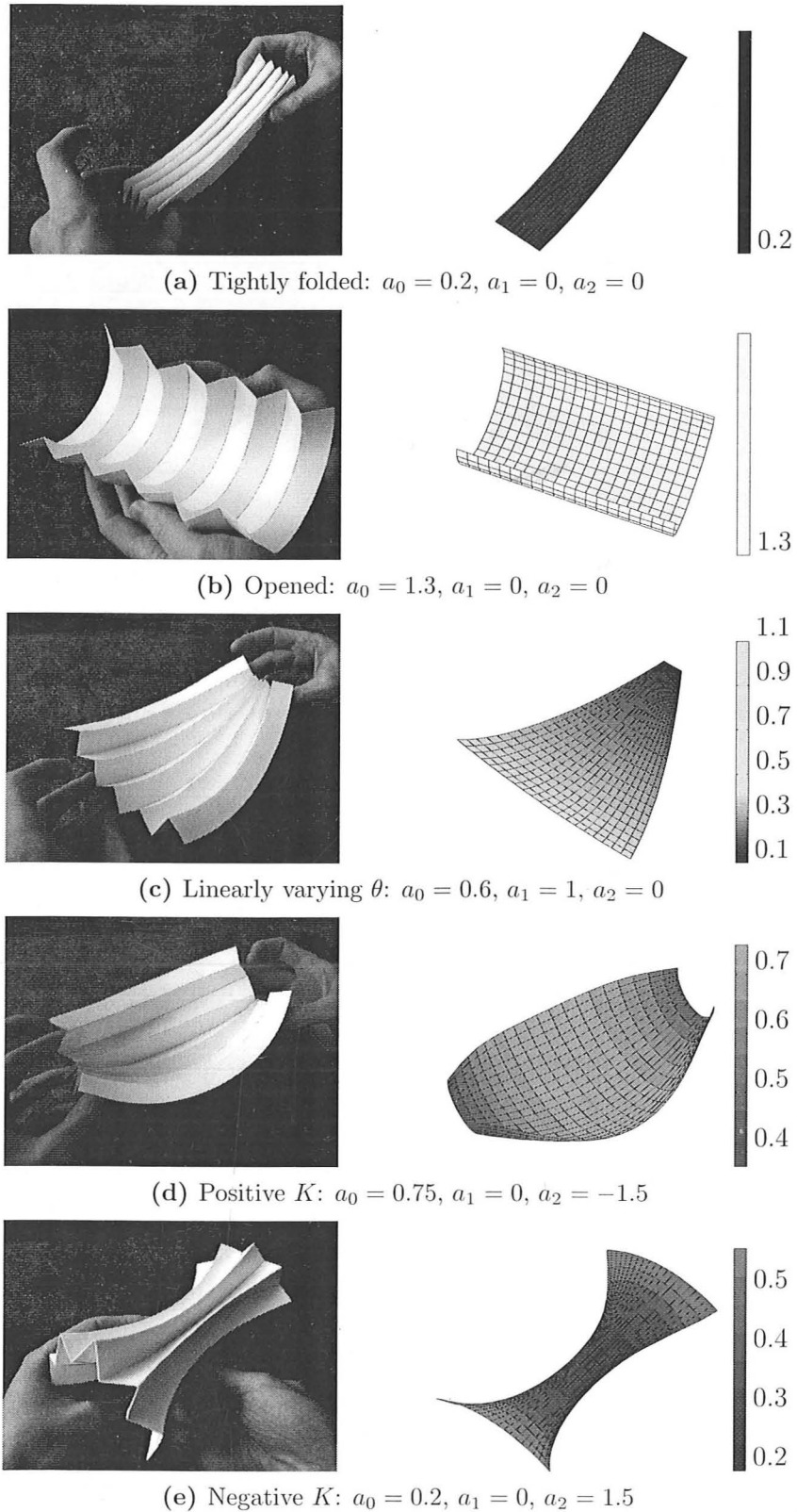


Figure 6.12: Comparison of the physical model (left) to the analytical model (right) with quadratic variation of θ with X , with coefficients a_n as described by Eqn 6.20. These coefficients are chosen by trial and error to match the observed behaviour. They are dimensionless with respect to the length of the shell. On the computer plots, colour denotes the angle θ in radians, as per the colourbars on the right.

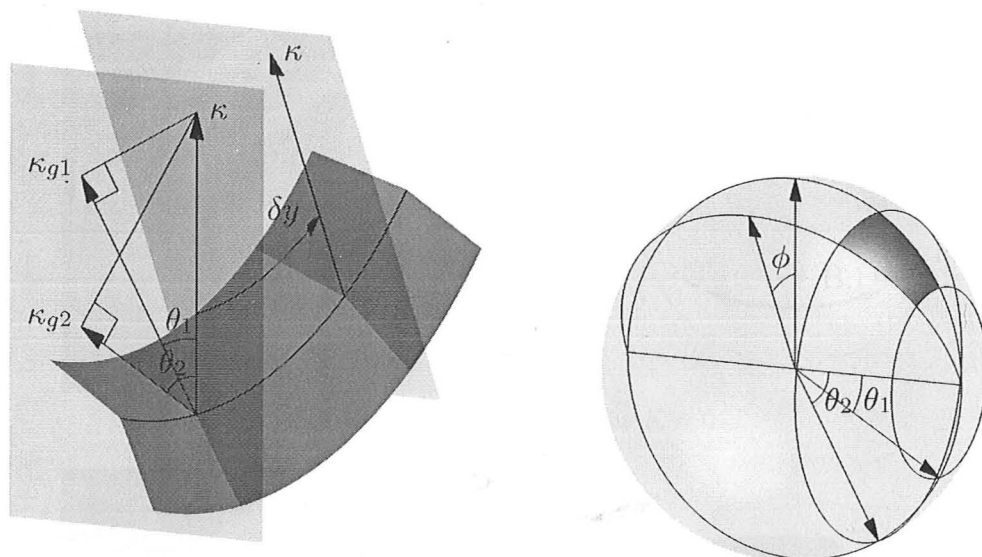


Figure 6.13: The solid angle β subtended by a crease (left), represented as the area that the crease covers on a unit sphere (right, β shaded). The crease is between strips 1 and 2 of geodesic curvatures κ_{g1} and κ_{g2} respectively. The curvature κ of the crease line can be varied, causing the angles θ_1 and θ_2 of the strips to vary. However, as the text shows in Eqns 6.23–6.24, varying κ does *not* affect β , and so the Gaussian curvature of the creased shell is invariant.

the shape properties

$$\theta = a_2 X^2 + a_1 X + a_0 \tag{6.21}$$

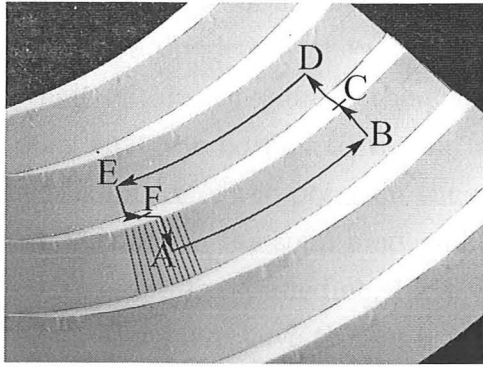
$$K = (2a_2 X + a_1)^2 - 2a_2 \cot \theta \tag{6.22}$$

θ must lie in the range $0 \leq \theta \leq \pi/2$, so $\cot \theta$ is always positive. So, if θ varies linearly ($a_2 = 0$, Fig. 6.12c), its Gaussian curvature, K , must be positive, but a positive a_2 can give negative K .

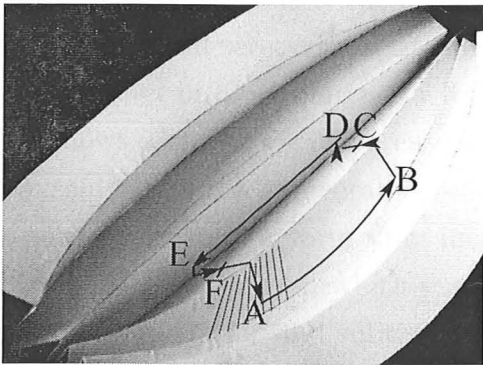
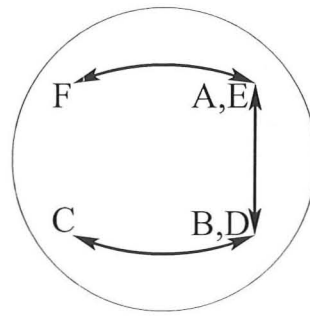
In Fig. 6.12, these equations are used to describe the shape change of a simulated mid-surface, which is compared to the paper shell. Values of a_n are chosen by trial and error such that the surfaces from the simulation match as closely as possible the mid-surfaces of the shell when photographed in various configurations. The agreement is very good, despite the limited specification of θ , and the essential behaviour is captured.

6.3.3 Local Gaussian curvature

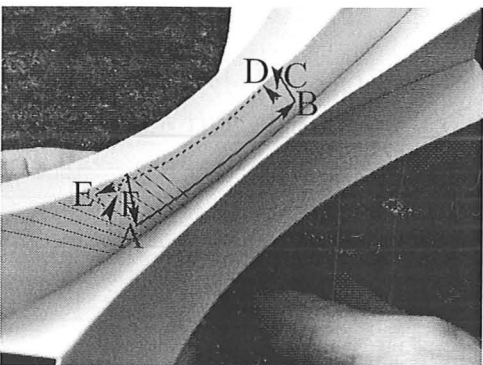
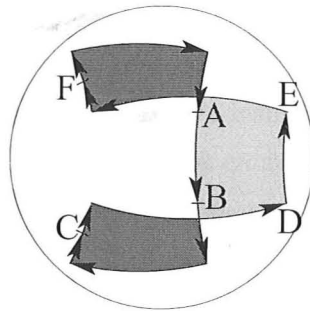
This study has shown how the equivalent mid-surface of the corrugated shell undergoes large transverse strains, leading to large changes in its Gaussian curvature. At the same time, the corrugated shell suffers no extensional strains and therefore, by definition from Gauss' *Theorema Egregium*, no change in the local Gaussian curvature of shell. This section attempts to resolve this apparent paradox.



(a) Homogenised surface has $K = 0$



(b) Homogenised surface has $K > 0$



(c) Homogenised surface has $K < 0$

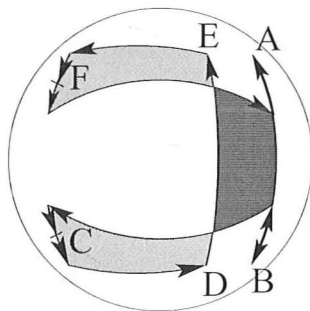


Figure 6.14: Solid angles subtended by regions on the doubly-curved shells. In all cases, the net solid angle is zero, and therefore so is the Gaussian curvature. This is not a mathematical proof, but a graphical demonstration of how the principle of no change in Gaussian curvature for an inextensional shell can hold for this case despite appearances to the contrary.

On the left, faint lines denote lines of zero principle curvature, *i.e.*, lines along which the membrane can be imagined to be hinging: these lines are straight, and therefore each equates to a single point on the unit spheres on the right.

On the right are overhead views of the region mapped onto a unit sphere, which region's area is the solid angle. Positive-area regions are light grey, and negative-areas are dark grey. Curves flowing generally up-down signify movement across the faint 'virtual' hinges, while curves flowing left-right are sections of 'great arcs' and signify moving across the real hinges running along the corrugations.

The Gaussian curvature of a region of a shell can be defined as the solid angle subtended by that region divided by the area of the region. The solid angle stems from the general idea that, within a region of the shell, all points are mapped onto a sphere of unit radius, such that the normal to the surface of the point on the shell is parallel to the normal to the sphere of the point on the sphere. The area covered by the points on the unit sphere is equal to the solid angle subtended by that region of the shell. This is explained in more detail by (Calladine, 1983, chap. 4).

All points on a flat plate have the same normal, and lie on a single point on the unit sphere: so, a flat surface has a solid angle of zero. A developable surface, which can be inextensionally flattened, maps to a line on the sphere so that its area on the sphere, and hence its solid angle, is still zero; correspondingly, the surface can be considered as a plate with an infinite number of hinges aligned with the directions of zero principal curvature.

Figure 6.13 shows a length, δy , of a crease between two strips of geodesic curvature, κ_{g1} and κ_{g2} , where said crease has an overall curvature, κ . The two strips each form a conical section, and, on the unit sphere, form rings inclined at angles θ_1 and θ_2 to the horizontal. The subtended angle of the region which encloses this length of crease is the four-sided shape between these two rings, and subtends an angle of $\phi = \kappa\delta y$. From Section 6.2.1

$$\cos \theta_1 = \frac{\kappa_{g1}}{\kappa} \qquad \cos \theta_2 = \frac{\kappa_{g2}}{\kappa} \qquad (6.23)$$

The subtended angle β and, hence, the area on the unit sphere can be calculated by integrating the area of a ring at θ , equal to $2\pi \cos \theta \, d\theta$, from θ_1 to θ_2 and then taking a proportion $\phi/2\pi$;

$$\begin{aligned} \beta &= \frac{\phi}{2\pi} \int_{\theta_1}^{\theta_2} 2\pi \sin \theta \, d\theta \\ &= \kappa\delta y [-\cos \theta]_{\theta_1}^{\theta_2} \\ &= \kappa\delta y (\cos \theta_1 - \cos \theta_2) \\ &= (\kappa_{g1} - \kappa_{g2}) \delta y \end{aligned} \qquad (6.24)$$

which is completely independent of κ or ψ . So, if the shell deforms inextensionally, the subtended angle β does not change, and so nor does the Gaussian curvature K . With the aid of Fig. 6.14, it is now explained how this result holds true for a surface which *apparently* does undergo an inextensional change in double curvature:

In Fig. 6.14, since each half-corrugation is a developable shell, it is represented by a single line on the unit sphere. The direction of the curvatures of each half-corrugation indicates the direction of zero principal curvature, and therefore the direction of the 'hinges', which are marked on Fig. 6.14. This figure demonstrates how it is that, as the region on the shell subtends some non-zero solid angle due to the Gaussian curvature of

the mid-surface, there is also now some solid angle subtended of the opposite sign, which can cancel out the former. Specifically, in cases of both positive and negative curvature, it shows that a region which subtends a net solid angle of zero in the singly-curved state, Fig. 6.14a, when deformed so that the mid-surface is doubly-curved, can *still* subtend zero net solid angle, and so still have zero Gaussian curvature. This is not a rigorous proof: rather, it merely describes graphically how the Gaussian curvature need not change.

6.4 Conclusions

It is generally known that a shell structure cannot undergo a change in Gaussian curvature without significant stretching of the surface. This true in this case, and the shells in this chapter are, indeed, considered inextensional, and therefore cannot undergo changes of Gaussian curvature. However, the *mid-surface* of a corrugated sheet is *not* inextensional. Accordingly, as shown in this chapter, a corrugated shell with some initial curvature across the corrugations *can* experience very large changes in the Gaussian curvature and shape of its mid-surface. Such behaviour may prove useful in the design of novel morphing surfaces, for it extends the range of kinematical performance to that not obtained with conventional shells. It is important to note that this behaviour depends on the existence of an initial out-of-plane curvature of the corrugated shell, along the line of corrugations. In Chapter 4, this curvature is absent, making the mid-surface initially flat, and the shell is completely developable: therefore, we are justified in the assumption of an *inextensible* mid-surface in Section 4.2.1.

The compact analytical model presented in Section 6.3.1 is applied only to a shell consisting of strips of equal magnitude of geodesic curvature: however, the same model could be applied to a general shell, once that shell is considered as a series of strips of known geodesic curvature. It has been shown that a simpler triangular wave corrugation can provide a reasonably accurate description of the geometric behaviour of shells of a continuous corrugation wave. The next step in this work is a study of the structural mechanics of these shells, and this is the subject of the next chapter.

Chapter 7

Curved corrugated shells (ii): constitutive relations

In Chapter 6, compatibility relations are derived to describe the shape-changing behaviour of curved corrugated shells. It is concerned solely with geometric effects, without equilibrium. For all applications to structural engineering, the stiffness properties are significant, and so this chapter reintroduces these concepts as follows.

Two separate analyses are performed. Firstly, in Section 7.1, a modal analysis evaluates the natural modes of vibration of the shell: the lowest-frequency modes correspond to the least-stiff modes of deformation, which in turn teach us something of how the shell will behave under loading. Secondly, in Section 7.2, full constitutive relations for the averaged mid-surface of the shell are derived from energy equations: these relations are non-linear and apply to large displacements. These constitutive relations mimic the traditional expressions of generalised Hooke's laws for the uniform deformation of a shell element, as in Eqn 3.7. In this case, such an element is considered as larger than the individual corrugations, so that the equivalent mid-surface properties are being considered, but much smaller than the whole shell, so that loads and deformations can be considered uniform across it. Section 7.2.3 is an attempt to verify these relations against finite-element and physical test results, and conclusions for the whole chapter are presented in Section 7.3.

7.1 Modal analysis

This analysis determines the natural modes of vibration of a curved corrugated shell. Since there is a close relationship between the frequency of a modal vibration and the stiffness of the shell in that mode, the results can tell us something about the shell's least-stiff modes of deformation, which is our focus in this section.

For reference, these modes will be compared with a similar analysis of corrugated flat shells and uncorrugated curved shells, so that useful comparisons can be drawn regarding their behaviour. This, it is hoped, will justify the comments on practical behaviour at the beginning of Chapter 6, where it is claimed that curved corrugated shells display radical modes of behaviour that are not otherwise seen. Specifically, we are looking to find that curved, corrugated shells can deform between shapes of positive and negative Gaussian curvature, in a way that is not seen with uncurved *or* uncorrugated shells.

7.1.1 Finite element model

The model is set up using MATLAB to generate the shape of the shell and output the nodal coordinates in the form of an ABAQUS input file. The shells are each designed to be square in the *local* plane: if the corrugations are flattened out, then the length of the shell across the corrugations is equal to the length along the corrugations. This is performed, rather than have an initially square planform, so that all three shells considered here have the same total area of material: also this is consistent with the approach in Chapter 6, where strain ϵ_{YY} across the corrugations is measured relative to the uncorrugated shell. Each shell is divided into ten elements along corrugations: across the corrugations, there are two elements per quarter-corrugation and five corrugations, making a total of 40 elements. Therefore, the corrugated shells each have $40 \times 10 = 400$ elements, and the uncorrugated shell has $10 \times 10 = 100$ elements. All edges are unconstrained.

This is a very small number of elements, *i.e.* a very *unrefined* mesh, if the purpose of this model is to describe accurately the vibration properties of a shell. Particularly, the number of elements may have a significant effect on the frequencies observed, since we expect a mesh of fewer elements to give a greater stiffness. However, our purpose here is merely to demonstrate that the mid-surface exhibits doubly-curved behaviour at low stiffnesses: that our unrefined mesh is artificially stiff even reinforces this point.

The analysis itself is a standard ABAQUS modal analysis. The analysis is set to produce, as output, the first ten modes, of increasing natural frequency. The central node of the shell is pinned, so that rigid-body translations are not possible, but there will still be rigid-body rotational modes, of zero frequency: accordingly, a very small non-zero minimum frequency is specified, so that rigid-body modes of deformation are not counted, as outlined in Section 3.2.3.

The initial, undeformed shapes are shown in Fig. 7.1a. The material properties in the simulation are those of CuBe alloy, rather than HIPS, because, for the sheet thicknesses that we have used, it has a higher ratio of stretching stiffness to bending stiffness. The shell thickness is 0.1 mm, to match that used in many of our prototypes. The shell size is 125 mm \times 125 mm, giving five corrugations of 25 mm wavelength and an initial $\epsilon_{yy} = -0.3$: the corrugation curvatures then have a radius of 2 mm at their tightest.

7.1.2 Natural-mode results

Figures 7.1–7.2 present the first seven natural modes, labelled I–VII, and corresponding frequencies for the three types of shell, and comment upon them. In all three cases, the lowest-frequency natural mode is a twisting mode, seen in Fig. 7.1b. However, while the corrugated and the curved shells have a simple cylindrical curvature for their second-lowest mode, the curved-corrugated shell is doubly-curved, in Fig. 7.1c. Unsurprisingly, the corrugated shell is stiffer, having a higher natural frequency in each mode than the uncorrugated shell: the curved-corrugated shell, which has double curvature, is stiffer than both, especially at Mode II.

From Mode III onwards, most modes are relatively uninteresting, displaying higher-order variants of behaviour already seen in the lower modes. One point of interest is that the folding-up, or flattening-out, of corrugations is at rather higher frequency, and hence stiffness, than several of the modes that curve the sheet across the corrugations: for the flat corrugated sheet, one end is pinched together in Mode VII (Fig. 7.2d), and the whole shell is folded up in Mode X, which is not shown: for the curved corrugated sheet, these are Modes VI and VII. This curved-corrugated Mode VII is the mode where the shell curves in the X - X direction with an expansion in the Y - Y direction, which behaviour is the subject of Section 6.2, above, and Section 7.2.3, below. It is the lowest-frequency mode at which the curvature along the corrugations changes significantly: for the uncurved corrugated sheet, there is no such mode.

Fig. 7.1c shows the curved-corrugated shell deforming into a bowl shape of positive Gaussian curvature. The same mode, with reversed sign, becomes a saddle shape of negative Gaussian curvature: see Fig. 7.3. In other words, natural oscillation at 405 rad s⁻¹ consists of an oscillation between the bowl shape and the saddle shape. For such a curved corrugated sheet, this double curvature can be interpreted thus: the curvature along the corrugations is approximately constant, but the curvature *across* the corrugations oscillates between positive and negative values, so that the Gaussian curvature oscillates similarly. In conclusion, we see that at relatively low frequencies, the curved *and* corrugated sheet does display a behaviour that gives the mid-surface large variations in Gaussian curvature, in a fashion that is not seen in sheets that are merely curved *or* corrugated.

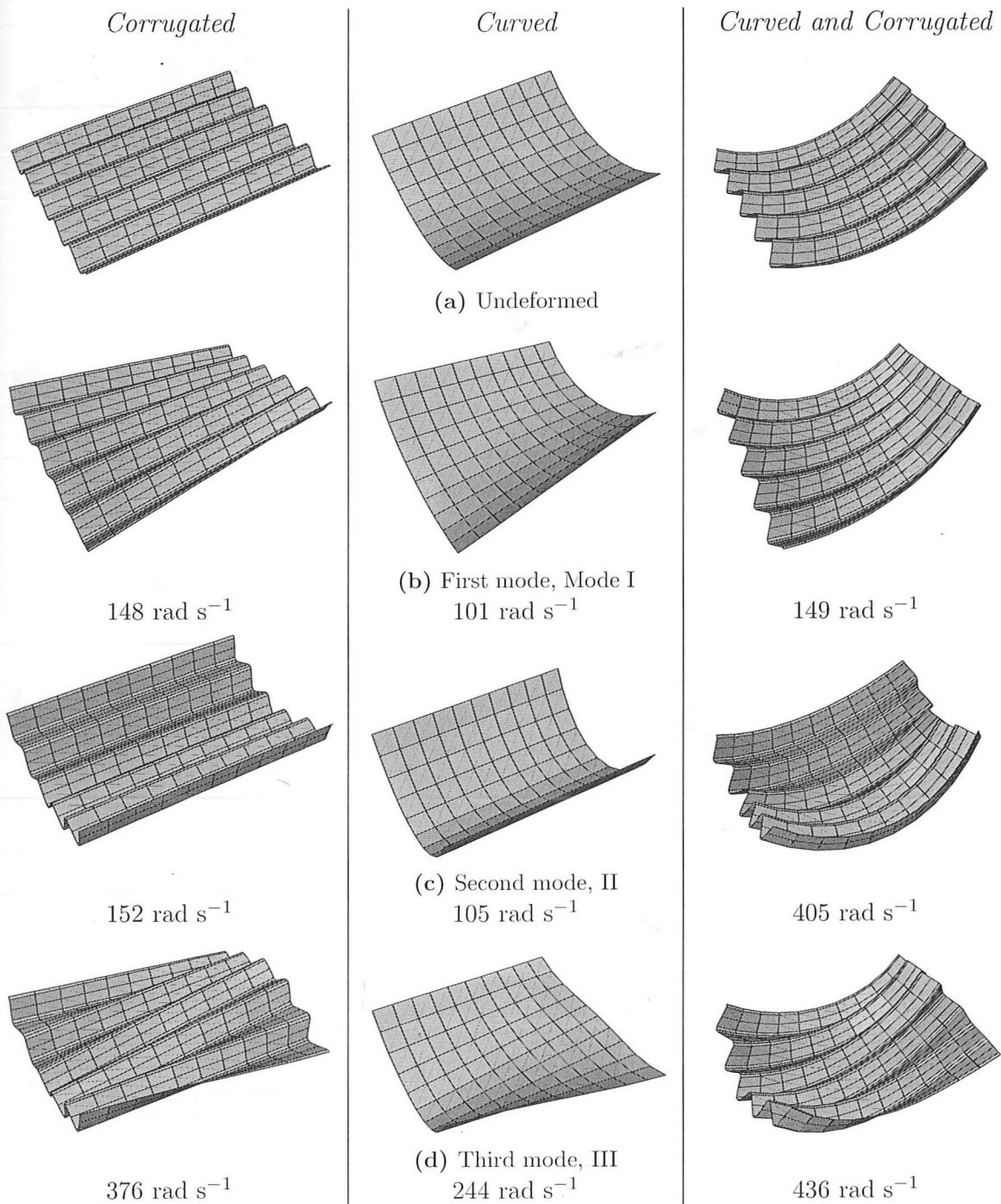


Figure 7.1: Natural modes of vibration (i), with frequencies labelled. In all three cases, the lowest-frequency natural mode, Mode I, is a twisting mode. However, while the corrugated and the curved shells have simple cylindrical curvature for their second-lowest mode, the curved-corrugated shell is doubly-curved: this is discussed further in Fig. 7.3. Further interesting modes appear in Fig. 7.2.

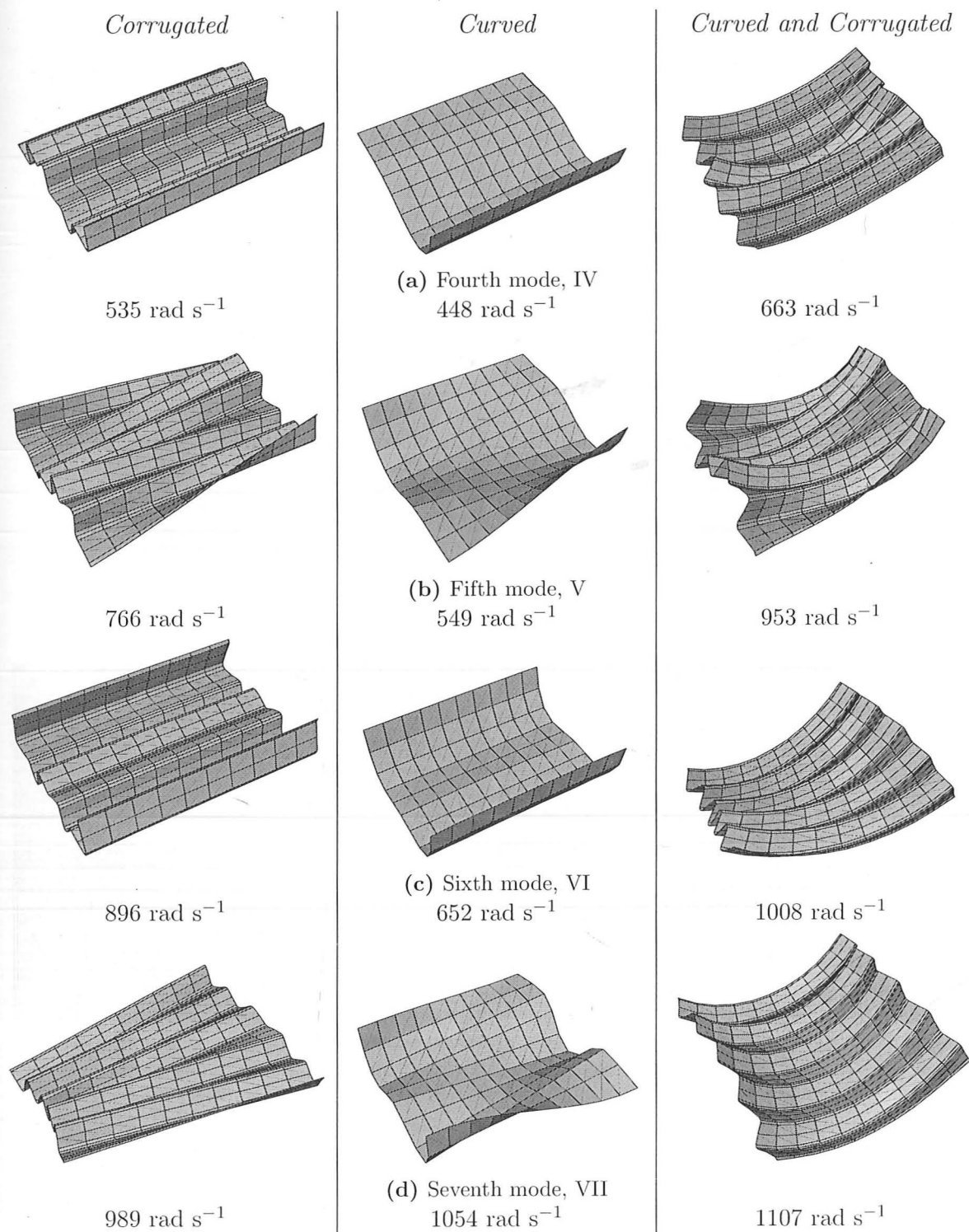
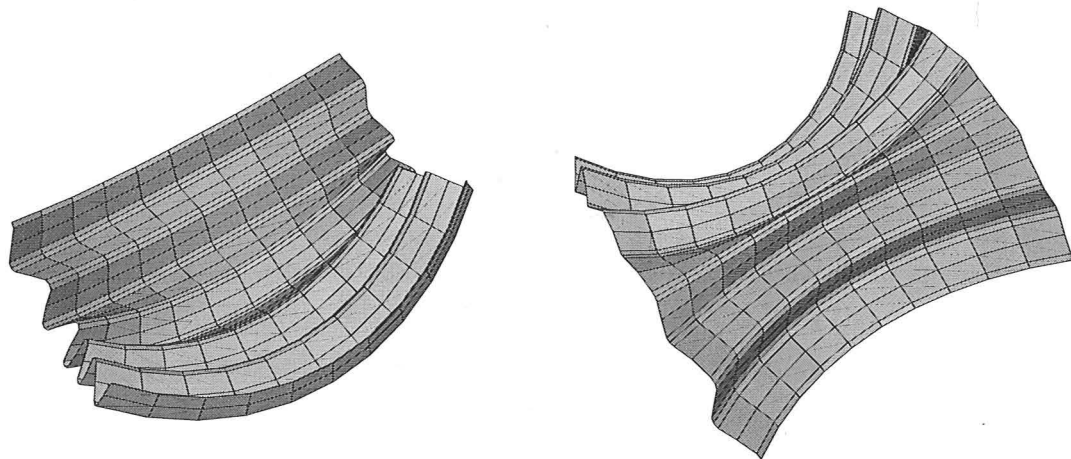
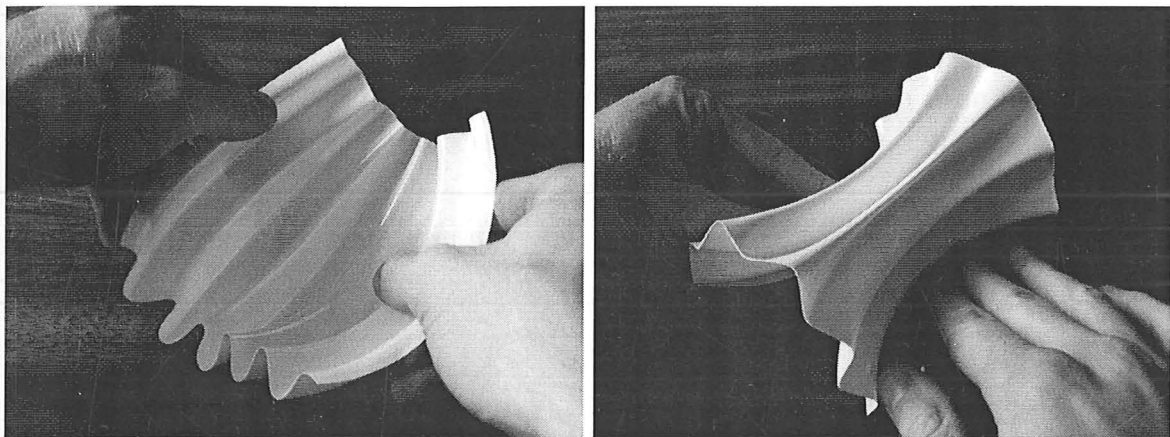


Figure 7.2: Natural modes of vibration (ii), again with frequencies labelled. Of interest here is that the modes corresponding to the folding-up of the corrugations appear at relatively high frequencies: fifth for the curved-corrugated sheet, and sixth for the uncurved-corrugated sheet. The stretching mode shown earlier in Fig. 6.1b appears as Mode VII: an equivalent folding-up of the uncurved-corrugated sheet appears as Mode X, which is not shown here.



(a) The second natural mode of vibration, with positive and negative magnitudes



(b) The plastic prototype, manually deformed

Figure 7.3: Comparison of the doubly-curved modes between the FE model and the prototype. The Mode II natural-frequency oscillation of Fig. 7.1c is an oscillation between these two shapes, and so their frequency is identical: note that the along-corrugation curvature hardly varies, but the cross-corrugation curvature is oscillating between positive and negative values, giving the oscillation in Gaussian curvature.

7.2 Derivation and testing of constitutive relations

In this section, a full set of constitutive relations for the curved corrugated shells is derived algebraically, and a part of these relations is tested against both physical testing and finite-element simulations. These algebraic relations retain the following simplifying assumptions from Chapter 6:

- (i) on a local scale, the shells do not undergo any stretching strains, but only bend; and
- (ii) the depth of the corrugations is negligible with respect to the radius of the curvatures of the shell.

Firstly, in Section 7.2.1, the compatibility relations of Section 6.2.1 are expanded to produce a full set of equations relating the local curvatures, κ_{ij} , to the global curvatures, κ_{IJ} . From this, Section 7.2.2 derives the internal strain energy density as a function of the global curvatures, from which the compatibility equations can be produced.

7.2.1 Curvatures and strains

Referring to the corrugated-sheet coordinate system described in Fig. 6.2, we now introduce $\psi = 90 - \theta$, as the angle between the local and mid-surface coordinate systems: θ was used previously because the shells were being related to the 'locked' state, when $\theta = 0$.

The curvature κ_{xx} is, from Eqn 6.3,

$$\kappa_{xx} = \kappa_{XX} \sin \theta = \kappa_{XX} \cos \psi \quad (7.1)$$

Next, we will look at the relationship between κ_{yy} and κ_{YY} .

An equivalent mid-surface curvature κ_{YY} can be thought of as a change in angle over a distance ΔY of $\Delta Y \kappa_{YY}$. Following the 'local' path along the corrugations, the distance is $\Delta y = (1 + \epsilon_{YY})^{-1} \Delta Y$, but the angle change must be the same. So, the component of local curvature due to the mid-surface curvature is found to be

$$\kappa_{yy} = \frac{\Delta Y \kappa_{YY}}{\Delta y} = \frac{\Delta Y \kappa_{YY}}{\Delta Y (1 + \epsilon_{YY})^{-1}} = (1 + \epsilon_{YY}) \kappa_{YY} \quad (7.2)$$

In practice, as the local surface curves, the corrugation pattern will distort, and the mid-surface may shift. This will cause the relationship between κ_{YY} and κ_{yy} to depend on the corrugation shape, and other factors. However, if we stipulate, as before, that the radius of the applied curvature, κ_{YY}^{-1} , is much larger than the corrugation amplitude or wavelength, the change in the corrugation shape will be very small, and the above relationship holds.

This is only part of κ_{yy} : there is also a curvature due to the corrugations themselves that is equal to $d\psi/dy$, as in Eqn 6.4, so that in total,

$$\kappa_{yy} = (1 + \epsilon_{YY})\kappa_{YY} + \frac{d\psi}{dy} \quad (7.3)$$

Twist κ_{XY} is unaffected by the strain ϵ_{YY} , as noted by Briassoulis (1986), and so we can produce a complete set of equations relating local to mid-surface curvatures, including also the curvatures of the corrugations themselves:

$$\kappa_{xx} = \kappa_{XX} \cos \psi \quad (7.4)$$

$$\kappa_{yy} = \kappa_{YY}(1 + \epsilon_{YY}) + \frac{d\psi}{dy} \quad (7.5)$$

$$\kappa_{xy} = \kappa_{XY} \quad (7.6)$$

These equations are of limited use, since they are functions of ψ , which changes as the shell deforms. It is far more useful to arrange them in terms of κ_g , since the variation of κ_g across the corrugations is fixed during manufacture and is therefore constant during deformation. From Eqn 6.6,

$$\sin \psi = \frac{\kappa_g}{\kappa_{XX}} \quad (7.7)$$

and thus

$$\cos \psi = \sqrt{1 - \left(\frac{\kappa_g}{\kappa_{XX}}\right)^2} \quad (7.8)$$

We can find the derivative of ψ with respect to y as a function of κ_g using Eqn 7.7, whereby

$$\frac{d\psi}{dy} = \sec \psi \frac{d}{dy} (\sin \psi) = \frac{1}{\kappa_{XX} \cos \psi} \frac{d\kappa_g}{dy} = \frac{d\kappa_g}{dy} (\kappa_{XX}^2 - \kappa_g^2)^{-\frac{1}{2}} \quad (7.9)$$

Substituting Eqns 7.8 and 7.9 into Eqns 7.4–7.6, we find the local curvatures, κ_{ij} , as functions of the curvatures of a shell equivalent to the mid-surface of the corrugated sheet, κ_{IJ} , and the geodesic curvature of the corrugated sheet, $\kappa_g(y)$:

$$\kappa_{xx} = (\kappa_{XX}^2 - \kappa_g^2)^{\frac{1}{2}} \quad (7.10)$$

$$\kappa_{yy} = \kappa_{YY}(1 + \epsilon_{YY}) + \frac{d\kappa_g}{dy} (\kappa_{XX}^2 - \kappa_g^2)^{-\frac{1}{2}} \quad (7.11)$$

$$\kappa_{xy} = \kappa_{XY} \quad (7.12)$$

7.2.2 Stiffness

For linear, small-deflection analysis of shells, the constitutive equations can be derived from equilibrium alone. However, in this case, there is large coupling between stretching ϵ_{YY} and bending κ_{XX} . Such a deformation can be caused either by a tension per unit length, N_{YY} , or a bending moment per unit length, M_{XX} , or by some combination of the two: this system is statically indeterminate, in that more than one set of stresses could satisfy equilibrium.

We are left, then, with energy as a means to find the forces acting on the shell, as follows. For any deformation, the elastic strain energy density relative to a predefined initial state can be calculated as a single value. Then, the rate of change of this energy density with a specific deformation will be the force, or moment, acting in the direction of that deformation: in other words, the forces and moments are the partial derivatives of energy with respect to the relevant deformations.

The local shell is a linear isotropic shell, and therefore obeys the conventional relationship of energy to the change in curvatures from the initial state, as defined earlier by Eqn 3.11:

$$U = \frac{1}{2}D [(\Delta\kappa_{xx})^2 + (\Delta\kappa_{yy})^2 + 2\nu\Delta\kappa_{xx}\Delta\kappa_{yy} + 2(1-\nu)(\Delta\kappa_{xy})^2] \quad (7.13)$$

The curvature changes here must be related to the curvatures of the equivalent mid-surface, which, from Section 7.2.1, are

$$\Delta\kappa_{xx} = (\kappa_{XX}^2 - \kappa_g^2)^{\frac{1}{2}} - (\kappa_{XX_0}^2 - \kappa_g^2)^{\frac{1}{2}} \quad (7.14)$$

$$\Delta\kappa_{yy} = \kappa_{YY}(1 + \epsilon_{YY}) - \kappa_{YY_0}(1 + \epsilon_{YY_0}) + \frac{d\kappa_g}{dy} \left[(\kappa_{XX}^2 - \kappa_g^2)^{-\frac{1}{2}} - (\kappa_{XX_0}^2 - \kappa_g^2)^{-\frac{1}{2}} \right] \quad (7.15)$$

$$\Delta\kappa_{xy} = \kappa_{XY} - \kappa_{XY_0} \quad (7.16)$$

where, as before, Δ denotes the change from an initial unstressed state, which state is denoted by subscript 0.

The above equations define the strain energy density in terms of the curvatures of the shell. We define an incremental change in strain energy density in terms of the moments applied and the changes in curvature in the following equation. Since we are developing a homogenised model of shell behaviour, we are interested in the equivalent mid-surface moments, M_{XX} , M_{YY} and M_{XY} . For incremental changes in the curvatures $\delta\kappa_{ij}$, the incremental change in energy δU is given by

$$\delta U = M_{XX}\delta\kappa_{XX} + M_{YY}\delta\kappa_{YY} + 2M_{XY}\delta\kappa_{XY} + N_{YY}\delta\epsilon_{YY} \quad (7.17)$$

Taking partial derivatives of U from Eqns 7.13 and 7.17 gives a set of three equations for

our three unknown moments, in terms of the curvatures and N_{YY} :

$$\begin{aligned}
 \frac{\partial U}{\partial \kappa_{XX}} &= M_{XX} + N_{YY} \frac{d\epsilon_{YY}}{d\kappa_{XX}} \\
 &= D \left\{ \Delta \kappa_{xx} \frac{\partial \Delta \kappa_{xx}}{\partial \kappa_{XX}} + \Delta \kappa_{yy} \frac{\partial \Delta \kappa_{yy}}{\partial \kappa_{XX}} \right. \\
 &\quad \left. + \nu \left[\Delta \kappa_{xx} \frac{\partial \Delta \kappa_{yy}}{\partial \kappa_{XX}} + \Delta \kappa_{yy} \frac{\partial \Delta \kappa_{xx}}{\partial \kappa_{XX}} \right] \right\} \\
 &= D \left\{ \kappa_{XX} - \kappa_{XX} (\kappa_{XX_0}^2 - \kappa_g^2)^{\frac{1}{2}} (\kappa_{XX}^2 - \kappa_g^2)^{-\frac{1}{2}} \right. \\
 &\quad + [\kappa_{YY}(1 + \epsilon_{YY}) - \kappa_{YY_0}(1 + \epsilon_{YY_0})] \left[\kappa_{YY} \frac{d\epsilon_{YY}}{d\kappa_{XX}} - \kappa_{XX} \frac{d\kappa_g}{dy} (\kappa_{XX}^2 - \kappa_g^2)^{-\frac{3}{2}} \right] \\
 &\quad + \frac{d\kappa_g}{dy} \left[(\kappa_{XX}^2 - \kappa_g^2)^{-\frac{1}{2}} - (\kappa_{XX_0}^2 - \kappa_g^2)^{-\frac{1}{2}} \right] \left[\kappa_{YY} \frac{d\epsilon_{YY}}{d\kappa_{XX}} - \kappa_{XX} \frac{d\kappa_g}{dy} (\kappa_{XX}^2 - \kappa_g^2)^{-\frac{3}{2}} \right] \\
 &\quad + \nu \left[(\kappa_{XX}^2 - \kappa_g^2)^{\frac{1}{2}} - (\kappa_{XX_0}^2 - \kappa_g^2)^{\frac{1}{2}} \right] \left[\kappa_{YY} \frac{d\epsilon_{YY}}{d\kappa_{XX}} - \kappa_{XX} \frac{d\kappa_g}{dy} (\kappa_{XX}^2 - \kappa_g^2)^{-\frac{3}{2}} \right] \\
 &\quad + \nu [\kappa_{YY}(1 + \epsilon_{YY}) - \kappa_{YY_0}(1 + \epsilon_{YY_0})] \kappa_{XX} (\kappa_{XX}^2 - \kappa_g^2)^{-\frac{1}{2}} \\
 &\quad \left. + \nu \frac{d\kappa_g}{dy} \left[(\kappa_{XX}^2 - \kappa_g^2)^{-\frac{1}{2}} - (\kappa_{XX_0}^2 - \kappa_g^2)^{-\frac{1}{2}} \right] \kappa_{XX} (\kappa_{XX}^2 - \kappa_g^2)^{-\frac{1}{2}} \right\} \quad (7.18)
 \end{aligned}$$

$$\begin{aligned}
 \frac{\partial U}{\partial \kappa_{YY}} &= M_{YY} \\
 &= D \left\{ \Delta \kappa_{yy} \frac{\partial \Delta \kappa_{yy}}{\partial \kappa_{YY}} + \nu \Delta \kappa_{xx} \frac{\partial \Delta \kappa_{yy}}{\partial \kappa_{YY}} \right\} \\
 &= D (1 + \epsilon_{YY}) \{ \kappa_{YY}(1 + \epsilon_{YY}) - \kappa_{YY_0}(1 + \epsilon_{YY_0}) \\
 &\quad + \frac{d\kappa_g}{dy} \left[(\kappa_{XX}^2 - \kappa_g^2)^{-\frac{1}{2}} - (\kappa_{XX_0}^2 - \kappa_g^2)^{-\frac{1}{2}} \right] \\
 &\quad + \nu \left[(\kappa_{XX}^2 - \kappa_g^2)^{\frac{1}{2}} - (\kappa_{XX_0}^2 - \kappa_g^2)^{\frac{1}{2}} \right] \} \quad (7.19)
 \end{aligned}$$

$$\begin{aligned}
 \frac{\partial U}{\partial \kappa_{XY}} &= 2M_{XY} \\
 &= D \left\{ 2(1 - \nu) \Delta \kappa_{xy} \frac{\partial \Delta \kappa_{xy}}{\partial \kappa_{XY}} \right\} \\
 &= 2D(1 - \nu) (\kappa_{XY} - \kappa_{XY_0}) \quad (7.20)
 \end{aligned}$$

Since these are equivalent mid-surface properties, they must be averaged across a corrugation (*i.e.*, in the y -direction), to give the mid-surface moments. The only component of Eqns 7.18–7.20 that varies over the shell is κ_g . The powers of $(\kappa_{XX}^2 - \kappa_g^2)$ are powers of $\cos \psi$, and since ψ oscillates about 0, these terms average to a non-zero value. However, since κ_g itself varies with $\sin \psi$ and so averages to zero across a corrugation, its derivative $d\kappa_g/dy$ also averages to zero, but the square of said derivative does not. Thus, we are left with a complete set of constitutive equations for the equivalent mid-surface of the shell,

where an overbar denotes average:

$$\begin{aligned}
 M_{XX} = D \left\{ \overline{\kappa_{XX} \Delta \kappa_{xx} (\kappa_{XX}^2 - \kappa_g^2)^{-\frac{1}{2}} + [\kappa_{YY}(1 + \epsilon_{YY}) - \kappa_{YY_0}(1 + \epsilon_{YY_0})] \kappa_{YY} \frac{d\epsilon_{YY}}{d\kappa_{XX}}} \right. \\
 \left. - \kappa_{XX} \left(\frac{d\kappa_g}{dy} \right)^2 \overline{\Delta \kappa_{xx} (\kappa_{XX}^2 - \kappa_g^2)^{-\frac{3}{2}} + \nu \overline{\Delta \kappa_{xx} \kappa_{YY} \frac{d\epsilon_{YY}}{d\kappa_{XX}}}} \right. \\
 \left. + \nu (\kappa_{XX}^2 - \kappa_g^2)^{-\frac{1}{2}} [\kappa_{YY}(1 + \epsilon_{YY}) - \kappa_{YY_0}(1 + \epsilon_{YY_0})] \kappa_{XX} \right\} - N_{YY} \frac{d\epsilon_{YY}}{d\kappa_{XX}} \quad (7.21)
 \end{aligned}$$

$$M_{YY} = D(1 + \epsilon_{YY}) \{ \kappa_{YY}(1 + \epsilon_{YY}) - \kappa_{YY_0}(1 + \epsilon_{YY_0}) + \nu \overline{\Delta \kappa_{xx}} \} \quad (7.22)$$

$$M_{XY} = D(1 - \nu) (\kappa_{XY} - \kappa_{XY_0}) \quad (7.23)$$

with the average of a term, $f(y)$, being calculated as

$$\overline{f(y)} = \frac{1}{\lambda} \int_0^\lambda f(y) dy \quad (7.24)$$

where λ is the material corrugation wavelength. In the rest of this chapter, these averages are calculated by numerical integration.

For the compatibility relations, it is found in Chapter 6 that an approximation to a triangular-wave corrugation simplifies the equations: it trivialises the integrations, since the magnitude of κ_g becomes constant over the shell, and yet produces a usefully accurate result. However, for constitutive relations, the resulting discontinuities when κ_g flips direction create infinite derivatives $d\kappa_g/dy$, so that the averages of Eqn 7.21 are themselves infinite. The triangular-wave approximation cannot, then, be so simply applied to the constitutive relations. Specifically, the problem relates to the corrugation-profile curvatures, and the associated elastic strain energy as the corrugations are deformed.

It may be feasible to use a triangular-wave approximation where possible, combined with some alternative function $\kappa_g(y)$ where necessary: however, attempts so far have not found such a model that accurately imitates the behaviour of a sinusoidal corrugation. The triangular-wave approximation results in a constant magnitude of κ_g , and is perfectly close enough to usefully simplify, without reducing the accuracy of, the terms considering only $\Delta \kappa_{xx}$ in Eqns 7.21–7.22, which terms relate purely to the curvature of the local shell along the corrugations, *without* considering curvature across the corrugations. Briassoulis (1986) considers the stiffness of a corrugated sheet across the corrugations, and produces a convenient simplified model in the first appendix of that paper: that model considers *only* curvature across the corrugations. However, Eqn 7.21 contains a term that multiplies the cross-corrugation curvature, or rather, the $d\kappa_g/dy$ derived from it, with the change in along-corrugation curvature, $\Delta \kappa_{xx}$: it is in this term that a straightforward combination of the two simplified models proves unsatisfactory.

7.2.3 Testing of constitutive relations

The principal challenge to any testing of the constitutive relations derived above is that the shells described in this chapter cannot, under any loadings, be flattened out. Therefore, over a shell of finite size, all deformation components are coupled, so that it is impossible to produce tests to verify the stiffness components of Section 7.2 individually, with just one exception: the relationship between ϵ_{YY} and N_{YY} .

In Section 6.2.2, a test has already been performed that loads the shell across the corrugations and measures the strain, keeping all other loads zero. Exactly the same test, and exactly the same finite-element analysis, produces the results in this section: both the finite-element analysis and the physical test already produce data for the applied load.

For the finite-element simulation and for the algebraic model described in Section 7.2.2, we need three shell properties: the Poisson's ratio, the Young's modulus and the shell thickness. The Poisson ratio and Young's modulus are given in Section 6.2.2. The shell thickness varies slightly over the shell due to the nature of the vacuum-forming process, but averages to be 0.30 mm.

The limitation of this is that the HIPS does not behave in the linear-elastic fashion of the finite-element or algebraic models. Crucially, it has a strong creep effect, so that the rate of loading is significant: the rate is set so as to give approximately the same test duration as the material tests of Appendix B, which results in the same rate of loading, 1 mm s^{-1} . This is particularly noticeable in Test 1, in the results of Fig. 7.4. This test was one of those run in Section 6.2.2, and the test was repeatedly stopped for measurement of κ_{XX} . Each of these pauses in the test is identifiable as a drop in N_{YY} as the material crept.

Looking at Fig. 7.4, there is very strong correlation between the algebraic and FE analyses. This is reassuring, since they share a model of the material. There are three principal differences that can explain the discrepancies:

- (i) the algebraic model assumes that the polymer does not undergo any in-plane strain at all, unlike the FE model;
- (ii) the algebraic model assumes that the depth of the corrugations is negligible compared to the radius of curvature of κ_{XX} ; and
- (iii) the FE model is, of course, a numerical approximation, dividing the shell into a relatively small number of discrete and simple elements, as shown in Fig. 6.10: the algebraic model, too, involves a numerical integration across the corrugations.

Items (i) and (ii) are the two principle simplifying assumptions on which the model is built: that they make so little difference to the result of Fig. 7.4 implies that they are justified.

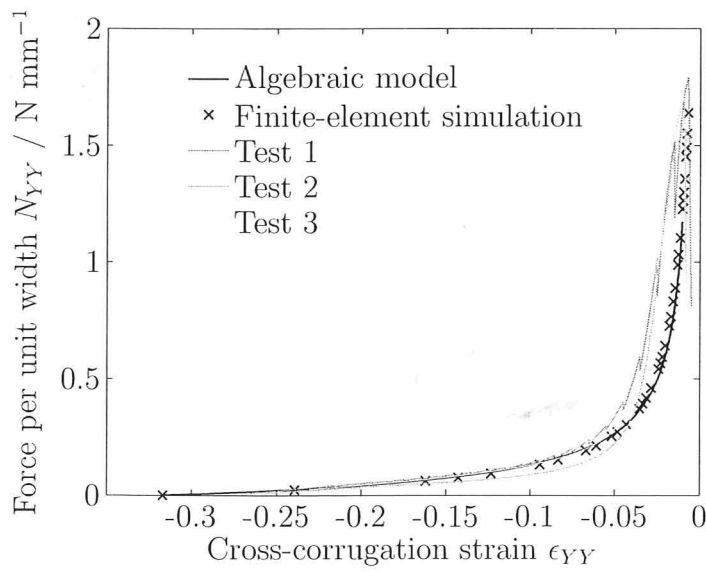


Figure 7.4: $N_{YY}-\epsilon_{YY}$ plot, comparing physical tests to analyses. The analyses assume a linear-elastic material, which HIPS is not. Test 1 was paused numerous times, and demonstrates drops at each occasion as the stresses relax over time due to creep.

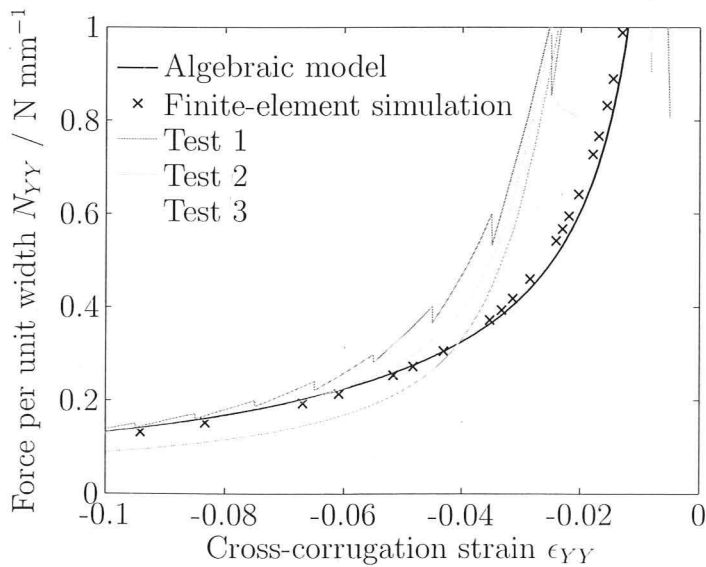


Figure 7.5: Close-up of the $N_{YY}-\epsilon_{YY}$ plot in Fig. 7.4

Comparing the theoretical models with the test results, there is a strong qualitative similarity, but anything otherwise would be surprising. In the early stages of the test, there is a good correlation for two of the three tests, as the corrugations expand significantly and the curvature κ_{XX} increases slowly. However, later, κ_{XX} increases more dramatically as the corrugations become significantly flattened, as shown in Fig. 6.11: the force is then significantly higher than predicted. Fig. 7.5 is a closer view of the region in which the tests begin to differ more from the predictive models. Fig. 6.11 shows the curvature κ_{XX} falling away from the strain at these loads, implying that the shell is stretching but not curving as far as it should. The relation between these two was derived from compatibility in Section 6.2, and so it appears that some stretching of the material must be occurring: this may account for the dramatic increase in N_{YY} above the prediction.

7.3 Conclusions

Chapter 6 established that large changes of shape seem to be possible for curved, corrugated shells, *without* any significant strain in the material, thereby implying that large changes of shape are possible with relatively low forces and without the risk of plastic deformation in the material. This was supported by the behaviour of physical prototypes. In this chapter, Section 7.1 performs a modal analysis, to find the least-stiff modes of deformation of a finite shell. Within the seven lowest-stiffness natural modes are found all of the interesting behavioural features outlined in Chapter 6: this strongly supports the above implication.

Having established that this behaviour is feasible, Section 7.2 produces a set of constitutive relations for these shells, considering them as an equivalent mid-surface, and relating the moments and forces applied to this mid-surface to its curvatures and strains. In the process, some simplifying assumptions are carried over from Chapter 6, specifically, that the corrugation depth is much smaller than the radii of the curvatures of the mid-surface, and that the material of the shell deforms purely in bending, never stretching. The constitutive relations are easily produced from these assumptions, *but* they are found to be strongly non-linear and difficult to simplify further.

Finally, an attempt is made in Section 7.2.3 to verify the constitutive relations by comparing them with physical tests and with finite-element simulations. The latter succeeds in showing a very strong correlation for one particular deformation: the physical tests show a greater discrepancy. However, this is partly due to the inadequacy of our simple material model for the polymer used in physical prototypes. It would be informative to repeat the test with a CuBe shell, which is much harder, and does not display creep. However, manufacturing such a shell from a flat CuBe sheet involves imposing double curvatures, involving large in-plane strains, which poses severe practical challenges for small-volume manufacture.

Chapter 8

Doubly-corrugated shells

The use of doubly-curved shells as morphing structures follows on naturally from the work on singly-corrugated shells in Chapters 4–7. However, it opens up the field into more directions than this thesis has time to cover, and so it is being pursued by other researchers at Cambridge University. One is measuring the stiffnesses experimentally and performing finite-element simulations; another is focussing on a modal analysis, and Section 8.2.1 replicates some of his results from identical concepts but using a markedly different methodology.

In Section 8.1, models are constructed from two very different materials, using very different manufacturing methods. Their behaviour is studied, and found to be very similar, as is that of an eggbox and a comparatively irregular sweet-tray, and therefore general conclusions are drawn about the compliant properties of doubly-corrugated shells. Section 8.2 applies a modal analysis to these shells, in order to compare the lowest-frequency natural modes of the shell with the apparent lowest-stiffness modes of deformation found in Section 8.1. Finally, conclusions are drawn in Section 8.3.

8.1 Physical models

Two forms of prototype are produced: in Section 8.1.1, paper models, and in Section 8.1.2, HIPS models. In both cases, the qualitative behaviour in shape change is described. In Section 8.1.3, two doubly-corrugated trays from everyday use are briefly studied and compared with the prototypes, and Section 8.1.4 summarises what is learnt from the various shells.

8.1.1 Paper models

Triangular-wave paper models are easy to make, and this section will demonstrate that they exhibit all of the interesting behaviours of the more complex, curved shapes in Section 8.1.2.

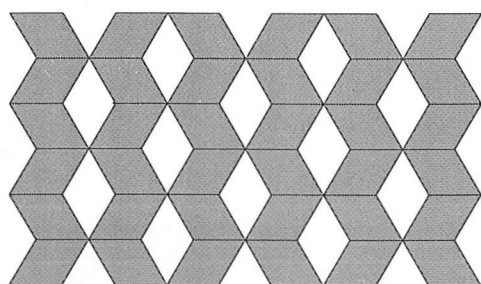
Manufacture

Figure 8.1 shows how the models can be constructed from the series of zig-zag paper strips of Fig. 8.1a. When adjacent edges are joined together, the shape in Fig. 8.1b is produced. This model has, as a doubly-corrugated shell must, a series of alternating peaks, troughs and saddle points: the peaks and troughs are regions of positive double curvature, the saddles regions of negative double curvature.

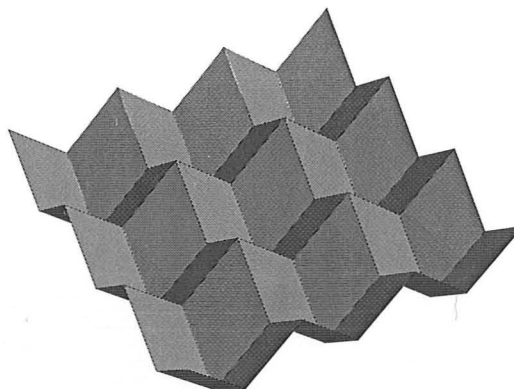
Section 6.3.3 describes how the double curvature is related to the *solid angle* subtended by a unit area. Calladine (1983) demonstrates how, for a shell composed of flat plates, the solid angle subtended by a vertex is exactly the *angular defect* at that vertex: if the angles of the corners of the plates meeting at that vertex are summed, the angular defect is the amount by which that sum is less than 360° . If these angles exactly add up to 360° , the sheet must be flat or cylindrically curved, and the Gaussian curvature, $K = 0$; if they add up to less than 360° , there is a positive defect and hence a positive Gaussian curvature, producing the peaks and troughs of Fig. 8.1b; and if they add up to more than 360° , there is a negative defect and hence a negative K , producing the saddle points of Fig. 8.1b.

In fact, producing a model as outlined above will produce a behaviour that is inconsistent between the two principle directions: if, for example, the strips are taped together, then in one direction, the stiffness of the shell is controlled by that of the tape, and in the other, that of folded paper. Therefore, a more complex method is employed here. A shell is constructed from two layers of paper strips, running in orthogonal directions, to create a uniform effect over the entire shell. There are two ways to do this:

- (i) the strips are woven together. This is difficult to produce neatly, and the two surfaces are best joined with glue: double-sided tape would require many small, rhomboid pieces, which would take an unfeasibly long time to produce; or



(a) The net for the paper model, shaded grey and laid flat. Evidently, joining adjacent edges together will force the sheet into a three-dimensional shape.



(b) A perspective view of the assembled shell

Figure 8.1: The net (left), and the completed doubly-corrugated paper model made from it (right). Where a vertex is made from paper angles adding up to less than 360° , a peak or trough is created (positive double curvature): where the paper angles at a vertex add up to more than 360° , a saddle is created.

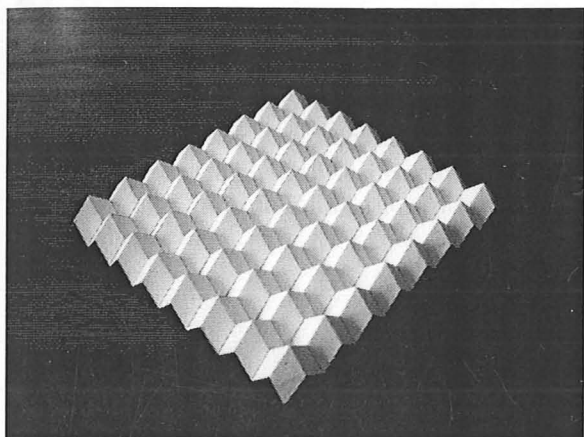
- (ii) the strips are *not* woven together, with, for example, X -wise strips above and Y -wise strips below. This is much easier to produce, and can be assembled more easily with double-sided tape, since one side of each strip is completely covered in tape. The disadvantage is that this is an antisymmetric layup, which will produce some antisymmetry in the stiffness properties.

This shell is intended to demonstrate general principles of behaviour, and will not be used to measure precise stiffnesses. Therefore, it is decided to use the second, simpler method.

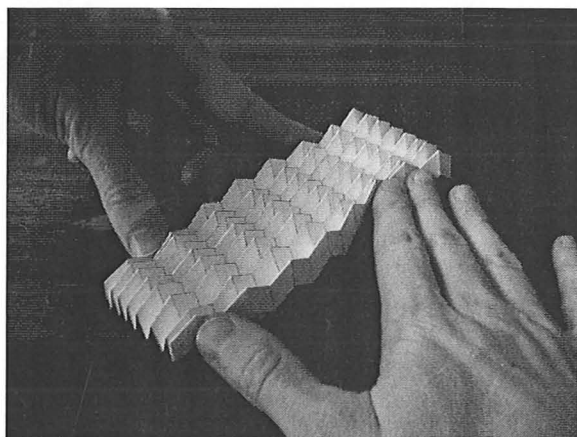
Behaviour

Figure 8.2a shows the paper shell at rest. Considering the behaviour of the mid-surface of the shell, it is capable of large changes of in-plane strains, as shown in Fig. 8.2b: large rates of change of in-plane strains are necessary to give large changes in the Gaussian curvature of a shell. These strains involve a positive-Poisson-ratio effect: as, for example, it is compressed in the X -direction, so it must expand in the Y -direction. However, this behaviour is dependant on the direction of the strain: the shell is much stiffer at 45° to the corrugations. In other words, the shell is rigid in in-plane shear, despite its lack of rigidity in in-plane tension along the corrugations. If our coordinate system is rotated by 45° , this becomes a system that is rigid in stretch but freely shears.

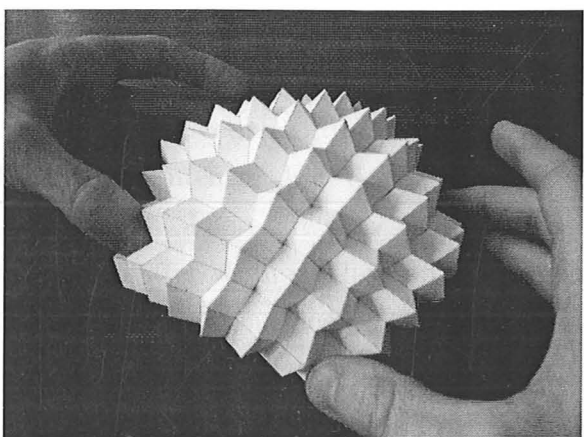
In curvature, the shell behaves more akin to a shell with a negative Poisson ratio. As it is curved in the X direction, it must take on a curvature of the same sense in the Y direction, producing a bowl shape as shown in Fig. 8.2c. In Fig. 8.2c, the two curvatures



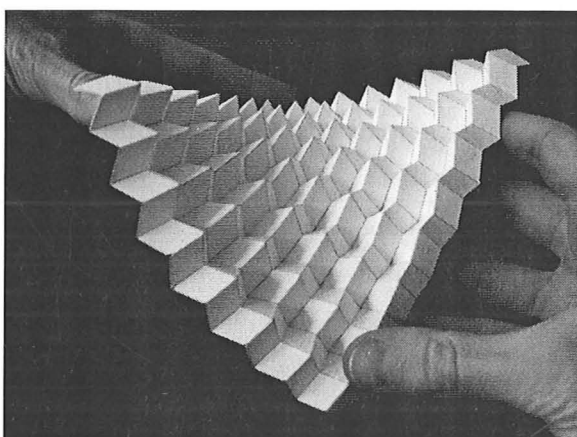
(a) The initial shape, unstressed



(b) Large compressive and tensile strains are possible (the two are coupled together).

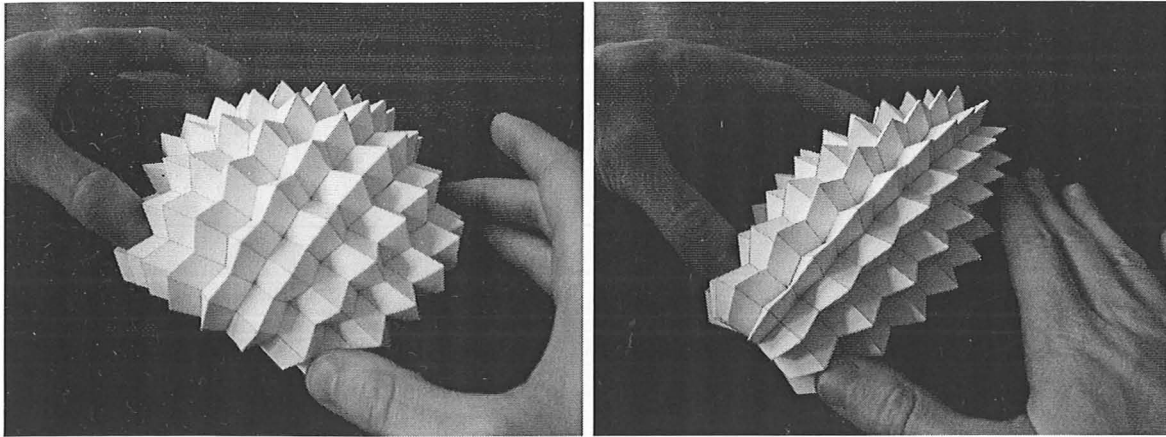


(c) A positive curvature in one direction induces a similar curvature in the other direction, and the shell becomes bowl-shaped.



(d) The shell is also flexible in twist, allowing this saddle shape, where the two principle directions are *not* aligned with the X and Y axes.

Figure 8.2: A doubly-corrugated shell: these images are all of the same shell, made from light cardboard. The corrugation is a simple triangle-wave in both the X and Y directions.



(a) At no strain, the two principal curvatures must be equal, and the deformation is spherical.

(b) As there is a tensile strain in the X direction and a corresponding compression in the Y direction, so the ratio between the curvatures is altered, so that the deformation is now ellipsoidal: *i.e.*, cigar-shaped.

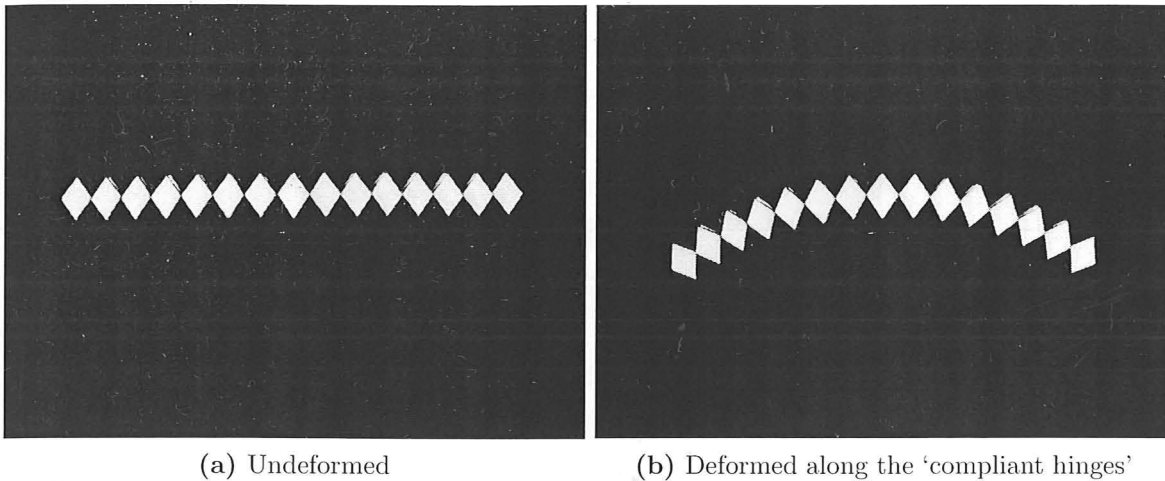
Figure 8.3: The variation of the ratio between the two principal curvatures with the in-plane strain.

are of the same magnitude, making a spherical cap. However, the ratio between these two curvatures is variable, being controlled by the in-plane strain of the shell. Fig. 8.3 explores how this coupling between κ_{XX} and κ_{YY} varies with strain.

As we rotate our coordinate system round, the coupling between curvatures diminishes. This is evident from Fig. 8.4, which looks along the 45° direction of a shell with no in-plane strain. There are now evident compliant ‘hinges’ along which the shell can bend with no greater stiffness than an uncorrugated sheet, and in bending along these hinges, the averaged mid-surface of the shell can take on a purely cylindrical curvature. This direction of low stiffness will rotate slightly as the shell undergoes in-plane strain.

In Section 7.1.2, it is observed that the positive- and negative-Gaussian curvature behaviour is one and the same, occurring at a single natural frequency: this occurs because the curvature in one direction is virtually constant, and the curvature in the other direction oscillates. In the doubly-corrugated shell, however, both curvatures are changing, and the positive- and negative- K modes appear by fundamentally different mechanisms, so that their behaviour is distinct. To explain why, note firstly that a positive- K shape can be directionless: the curvatures of a spherical bowl are independent of the direction in which they are measured, although an ellipsoidal bowl, as in Fig. 8.3b, has two clearly defined principle directions. A negative- K shape, or saddle, however, *always* has a clear directionality to its properties: one principal curvature is positive and one negative, and between the two principal curvature directions are two directions of zero curvature.

Referring to the Mohr’s circle of Fig. 3.3, we can see that a saddle shape is possible even when κ_{XX} and κ_{YY} are of the same sign (*i.e.*, the same sense), as long as there is



(a) Undeformed

(b) Deformed along the 'compliant hinges'

Figure 8.4: The doubly-corrugated shell, viewed side-on at 45° to the X and Y axes. Note that, in this direction, the shell effectively has compliant 'hinges', and so it curves cylindrically with very little stiffness in this direction.

a large enough twist κ_{XY} . So, in this case, the bowl shape is caused by the interaction between κ_{XX} and κ_{YY} . The saddle shape, however, is produced by a twist κ_{XY} .

8.1.2 Vacuum-formed models

Plastic prototypes are formed with the same equipment, material and method as in Section 6.2.2. Fig. 8.5 shows the mould used: the shape is sinusoidal in both directions. The surface is defined by its local height a as a function of X and Y of the mid-plane, as

$$a = \frac{1}{2}A \left(\cos \frac{2\pi X}{\Lambda} + \cos \frac{2\pi Y}{\Lambda} \right) \quad (8.1)$$

where A is the peak-to-trough amplitude of the corrugations in one direction, and Λ the corrugation wavelength, as throughout this thesis.

Figure 8.6 shows the behaviour of this shell: again, the shell displays synclastic behaviour, where curving along one line of corrugations produces a same-sense curvature along the other, shown in Fig. 8.6c. Also, the twisting behaviour is still present, as is the low bending stiffness at 45° to the corrugations. One principle difference from the behaviour of the paper shell is that in-plane strains require noticeably much more effort than out-of-plane deformations: a deal of effort is required to hold even the modest deformation in Fig. 8.6b. This is a result of the tight curvatures being imposed on the 'ridges' of the corrugations during this deformation.

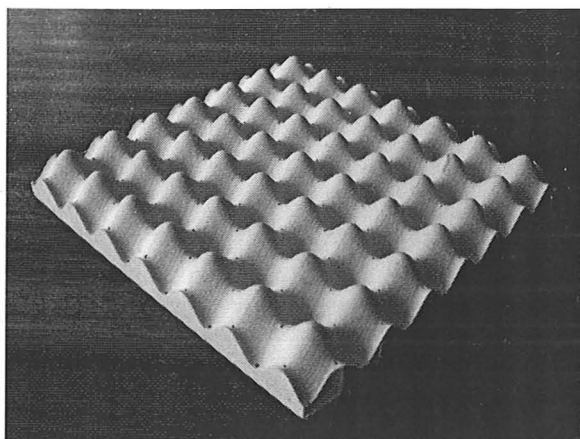


Figure 8.5: The computer-machined vacuum-forming mould for the doubly-corrugated plastic shell: holes have been drilled through the troughs, so that they are properly evacuated during forming.

8.1.3 Chocolate trays and eggboxes

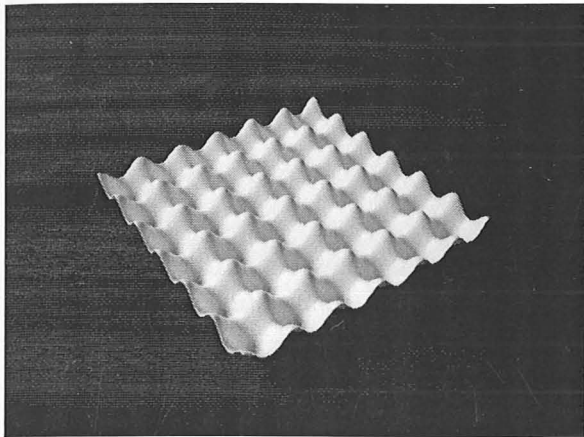
The paper and plastic shapes are, deliberately, very ‘pure’, containing exact triangle waves and exact sinusoids. However, Figs 8.7–8.8 show that even strongly irregular doubly-corrugated shells display the synclastic behaviour; it is not sensitive to the corrugation shape, nor is it even sensitive to the orthogonality of the corrugation directions: the chocolate tray of Fig. 8.7 has, in part, a hexagonal pattern, where the shell is corrugated in three directions. However, a noticeable difference with the chocolate tray is that the low stiffness at 45° has vanished.

With regard to in-plane stretching and compression, both trays are relatively rigid, which constrains their ability to undergo the large shape changes seen in Figs 8.7b and 8.8b. This, then, appears to be a feature with regard to which the corrugation profile is significant.

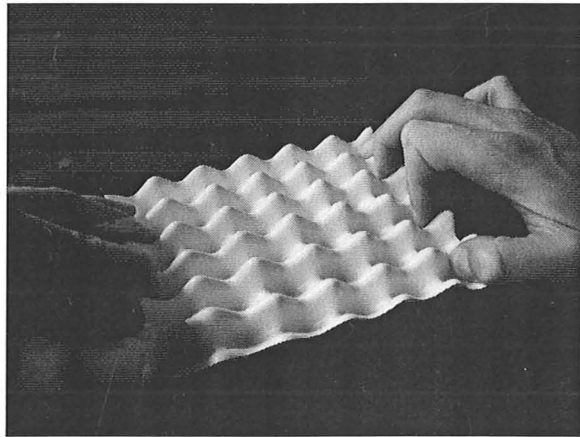
8.1.4 Summary of behaviour

All of the physical models described above flatly contradict Hale (1970) in his patent on doubly-corrugated shells. Hale insists, as reported in Section 2.2.2, that his shells are *anticlastic*. In all cases, however, a curvature in one direction (x or y) forces a curvature in the same sense in the orthogonal direction, producing a positive Gaussian curvature, and behaviour that is *synclastic*. Positive Gaussian-curvature shapes have no directionality: however, it is specifically the case here that a positive κ_{XX} *must* accompany a positive κ_{YY} , and vice-versa. On the other hand, anticlastic shapes *are* possible, but are due to the twist κ_{XY} , and are therefore only possible if the principle curvatures of the saddle lie at around 45° to x and y .

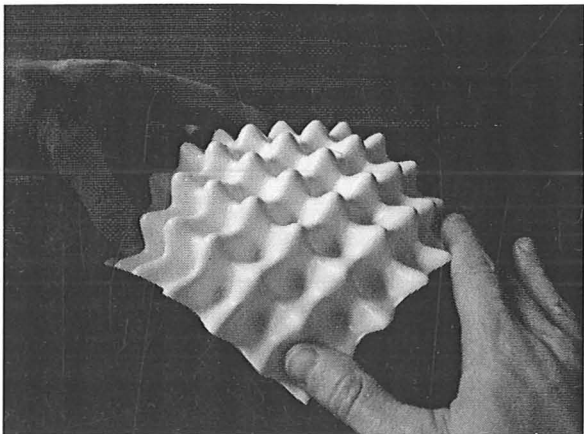
The paper model shows a low stiffness in in-plane compression: this low stiffness is



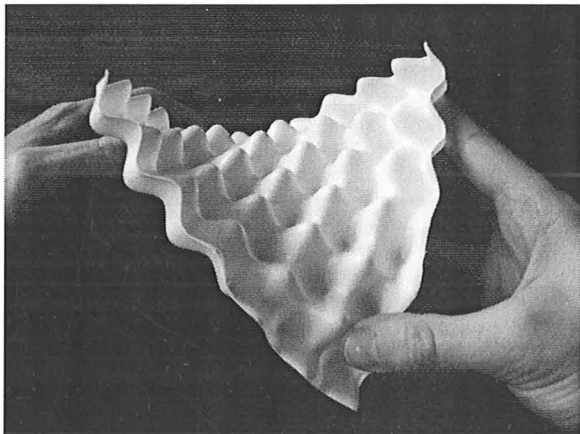
(a) The initial shape, unstressed



(b) In-plane compressive and tensile stresses are resisted much more in this shell than in the paper shell of Fig. 8.2b.

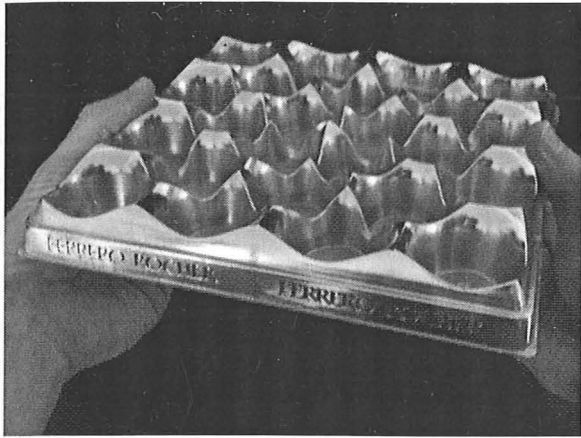


(c) A positive curvature in one direction induces a similar curvature in the other direction, as for the paper shell, and the shell becomes bowl-shaped.

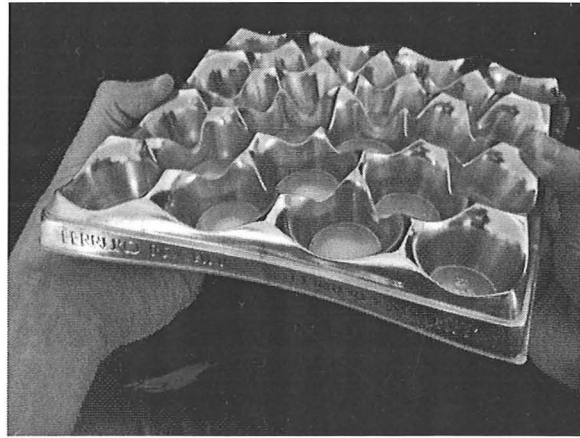


(d) The shell is also, again, flexible in twist, allowing this saddle shape.

Figure 8.6: A doubly-corrugated shell, this time constructed from high-impact polystyrene ('HIPS'), with sinusoidal corrugations in both directions.

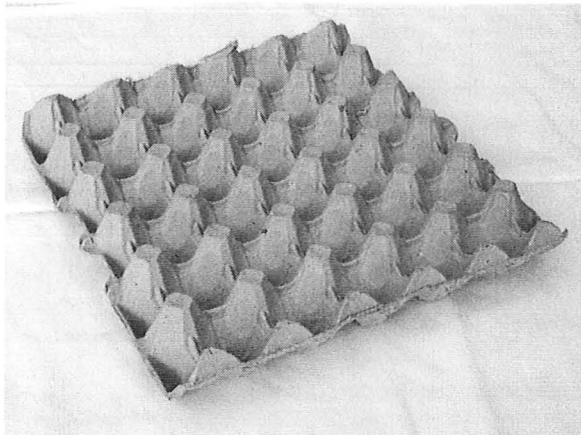


(a) The initial shape, unstressed

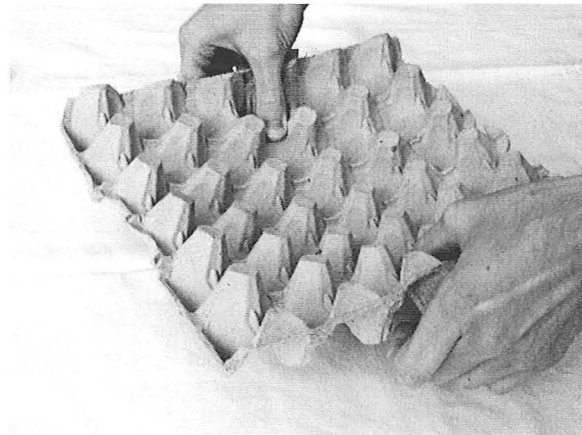


(b) When curved in one direction, it curves in the same sense in the other.

Figure 8.7: Synclastic behaviour in a chocolate tray – note that its shape and pattern are distinctly irregular, and yet the synclastic behaviour is still present.



(a) The initial shape, unstressed

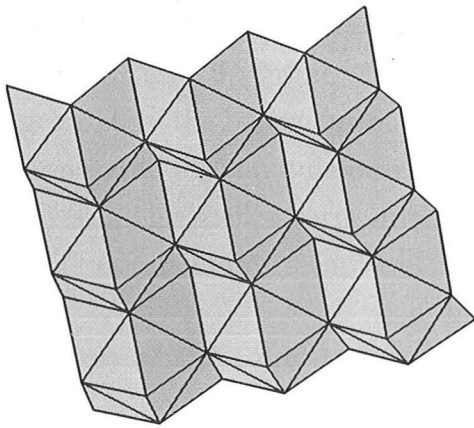


(b) When curved in one direction, it curves in the same sense in the other: following the line of the corrugation peaks, the curvature in both directions becomes evident.

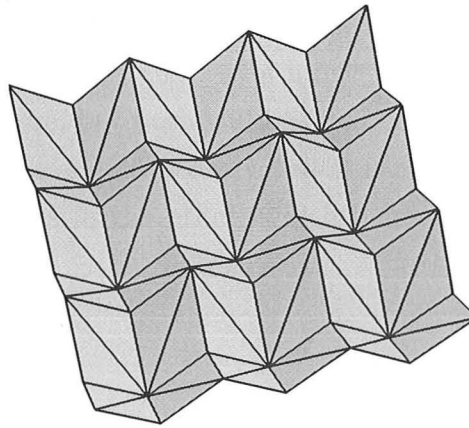
Figure 8.8: Synclastic behaviour in an eggtray.

not so strongly observed in the plastic model, and absent in the chocolate and egg trays. Therefore, we can conclude that this in-plane stiffness is sensitive to the exact corrugation profile. This is important, since a low in-plane stiffness is essential for a structure that must morph between shapes of differing double curvature.

The shells of Chapters 4–5 have zero Gaussian curvature in their initial form, and their mid-surface is constrained to be developable throughout: the shells of Chapters 6–7 have some initial non-zero K over the shell, and their mid-surface can deform through shapes of varying K . For the doubly-corrugated shells, there is significant local double curvature in the peaks, troughs and saddles of the shells, but, overall, the initial shell has an average $K = 0$ (neglecting any minor discrepancies at the edges). Nonetheless, as for Chapters 6–7, large changes in the K of the mid-surface are observed to be possible.



(a) Quadrilateral elements hinged between the closer two nodes.



(b) Quadrilateral elements hinged between the farther node pair.

Figure 8.9: The model used for the modal analysis. The in-plane stiffness of the plates is modelled as pin-jointed bars joining the nodes, and is set to be much greater than the bending stiffness between facets, so that the structure undergoes effectively inextensional deformation, mimicking the behaviour of paper. On the left, the quadrilateral elements of which the paper is composed are hinged between the closer of their two nodes: on the right, they are hinged between the farther node pair. The former seems intuitively more likely to describe the observed behaviour.

8.2 Modal analyses

The principles of a modal analysis are explained in Section 3.2.3. Examining the paper models of Section 8.1.1, it seems obvious that these can be modelled as folded plates. Each fold line on the paper is represented by a rigid bar, and there is a small bending stiffness to relative rotations between adjacent facets. This is a very simple model, which has a very natural discretisation, and therefore produces clear results regarding the behaviour of the structure, and so Section 8.2.1 carries out this form of analysis. For a fuller treatment of the same analysis, see Schenk (2008).

Section 8.2.2 presents a finite-element modal analysis of the doubly-corrugated shells, to match the polymer prototypes. Finally, in Section 8.2.3, the results from the two modal models are compared with each other and with the observations from prototyping, to confirm that the modal results are physically meaningful.

8.2.1 Folded-plate modal analysis

The modal analysis is based on the paper models described in Section 8.1.1. The assumption is made that the paper can be assumed to be inextensional. Therefore, the structure is considered as a folded plate of triangular facets, where in-plane stiffness is much higher than the bending stiffness between the adjacent facets. This model is described in Fig. 8.9.

Note that each quadrilateral in the paper model can be converted into a triangular

facet in one of two ways: with the hinge across the short or long axis of the quadrilateral, as shown in Fig. 8.9. Intuitively, it seems likely that the short-axis hinge will replicate more accurately the behaviour of the paper structure, but both will be tried. Since paper is inextensional, it cannot deform along both hinges simultaneously, but it is conceivable that parts of the shell deform in one way and parts in the other, which behaviour this model will not attempt to capture.

Generation of the folded plate stiffness matrix

From Section 3.2.3, a modal analysis requires a vector of all nodal displacements, \mathbf{d} , a vector of the loads applied to each node in the direction of said displacements, \mathbf{p} , a stiffness matrix \mathbf{K} relating \mathbf{p} to \mathbf{d} and an inertia matrix \mathbf{M} .

There are numerous ways to conceive of an inertia matrix. For a truss structure, the most accurate solution is to define the total kinetic energy T (see Eqn 3.16) due to the translational and rotational velocities of the bars, considering the linear and rotational inertia of each bar: for a slender bar, only the component of rotation that is perpendicular to the bar is significant, and the rotational inertia in this direction is simple to calculate. From this total kinetic energy, and Eqn 3.16, the inertia matrix can be derived.

In our case, the structure is a series of rigid triangular plates. Then, the kinetic energy is composed of the linear and rotational kinetic energies of each individual plate. However, the rotational inertia of a plate is much more complex than that of the bar: it has non-zero moments of inertia about all possible axes of rotation.

Both of the above methods, while accurate for their respective systems, are complex to calculate. As a gross simplification, all of the mass can be considered to be concentrated at the nodes, and the plates and bars are considered massless. If each node is given an equal mass, \mathbf{M} becomes an identity matrix. This still fulfils the function of applying an inertia to each part of the system, and, as Section 8.2.3 shows, the results exhibit no strong differences from the finite-element simulation, which follows the plate approach described in the last paragraph.

With such a simple inertia matrix, the main challenge is the production of the stiffness matrix \mathbf{K} such that $\mathbf{p} = \mathbf{K}\mathbf{d}$, whereupon the natural modes are the eigenvectors of $\mathbf{M}^{-1}\mathbf{K}$.

For two points connected by a pin-jointed bar, of initial position vectors \mathbf{x}_1 and \mathbf{x}_2 , the forces due to the extension of the bar are simply calculated. The displacements of the two vectors are defined here as \mathbf{d}_1 and \mathbf{d}_2 , and the bar itself is the vector $\mathbf{x}_2 - \mathbf{x}_1$. Then, the strain of the bar is its extension over its length:

$$\varepsilon = \frac{(\mathbf{d}_2 - \mathbf{d}_1) \cdot (\mathbf{x}_2 - \mathbf{x}_1)}{(\mathbf{x}_2 - \mathbf{x}_1)^2} \quad (8.2)$$

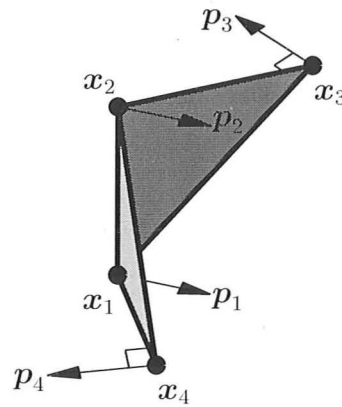


Figure 8.10: The nodal loads imposed by the inter-facet folds. For each connected pair of facets, the rotation of each facet about the hinge is calculated, to give the relative rotation of each hinge: this rotation vector gives the torque on each hinge, which, when divided by the distance from the hinge to the further corners of the facets (nodes x_3 and x_4), gives the forces p_3 and p_4 on each of those corners, which are perpendicular to their respective facets. Forces p_1 and p_2 are equal in direction, and are applied to the nodes on the hinge, nodes x_1 and x_2 , such that the whole is in equilibrium.

Assigning each bar a cross-sectional area A and a Young's modulus E , the forces on the nodes, p , become

$$p_1 = EA \frac{(d_2 - d_1) \cdot (x_2 - x_1)}{|x_2 - x_1|^3} (x_2 - x_1) \quad (8.3)$$

$$p_2 = -EA \frac{(d_2 - d_1) \cdot (x_2 - x_1)}{|x_2 - x_1|^3} (x_2 - x_1) \quad (8.4)$$

Each d component appears only once, the two d components are not multiplied together, and there are no terms that are independent of d : consequently, these equations can produce a linear stiffness matrix, which is our immediate goal. With regard to the bending stiffness between facets, the implementation is less obvious, and the mathematics more complex: a summary of the method is given in Fig. 8.10.

In implementing these equations, matrices of connectivity are generated for each of the structures shown in Fig. 8.9. Then, an algorithm scans through these connections, entering the relevant terms in the stiffness matrix due to each bar and hinge. In fact, two stiffness matrices are produced, one for the bars and one for the hinges: then, each can be multiplied by its relative stiffness. In order to simulate a material with virtually infinite stretching stiffness, the in-plane stiffnesses are multiplied by 10^6 relative to the hinge stiffnesses. Finally, the resulting matrix is checked for symmetry, and its eigenvalues and eigenvectors found by a pre-existing function in Mathworks' MATLAB.

Results and observations from the folded-plate analysis

As outlined above and shown in Fig. 8.9, the analysis is attempted with equilaterally triangular facets and with rather more acute facets. A paper model can display either, and within a paper model, different facets can hinge about different axes. Accordingly, Fig. 8.11 tabulates the mode shapes observed with each facet design, with the corresponding frequency given. The absolute magnitudes of the frequencies are meaningless, since the stiffnesses and masses have been given arbitrary dimensionless values: they are given for comparison with each other. To simplify this section, modes on the shell with hinges between the nearer two nodes on each facet are referred to as modes $N1$, $N2$ &c., and modes on the shell with hinges between the farther two nodes are referred to as modes $F1$, $F2$ and so on.

Some modes are observed to appear in orthogonal pairs of identical frequency: modes $N3-N4$, $N7-N8$, $F3-F4$ and $F7-F8$. Modes $N10-N11$ are also a pair, although mode $N11$ is not shown on Fig. 8.11. The undeformed shell has three axes of symmetry: therefore, any mode shape which does not have at least two axes of symmetry *must* be one of a mirrored pair; the third axis of symmetry is broken in the direction in which the shell oscillates.

Of these pairs, modes $N3-N4$, $N7-N8$ and $F3-F4$ all consist of a developable curvature at 45° to the corrugations. Therefore, within each pair, these modes are mutually exclusive: a combination of modes $N3$ and $N4$ would involve large strains at 45° to the corrugations, in which direction Section 8.1.1 describes these shells to be rigid. That these modes are 'immiscible' is demonstrated by the existence of one axis of symmetry in each mode. Modes $F7-F8$ and $N10-N11$ have no axes of symmetry. They involve purely in-plane behaviour, and within each pair, the two modes may be freely combined: therefore, the computational solution has simply picked an orthogonal pair from the infinite number of modes occurring at that frequency. A pair *can* be picked that display one axis of symmetry, but this pair has not naturally arisen from the computational approach.

The first six modes for the equilateral model are all found for the acute model, but at much higher frequencies, implying that the deformation is much stiffer, as is to be expected. However, the seventh mode for the equilateral model appears at exactly the same frequency for the acute model, making it the fifth acute mode. This is easily explained: in this mode, each facet remains undeformed and the sheet is 'folding up' by its 'ridge' hinges only, making the difference between the models irrelevant. Other modes that feature only in-plane strains have also 'bobbed up', being at much lower mode numbers for the N shell than for the F shell: for example, modes $N10-N11$ and $F7-F8$ are equivalent, as are modes $N12$ (not shown) and $F9$.

In conclusion, all of the interesting modes (*i.e.*, the modes at low enough frequencies to provide meaningful insights to the behaviour of the shell) occur at lower or identical

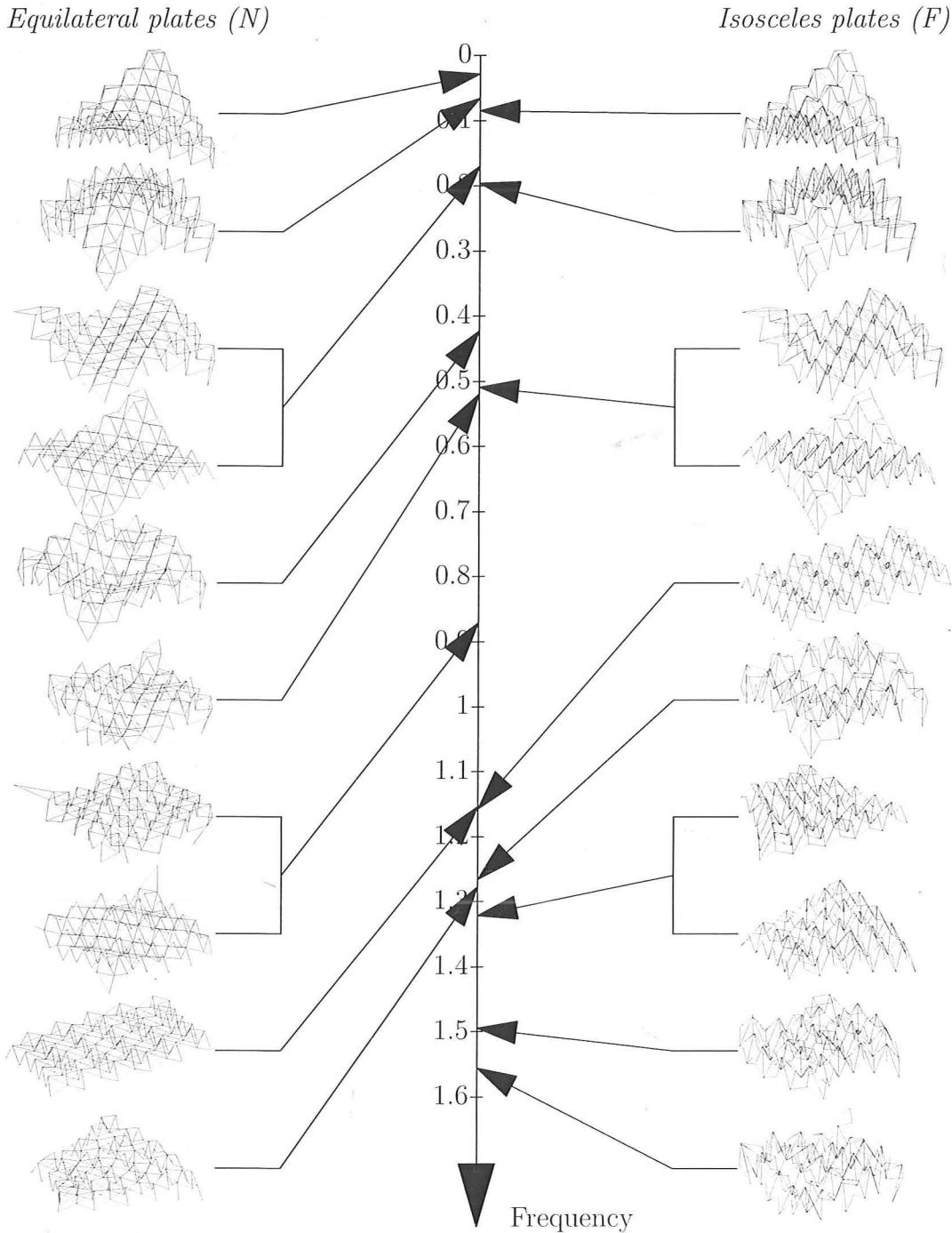


Figure 8.11: The first ten modes for the folded-plate model, for (left) facets hinged across their short side, making equilaterally triangular plates, and (right) along the long side, making isosceles plates. Modes on the left are referred to as modes $N1, N2$ &c., modes on the right, $F1, F2$ &c. Some modes occur in orthogonal pairs of identical frequency, and are marked as such: also, modes $N10-N11$ are such a pair, although $N11$ is not shown. The cutoff of ten modes was chosen because, with mode $F11$, the frequency jumps to over 2. Then, $F11-F12$ are another pair, imitating the shape of modes $N7-N8$. Note how, in general, all modes with out-of-plane deformation ($N1-N8$) appear with at least double the frequency (*i.e.*, a much higher stiffness), in shell F , becomes modes $F1-F4, F6$ and $F10-F12$.

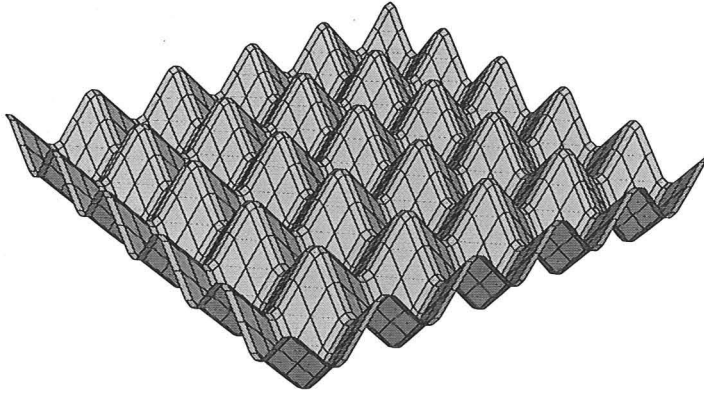


Figure 8.12: The initial mesh for the finite-element analysis of the doubly-corrugated shell. Unlike the folded-plate model of Section 8.2.1, this model uses a sinusoidal corrugation profile.

frequencies in the N shell than the F shell. Therefore, only the equilateral-plate shell results are considered in the remainder of this chapter.

8.2.2 Finite-element modal analysis

The folded-plate model of Section 8.2.1 involves a triangular-wave corrugation profile. The finite-element simulation is better suited to a smooth profile, and so, as in Section 7.1.1, a sinusoidal profile is used.

The model is set up using Mathworks' software package MATLAB to generate the shape of the shell and output the nodal coordinates in the form of an ABAQUS input file, as in Section 7.1.1. Again, each quarter-corrugation spans two elements, and there are five corrugations per side, so that the shell consists of $40 \times 40 = 1600$ elements. These elements are the type referred to in ABAQUS as 'S4R5', denoting four-node thin shell elements which can only undergo small in-plane strains, in keeping with our assumption that these shells can be considered as locally inextensible.

The analysis, again, is a standard ABAQUS modal analysis. In this case, it is set to produce, as output, the first twenty modes: *i.e.*, the ten modes of lowest natural frequency. The central node of the shell is pinned, so that rigid-body translations are not possible, but there will still be rigid-body rotational modes, of zero frequency: therefore, a very small non-zero minimum frequency is specified, so that rigid-body modes of deformation are not counted.

The initial, undeformed mesh is shown in Fig. 8.12. The material properties in the simulation are, as in Section 7.1, those of CuBe alloy. The shell thickness is 0.1 mm, and the shell length along each corrugation is 125 mm. Since it is corrugated, the overall plan has an area of just $85.5 \text{ mm} \times 85.5 \text{ mm}$. It is irrelevant that these material properties

do not match those of the prototype described in Section 8.1.2, since no attempt will be made in this thesis to measure the natural frequencies of oscillation of the plastic shell: since the CuBe material is thinner and harder, it approximates an inextensional shell more closely, and a key goal of this thesis is to demonstrate that interesting behaviour is found *without* extension.

Finite-element model results

Section 8.2.1 studies the modal behaviour of the folded-plate model, which applies equally well to this model: therefore, this section will concentrate on the comparison between the two, rather than repeat the previous section for what is a very similar set of results.

Figure 8.13 shows the shapes and frequencies of the first nineteen modes for the finite-element simulation. In frequency, they span a twenty-fold range. On the same plot are shown the frequencies of the same modes for the folded-plate model, all normalised by the frequency at Mode I.

The two shells behave identically for the first two modes. From Mode VII onwards, their behaviour is very similar: there is approximately a factor of five difference, but this is an artefact of the arbitrary normalisation. So, the main difference in frequency behaviour is between the second and seventh modes, where the folded-plate model becomes stiffer far more quickly. One interpretation is that the folded-plate shell exhibits a greater difference in stiffness between its first two modes and the higher-order modes than does the sinusoidally-corrugated shell, so that these modes (which correspond to strong double-curvature) are more obviously preferred modes of deformation.

Finally, note that there is some variation in the order of the natural modes, between the two models. The strongest example is at Mode VII on the finite-element analysis. In Fig. 8.13, it can be seen that for the folded-plate model, this mode occurs at a higher frequency than the next two modes, and accordingly, Fig. 8.11 places that mode at Mode X. Similarly, finite-element Mode XIII is folded-plate mode XIX, and thereafter there are many more discrepancies in the ordering.

8.2.3 Discussion of the modal results

Figures 8.14–8.15 show the undeformed shapes and the first nine modes of both models, alongside, where it is helpful, relevant photographs of the polymer prototype. What is immediately striking, and distinct from the curved-corrugated shells in Section 7.1, is that the lowest-frequency modes are the doubly-curved modes, with modes of developable mid-surface not appearing until the third mode. The lowest-frequency mode is a negative- K saddle-shape, and the second lowest, in Fig. 8.14c, a positive- K bowl-shape. Unlike the curved-corrugated shell of Section 7.1, the positive- and negative-Gaussian curvature

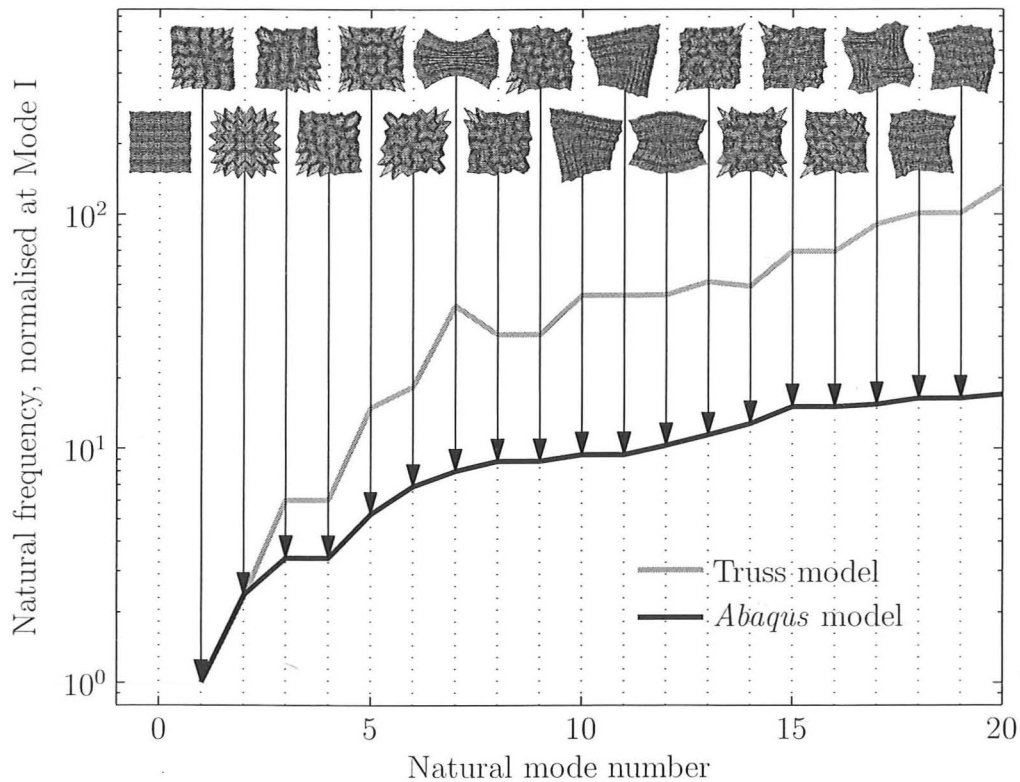


Figure 8.13: The first nineteen natural modes for the finite-element simulation, compared with the frequencies at which the same modes occur for the folded-plate shell, all normalised by the frequency at the first mode (note that frequency is plotted on a logarithmic scale). In the first two modes, and from the seventh mode onwards, the two are very similar, observing the shape of the mode-frequency curve. However, the folded-plate model has a more rapid increase in stiffness between the second and seventh modes. This may be a sign that, in the first two modes, the folded-plate model is exceptionally soft: as the mode-shapes get more complex, so the difference between the triangular-wave and sinusoidal corrugation profiles becomes less significant.

shapes are distinct modes with distinct frequencies: Section 8.1, above, explains how the two forms behave differently for this shell.

Finally, both models produce a mode in which there is stretching but no curvature of the mid-surface: it appears as Mode IX for the folded-plate model (Fig. 8.15e), and Mode VII for the finite-element model (Fig. 8.15c).

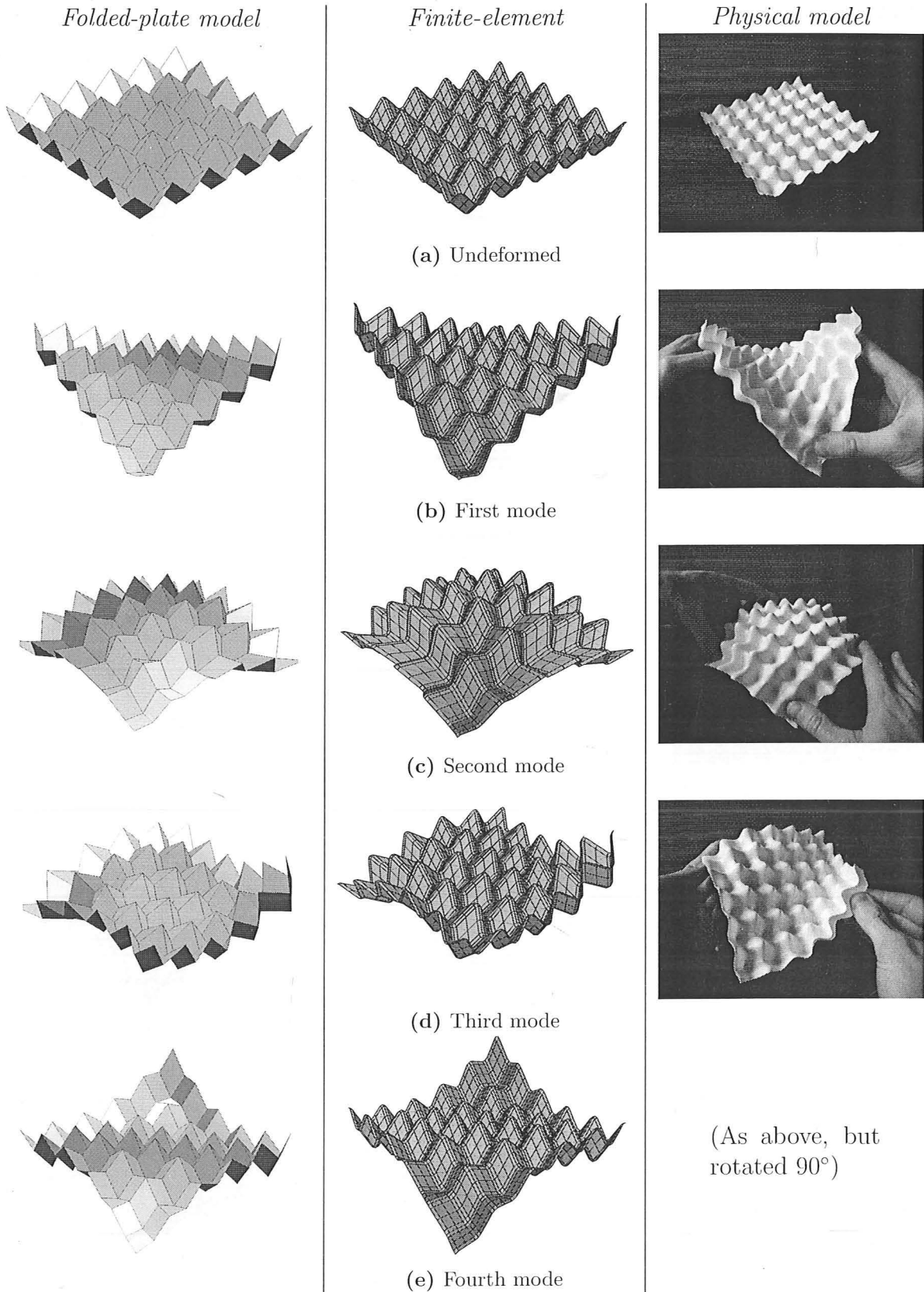


Figure 8.14: Natural modes of vibration (i), alongside relevant photographs. Even the first mode has a strong (negative) double curvature of the mid-surface, and Mode II has an equally strong double curvature. The lowest-frequency cylindrically-curved mode is Mode III (Fig. 8.14d), where the shell is hinged along the lines shown by Fig. 8.4.

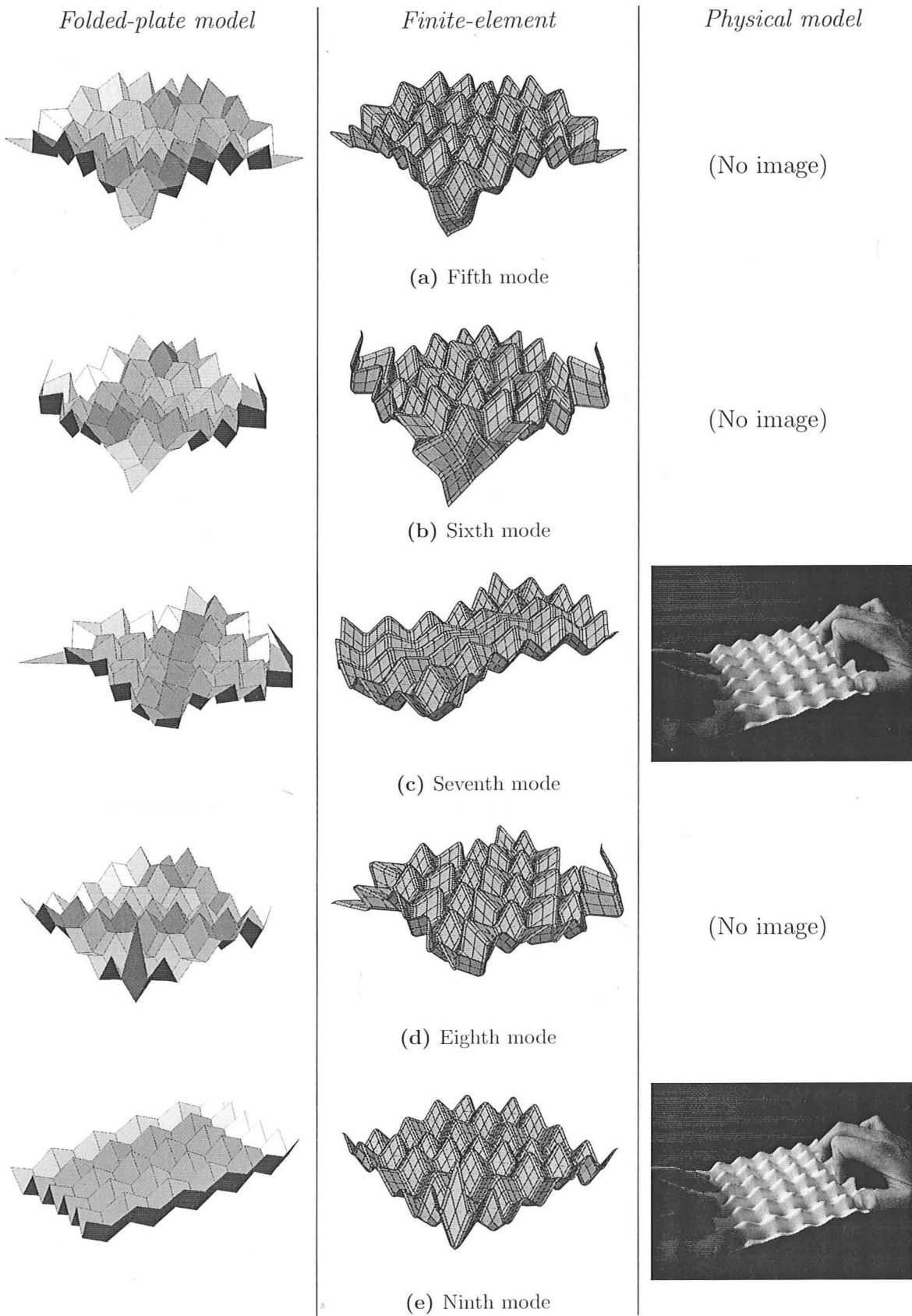


Figure 8.15: Natural modes of vibration (ii). A difference appears between the two: a large cross-corrugation strain, as photographed, appears as Mode VII on the FE model (Fig. 8.15c), but as Mode IX on the folded-plate model (Fig. 8.15e).

8.3 Conclusions

Doubly-corrugated shells have been shown, through physical models, to deform elastically through dramatic changes in shape, a single shell being able to morph between bowl, saddle and more complex shapes. What is more, a strong coupling has been observed, in Section 8.1, between the curvatures and strains in both directions. This behaviour appears to be very robust, in that it is observed in a diverse array of doubly-corrugated sheets, ranging from eggtrays to chocolate trays (Section 8.1.3).

This behaviour flatly contradicts a patent by Hale (1970), and so a more rigorous test was devised to determine whether this behaviour is as natural to the shell as it appears. Two different modal analyses have been performed, in Section 8.2: the behaviour described in Section 8.1 is found to match the lowest-frequency natural modes of vibration of a finite shell. In conclusion, therefore, we can say that doubly-corrugated shells are ideal for the development of morphing structures, as not only do they display low stiffness through large changes of double curvature, but this stiffness is even lower than that displayed in purely developable deformations.

Chapter 9

In summary:

further work and conclusions

This research has pursued a diverse array of analyses within the general theme of corrugated compliant structures, and at the end of each individual chapter, conclusions are drawn. By way of conclusion, this chapter first explores the principal outstanding questions, and in Section 9.1, diverse avenues for further work are explored. Finally, Section 9.2 summarises the successes, failures and findings of the thesis as a whole.

9.1 Avenues open for further work

There are two aspects to the further work opened up by this thesis: firstly, there are aspects that require further experimental verification before they can be practically applied, and secondly, avenues are opened for new forms of structure, developed from the structures analysed in this thesis.

9.1.1 Further quantitative verification of existing models

Of the analyses presented in this thesis, that of Chapter 4 has the least quantitative support from physical tests or simulation. Gentilini *& al.* (2008) perform an in-depth finite-element analysis of the Mode I bistability described in Chapter 4, but the limitations described in Section 4.4 still apply to their work. They get rather closer to the conditions in Chapter 4 than a three-point bending test: their model effectively encases the two ends of the shell in a rigid beam, and applies a rotation to these beams in order to impose a moment, and applies a thermal gradient through the shell to impose internal stresses. However, there is still sufficient difference in the conditions between their model and the analysis of Chapter 4 that a quantitative match is neither seen nor expected to be seen. Accordingly, there is still room for further attempts to verify or falsify this model.

In Chapter 7, specifically, in Section 7.2, full and general constitutive relations for the curved-corrugated shell are produced. These can be applied to any general shell, over any deformation: in Section 7.2.3, they are applied purely to tension in one direction over a uniform shell, and so there is, again, room for further verification of this model. Since such a shell cannot be flattened out, all deformation components are coupled over a shell of finite size, making it impossible to produce further tests that verify the stiffness components of Section 7.2 individually, and therein lies the challenge in the further verification of what is potentially a useful set of equations.

9.1.2 More complex forms for morphing corrugated shells

So far, only uniform corrugations have been considered, and these shells have been undergoing simple global behaviour, deforming between bowls, saddles and cylinders. The following are a sample of more complex shells that may prove worth pursuing:

- (i) the corrugations can curve in the plane of the shell, producing something akin to a scallop shell, as in Fig. 9.1;
- (ii) a single shell can combine regions of single and double corrugation, enabling precisely tailored elastic behaviour, useful for, *e.g.*, aeroelastic wings, as introduced in Section 2.2;

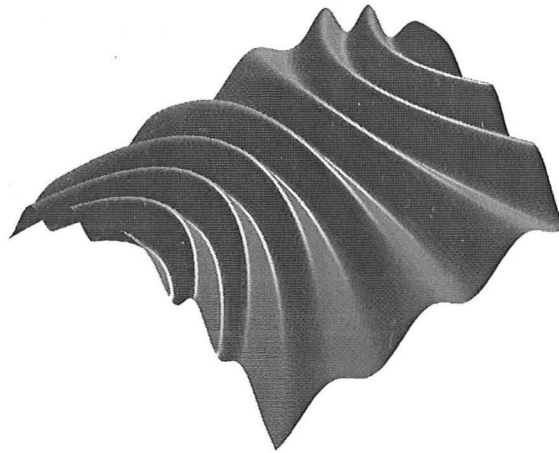


Figure 9.1: An example of a surface in which the corrugations curve in the plane of the shell. A common example of this behaviour is the scallop shell.

- (iii) as the shapes of shells cease to be just a simple cylindrical curvature, acquiring further global features, multistability will become more prevalent; and
- (iv) all shells considered here have been fully open. Partly or fully closed corrugated shells with interesting morphing behaviour may be possible, given the large deformations seen in open shells.

More general methods will be required to analyse the morphing of these surfaces. This may be simpler than it seems: Appendix D presents a method employing the concepts of differential geometry to predict the deformation of a shape, having subdivided that shape into a finite number of long, thin, developable strips. This matches the approach taken in Chapter 6 to analyse curved corrugated shells, and will be a computationally-applied method.

Regarding the stiffness of these shells, Section 7.2 shows a high complexity and non-linearity of the constitutive equations when curved corrugated shells are considered: this implies, again, that finite-element computational methods of varying kinds will prove crucial in the further development of these shells.

9.2 Final conclusions

From the literature review (Chapter 2), we can see that there is global interest in morphing and multistable structures, in fields ranging from the everyday to the cutting edge of high technology, and that, independently, corrugated shells of various forms are also well known and frequently utilised across a similar spectrum: this thesis succeeds in demonstrating that corrugated shells have a lot to offer the field of morphing and multistable structures, and by the end of this thesis, the surface has still barely been scratched with regard to exploiting this potential.

In Chapters 4–5, multistability in flat corrugated shells is described qualitatively and analysed quantitatively, using an analysis based on stored internal strain energy. This analysis matches the observed behaviour, justifying our claim to understand the underlying effects involved in this multistability. In addition, in Chapter 5, a plastic flow analysis models the manufacture of these shells, again supporting our understanding of what is happening within the shells.

Chapters 6–7 explore curved corrugated shells, and show that, unlike the shells of Chapters 4–5, changes in the double curvature of the equivalent mid-surface of the shell are possible. This is a dramatic development, since this is behaviour that is not possible to replicate simply with any other means: rather than improving the performance of existing devices, this technology permits new forms of machine to be devised. Similar behaviour is seen in doubly-corrugated shells in Chapter 8.

A further way to view these phenomena is as the effect of ‘textures’ on shells; these textures (in this case, corrugations) are features of the shell which are of an intermediate scale between the thickness of the material itself and the global shape of the shell. This way of understanding these shells is the basis of a short conference paper by Norman *et al.* (2008a).

In conclusion, this thesis is very far from being the last word on morphing and multistable corrugated shells: it presents a broad range of designs and analyses that may be used generally, and demonstrates at least part of the potential of such shells, in the confident expectation that further research and very practical developments can follow.

Bibliography

- R. Aboulafia. The U.S. tactical aircraft crisis. *Aerospace America*, pages 26–29, Apr 2008.
- M. Abramowitz and I. A. Stegun. *Handbook of Mathematical Functions with Formulas, Graphs, and Mathematical Tables*, chapter 17. Dover, New York, 9th edition, 1972.
- J. Arkell. Improvement in paper for packing. US Patent 623695, Apr. 1899.
- C. Arne. Plane expansible corrugations. US Patent 3279973, May 1966.
- E. L. Axelrad. Flexible shell theory and analysis of tubes and bellows. *Journal of the Brazilian Society of Mechanical Sciences*, 144:369–386, 1992.
- E. L. Axelrad. Shell theory and its specialized branches. *International Journal of Solids and Structures*, 37(10):1425–1451, 2000. ISSN 0020-7683.
- D. Briassoulis. Equivalent orthotropic properties of corrugated sheets. *Computers & Structures*, 23(2):129–138, 1986.
- Brush Wellman, Inc. *Guide to Copper Beryllium*. Brush Wellman, Inc., Cleveland, Ohio, Sept. 2008. url: www.brushwellman.com/alloy/tech_lit/GuideToCopperBeryllium.pdf.
- C. R. Calladine. *Theory of Shell Structures*. Cambridge University Press, 1983. ISBN 0521238358.
- C. R. Calladine. *Plasticity for Engineers*. Ellis Horwood, 2000. ISBN 1898563705.
- R. C. Coates, M. G. Coutie, and F. K. Kong. *Structural Analysis*, chapter 10, pages 379–391. Chapman & Hall, 1988.
- J. W. Edwards, editor. *H. Reissner Anniversary Volume: Contributions to Applied Mechanics*. Ann Arbor, 1949.
- D. A. Galletly and S. D. Guest. Bistable composite slit tubes. I. A beam model. *International Journal of Solids and Structures*, 41(16-17):4517–4533, Aug. 2004.

- C. Gentilini, K. A. Seffen, and S. D. Guest. Numerical analysis on the bending behaviour of corrugated plates and of tape-springs with a prestress. Technical report, Cambridge University Engineering Department, 2008.
- H. Gluck. Almost all simply connected closed surfaces are rigid. In *Lecture Notes in Mathematics 438, Geometric Topology*, pages 225–239. Springer-Verlag, 1975.
- S. D. Guest and J. W. Hutchinson. On the determinacy of repetitive structures. *Journal of the Mechanics and Physics of Solids*, 51(3):383–391, Mar. 2003.
- S. D. Guest and S. Pellegrino. Analytical models for bistable cylindrical shells. *Proceedings of the Royal Society A: Mathematical, Physical and Engineering Sciences*, 462(2067):839–854, Mar. 2006.
- J. R. Hale. Anticlastic cellular core structure having biaxial rectilinear truss patterns. US Patent 3525663, Aug. 1970.
- J. Heyman and F. A. Leckie, editors. *Engineering Plasticity*. Cambridge University Press, 1968.
- D. Hibbitt, B. Karlsson, and P. Sorensen. *Abaqus Version 6.7*. Hibbitt, Karlsson & Sorensen, Inc., Pawtucket, Oct. 2008.
- R. Hill. *The Mathematical Theory of Plasticity*. Oxford University Press, 1950.
- P. G. Hodge. *Plastic Analysis of Structures*. McGraw-Hill, 1959.
- R. G. Hutchinson, N. Wicks, A. G. Evans, N. A. Fleck, and J. W. Hutchinson. Kagome plate structures for actuation. *International Journal of Solids and Structures*, 40(25):6969–6980, Dec. 2003.
- M. W. Hyer. Calculations of the room-temperature shapes of unsymmetric laminates. *Journal of Composite Materials*, 15:296–310, July 1981.
- N. L. Johnson. GMS global initiative on automotive applications of smart materials. *AIAA & ASME Adaptive Structures & Material Systems Newsletter*, pages 2–3, Spring 2008.
- W. Johnson and P. B. Mellor. *Engineering Plasticity*. Ellis Horwood, 1983.
- A. Jones. Improvement in paper for packing. US Patent 122023, Dec. 1871.
- E. Kebabze, S. D. Guest, and S. Pellegrino. Bistable prestressed shell structures. *International Journal of Solids and Structures*, 41(11-12):2801–2820, June 2004.

- S. Kota, J. A. Hetrick, R. Osborn, D. Paul, E. Pendleton, P. Flick, and C. Tilmann. Design and application of compliant mechanisms for morphing aircraft structures. *Proceedings of the SPIE*, 5054(1):24–33, Aug. 2003.
- J. H. Lau. Stiffness of corrugated plate. *Journal of the Engineering Mechanics Division of the ASCE*, 107(1):271–275, 1981.
- E. H. Lee and P. S. Symonds, editors. *Plasticity*. Proceedings of the Second Symposium on Naval Structural Mechanics, Brown University, 1960. Pergamon, 1960.
- K. M. Liew, L. X. Peng, and S. Kitipornchai. Nonlinear analysis of corrugated plates using a FSDT and a meshfree method. *Computer methods in applied mechanics and engineering*, 196:2358–2376, 2007.
- K.-J. Lu and S. Kota. Design of compliant mechanisms for morphing structural shapes. *Journal of Intelligent Material Systems and Structures*, 14(6):379–391, June 2003.
- T. J. Lu and G. Zhu. The elastic constants of corrugated board panels. *Journal of Composite Materials*, 35(20):1868–1887, 2001.
- A. H. Mang, V. C. Giryavallabhan, and H. J. Smith. Finite element analysis of doubly corrugated shells. *Journal of the Structures Division of the ASCE*, 102:2033–2050., 1976.
- J. B. Martin. *Plasticity: fundamental theorems and general results*. MIT Press, 1975.
- A. Nadai. *Theory of Flow and Fracture of Solids*, volume I. McGraw-Hill, 1950.
- A. D. Norman, M. R. Golabchi, K. A. Seffen, and S. D. Guest. Multistable textured shell structures. *Advances in Science and Technology*, 54:168–173, 2008a.
- A. D. Norman, K. A. Seffen, and S. D. Guest. Multistable corrugated shells. *Proceedings of the Royal Society of London A*, 464:1653–1672, 2008b.
- H. F. Parker. The Parker variable camber wing. Technical Report No. 77, NACA, 1920.
- W. Prager and P. G. Hodge. *Theory of Perfectly Plastic Solids*. John Wiley, 1951.
- T. Purnell and P. Wright. *Formula One 2011: Chassis Regulation Framework*. A Briefing Note in preparation for the Formula One Manufacturers Advisory Committee, June 2007.
- J. W. S. Rayleigh. *The Theory of Sound*, volume I. Macmillan, 1877.
- K. F. Riley, M. P. Hobson, and S. J. Bence. *Mathematical Methods for Physics and Engineering*. Cambridge University Press, 2nd edition, 2002.

- J. A. Rinde. Poisson's ratio for rigid plastic foams. *Journal of Applied Polymer Science*, 14:1913–1926, 1970.
- A. Samanta and M. Mukhopadhyay. Finite element static and dynamic analyses of folded plates. *Engineering Structures*, 21(3):277–287, Mar. 1999.
- M. J. Santer and S. Pellegrino. Topology optimization of adaptive compliant aircraft wing leading edge. In *48th AIAA/ASME/ASCE/AHS/ASC Structures, Structural Dynamics and Materials Conference, Honolulu, Hawaii, 23-26 April, 2007*.
- C. Scarborough and B. Goren. Analysis: movable floor the new buzzword. *autosport.com/news*, Mar. 2007. url: www.autosport.com/news/report.php/id/57511.
- M. Schenk. Textured shell structures. First-year PhD report at CUED, 2008.
- J. C. Schluter. Corrugated structural metal plate. US Patent 6524722, Feb. 2003.
- M. R. Schultz. A new concept for active bistable twisting structures. In A. B. Flatau, editor, *Proceedings of SPIE*, volume 5764, pages 241–252. Composite Technology Development, Inc. (USA), SPIE, 2005.
- K. Seffen. Mechanical memory metal: a novel material for developing morphing engineering structures. *Scripta Materialia*, 55(4):411–414, Aug. 2006.
- K. Seffen, S. D. Guest, and A. D. Norman. Multistable structural member and method for forming a multistable structural member. GB Patent 0612558.7, July 2006.
- E. B. Seydel. Schubknickversuche mit wellblechtafeln. In *Jahrbuch d. Deutsch. Versuchsanstalt für Luftfahrt*, pages 233–235. E.V. München und Berlin, 1931.
- R. A. Shimansky and M. M. Lele. Transverse stiffness of a sinusoidally corrugated plate. *Mechanics Based Design of Structures and Machines*, 23(3):439–451, 1995.
- R. Szilard. *Theory and Analysis of Plates*, page 381. Prentice-Hall, 1974.
- Technical Service Department, Brush Wellman Inc. Shape distortion of copper beryllium. Technical report, Brush Wellman Inc., Cleveland, Ohio, Aug. 2004. url: http://www.brushwellman.com/alloy/tech_lit/AT0009_0696.pdf.
- S. Timoshenko and S. Woinowsky-Krieger. *Theory of Plates and Shells*, pages 367–368. McGraw-Hill, 1959.
- V. Z. Vlasov. *General theory of shells and its applications in engineering*. NASA Technical Translation F-99, 1964.

BIBLIOGRAPHY

H. N. G. Wadley. Multifunctional periodic cellular metals. *Philosophical Transactions Of The Royal Society A*, 364(1838):31–68, Jan. 2006.

W. O. Weber. Corrugated product. US Patent 3317363, Nov. 1963.

N. Wicks and S. D. Guest. Single member actuation in large repetitive truss structures. *International Journal of Solids and Structures*, 41(3-4):965–978, Feb. 2004.

C. D. Wood. Improvement in paper for packing. US Patent 1189518, Aug. 1914.

Appendix A

Bistable sandwich structures

Figures A.1a and A.1d show x - and y -direction views of two layers of an isotropic material, each of thickness t , of respective rest curvatures κ_{0x} and κ_{0y} , which have been elastically flattened in Figs A.1b and A.1e. The bending stresses thus created are labelled: the centreplane, *i.e.*, the neutral axis, of each sheet is unstretched. They are then joined rigidly together at the interface, assuming a glue of negligible thickness and negligible shear flexibility. The result is a bistable shell, of a kind described by Schultz (2005).

This sandwich shell is released in the x direction to some curvature κ_{1x} , as shown in Figs A.1c and A.1f. Now, there will also be some extension of the shell. Each layer can be considered to have stretched by a distance $\pm\varepsilon_{1x} = \pm\kappa_{1x}\frac{t}{2}$. The forces generated by this are given from Eqn 3.8, and are shown on Figs A.1c and A.1f. The tensile forces each produce a moment about the centreplane of the sandwich, given by

$$\frac{Et}{1-\nu^2}\varepsilon \times \frac{t}{2} = \frac{E}{1-\nu^2}\kappa\frac{t^2}{2} \times \frac{t}{2} = \frac{Et^3}{12(1-\nu^2)} \times 3\kappa = 3D\kappa \quad (\text{A.1})$$

Summing the moments of the forces gives the overall shell bending moment

$$M_{1x} = D [8\kappa_{1x} - (\kappa_{0x} + \nu\kappa_{0y})] \quad (\text{A.2})$$

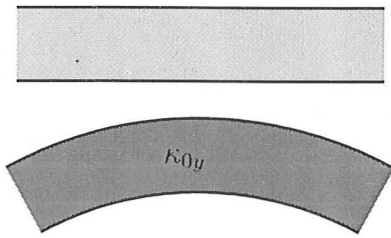
$$M_{1y} = D [8\nu\kappa_{1x} - (\kappa_{0y} + \nu\kappa_{0x})] \quad (\text{A.3})$$

Assuming that membrane stresses act to create equilibrium in the yy direction and that the shell has a zero force constraint in the xx direction, $M_{1x} = 0$, giving the equilibrium value

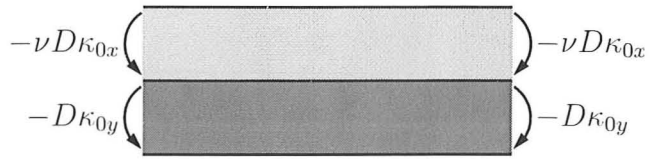
$$\kappa_{1x} = \frac{1}{8}(\kappa_{0x} + \nu\kappa_{0y}) \quad (\text{A.4})$$

Thus, the rest curvature of the sandwich sheet is of the order of 1/8 of the original curvatures of the individual layers.

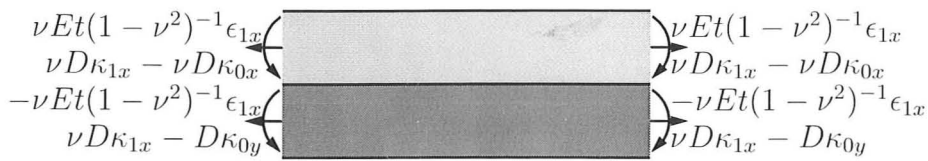
Looking along the x -axis



(a) Two separate shells, of rest curvatures κ_{0x} and κ_{0y} .

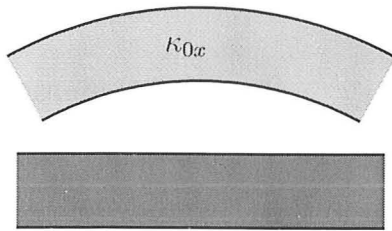


(b) The shells are flattened (with no extension or shear) before being rigidly joined on one surface.

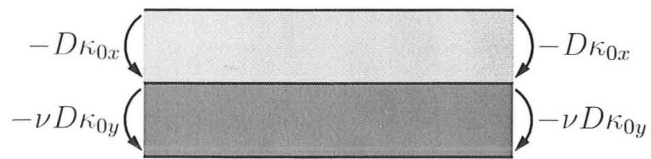


(c) The new sandwich shell is released to curve in the xx direction.

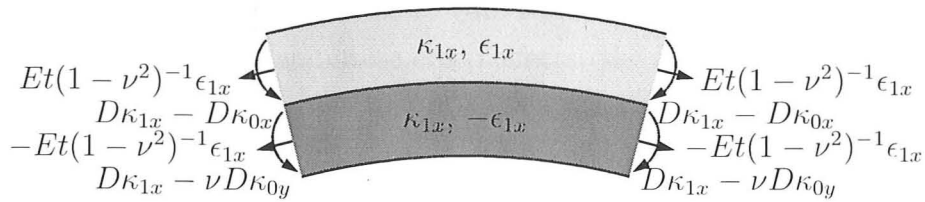
Looking along the y -axis



(d) Two separate shells, of rest curvatures κ_{0x} and κ_{0y} .



(e) The shells are flattened (with no extension or shear) before being rigidly joined on one surface



(f) The new sandwich shell is released to curve in the xx direction.

Figure A.1: A three-stage elastic analysis of a ‘sandwich’ shell composed of two pre-stressed shells whose curvatures are mutually perpendicular. The shells have a thickness t , elastic stiffness modulus E and bending stiffness modulus D (defined by Eqn 3.9). These sections are assumed to be well away from any edges, so that the stresses are those that would be found in a uniform infinite sheet. Applied forces and moments are labelled at the centreplanes of the layers.

Appendix B

Elastic properties of materials

The purpose of this appendix is to measure the elastic modulus, E , of the two materials used in this thesis: age-hardened Copper-Beryllium ('CuBe') alloy, and vacuum-formed High-Impact Polystyrene ('HIPS'). Although a pure tension test is a more accurate test for elastic modulus, we use a three-point bending test here: firstly, it is much simpler to set up, and secondly, since this thesis is almost exclusively concerned with bending stresses, it is more appropriate to the loadings that this modulus will be employed to analyse.

Experimental method

Figure B.1 shows the equipment set up for a test, with a sample installed. The load cell used is calibrated up to 100 N: in the course of the tests, the maximum load observed is 6.5 N. CuBe alloy is not known to creep at room temperature and pressure, so the load speed is not critical. Polymers, however, *do* exhibit creep behaviour, and so the speed at which the test is run is significant. The tests in this section are set to run at such a speed that they take under 30 seconds to run, slow enough that dynamic effects are not significant but fast enough to minimise creep effects: the specific speed is 1 mm s^{-1} , with ten measurements taken per second. In both cases, the test is run to a central deformation of 12 mm, by which point the force has peaked and there is clearly some slight plastic behaviour.

The three-point bending test uses a total span of 25 mm, a width of 20 mm and a total sample length of 50 mm. This is two orders of magnitude greater than either material thickness, and so we can safely assume that deformation is dominated by bending, with negligible contribution from shear. However, it is also sufficiently small that the shell does not noticeably 'droop' under its own weight while in the test rig.

In both cases, the material has a clear 'rolling' direction from its initial manufacturer, and so samples are taken from each direction (parallel and perpendicular to the rolling) to check that the material is isotropic.

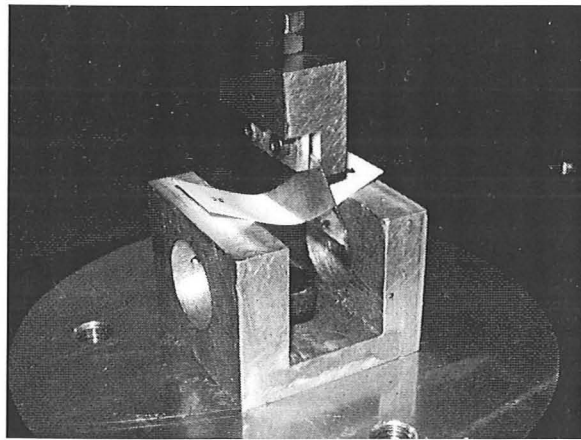


Figure B.1: The equipment for testing the elastic modulus in flexure of High-Impact Polystyrene ('HIPS'). This is a three-point bending test.

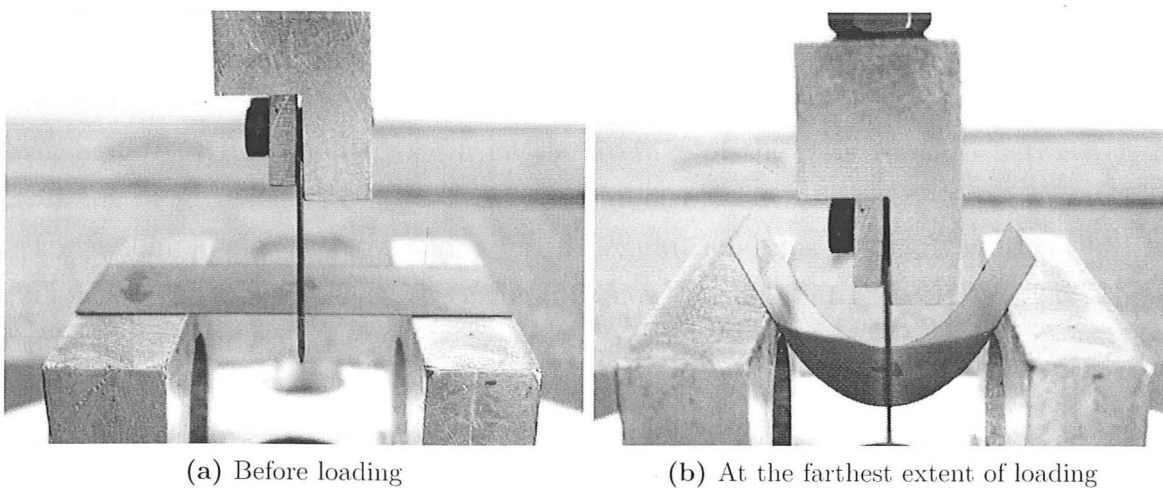


Figure B.2: The three-point bending test in progress for CuBe alloy: on the left, the sample before loading, and on the right, at the end of loading. The load is applied vertically downwards in the centre by a displacement-controlled load cell, which is calibrated to read up to 100 N.

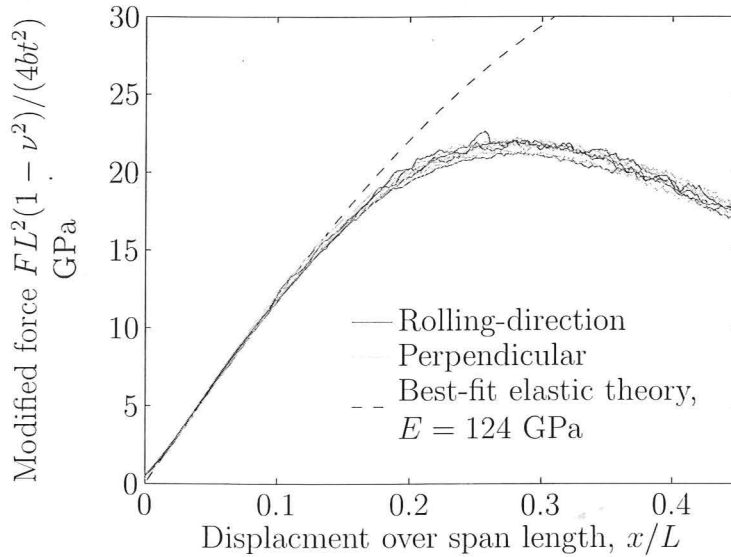


Figure B.3: Results from the three-point bending test of CuBe alloy. On the horizontal axis is the vertical displacement of the load-point, made dimensionless with respect to the total span. On the vertical axis is force, scaled with various other properties of the sample so that the initial gradient of the curve is exactly the elastic modulus, E . Note that the relation of the direction of the stress to the rolling direction of the sheet has no discernable effect.

Results: CuBe elastic properties

Figure B.2 shows the test in progress, and Fig. B.3 presents the test results. The CuBe alloy samples are age-hardened for 3 hours at 315 °C, and are each consistently 5 thousandths of an inch thick, *i.e.*, 0.127 mm. As can be seen, there is no discernable difference between the results in the two directions, nor is there much variation at all: the ‘Root Mean Squared’ (RMS) difference from the average of the data remains between 1–2 % across the range, with no outliers, and a modal error of 1.25 %.

For a sample of length L , width b and flexural modulus per unit width D , a linear equilibrium analysis will show the generally known result that the vertical displacement, d , is related to vertical load, F , by

$$d = \frac{FL^3}{48Db} \quad (\text{B.1})$$

From Eqn 3.9, we can split D into its various components. Making d dimensionless with respect to L is an obvious step, so that

$$\frac{d}{L} = \frac{1}{E} \times \frac{FL^2}{4bt^3} (1 - \nu^2) \quad (\text{B.2})$$

where E is the unknown that this test is to determine. As is evident in Fig. B.2b, however, the shell deflects well beyond linear behaviour. Consequently, Fig. B.3 presents the fully

non-linear elastic analysis for a simply-supported beam, and estimates E by finding the best fit to the data over the elastic regime. This occurs at $E = 124$ GPa: compare this to $E = 131$ GPa, as given by the CuBe manufacturer and summarised above in Section 5.1. The latter is given as a 'typical value', and minor differences may be caused by subtle differences in the performance of the equipment used for heat treatment, as well as differences between batches of material, accounting for the 5 % disagreement.

Results: HIPS elastic properties

The HIPS samples are thicker than the CuBe, generally around 0.5 mm. Each sample is been 'processed' in the same fashion as the prototypes, *i.e.*, vacuum-formed at a high enough temperature to soften the polymer. However, the vacuum-forming process leads to some variation in thickness, so that the thickness of each sample must be measured individually before testing.

The thickness has a significant effect: in the force term of Fig. B.4, there is a t^3 term. The samples ranged in thickness from 0.32 mm to 0.52 mm, which, when cubed, is a difference of a factor of 4.3. Each samples varies in thickness by up to 0.04 mm, which gives a difference of up to 50 % when cubed. For each sample, the thickness at each end and the centre is measured to 0.01 mm, and the average taken: if the thickness is accurately measured to 0.01 mm, the error when cubed can be up to 10 %. To minimise the effects of these errors, rather more samples of HIPS are tested than of CuBe, above: ten samples are taken oriented along the sheet and ten oriented across.

Figure B.4 presents the results, duly adjusted for the variation in thickness. There is no noticeable variation between the parallel- and perpendicular-oriented samples in their elastic behaviour, and no statistically significant variation in their plastic behaviour. The variation in yield in Fig. B.4 is related to the variation in sample thickness, and does not necessarily represent variation in the yield stress of the material. Given the comments above regarding the effect of thickness, the results display surprisingly little variation: the RMS error between the test results and the elastic best fit is under 9 %, dropping to under 3 % if the four outliers are omitted.

The Poisson ratio for the material was taken from Rinde (1970), as being 0.34, and given this information, the best-fit plot is calculated to lie at $E = 1.61$ GPa. In this calculation, the four 'outlier' results are neglected.

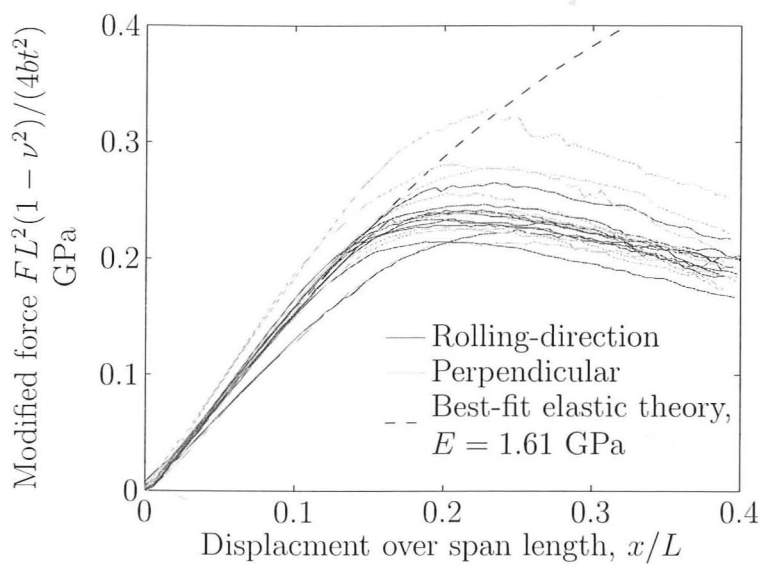


Figure B.4: Results from the three-point bending test of HIPS. On the horizontal axis is the vertical displacement of the load-point, made dimensionless with respect to the total span. On the vertical axis is force, scaled with various other properties of the sample so that the initial gradient of the curve is the elastic modulus, E . Note that the relation of the direction of the stress to the rolling direction of the sheet has no discernable effect.

Appendix C

Locking of sinusoidal corrugations

The purpose of this section is to demonstrate that when a sinusoidally-corrugated sheet, curved along its corrugations, 'locks' in the fashion shown in Section 6.2.1, the corrugations take on an elliptic shape. In other words, a sinusoidally-corrugated shell and a shell with semi-elliptic corrugations are *the same shell*, in a different state of inextensional deformation.

Consider a generic sinusoidal corrugation of trough-to-peak amplitude A and wavelength Λ , as shown in Fig. C.1a. A particular element of material is at a distance s along the material path of the corrugation from the origin, and is at location (Y, Z) , making an angle Ψ to the Y -axis. It then deforms to the locked situation in Fig. C.1b. The same element is now at position (y, z) , making an angle ψ to the y -axis. Since the material is assumed not to stretch, s remains unchanged. This appendix will assume that the locked shape is elliptical, and then prove this to be so.

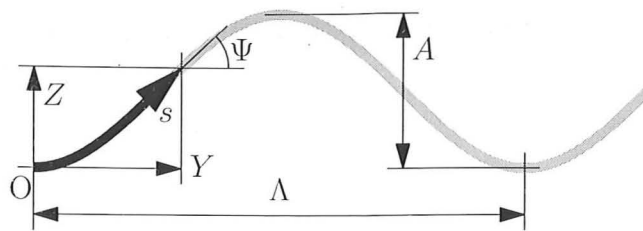
The initial, sinusoidal, corrugation is described in Y - Z space as

$$Z = \frac{1}{2}A \left(1 - \cos \frac{2\pi Y}{\Lambda} \right) \quad (\text{C.1})$$

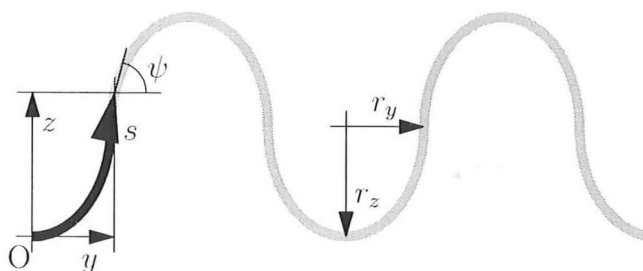
and Ψ is given by

$$\tan \Psi = \frac{dZ}{dY} = \frac{A\pi}{\Lambda} \sin \frac{2\pi Y}{\Lambda} \quad (\text{C.2})$$

The path length, s , along the corrugations from the origin to this point (Y, Z) is the



(a) The corrugations in their initial sinusoidal configuration, with amplitude A and wavelength Λ



(b) The same corrugations, to the same scale, when deformed to their 'locked' configuration

Figure C.1: An initially sinusoidal corrugation (Fig. C.1a) and its 'locked' shape (Fig. C.1b). This appendix proves that the latter shape is composed of half-ellipses, of radii r_y and r_z .

integral

$$\begin{aligned}
 s &= \int_0^Y \sqrt{1 + \left(\frac{dZ}{dY}\right)^2} dY \\
 &= \int_0^Y \sqrt{1 + \left(\frac{A\pi}{\Lambda} \sin \frac{2\pi Y}{\Lambda}\right)^2} dY \\
 &= \frac{\Lambda}{2\pi} E\left(\frac{2\pi Y}{\Lambda} \middle| - \left[\frac{\pi A}{\Lambda}\right]^2\right)
 \end{aligned} \tag{C.3}$$

where $E(\phi|m)$ is an 'Incomplete Elliptic Integral of the Second Kind', as described by, *i.a.*, Abramowitz and Stegun (1972).

The next step will be to find the 'locked' shape: we can determine final angle ψ in terms of the *initial* position (Y, Z) . Recall from Section 6.2.1 that for any specific material point, $\kappa \sin \psi$ is constant (see Eqns 6.3). The curvature along the corrugations, κ , is uniform over the shell at any specific point in time. Therefore, the ratio at any specific material point between the initial curvature and final curvature is uniform over the whole shell, and so the ratio between $\sin \Psi$ and $\sin \psi$ is, likewise, uniform over the whole shell. The curvature change at 'lock' is controlled by the curvature change at the steepest point, where ψ goes to 90° and $\sin \psi$ goes to 1. Therefore, the ratio at any point between $\sin \psi$

and $\sin \Psi$ is simply the maximum value of $\sin \Psi$, which occurs at $2\pi Y/\Lambda = \pi/2$, so that

$$\sin \psi = \frac{\sin \Psi}{\max(\sin \Psi)} \quad (\text{C.4})$$

Using the general identities that

$$\sin \theta \equiv \frac{\tan \theta}{\sqrt{1 + \tan^2 \theta}} \quad \tan \theta \equiv \frac{\sin \theta}{\sqrt{1 - \sin^2 \theta}} \quad (\text{C.5})$$

we find that

$$\sin \psi = \frac{\frac{\frac{A\pi}{\Lambda} \sin \frac{2\pi Y}{\Lambda}}{\sqrt{1 + \left(\frac{A\pi}{\Lambda} \sin \frac{2\pi Y}{\Lambda}\right)^2}}}{\frac{\frac{A\pi}{\Lambda}}{\sqrt{1 + \left(\frac{A\pi}{\Lambda}\right)^2}}} = \frac{\sqrt{1 + \left(\frac{A\pi}{\Lambda}\right)^2} \sin \frac{2\pi Y}{\Lambda}}{\sqrt{1 + \left(\frac{A\pi}{\Lambda} \sin \frac{2\pi Y}{\Lambda}\right)^2}} \quad (\text{C.6})$$

leading to an expression for the locked angle ψ ,

$$\tan \psi = \frac{\sqrt{1 + \left(\frac{A\pi}{\Lambda}\right)^2} \sin \frac{2\pi Y}{\Lambda}}{\sqrt{1 + \sin^2 \frac{2\pi Y}{\Lambda}}} \quad (\text{C.7})$$

An interesting result here is that the locked shape is a function of the initial shape only, and is independent of the initial X - X curvatures, κ_{xx} and κ_g .

To verify that this coincides with an elliptical corrugation, we now need to find ψ in terms of the material's final position (y, z) . The first quarter-corrugation of a generic corrugation is defined by the equation below, in terms of y and z and with the material having rotated to angles ψ :

$$\left(1 - \frac{z}{r_z}\right)^2 + \left(\frac{y}{r_y}\right)^2 = 1 \quad (\text{C.8})$$

$$\tan \psi = \frac{dz}{dy} = \frac{\frac{r_z}{r_y} \cdot \frac{y}{r_y}}{\sqrt{1 - \left(\frac{y}{r_y}\right)^2}} \quad (\text{C.9})$$

where r_y and r_z are the horizontal and vertical radii of the ellipse, as shown in Fig. C.1b.

The arc length s is, again, the integral over

$$\begin{aligned}
 s &= \int_0^y \sqrt{1 + \left(\frac{dz}{dy}\right)^2} dy \\
 &= \int_0^y \sqrt{1 + \frac{\left(\frac{r_z}{r_y} \cdot \frac{y}{r_y}\right)^2}{1 - \left(\frac{y}{r_y}\right)^2}} dy \\
 &= r_y E \left(\arcsin \frac{y}{r_y} \left| 1 - \left[\frac{r_z}{r_y}\right]^2 \right. \right) \quad (C.10)
 \end{aligned}$$

In order to demonstrate that this is the locked shape of the sinusoidal corrugations, we have to find values of r_y and r_z such that Eqns C.7 and C.3 are equivalent to Eqns C.9 and C.10. This occurs when

$$r_y = \frac{\Lambda}{2\pi} \qquad r_z = \frac{1}{2} A \sqrt{1 + \left(\frac{\Lambda}{A\pi}\right)^2} \quad (C.11)$$

with a relationship between the initial and final positions

$$y = \frac{\Lambda}{2\pi} \sin \frac{2\pi Y}{\Lambda} \qquad z = Z \sqrt{1 + \left(\frac{\Lambda}{A\pi}\right)^2} \quad (C.12)$$

Thus, a sinusoidal corrugation has been shown to lock to an elliptical corrugation. Likewise, starting with an elliptically corrugated sheet that is curved in the X direction, which is then coiled up in the X direction, the corrugation profile will deform, and will, at one unique instant, take an exactly sinusoidal profile.

Appendix D

Differential geometry applied to shape change: an example

This appendix presents an example of a method that uses the techniques of differential geometry to simulate inextensional deformation of a general three-dimensional shell structure. The structure is divided into a series of thin strips, and by manipulating the edge of one strip, the shape of the entire shell is determined (see Fig. D.1 for an example). Each of these strips is modelled as a thin developable shell: it can be imagined as being similar to a paper shell, in displaying negligible resistance to bending but an infinite resistance to stretch. Each strip, being developable, is defined by the two-dimensional shape that it takes when laid flat.

We begin with a line in 3D space, which could be described by its position \mathbf{x} as a function of distance along the line s , *i.e.*, $\mathbf{x} = \mathbf{x}(s)$. This line has, at any point, a tangent unit vector $\mathbf{t}(s) = d\mathbf{x}/ds$, a curvature magnitude $\kappa(s)$, a normal unit vector $\mathbf{n}(s)$ in the plane of the curvature such that $\kappa\mathbf{n} = d\mathbf{t}/ds$ and a twist $\tau(s) = (d\mathbf{n}/ds) \cdot \mathbf{b}$, where the unit vector $\mathbf{b}(s)$ is defined by $\mathbf{b} = \mathbf{t} \times \mathbf{n}$, all as outlined in Section 3.1.1.

The line on the developable shell which is being conformed to this 3D curve can be described as $\mathbf{x}'(s)$; this line is purely two-dimensional, being a description of its shape when flattened. Again, it has a tangent $\mathbf{t}' = d\mathbf{x}'/ds$ and curvature vector $\kappa_g\mathbf{n}' = d\mathbf{t}'/ds$. κ_g is the geodesic curvature, *i.e.*, the curvature of the line when the surface is flattened (which is done inextensionally, as are all operations on this surface). Note that this line cannot twist, being two-dimensional.

In being conformed to $\mathbf{x}(s)$, the shell must have some out-of-plane curvature, which we can describe as $(\kappa_{t't'}, \kappa_{n'n'}, \kappa_{t'n'})$, or the shell curvature vector $\boldsymbol{\kappa}'$. Then, the absolute curvature in 3D of the two lines must match, so

$$\kappa^2 = \kappa_g^2 + \kappa_{t't'}^2 \quad (\text{D.1})$$

Following on, the normal vectors of the curve (\mathbf{n}) and of the shell (\mathbf{n}') will be separated

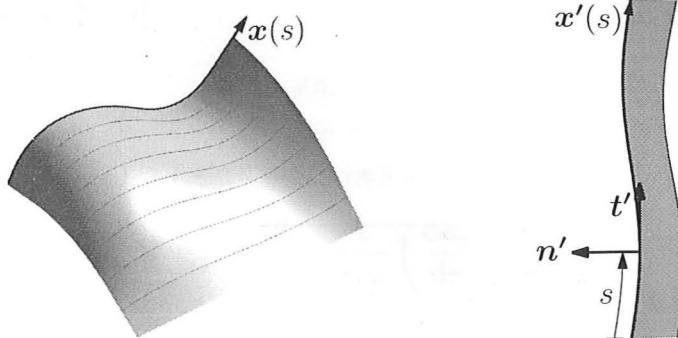


Figure D.1: A shell subdivided into developable strips. Each strip is assumed to be inextensible, with negligible resistance to bending. This appendix demonstrates how, given the flattened-out profiles of each strip, the entire shape can be controlled by the manipulation of a single edge, *e.g.*, $x(s)$. On the right is a typical strip, flattened out, showing the edge $x'(s)$. t' and n' are tangent and normal vectors.

by an angle $\theta(s)$ where

$$\cos \theta = \frac{\kappa_g}{\kappa} \tag{D.2}$$

Note, firstly, that θ can be positive or negative, but for a continuous shell, θ must be continuous. In other words, subject to the conditions developed later, there can be two possible solutions, with each solution bifurcating into two further solutions at each point at which θ is 0 or 180°. Note, secondly, that we now have a constraint on the 3D curve to which the developable surface can be conformed; at any s , $|\kappa_g|$ must be less than or equal to $|\kappa|$.

Defining θ as positive if it is the angle from n to n' in a right-handed sense about the axis t , the twist of the shell is

$$\kappa_{t'n'}(s) = -\tau - \frac{d\theta}{ds} \tag{D.3}$$

We now need $\kappa_{n'n'}$. This is constrained because the shell is developable; in other words, if we calculate the two principle curvatures $\kappa_{1'}$ and $\kappa_{2'}$, one will have a magnitude of zero. This is easiest to solve by reference to the Mohr's Circle of curvature (Fig. 3.3);

$$\kappa_{1'} = \kappa_{t't'} + \kappa_{n'n'} \tag{D.4}$$

$$\kappa_{2'} = 0 \tag{D.5}$$

$$(\kappa_{1'} - \kappa_{2'})^2 = (\kappa_{t't'} - \kappa_{n'n'})^2 + (2\kappa_{t'n'})^2 \tag{D.6}$$

$$\therefore (\kappa_{t't'} + \kappa_{n'n'})^2 = (\kappa_{t't'} - \kappa_{n'n'})^2 + (2\kappa_{t'n'})^2 \tag{D.7}$$

$$\therefore \kappa_{t't'}\kappa_{n'n'} = \kappa_{t'n'}^2 \tag{D.8}$$

So, given $\kappa(s)$, $\kappa_g(s)$ and $\tau(s)$;

$$\theta(s) = \pm \arccos\left(\frac{\kappa_g}{\kappa}\right) \quad (\text{D.9})$$

$$\kappa_{t't'}(s) = \kappa \sin \theta = \kappa_g \cos \theta = \pm \sqrt{\kappa^2 - \kappa_g^2} \quad (\text{D.10})$$

$$\kappa_{t'n'}(s) = -\tau - \frac{d\theta}{ds} = \frac{1}{\kappa_{t't'}} \left(\frac{d\kappa_g}{ds} - \frac{\kappa_g}{\kappa} \frac{d\kappa}{ds} \right) - \tau \quad (\text{D.11})$$

$$\kappa_{n'n'}(s) = \frac{\kappa_{t'n'}^2}{\kappa_{t't'}} \quad (\text{D.12})$$

We can also define the local plane of the strip, being composed of unit vectors \mathbf{t}' and \mathbf{n}' ; \mathbf{t} and \mathbf{t}' are coincident, while \mathbf{n}' and the unit vector out of the shell surface \mathbf{b}' are defined by

$$\mathbf{n}'(s) = \mathbf{n} \cos \theta + \mathbf{b} \sin \theta \quad (\text{D.13})$$

$$\mathbf{b}'(s) = \mathbf{b} \cos \theta - \mathbf{n} \sin \theta = \mathbf{t}' \times \mathbf{n}' \quad (\text{D.14})$$

We have now completely defined the shape of the developable strip: therefore, we have defined the line describing its second, formerly free, edge, and can repeat the above process to attach the next strip to this. Continuing the process, the shape of the entire shell is described.